SETCOR
Conferences & Events

Nanotech France 2015
International Conference
Proceeding

http://www.setcor.org/conferences/Nanotech-France-2015

Physico-chemical properties of Fe-doped alumino-silicate nanotubes by an isomorphic substitution of Fe^{3+}/Al^{3+}

E. Bahadori [a], E. Shafia [a], S. Esposito [b], M. Armandi [a], E. Garrone [a] and B. Bonelli[a,*]

[a] Department of Applied Science & Technology, Unit of Torino Politecnico, Corso Duca degli Abruzzi 24, Turin, Italy.
[b] Department of Civil & Mechanical Engineering, Università degli Studi di Cassino e del Lazio Meridionale, Via G. Di Biasio 43, 03043 Cassino (FR), Italy.

Abstract: Surface functionalization of inorganic nanostructures is an effective approach for enriching their potential applications. Methyl-Imogolite (MeIMO) with a chemical formula of $(OH)_3Al_2O_3SiOH$, is a an alumino-silicate nanotube material and like IMO NTs is diamagnetic and behaves as an insulator. However, doping with small amount of iron could lead to new magnetic and conductive properties. Moreover, Fe replacing Al in the outer surface of NTs, leads to interesting catalytic properties. In the present work, textural and surface properties of Fe-doped MeIMO nanotube were obtained by 1.4 wt% of Fe content in either direct synthesis (Fe-x-MeIMO) or ion exchange in post synthesis loading (Fe-IE-MeIMO) methods. Samples properties were investigated by XRD; N_2 sorption isotherms at 77 K and (DR) UV-Vis spectroscopy. According to analysis results, in a post synthesis sample occurrence of isomorphic substitution of Al^{3+} by Fe^{3+} ions is more considerable, following by the larger mesoporous volume, which confirms the loading of Fe^{3+} ions on the external surface of NT. In addition, the small proportion of Fe oxo-hydroxide nanoclusters are detectible in UV-Vis spectra of post synthesis samples comparing to direct synthesis, due to the tendency of Fe to form Fe-O-Fe bridges.

Keywords: methyl Imogolite (MeIMO); nanotubes; isomorphic substitution; Fe-doping; Ion exchanging; adsorption; synthesis.

Experimental section

MeIMO was obtained as described in the previous research [1]. Fe-x-MeIMO samples were obtained by direct synthesis as follows: a proper amount of $FeCl_3*6H_2O$ was added to 20 mM solution of $HClO_4$, then MEOS (Methyltrietoxysilane) and Al-sec-butoxide were added to the solution, stirred at room temperature for 18h, diluted to 20 mM in Al, autoclaved at 100 °C for 4 days, filtered, washed and dried overnight at 50 °C in oven.

Fe-IE-MeIMO was prepared by adding a proper amounts MeIMO powder into the aqueous solution of $FeCl_3*6H_2O$ for 24 h under stirring. The solid was then filtered, washed and dried in the oven at 50 °C overnight.

XRD patterns were obtained on a X'Pert Phillips diffractometer (Cu Ka radiation:1.541874 Å, step width: 0.02˚, time per step: 2.00s). To determine the BET SSA (Brunauer- Emmett-Teller Specific Surface Area) and porous volume quantities reported in Table 1, N_2 isotherms were measured at -196°C on samples previously out-gassed at maximum temperature of 250 °C, in order to remove water and other atmospheric contaminants which contained in the NT structure [2,3]. NL-DFT (Non Local Density Functional Theory Method) was used to determine the Pores Size.

Distributions Diffuse Reflectance (DR) UV-Vis spectra of out-gassed samples were measured on a Cary 5000 UV-Vis-NIR spectrophotometer (Varian instruments).

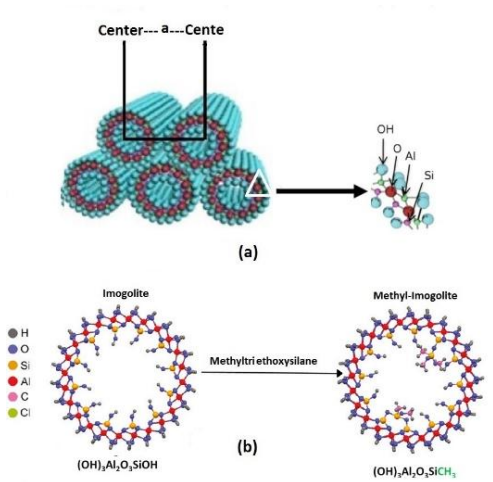

Figure 1. (a) Imogolite type NTs structure, The cell parameter *a* corresponds to the distance between the centres of two NTs within a bundle [4]. (b) Section of Imogolite and Methyl-Imogolite nanotubes, in which ferric ions can replace Al^{3+}sites [5, 6].

Results and discussion

Evidence is given of the isomorphic substitution of Fe for Al in Fe- IE- MeIMO obtained by ion exchange in post synthesis method:

i) according to UV-vis spectroscopy, both Fe-containing samples exhibit UV bands , which can be attributed to ligand-to-metal (O–Fe) charge-transfer transitions of isolated Fe(III) ions in octahedral environment [7] and to a small amount of Fe_xO_y nanoclusters;

*Corresponding author: Prof. Barbara Bonelli
E-mail: barbara.bonelli@polito.it
Tel: +39-3392803713

ii) XRD patterns of both Fe containing samples, indicates that incorporation of Fe atoms in tube structure without alteration of IMO structure is limited, which can be seen in a value of 2 theta in the first intense peaks, correlating atomic distance (Table 1). However, in Fe doped samples, the d_{100} has a slight increase in the case of post synthesis (Fe-IE-MeIMO), and a decrease in the case of direct synthesis (Fe1.4-MeIMO). Increasing the d_{100} corresponding to the cell parameter, offers the possibility of isomorphic substitution Al^{3+} in an octahedral coordination with Fe^{3+} during the post synthesis process. The small increase in the "a" value is attributed to the larger Shannon radius of isolated Oh Fe^{3+} comparing to Al^{3+}. In a case of direct synthesis Fe1.4-MeIMO, substitution of smaller Cl^- anions instead of ClO^{4-} anions in a lattice matrix during the synthesis, resulted in the smaller "a" lattice parameter [8-10].

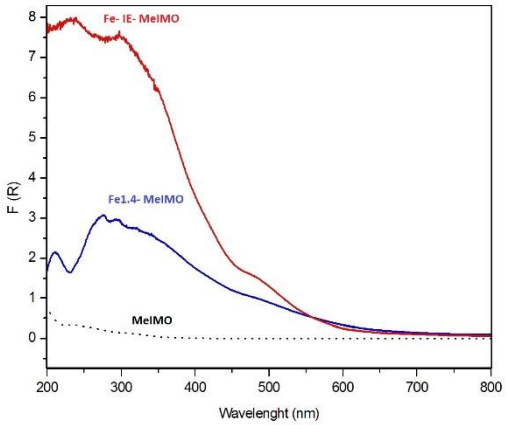

Fig. 3. UV-Vis spectra of Imogolite and Me-Imogolite, loaded with 1.4 wt% of Iron, by a means of Ion exchange process

Table 1 Samples textural properties as derived by N_2 sorption iso therms at -196 °C and low angles XRD patterns

Sample	*Fe wt%*	*BET SSA, $m^2 g^{-1}$*	*Total Pore Volume, $cm^3 g^{-1}$*	*Micropore volume $(cm^3 g^{-1})^a$*	*d_{100}, nm*	*a, $(nm)^b$*
MeIMO	---	587	0.34	0.13	2.45	2.83
Fe-IE-MeIMO	1.4	560	0.33	0.10	2.50	2.87
Fe1.4-MeIMO	1.4	579	0.30	0.19	2.37	2.74

a) As obtained by applying the *t*-plot method.
b) As calculated by applying the eq.: $a = 2d_{100}/\sqrt{3}$

Studying the BET surface analysis results are confirme the isomorphic substitution of Al^{3+}/Fe^{3+}. The comparison of the PSDs of three samples show that all samples have both micropores and mesopores, although with different relative abundance. In Fe-IE-MeIMO sample, formation of additional mesopores following by larger mesoporous volume are noticed. The larger mesoporous volume, can be attributed to changing the direction and alignment of bundles due to Fe^{3+} ions loading on the external surface of tubes, which are also in favour of an increase in an inner diameter of Fe-IE-MeIMO and consequently the high probability of isomorphic substitution of Fe^{3+}/Al^{3+} in nanotube structure.

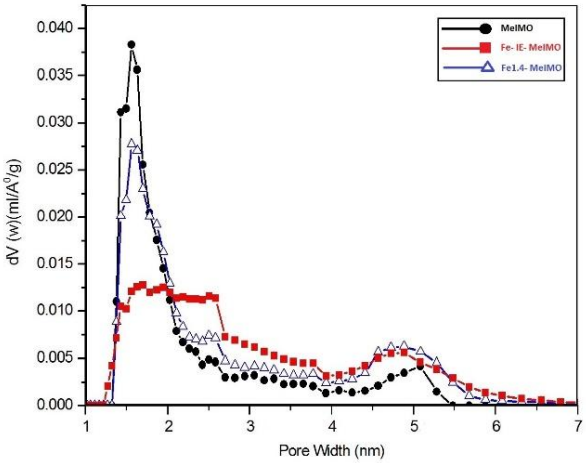

Figure 3 NL-DFT Pore Size Distributions of MeIMO NTs, obtained by applying a N_2 –zeolite kernel to adsorption branches

Conclusion

Present research concerning the synthesis and characterization of a new kind of modified aluminosilicate nanotubes (MeIMO), by iron doping, either by direct or post-synthesis reactions. Unexpectedly, the post-synthesis loading procedure led to some Al^{3+}/Fe^{3+} isomorphic substitution by means of cation exchange. Direct synthesis method proved to be very difficult, due to the presence of Fe-precursor in the synthesis medium, finally lowering the reaction yield. Consequently, the ionic exchange could be a promising method to allow doping IMO NTs not only with iron, but also with other trivalent cations that could repace external Al, without altering the synthesis medium and Fe-IE-MeIMO can consider as a highly potential material for a shape and size selective catalyst in some chemical reactions.

Refrences

[1] Suzuki, M., Inukai, K. (2010), Metal Nanot Mater, App Phy, Vol. 117, pp. 159-167.
[2] Bonelli B., Bottero, I., Ballarini, N., Passeri, S., Cavani, F., Garrone, E. (2009), J of Cat, Vol. 264, pp. 15-30.
[3] MacKenzie, K.J., Bowden, M. E., Brown, J. W. M., Meinhold, R. H. (1989), Clay & Clay Min, Vol. 37, pp. 317.
[4] Wada. S. I., Eto, A. And Wada, *K*. (1979), J of soli sci, Vol. 30, pp. 347-355.
[5] Cradwick, P. D. G., Farmer, V. C., Russell, J. D., Wada, K., Yoshinaga, N. (1972), Nat Phy Sci, Vol. 240, pp. 187-189.
[6] Farmer, V. C., Fraser A. R. (1978), Proc of Inter Clay Conf, pp. 547-554. Amsterdam, Netherlands.
[7] Wang, Y., Zhang, Q. H., Shishido. T., Takehira, K. (2002), J of Catal, Vol. 209, pp. 186-196.
[8] McBride, M. B., Farmer, V. C., Russell, L. D., Tait, J. M., Goodman, B. A. (1984), Clay Min, Vol. 19, pp. 1- 8.
[9] Inoue, K., Huang, P. M. (1984), Nature, Vol. 308, pp. 58-60.
[10] Henmi, H., Huang, P. M. (1985), Proc of 8th Inter Clay Conf. USA.

Fluid Loss Characteristics and Rheological Properties of Nano-Based Drilling Fluids

Z. Vryzas,[1*] O. Mahmoud,[2] H. Nasr-El-Din [2], V. C. Kelessidis [1]
[1]Texas A&M University at Qatar, Petroleum Engineering Program, Doha, Qatar
[2]Texas A&M University, Petroleum Engineering Program, College Station, U.S.A.
* Presenting author; zisis.vryzas@qatar.tamu.edu

Abstract

Nanotechnology has already contributed significantly to technological advances in energy industry and has the potential to revolutionalize drilling industry. Nanomaterials are considered to be among the best candidates for smart fluids formation which can improve the performance of conventional drilling fluids. The demand for more efficient drilling technologies necessitates development of innovative drilling fluids. Drilling deeper, longer and more challenging wells in harsh HPHT (High-Pressure and High-Temperature) environments is made possible by improvements in drilling technologies, including more efficient and effective drilling fluids. The key challenge in developing such drilling fluids is to maintain the stability of key fluid properties such as rheology and fluid loss particularly at higher temperatures and pressures. Formulation of novel water-based fluids under optimal concentrations, increase the efficiency of drilling operations for the maximum recovery of new and matured HPHT reservoirs. The aim is for oil industry to apply improved drilling fluid recipes, so as to achieve more efficient drilling process with a simultaneous reduction in the environmental footprint. Nanoparticles can play significant role in the development of such smart drilling fluids due to their small size which contributes to unique filtration properties.

This work focuses on lab techniques for assessing and analyzing advanced water-based drilling fluids containing iron oxide and silica nanoparticles. These nanofluids are used to reduce fluid loss in water-based drilling fluid containing bentonite. Their performance is assessed utilizing API HPHT/LPLT (American Petroleum Institute, Low-Pressure and Low-Temperature) filter press. Scanning Electron Microscope (SEM) pictures were used to analyze the nanoparticle size range. Analysis by SEM of the filter cake produced reveals their good performance by giving deep insights for their microstructure, the interfacial phenomena and the interaction between bentonite particles and the nanoparticles. Zeta potential measurements using Phase Analysis Light Scattering (PALS) method were used to assess the stability of the developed suspensions. The changes in the rheological properties of the nanofluids were measured at HTHP conditions using a standard Fann type viscometer and concentric cylinder rheometer and showed good rheological behavior.

The examined nanoparticles have the potential not only to significantly reduce the fluid losses but also to maintain the rheological properties of the fluid. Their relatively low concentration in the drilling system provides a base for more efficient, environmental friendly and safer drilling practices. Their unique characteristics are expected to play a vital role in solving many technical challenges encountered during oil and gas drilling operations.

1. Introduction

Drilling operations are time and cost consuming for the oil companies. Their success is heavily dependent on the drilling fluid (mud) that is used. Rheological and fluid loss characteristics should be examined carefully so as to achieve the optimal performance of the drilling process.

Addition of nanoparticles can improve or at least maintain their properties even at high temperatures [1]. This research aims at understanding the vital role of iron oxide and silica nanoparticles as drilling fluid additives to preserve or even improve drilling fluid properties at high temperature conditions by examining their filtration characteristics and rheological profile. This work also aims at finding out what is the optimal concentration of such nanoparticles. By formulating novel water-based fluids with optimal concentrations of the given nanoparticles, one expects increase in drilling operation efficiency with the improved filtration and rheological characteristics of these fluids.

Nanoparticles were found to be valuable additives and showed promising potential in several oilfield applications in the upstream oil and gas industry [2]. Because they exhibit different adsorption and transportation behavior in different porous media, nanoparticles have been used successfully as stabilizers in emulsions and foams, as rheology modifiers, as fluid loss additives in surfactant-polymer or water based drilling fluids, and for preventing migrating of fines in formations [3].

Drilling fluid loss is considered as the major source of capital expenditure during drilling operations.

Nanoparticles have been proved to be more effective in reducing the filtrate losses than conventional fluid loss reducer (Poly Anionic Cellulose-PAC) [4]. Nanoparticles have the potential to solve or to improve this problem predominantly by utilizing their properties, which stem from their small sizes [5]. Rheological properties and filter cake formation are important factors that affect fluid loss behaviour and subsequently formation damage particularly under HPHT conditions [6,7]. Addition of iron oxide nanoparticles have been examined and showed a slight increase in the filter cake thickness and small changes in rheological characteristics [8]. The objective of this work is to present a comprehensive experimental analysis on the implementation of iron oxide and silica nanoparticles in water-based mud (WBM) to improve filtration characteristics, by identifying their optimal concentrations in the drilling fluid system both at LPLT and HPHT conditions. Produced filter cakes were examined and analyzed with SEM technique which allows deep insights for their microstructure.

2. Experimental

2.1. Materials and sample preparation

The bentonite (Gold Seal) was supplied by Halliburton in powder form. The water bentonite suspension gives a mixture of a pH range 8-10. The iron oxide nanoparticles were purchased by Sigma-Aldrich in powder form, black in color, with a spherical shape and an average diameter of <50 nm. Nanosilica was purchased by Sigma Alrich in powder form with a spherical shape and an average diameter of 12nm. De-ionized water with pH range 6.8-7.2 was used along with the bentonite to prepare the base fluid. All the prepared samples had pH in the range of 7.9-8.3.

The preparation of the samples was carried out following American Petroleum Institute Standards, API Specifications 13A and API 13B-1 [9 & 10]. The base fluid (BF) was formulated using a bentonite concentration of 7wt. % in 600 ml de-ionized water. Different concentrations of iron oxide nanoparticles and nanosilica were used of 0.5%, 1.5% and 2.5% by weight (Table 1).

Table 1. Concentrations of produced samples.

Base Fluid (BF)	Concentration of nanoparticles, wt. %	Bentonite, g.	nanoparticles, g.
De-ionized water (600 ml)	0.0	45.161	0.000
	0.5	45.405	3.243
	1.5	45.901	9.836
	2.5	46.408	16.574

2.2. Rheological Measurements

The rheological properties of the different fluids were measured using a rotational standard Fann type viscometer at different temperatures as per API procedures and fitted to the Herschel-Bulkley model given by

$$\tau = \tau_{HB} + K\left(\dot{\gamma}\right)^{n} \quad (1)$$

uses three rheological parameters, the Herschel-Bulkley yield stress (τ_{HB}), the flow consistency index (K) and the flow behavior index (n) that shows shear thinning or shear thickening behavior. The Herschel-Bulkley rheological model has proven to be a good choice for many water-bentonite suspensions as well as for many drilling fluids and its usage is favored over the other models [11, 12]. Obtaining yield stress is a very difficult process because it depends not only on the measuring technique but also on the model used to assess the data [13].

2.3. Fluid Loss Measurements

The filtration characteristics of the drilling fluids were obtained following the API procedure. Data was collected using a standard LPLT and a HTHP filter press. A differential pressure of 300 psi and a temperature of 250°F were applied for HTHP measurements. For SEM analysis the filter cakes were dried in the oven at 250˚F for three hours before making the measurements.

2.4. Zeta Potential Measurements

The Zeta potential of the samples was determined using a Zeta Potential Analyzer (ZetaPALS) from Brookhaven Instruments Corporation. It determines zeta potential using Phase Analysis Light Scattering (PALS). The instrument's electrodes were coated with palladium, and a He-Ne laser was used as a light source. Zeta potential values used as an indicator of the stability of the examined nanoparticles in suspension.

3. Results and Discussion

3.1. Rheology

Rheological data were analyzed via the Herschel-Bulkley rheological equation. The rheogram for the 7.0% (w/w) bentonite aqueous suspensions with different concentrations of iron oxide nanoparticles at room temperature are shown in Fig. 1. It can be clearly seen that the addition of the iron oxide nanoparticles changes the rheological behavior of the nanobased fluid with respect to the base fluid. The yield stress at 25.5˚C, increases dramatically and almost quadruples from 3.41 Pa in the base fluid to

12.75 Pa, which is upon the addition of 2.5% (w/w) iron oxide nanoparticles.

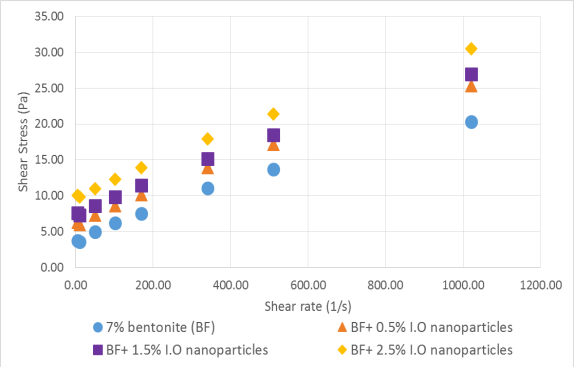

Figure 1. Rheogram for 7% (w/w) bentonite aqueous suspensions with different concentrations of iron oxide nanaoparticles at 25.5˚C.

On the other hand, samples containg nanosilica exhibited a complex pattern regarding yield stress variations (Fig. 2). At 40˚C the yield stress showed an increase for all the different concentra-tions used, but at 60˚C the yield stress decreased and reached the lowest value of 2.1 Pa upon the addi-tion of 0.5% silica nanoparticles.

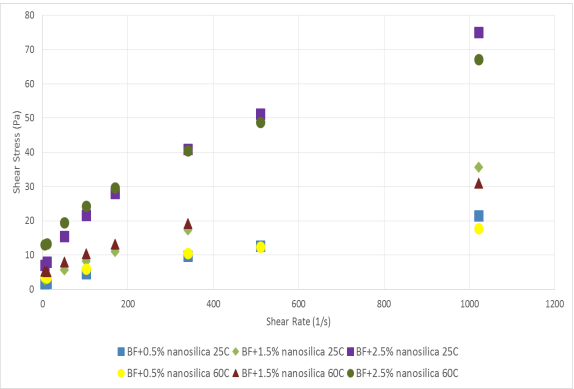

Figure 2. Rheogram for 7% (w/w) bentonite aqueous suspensions with different concentrations of silica nanopowder at different temperatures.

3.2. Fluid Loss Measurements

LPLT filtration results for samples containing iron oxide nanoparticles are shown in Table 2. Addition of iron oxide nanoparticles causes reduction of fluid loss for all samples. More specifically, the base fluid had a 30-minute filtrate volume of 10.9 ml. The sample with 0.5% iron oxide nanoparticles improved the filtration loss to 9.8 ml (10% less than the base fluid). The samples with 1.5% and 2.5% iron oxide recorded 9.1 ml and 8.7 ml fluid loss respectively, resulting in 16.5% and 20.2% reduction in the filtrate volume respectively.

In contrast, samples containing silica nanoparticles (Fig. 3) exhibited a significant increase in the filtration volume with the biggest to be upon the addition of 2.5% nanosilica with 57.8% increase compared to the base fluid. Addition of 0.5% and 1.5% of nanosilica resulted in an increase by 54.1% and 46.8% respectively.

Table 2. Filtration characteristics for the different samples containing iron oxide nanoparticles at LPLT.

Sample / % iron oxide (w/w)	0%	0.5%	1.5%	2.5%
Filtration volume at 30 min (ml)	10.9	9.8	9.1	8.7
Uncertainty, (ml)	± 0.2	± 0.2	± 0.2	± 0.2
Fluid loss change %	N/A	-10.0	-16.5	-20.2

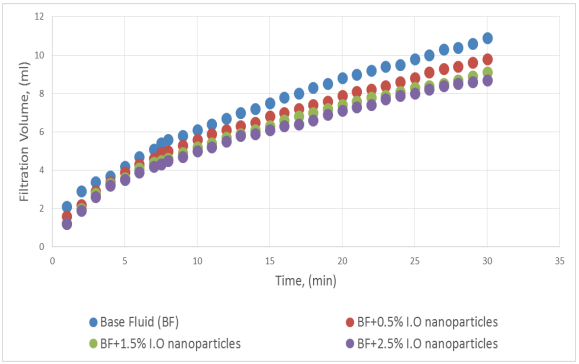

Figure 3. Filtration characteristics at LPLT conditions of samples containg different concentrations of silica nanoparticles at 30 min test.

Filtration results for samples containing iron oxide nanoparticles at HPHT conditions are shown in Fig. 4. Addition of 0.5 wt.% iron oxide results in a significant improvement in the filtrate volume by 42.5% compared to the base fluid. In contrary, at HTHP static conditions addition of 0.5 wt.% silica nanopowder adversely affect the filtration characteristics with an increase in the filtration volume by 13% compared to base fluid (Fig. 5).

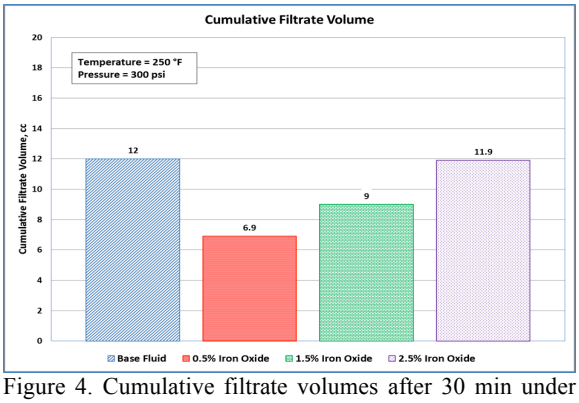

Figure 4. Cumulative filtrate volumes after 30 min under static conditions at dffferential pressure of 300 psi and a temperature of 250˚F for samples containing different cincentrations of iron oxide nanoparticles.

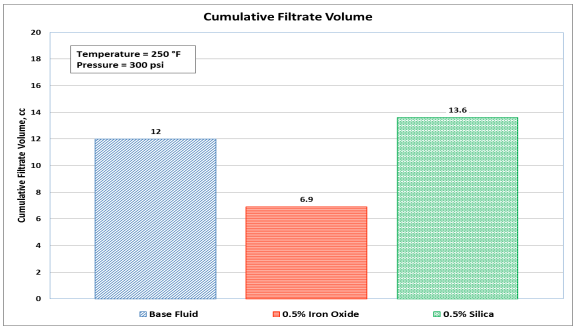

Figure 5. Comparative cumulative filtrate volumes after 30 min under static conditions at dffferential pressure of 300 psi and a temperature of 250˚F, for BF, BF+0.5% iron oxide nanoparticles and BF+0.5% silica nanoparticles.

3.3. Scanning Electron Microscopy (SEM)

The homogeneous and well textured mudcake reveals another positive characteristic of the nano-based fluids. The well dispersed mudcakes that are created from the fluids containing iron oxide nanoparticles demonstrate their high potential for decreasing drilling and production problems that are caused from poor mudcakes. The interpretation of the SEM images (Fig. 6) produced from the HPHT test from samples containing iron oxide nanoparticles, shows that the filter cake of the 0.5 wt.% iron oxide nanoparticles has a smoother surface compared to that formed using the base fluid. Another noticeable point is that small agglomerates have been formed between the bentonite and iron oxide nanoparticles which can affect the flow characteristics of the drilling fluid.

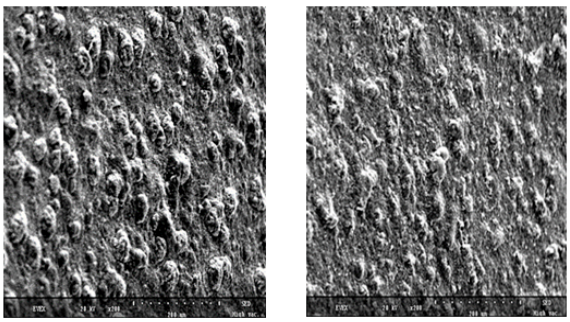

Figure 6. Scanning Electron Microscope (SEM) images, from the mudcake at HPHT conditions for base fluid (left) and upon the addition of 0.5% (w/w) iron oxide nanoparticles, at 200µm magnification (right).

3.4. Zeta potential Measurements

Zeta potential measurements of water-bentonite suspensions with different cocnentration of nanoparticles and at different temperatures showed that the iron oxide nanoparticles were stable in colloidal suspensions, whereas samples containing silica nanopowder were unstable under different temperatures (Fig. 7 and Fig. 8).

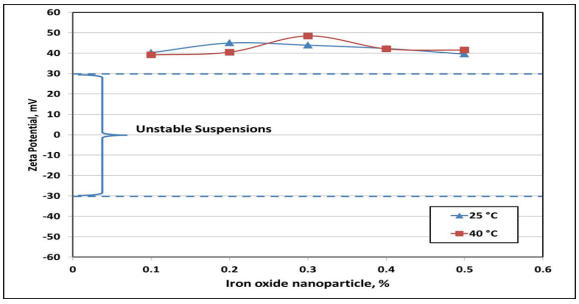

Figure 7. Zeta Potential of water - 7% bentonite suspensions containing iron oxide nanoparticle samples at different concentrations (0.1, 0.2, 0.3, 0.4 and 0.5 Wt%) at 25°C and 40°C.

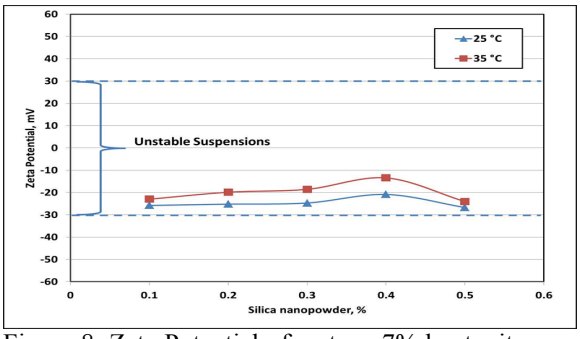

Figure 8. Zeta Potential of water - 7% bentonite suspensions containing silica nanopowder samples at different concentrations (0.1, 0.2, 0.3, 0.4 and 0.5 Wt%) at 25°C and 35°C.

4. Conclusions

The experimental research conducted hereby, illustrated the successful application of iron oxide nanoparticles in improving mud filtration characteristics in porous media using WBM. The main conclusions that can be extracted from this work are:

- Iron oxide nanoparticles were stable in colloidal suspensions of de-ionized water at different temperatures, have positive charge and improved filtration characteristics. Apparently at these concentrations, the net repulsive and attractive forces were in a ratio such that the clay platelets aligned in configurations which decreased drastically the filter cake permeability, which led to improved filtration characteristics.
- Samples containing silica nanopowder were not stable at different concentrations and had negative charges. These characteristics of silica nanopowder adversely affect the clay platelets configuration resulting in a lower efficiency filter cake with high fluid losses.
- At HPHT conditions iron oxide nanoparticles are more efficient at lower concentrations. Maximum reduction of filtration loss achieved upon the addition of 0.5 wt.% iron oxide nanoparticles, which proved to reduce filtrate losses by 42.5% compared to the base fluid.

- At LPLT conditions higher fluid loss reduction experienced at higher concentrations of iron oxide nanoparticles.
- Filtration behaviour both at LPLT and HPHT conditions of samples containing silica nanoparticles is affected negatively for all the different concentrations of nanosilica tested.
- Rheological measurements at different temperatures showed changes in the rheological properties and especially in the associated yield stress for iron oxide nanoparticles. The changes are not excessive, allowing their utilization plausibly without using additional rheological additives.
- Drilling fluid samples containing nanosilica at different concentrations demonstrated slight rheological changes with the most important to be the reduction in the yield stress for all the produced samples at 60˚C.
- Analysis of the produced filter cake images by SEM, showed that addition of iron oxide nanoparticles lead to smoother surfaces compared to that formed using the base fluid. Furthermore nanoparticles tend to agglomerate with the bentonite particles which may cause a huge impact in the drilling fluid flow characteristics.

Acknowledgement

The authors would like to acknowledge Qatar National Research Fund (a member of the Qatar Foundation). This publication was made possible by the NPRP award (NPRP 6 - 127- 2 - 050).

References

[1] Jung, Y., Barry, M., Lee, J., et al. 2011. Effect of Nanoparticle Additives on the Rheological Properties of Clay Based Fluids at High Temperature and High Pressure. Paper AADE-11-NTCE-2 was presented at the AADE National Technical Conference and Exhibition, Houston, Texas, 12-14 April.

[2] Amanullah, M., Yu, L., 2005. Environmental Friendly Fluid Loss Additives to Protect the Marine Environment from the Detrimental Effect of Mud Additives", Journal of Petroleum Science and Engineering 48, 199-208.

[3] Hoelscher, K.P., Young, S, Friedheim, J., and De Stefano, G., 2013. Nanotechnology Application in Drilling Fluids. Paper presented at the 11th Offshore Mediterranean Conference and Exhibition, Raven-na,

[4] Ragab, A., Noah, A., 2014. Reduction of Formation Damage and Fluid Loss Using Nano-sized Silica Drilling Fluids, Pet. Tech. Develop. Journal, Vol.2., 75-88.

[5] Contreras, O., Hareland, G., Husein, M., et al. 2014. Application of In-House Prepared Nanoparticles as Filtration Control Additive to Reduce Formation Damage. Paper SPE 168116 presented at the SPE International Symposium and Exhibition on Formation Damage Control, Lafayette, Louisiana, 26-28 February.

[6] Elkatatny, S. M., Mahmoud, M., Nasr-El-Din, H. A., 2012. Characterization of Filter Cake Generated by Water-Based Drilling Fluids Using CT Scan. Society of Petroleum Engineers. doi:10.2118/144098-PA, SPE Drilling & Completion, Vol.27., 282-293.

[7] Elkatatny, S. M., Mahmoud, M., Nasr-El-Din, H. A., 2013. Filter Cake Properties of Water-Based Drilling Fluids Under Static and Dynamic Conditions Using Computed Tomography Scan. Journal of Energy Resources Technology, doi: 10.1115/1.4023483 135(4):042201.

[8] Vryzas, Z., Arkoudeas, P., and Kelessidis, V.C., 2014. Improvement of Drilling Fluid Flow Parameters Using Nanoparticles for Optimization of Drilling Process. Paper presented at the International Conference on Safe and Sustainable Nanotechnology, Phitsanulok, Thailand, 14 – 17 October.

[9] American Petroleum Institute Specifications 13A. 1993. Specification for Drilling Fluid Materials.

[10] American Petroleum Institute Specifications 13B-1. 2003. Recommended Practice for Field Testing Water-Based Drilling Fluids, Washington, DC.

[11] Kelessidis, V.C., Maglione, R., 2008. Yield Stress of Water-Bentonite Dispersions, Colloids and Surfaces A: Physicochem. Eng. Aspects 318, 217-226.

[12] Kelessidis, V.C., Maglione, R., Tsamantaki, C., Aspirtakis, Y., 2006. Optimal Determination of Rheological Parameters for Herschel–Bulkley Drilling Fluids and Impact on Pressure Drop, Velocity Profiles and Penetration Rates During Drilling, Journal of Petroleum Science and Engineering, Vol.53, 203-224

[13] Amanullah, M., Arfaj, M., Abdullatif, Z., 2011. Preliminary Test Results of Nano-based Drilling Fluids for Oil and Gas Field Application, Paper SPE/IADC 139534 presented at the SPE/IADC Drilling Conference and Exhibition, Amsterdam, The Netherlands, 1-3 March.

[14] Zakaria, M., Husein, M., Hareland, G., 2012. Novel Nanoparticle-Based Drilling Fluid with Improved Characteristics, Paper SPE 156992 presented at the SPE International Oilfield Nanotechnology Conference, Noordwijk, The Netherlands, 12-14 June.

Effects of Nanotechnology Materials on Architectural Design – Applications, Possibilities and Future Trends

N.K.Parthenopoulou[1,3], M.Malindretos[2,3]

[1]Architect Engineer (Diploma, A.U.Th.), M.B.A. University of Macedonia, MSc in Construction Management A.U.Th., PhD Candidate in Architectural Design and Architectural Technology
[2]Professor of Architectural Design and Architectural Technology
[3]5th Department of School of Architecture, Faculty of Engineering, Aristotle University of Thessaloniki, University Campus, Postal Code 541 24, Thessaloniki

Abstract: Materials have been affecting architectural design since the beginning of human civilization and architectural expression. In the 20th century *Le Corbusier* quoted that a "house is a machine for living in". Nowadays, the 21rst century leads towards a new correlation: "a house can be a living machine, a living organism". The use of advanced technology has provided a wide range of possibilities in implementing architectural design. Nanotechnology in construction materials enables high performance in terms of energy, light, security and intelligence (Leydecker, 2008). Furthermore provides new, innovative and revolutionary materials that can alter design and performance of buildings. This has led to the launch of Nanoarchitecture, where nanotechnology integration concerns not only the use of nanomaterials and manipulation techniques but also the reconsideration of forms and design methods – ultra high performance buildings (dynamic, interactive) (Johansen, 2002). In this sense, external surfaces can react and adapt to the environment, featuring the qualities of self-assembly, self-healing and self-repair. Nanomaterials are proven to be very effective in aiding structures that suffer climatic strain both in performance and economy over time (Parthenopoulou, Angelides, 2010) and in enhancing existing structures. Throughout research in existing and potential applications of nanotechnology and use of smart materials in architecture, this study demonstrates the level of influence of nanomaterials on architectural design and attempts at setting the basis for proposing an innovative system of outer "skin".

Keywords: nanomaterials, nanoarchitecture, construction applications

Figure 1. Architectural nanotechnology projects: NanoVentSkin (left) is a surface system that consists of nanoturbines that filter the air and produce energy and Carbon Tower (right) is made entirely out of carbon nanofibers.

***Note:** This paper is a part of a dissertation research which is in progress under the supervision of the following advisory committee:

- M. Malindretos, Professor AUTh (School of Architecture),
- N. Kalogirou, Professor AUTh (School of Architecture),
- S. Logthetidis, Professor AUTh (School of Physics).

Outline

This paper outlines briefly a part of our research which is under development at the 5th Department of School of Architecture (Aristotle University of Thessaloniki, Faculty of Engineering).

The scope of the current research is to find the degree of influence (influence, affect or determine) which nanotechnology may have on architectural design of buildings and other infrastructure.

Our hypothesis expresses that since building materials are the inclusive means for expressing architectural ideas and realizing proposals for buildings, they could have severe influence on forms, structures, function, rhythm and other factors of architecture.

The Role of Material

Creating and implementing an idea comes as a result of a procedure, a *temporary effort in order to produce a unique product or result*. In this sense the "product" of architectural creation is considered as a project and architectural design is the continuous and dynamic process that follows a circular or a spiral route (Diagram 2). Materials traditionally belong to the implementation stage of the design cycle but they can enter from the beginning whereas they can also constitute the inspiration of the idea. They affect structure, form, aesthetics, cost, construction methods and techniques, as well as lifespan and performance of a specific construction. Materials are the means by which ideas are realized and architecture expresses itself.

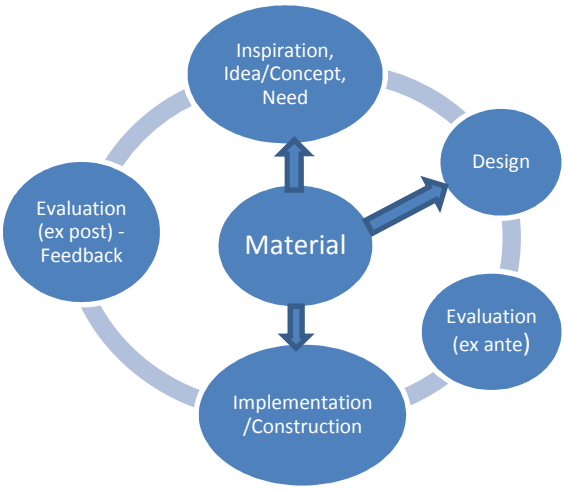

Diagram 2. 5 stage architectural design cycle.

Architects nowadays demand innovative materials that can combine high quality, performance and flexibility in serving the design needs. Not only in terms of economy, energy efficiency and quality of living in buildings but also in terms of producing structures that once was impossible. New culture of materials has ex post and ex ante effects: they can improve/restore existing buildings and they can create innovative new ones.

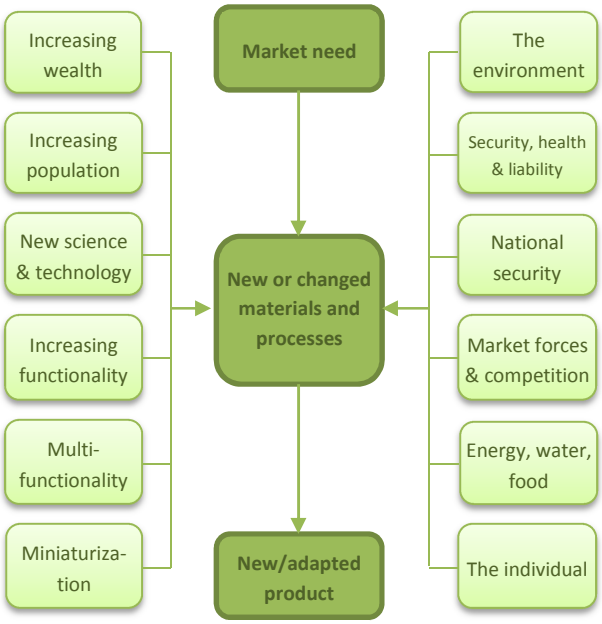

Diagram 1. Above are the forces of change that lead to the development of innovative new products (Ashby, Ferreira, & Schodek, 2009).

Nanotechnology Materials

Manipulation of materials at the nanoscale (10^{-9}m) has led to the development of new and/or improved properties, mechanical and chemical (PhysicsAuthGR, 2010). At nanoscale level, materials are more chemically reactive with stronger electrical properties and here quantum influences are dominant, affecting their optical, electrical and magnetic behaviour. Nanomaterials such as carbon nanotubes, nanofibers and organic electronics have revolutionized technology providing new abilities and increment existing ones.

Electron Microscope has provided knowledge of how nature has developed interesting properties i.e. the lotus effect, the mussels, the geckos, the morpho butterfly, some species of starfish etc. Those properties give the ability of self-cleaning, durable anchorage in the water, attachment to every surface, or even a strong colour effect that has nothing to do with pigments (Schulenburg, 2007, Leydecker, 2008). Science has already been utilizing this knowledge in various sectors of industry and especially in medical applications and electronics. Following this trend, the field of construction

industry has great potential of gaining ground in energy efficiency, cost reduction and sustainability.
Nanomaterials can be produced by "top down" and "bottom up" techniques. They can be distinguished in categories depending on how many dimensions are in nanoscale: materials with no dimensions (nanoparticles), one nanoscale dimension (nanofibers, nanotubes), two (nanocoatings) and three dimensions (quantum dots, nanocrystals, colloids) (NanoWerk, 2014).

Nanomaterials in Architecture and Construction

As materials evolve in this concept, architectural design and construction will follow this evolution as well. Nanotechnology presents the ability of change in the way we build throughout altering the basic properties of matter. For instance structures can be built by "bottom up" techniques because materials like carbon nanotubes have the capacity of self-assembling. Nanotechnology affects deeply architecture and construction industry on all scales. Therefore architecture will be able to operate at optimum levels. As new materials and manufacture processes are discovered, "nanoarchitecture" is emerging and this will unleash the imagination towards:

- discovering, production and use of new materials with integrated adjustment mechanisms to meet a prescribed statute of requirements,
- upgrading existing materials enriching them with new algorithms that will withdraw the desired physical and mechanical properties from a machine,
- developing "healing" materials, which will be able to restore failure from earthquakes in bearing structures, flaws or cracks due to aging or wear, erosion, damage from natural disasters or caused by human factor (bombings, terrorism etc.), or to enhance energy efficiency of existing buildings and other structures,
- producing materials for protection of structures, whose value and age makes them irreplaceable cultural property,
- revealing new forms that are now becoming possible and feasible because of the inherent properties of materials and can create complex structures and save weight, mass and energy in the implementation of plans,
- adding significant contribution at the climatic transformations that occur throughout the buildings.

If we take buildings as being climatic transformers, i.e. machines that alter the external environment in order to create quality climate conditions for living, working and resting within the interior, then we expect nanomaterials to play a major role in remodelling this climate. And, most important, they will achieve that consuming the energy which exists within the environment of buildings. Nowadays, large amounts of energy are spent to ensure thermal comfort inside buildings (heating, cooling, ventilation) taking the external climatic environment and partly modifying it with the use of energy. Using nanotechnology and nanomaterials this will be made possible, i.e. to transform the external climatic environments using the free energy that exists outside or inside of buildings. Paint, glass, frames, coatings, flooring and furnishings can be programmed through a holistic assurance system of quality requirements. All the above will affect dramatically the nature and function of materials, structure methods, construction techniques, speed of production (materials)/project implementation (building construction), as well as returns on investments and use capital. The most important is that it will significantly affect architectural morphology, rhythm, interior design, as well as urban design, planning and programming of urban life and development.
In architecture, two fundamentally different design approaches prevail when dealing with materials and surfaces: honesty of materials – "what you see is what you get": this approach is favoured by those architects for whom authenticity is a priority and who value high quality materials, and fakes – artificial surfaces that imitate natural materials: are chosen for cost reasons. In future, a third option will be available: functional nanosurfaces, emancipated from underlying material: the properties of such ultra-thin surfaces can differ entirely from the material they enclose and can be transparent and completely invisible. Additionally, it is possible to generate nanocomposites with new properties: nanoparticles or other nanomaterials are integrated into conventional materials so that their characteristics are improved and can be accorded new functional properties or even be made multifunctional (Leydecker, 2008).
Nanomaterials expand design possibilities. Aesthetic, functional and emotional qualities are expressed more easily and control is enabled, even upon the aging process, which gives a dynamic to the aesthetics of surfaces. The bright colour fully reflects the architectural concept. Pure forms and volumes are the objective at several architectural projects. Cleanliness of surfaces is of great importance when the target concept is a dialogue/contrast with the environment or the light-and-shadow play, which is degraded when surfaces are covered with dirt.
Once LeCorbusier assimilated the house with "a machine to live in", now at the beginning of 21rst century this leads to a new relationship that takes the building as a living organism.

As technology evolves, the field of molecular engineering presents a new frontier for architecture. Buildings are designed, developed and operate as a living organism. What was considered until recently a myth and fantasy is now a reality, and what today seems impossible will be reality in the near future (Johansen, 2002).

Originally, nanotechnology enables materials with high performance in terms of energy, light, security and intelligence. In the next stage, the growth of carbon nanotubes and other revolutionary materials could alter design and performance of buildings. For example, the distinction between the carrier body and the outer surface can be removed as new and very strong materials function simultaneously as a bearing structure and surface finish. Nanotechnology in serving Architecture derives the Nanoarchitectural style. "Nanoarchitecture" essentially means the use of nanotechnology practices in architecture. The integration of nanotechnology may involve either the use of nanomaterials and techniques, or reconsideration of forms and design methods. Construction projects that could not be realized with conventional materials now they become possible. The size of required materials is smaller, their assembly time is shorter and their lifecycle is considerably expanded. Augmented features of many materials launch design, enabling the most unrealistic projects and offering innovative solutions.

Buildings are now designed in order to interact with nature. The possibility of development of Ultra High Performance Buildings (dynamic, interactive), with an internal logic, is also given. These buildings maintain stability through negative feedback interactions and promote their development by applying positive feedback (Johansen, 2002). In this sense, the building can be programmed to monitor the environment (internal or external) and to adapt or change its form so that it is in harmony or in symbiotic relationship with nature and man. The cooperation of the sciences of biology and nanotechnology can provide biological characteristics in materials, structure and morphology. Surfaces can metabolize, respond and adapt to the environment, and have the properties of self-assembly, self-healing and self-repair.

Nanotechnology has already been used in construction materials such as concrete (stronger, more durable, easy to assemble), steel and metals (improved mechanical properties) and glass (self-cleaning). The use of nanotechnology leads to more effective usage of materials and reduction of environmental pollution deriving from their production processes. Nanomaterials allow constructors to offer better guarantee for their projects and customers to enjoy less maintenance cost (PRLog, 2007). The use of nanotechnology especially in the improvement/protection of materials that suffer climatic strain can be proven cost effective and efficient in enhancing mechanical properties and expanding life cycle (Parthenopoulou et al, 2010).

Construction nanomaterials can be categorized as follows (Zhu et al, 2004):

a) high performance structural materials: conventional materials such as steel and concrete reinforced with nanoparticles,
b) functional coatings and thin films: coatings augmented with properties such as self-cleaning, anti-bacterial properties, etc,
c) filler nanoparticles, additives and admixtures: carbon nanotubes, metal and non-metal oxides (e.g., TiO_2, SiO_2, $CaCO_3$),
d) environmental and performance monitoring Sensors,
e) new materials and new applications.

Materials in construction reinforced with nanoparticles may include low maintenance windows, long endurance and resistant to scratches floors, improved and high duration paint, healthy and safe climates (indoor), antimicrobial steel surfaces, anticorrosive metal coatings, concrete admixtures for self-healing and strength, nano-insulating materials of better energy efficiency and UV protective membranes.

Potential and Existing Architectural Applications

During our research we came across several interesting and intriguing projects of architectural activity. A brief review of the most innovative applications is necessary in order to prove the hypothesis, i.e. the degree of the effect of nanotechnology on architectural design and creation.

Carbon Tower:

A project proposal by Peter Testa, a building of 40 storeys,

Carbon Tower is made entirely from carbonfibers.

If this is built it would be the lightest and yet the strongest building of this type. The basic format is not complex: it is a cylindrical building which consists of 40 strands of

Figure 2. Carbon Tower - model (Peter Testa Architects)

carbonfibers (about 1 inch wide and nearly 650 feet long) that are arrayed in a helicoidal, or crosshatch, pattern. Filling the structure between floors is an advanced glass substitute – a kind of transparent foil. A pair of ramps on the building exterior offers circulation and it further stabilizes the structure.
In this example it is obvious that the form is more flexible and with plasticity, in comparison to a conventional tower – skyscraper. Its light weight is apparent and the use of transparent fillings gives the impression that this structure is free of constraints.

eTree:
Designed by Dennis Dollens (founder of Genetic Architecture Program of ESARQ), the eTree is a self-shading Tower and a project that is under study. It consists of a central spine whose structural code lends itself to multiple design paths resulting in different kinds of structural leafing and branching forms. While prominent in the developmental stages of the tower's panels, the eTree is eventually repressed in favour of the load-bearing monocoque façade supporting the building and held in compression and tension by the fifteen floor planes. The linking, chainmail-like components are part of an on-going search for load-bearing panels that can take on environmental performance duties - such as filtering and ventilation - as well as, in other design formulations, housing sensor-embedded monitoring. Additionally, the panel designs adjust easily to produce pockets where plant, algae, or other biological agents may be grown in living facades (Dollens, 2014).
Plasticity and movement is the visual outcome here as well. In addition, this concept is freed from the usual load bearing structure and borrows support principles from nature (trees in particular). The outer skin is serving other purposes as well, which are environmentally oriented.

Figure 3. eTree LA Tower (Dollens, 2014)

NanoHouse:
The NanoHouse™ Initiative is a collaboration scheme between Australian architects, engineers and designers for the creation of an energy efficient house through the possibilities that offers nanotechnology. The objective is to create a living environment, which allows climate control with the use of nanoengineered glass panels. Windows and walls will keep rooms cool with heat reflecting paint and coatings. Glass will shut out light at the flick of a switch and will clean itself in the rain. Kitchen and bathroom surfaces will be antibacterial (Masens, 2002). This project was inspired by Dr Masens (Nanoscale Technology Institute, Sydney) and held by the architect J.Muir.
In this case the use of glass is extended and with ease, as glass panels are the medium to achieve climate control. This could mean that glass can be used without limitation and without the collaboration of supporting systems (for instance air conditioning systems or shades).

Figure 4. The NanoHouse (Muir)

Soft House:
The "Soft House" was designed by KVA Matx. Many of the fixed surfaces found in conventional houses, are here replaced by semi-transparent, mobile energy collector curtains with embedded thin photovoltaic films. Central element of this project is a cylindrical curtain that plays the role of a skylight. Rechargeable batteries are enclosed in the curtain and can either store energy for later use or broadcast it elsewhere, while lighting elements in the fabric allow stored energy to be transmitted as light. The flexibility of the fabric allows the tubular structure to be used in many ways and direct the light to any area within the home. Even if placed lower, it can completely redefine the interior of the house, creating a completely independent and autonomous living and work area. These materials if placed in a house of

1,200 square feet (~ 110m^2) can produce 16 kilowatts DC or AC (KVA, 2009).
More than an energy generator, these curtains serve the architectural need for dynamic and ad hoc transformation of interior spaces, altering the inner spatial environment at will.

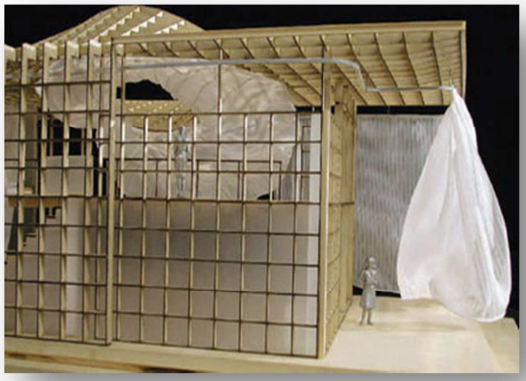

Figure 5. "Soft House" model (KVA, 2009)

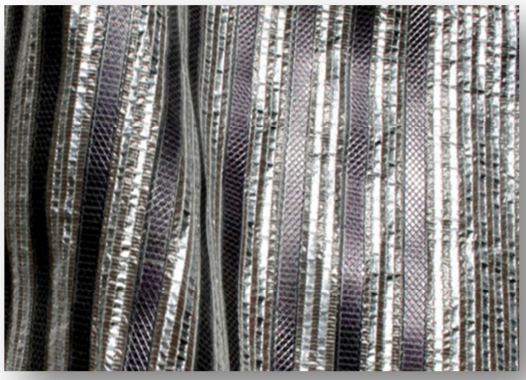

Figure 6. Photovoltaic curtain detail (KVA, 2009)

Nano Vent Skin:
This surface was designed by Mexican designer A.Otegui. It uses wind turbines in nanoscale (nanoturbines). The Nano Vent Skin consists of different types of microorganisms that can convert solar and wind energy into renewable energy and can absorb CO_2 from the atmosphere. The outer skin of the structure absorbs sunlight through an organic photovoltaic skin and transfers it to the nano-fibers, inside the nano-wires, which then is sent to storage units at the end of each panel. Each turbine on the panel generates energy by chemical reactions on each end where it makes contact with the structure. Polarized organisms are responsible for this process on every turbine's turn. The inner skin of each turbine works as a filter absorbing CO_2 from the environment as wind passes through it. Every panel has a sensor on each corner with a material reservoir. When one of the turbines has a failure or breaks, a signal is sent through the nano-wires to the central system and building material (microorganisms) is sent through the central tube in order to regenerate this area with a self-assembly process (NOS, 2008).

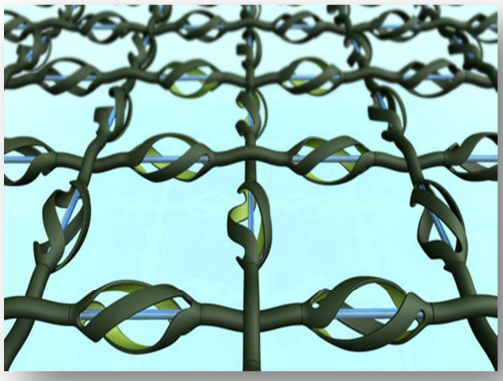

Figure 7. Surface detail (NOS, 2008)

Figure 8. NanoVentSkin on a building.

Highly innovative and energy efficient, this external skin-like surface (NanoVentSkin) protects the structure and also produces energy and filters air.
It may not serve aesthetic needs but provides energy autonomy and gives the opportunity for high performance.

Solar Ivy:
Mimicking the form of ivy and its relationship with the environment, this system is called SolarIvy. It was designed by Samuel and Teresita Cochran and consists of thin solar photovoltaic panels that resemble the leaves of ivy and generate power. This "skin" can be incorporated on the side of a building. When the sun is shining or the wind blowing, it can generate power (SolarIvy, 2011).
SolarIvy enriches the appearance of a building / structure, when it is applied on a façade, and simultaneously has the ability of providing energy

functioning as photovoltaic system. It is a bi-functional decorative element for external surfaces.

Figure 9. Example of application – 3d model (SolarIvy, 2011)

Figure 10. Form of ivy leafage (SolarIvy, 2011)

Phase Changing Materials (PCM) – Glass Façade Sur Falveng:

The Sur Falveng building (retirement home in the Swiss Alps) has 20 apartments with south orientation. All of them have openings in the south elevation and are heated actively or passively. The glass panels consist of 8cm composite glass element - this contains in the middle a hydrated filler material which functions as a latent solar heat storage medium and protects the room from overheating. The heat capacity of that element is equivalent to the heat capacity of a concrete wall 15cm thick. The glass façade becomes transparent when the material passes from the state of solid to liquid. Therefore, the change of state of the material has a direct impact on the appearance of the building (Leydecker, 2008).

This example shows the direct effect of the certain material on the aesthetics, as the appearance (façade) of the building has become dynamic. The former changes according to the climatic conditions: transparent when the weather gets warmer and non-transparent when the outside temperature drops.

Figure 11. Glass facade (148m^2) of Sur Falveng (Leydecker, 2008)

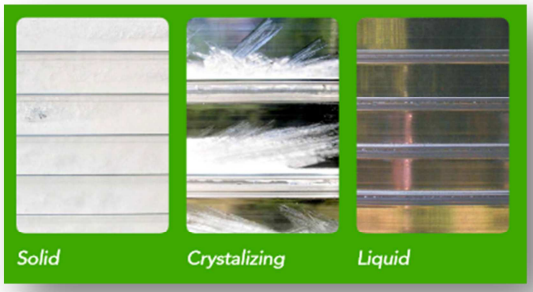

Figure 12. Glass panel with PCM in different states (GLASSX, 2013)

Further trends and research

As it has become obvious, nanotechnology provides great possibilities for innovative architectural creation, not only in terms of performance but also in terms of aesthetics and design dynamics. New nanomaterials, hybrid or not, may constitute by themselves a new mean (language) by which architectural ideas can be expressed. Taking all this experience as a starting point, our research continuous on, investigating the possibility of creating an outer "epidermis" in buildings, that is an intelligent system which could function as a structural as well as a secondary feature, combining innovative materials and forms in order to achieve high performance in architecture.

References:

Addington, D., & Schodek, D. (2004). *Smart Materials and Technologies: for the Architecture and Design Professions*. Boston: Architectural Press.

Ashby, M. F., Ferreira, P. J., & Schodek, D. L. (2009). *Nanomaterials, Nanotechnologies and Design*. USA: Butterworth-Heinemann (Elsevier).

Elvin, G. (2007). *Nanotechnology for Green Building*. Indianapolis: Green Technology Forum.

Johansen, J. (2002). *NanoArchitecture: A New Species of Architecture*. New York: Princeton Architectural Press.

Leydecker, S. (2008). *Nano Materials*. Berlin: Birkhauser Verlag AG.

Logothetidis, S. (2008). "Flexible organic electronic devices: Materials, process and applications". Materials Science and Engineering: B, 96-104.

Parthenopoulou, N., Angelides, D. (2010) *Construction Materials Protecting Structures that Suffer Climatic Strain*. Thessaloniki, AUTh.

Schramm, L. (2014). *Nano and Microtechnology from A-Z*. Germany: Wiley-VCH Verlag GmbH&Co. KGaA.

Zhu, W., Gibbs, J., & Bartos, P. (2004). *Application of Nanotechnology in Construction - Current Status and Future Potential*. 1rst International Symposium in Nanotechnology in Construction. Paisley Scotland: Royal Society of Chemistry.

GENNESYS. (2009). A NEW EUROPEAN PARTNERSHIP. (H. Dosch, & M. Van de Voorde, Eds.) Stuttgart: Max-Planck-Institut.

Dollens, D. (2014). *Digital Botanic Architecture 2 - eBook*. Retrieved from Desic.org: http://www.exodesic.org/TrussImages/DBA2-150.pdf

KVA. (2009). KVA Projects. Retrieved from KVA Matx: http://www.kvarch.net/projects/74

Market Research (2007). Retrieved from Market Research.com: http://www.marketresearch.com/?SID=55409288-488687767-510505503

Masens, C. (2002). Science Museum Nanotechnology. Retrieved from Science Museum: http://www.sciencemuseum.org.uk/antenna/nano/lifestyle/133.asp

Nanoarchitecture.net (2013). Nanoarchitecture.net. Retrieved from Nanoarchitecture.net: http://nanoarchitecture.net/

Nanoforum.org (2006). Retrieved from Nanoforum.org - European Nanotechnology Gateway: http://www.nanoforum.org/

NanoWerk (2014). Nanotechnology Introduction. Retrieved from NanoWerk: http://www.nanowerk.com/nanotechnology/introduction

NOS. (2008, April). Nano Vent Skin. Retrieved from Nano Vent Skin: http://nanoventskin.blogspot.be/

PRLog. (2007). Retrieved from PRLog: http://www.prlog.org/

Schulenburg, D. M. (2007). Nano Brochure. Retrieved from Cordis Europa: ftp://ftp.cordis.europa.eu/pub/nanotechnology/docs/nano_brochure_el.pdf

SolarIvy. (2011). Solar Ivy- the idea. Retrieved from Solar Ivy: http://solarivy.com/the_idea

Graphene mediated synthesis of gold nanoparticles and its nano-composite and their Applications

P. C. Pandey, *Yashashwa Pandey
Department of Chemistry, Indian Institute of Technology (BHU), Varanasi-221005, India

Abstract: The conversion of 3-Aminopropyltrimethoxysilane (3-APTMS) capped noble metal ions (Au^{3+} , Pd^{2+} , Ag^{+}) into respective nanoparticles in the presence suitable organic reducing agents constitute new rout of metal nanoparticle synthesis justifying potential applications in many biomedical applications. The choice of organic reducing reagent precisely govern the dispensability, nanogeometry, pH and salt tolerance of as synthesized nanoparticles for specific application. Some of the organic reducing agent enable the formation of organic –inorganic hybrid during nanoparticle synthesis justifying enhanced catalytic activity of nanomaterial. It was further investigated that the presence of graphene suspension along with reaction mixture facilitate the process of nanoparticles synthesis with significant change in electrocatalytic ability of the material. The presence of graphene allow nucleation site for nanoparticles and results the formation of hybrid nanomaterial having potentiality for biocompatible thin film formation. This study will also permit us to discuss a new rout of nanoparticles synthesis justifying the miceelar behaviour of 3-APTMS that precisely control the practical usability of nanomaterial in biomedical applications.

Keywords: Graphene, 3-APTMS, Nanoparticle Synthesis, Electrocatalytic ability, .

Introduction: Recently, graphene has emerged as a promising material for new technological evolution and has played an important role in electronic components, modified electrodes, and mechanical resonators, sensors. Nanosheets of reduced Graphene Oxide (rGO) tend to restack when used in graphite paste electrode and hence limit the electrocatalytic ability of graphene. For the fabrication of graphene paste electrodes, CNTs or other nano/micro sized particles (such as metallic nanoparticles) could be used as spacers to reduce the coalescence of graphene into graphite structures thus increasing the available surface area of the graphene sheets[2]. Noble metal nanoparticles formed by the reduction (with suitable organic reducing agents) of 3-APTMS capped noble metal ions (Au3+, Pd2+ , Ag+) into respective nanoparticles can serve as spacers between individual Graphene sheets and increase the electrocatalytic activity of the graphene paste electrode. The presence of graphene suspension along with reaction mixture facilitate the process of nanoparticles synthesis with significant change in electrocatalytic ability of the material. The presence of graphene allow nucleation site for nanoparticles and results the formation of hybrid nanomaterial having potentiality for biocompatible thin film formation.[7]. The as-synthesized rGO-AuNPs nanocomposite enablethe formation of nanocomposite (PBNPs–rGO-AuNPs) dispersion with Prussian blue nanoparticles (PBNPs).The resulting nanomaterial suspensions in one way, display excellent electrocatalytic activity during the electrochemical sensing of H2O2 as compared to Prussian Blue and PBNPs-AuNPs nanocomposite. The result on these line are reported in this communication.

Results and Discussion

Organic Reducing Agents and 3-APTMS Mediated Synthesis of AuNPs

AuNPs functionalized with primary amine have received great attention [7]. It has been found that the presence of organic reducing agents profoundly affects the properties of as formed AuNPs. The use of formaldehyde as a reducing agent enable the formation of AuNPs in 1-2 hours and their catalytic activity is better compared to that prepared with other organic reducing agent (ketones, GPTMS, etc.). This could be explained due to the formation of imine when interacting with 3-APTMS. Imines are typically formed by the condensation of primary amines (3-APTMS) and aldehydes (Formaldehyde) and are catalytic in nature [7].

Role of reduced Graphene Oxide (rGO) in synthesis of Gold Nanoparticles (AuNPs)

Reduced Graphene Oxide consists of graphene like sheets, chemically functionalized with oxygen groups such as hydroxyls and epoxides, these oxygen functionalities play an important role by providing reactive sites for the nucleation and growth of gold nanoparticles (Figure 1). Another important advantage of adhesion of AuNPs to graphene sheets is that the act as spacers and prevent aggregation/restacking of graphene sheets in dry state as well as in when using it in graphite paste electrode thereby making both faces of graphene accessible [2].

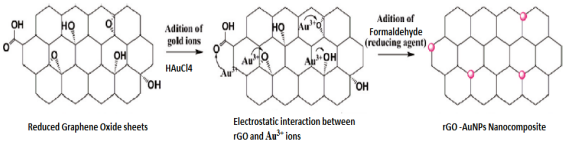

Figure 1. Schematic Representation of Nucleation of Gold Nanoparticles as functionalized Reduced Graphene Oxide surface.

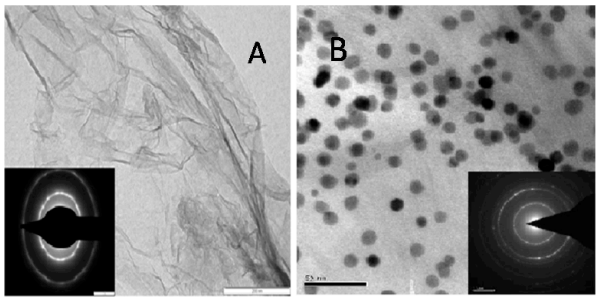

Figure 2 (A) show the TEM images and respective SAED of grapheme sheet, (B) show the TEM image and respective SAED of rGO-AuNPs nanocomposite.

Electrocatalytic reduction of H2O2

We subsequently examined the electrochemical behaviour of Graphene-AuNP-PB nanocomposite modified electrode. Figure 3a, 3b and 3c shows the cyclic voltammograms of the PBNPs (a), AuNP-PB nanocomposite (b) and Graphene-AuNP-PB nanocomposite (c) modified electrode in 0.1 M phosphate buffer (pH 7.0) in absence and the presence of 5 mM H2O2 (Figure 3). There is an increase in cathodic current on the addition of H2O2, the reduction currents for all the three electrodes (Figure 3). However, the graphene-AuNP-PB nanocomposite modified system shows higher reduction current(Figure 3c) as compared to only PB-system (Figure 3a), and PB-AuNPs system (Figure 3b) indicating better electrocatalytic activity of nanocomposite toward H2O2. The amperometric responses for these systems were recorded on the addition of varying concentrations of H2O2 (5 nM to 2 mM) in 0.1 M phosphate buffer (pH 7.0) at working potential of 0.0 V vs. Ag/AgCl as shown in Figure 4. It is clear from Figure 4 that the response was amplified in case of graphene-AuNP-PB nanocomposite (Figure 4c) than PBNPs (Figure 8a), and AuNP-PB nanocomposite (Figure 4c)again suggesting the good electrocatalytic behaviour of composite material towards the reduction of H2O2.

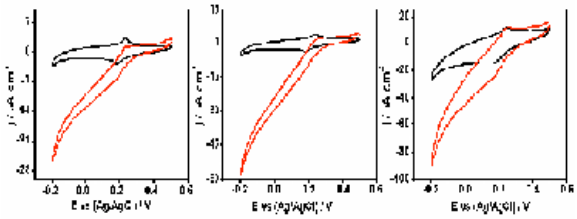

Figure 3: Cyclic Voltammogram of PBNPs (a) AuNP-PBNPs (b) rGO-AuNP-PBNP (c) modified electrode in absence (1) presence (2) of 5Mm H2O2.

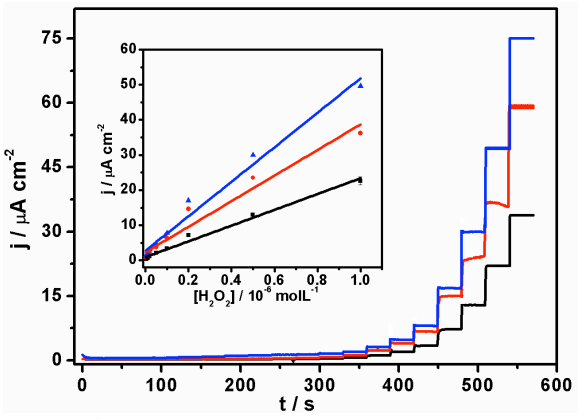

Figure 4: Ampereometric Response of PBNPs (a) AuNP-PBNPs (b) rGO-AuNP-PBNP (c) modified electrode on addition of varying concentration of H2O2 from 0.05 µM to 2mM at 0.0 V vs. AgCl in 0.1M Phosphate Buffer (pH 7) containing 0.5 M KCl.The inset shows calibration plots of H2O2 analysis respectively

The calibration curves for H2O2 analysis at modified electrodes were constructed using average currents recorded for each concentration point. The inset of Figure 4 depicts the calibration curves for H2O2 at PBNP (curve a), AuNP-PB nanocomposite (curve b) and Graphene-AuNP-PB nanocomposite (curve c) modified electrodes. The sensitivity of PBNPs, AuNP-PBNP nanocomposite and rGO-AuNP-PBNP nanocomposite modified system towards H2O2 has been calculated from the linear curve and found to be 23.08 ± 1.00, 39.21 ± 1.70 and 52.02± 1.00µAmM−1cm−2 respectively. The lowest detection limit for H2O2 analysiswas found to be 2 µm, 1µM and 50 nM respectively.

References:

1.. Luiz C. S. Figueiredo-Filho, Dale A. C. Brownson, Maria G´omez-Mingot, Jes´us Iniesta, Orlando Fatibello-Filhoa and Craig E. Banks(2013) Analyst, 138, 6354.

2. Gil Goncalves,Paula A. A. P. Marques, Carlos M. Granadeiro,Helena I. S. Nogueira,
M. K. Singh,and J. Gr_acio (2009) Chem. Mater. 21, 4796–4802.

3. Prem Chandra Pandeyand Dheeraj Singh Chauhan (2011)

4. Prem C. Pandey, Digvijay Panday and Gunjan Pandey (2014) RSC Adv., 4, 60563.

5.Pandey PC, Pandey AK (2013 Electrochemica Acta 87: 1-8.

6. P. C. Pandey, Gunjan Pandey, Jamal Haider, and Govind Pandey (2015) J. Nanosci. Nanotechnol. 15, 1–9

7. P. C. Pandey and D. S. Chauhan, Analyst 137, 376 (2012).

Reliability, Availability, Maintainability and Safety Analysis for the Development of a Nano-material Plant

Elahe Davarpanah
Chemical Engineer, Politecnico di Torino, Turin, Italy.

Introduction

Innovative technologies such as the nano-particle can potentially cause some risks for environment, health, and economic sustainability. For this reason, a suitable management plan should be developed in order to reduce those concerns and to establish an efficient and competitive business. Therefore, in this paper a Reliability, Availability, Maintainability and Safety Analysis (RAMS) is developed in order the mitigate the above-mentioned risks [1], [2].

Nanotechnology Benefits and Risks

Nano-materials are used in a variety of industries due to their unique characteristics. The application of nanotechnology in product development can bring some advantages such as response to customer needs, develop of a cost-effective process, and provide high quality products. Despite of the advantages, nano-particles show potential risks for safety and environment. For this reason, current studies focus on understanding the toxicology of nano-materials by performing hazard identification and exposure analysis [3], [4].

Studies performed on toxicology of nano-materials prove that the increased reactivity of nano-particles is due to their small size, their enlarged surface per unit of mass and their potential to agglomerate. All of these factors can represent sources of toxicity.

In addition, nano-powders in the presence of ignition are able to cause fire and explosion when in contact with air. On the other hand, some nano-materials have catalytic reaction depending on their composition and structure which can arise new safety concerns. Regarding the environmental contamination, the high usage of nano-materials in industrial applications such as nano-lubricants may lead to release of these materials into the environment.

RAMS Methodology

RAMS analysis is a risk assessment study applied during the design and operating phase of the industrial projects. The goals are to reduce the safety and environmental issues by improving the system architecture and enhancing the system performance and productivity [5]. In this study a RAMS approach is performed on a plant producing nano-materials. The general RAMS algorithm developed in this paper is demonstrated in Figure 1.

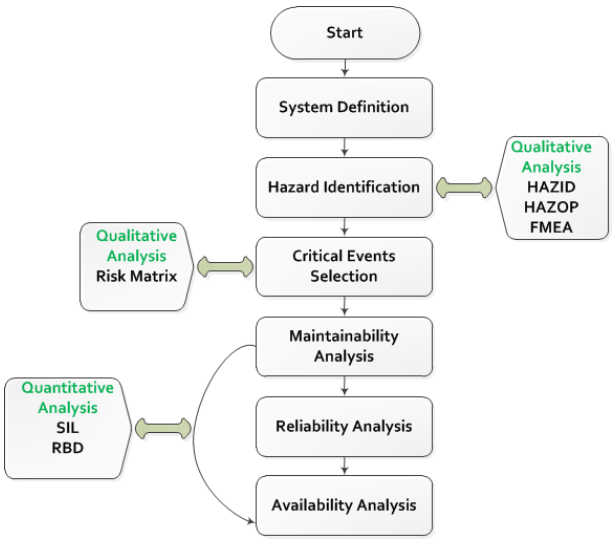

Figure 1: *RAMS Methodology Flowchart*

In addition, the study is focused on analysing the reliability of safety systems by performing a Safety Integrity Level Assessment (SIL) procedure. This helps to determine the adequacy of the safety system in order to mitigate any possible incidents inside the plant. The SIL levels defined as probability of failure on demand are shown below:

- SIL 1: 10^{-2} - 10^{-1}
- SIL 2: 10^{-3} - 10^{-2}

- SIL 3: 10^{-4} - 10^{-3}
- SIL 4: 10^{-5} - 10^{-4}

Conclusion

The approach reveals the plant design deficiencies, which could compromise the system functionality leading to production loss, human safety issues, and environment contamination. Furthermore, Figure 2 shows the distribution of the most critical components assessed from reliability and SIL analysis. In this figure each of the SIL category is composed by a different number of safety function. The particularity is that each of the safety functions within a specified SIL group have the same reliability degree. The safety functions with SILs equal to 3 or 4 are considered critical and therefore for their case provision of additional safeguards is required.

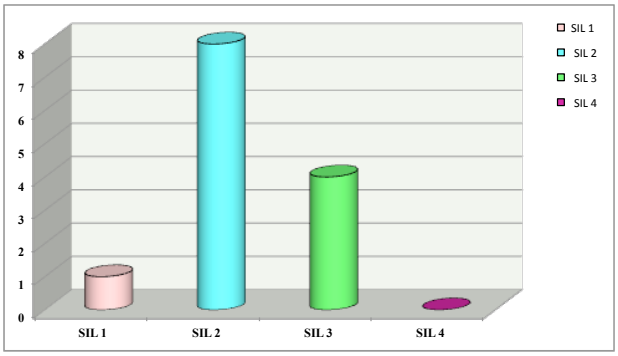

Figure 2: *SIL Assessment Results on Safety*

A number of safety functions with SIL 3 are as follows:

- The H_2S and H_2 detector which detect the gas leakage and initiates an alarm by the PLC0.
- The Shutdown valve, located on the gas pipelines, activates plant shutdown in case of high pressure.
- The Shutdown activation of the electrical power in case of high temperature in the furnace (reactor section).

Nevertheless, the optimal logistic solutions for the procurement of the maintenance and spare parts are suggested in order to improve the system reliability and integrity. Those activities include the periodical check and replacement of critical components.

References

[1] Sharma. R. K., Kumar. S., (2008) 'Performance modeling in critical engineering systems using RAM analysis', *International Journal of Reliability Engineering and System Safety*, Vol. 93, pp.891-897.

[2] Hameed. Z., Vatn. J., (2012) 'Important challenges for 10MW reference wind turbine from RAMS perspective', *International Journal of Energy Procedia*, Vol. 24, pp.263-270.

[3] Hallock. M. F., Greenley. P., DiBerardinis. Lou., Kallin. D., (2009) 'Potential risks of nanomaterials and how to safely handle materials of uncertain toxicity', *Journal of Chemical Health and Safety*, Vol. 16, pp.16-23.

[4] NIOSH (US National Institute for Occupational Safety and Health), (2009) 'Approaches to Safe Nanotechnology Managing the Health and Safety Concerns Associated with Engineered Nanomaterials', *www.cdc.gov/niosh*.

[5] Goddy. E., Benz. S.J., Scenna. N. J., (2015) 'An optimization model for evaluating the economic impact of availability and maintenance notions during the synthesis and design of a powder plant', *International Journal of Computers and Chemical Engineering*, Vol. 75, pp.135-154.

In-Situ Thermally-Reduced Graphene Oxide/Epoxy Composites: Thermal and Mechanical Properties

Ganiu B. Olowojoba[1*], Salvador Eslava[2,3], Eduardo S. Gutierrez[2], Anthony J. Kinloch[1], Cecilia Mattevi[2], Victoria G. Rocha[2], Ambrose C. Taylor[1]

[1]Mechanics of Materials Division, Department of Mechanical Engineering, Imperial College, London, UK
[2] Centre for Advanced Structural Ceramics, Department of Materials, Imperial College London, London, UK
[3] Department of Chemical Engineering, University of Bath, Bath, UK

Abstract
Graphene has excellent mechanical, thermal, optical and electrical properties and this has made it a prime target for use as a filler material in the development of multifunctional polymeric composites. However, several challenges need to be overcome in order to take full advantage of the aforementioned properties of graphene. These include achieving good dispersion and interfacial properties between the graphene filler and the polymeric matrix. In the present work we report the thermal and mechanical properties of reduced graphene oxide/epoxy composites prepared via a facile, scalable and commercially-viable method. Electron micrographs of the composites demonstrate that the reduced graphene oxide (rGO) is well-dispersed throughout the composite. Although no improvements in glass transition temperature, tensile strength, and thermal stability in air of the composites were observed, good improvements in thermal conductivity (about 36%), tensile and storage moduli (more than 13%) were recorded with 2 wt% of rGO.

Keywords: Thermal reduction, graphene oxide, reduced graphene oxide, tensile modulus, thermal conductivity, glass transition temperature, dispersion.

Introduction

Due to its remarkable mechanical, electrical, and thermal properties, graphene has evoked a lot of interest amongst researchers working on the development of multi-functional composites for a variety of applications [1, 2]. However, the inert nature of graphene makes it difficult to take full advantage of its excellent properties when used as a filler material in polymeric composites. Such composites are usually characterized by poor filler dispersion and poor interfacial properties between the filler and the polymeric matrix material, arising from the poor compatibility between graphene and many polymeric matrices. Functionalization of the graphene has been widely adopted as one of the ways of overcoming the aforementioned challenges, either by allowing the easy exfoliation of graphite platelets or increasing the compatibility between graphene sheets and the chosen polymeric matrix [3, 4]. Oxidized graphene sheets, known as graphene oxide (GO) sheets, are typically prepared by oxidization and exfoliation of graphite [5, 6] and have been used as the starting material in the production of graphene-based composites. Although some researchers have reduced GO in-situ using hazardous chemical reagents such as hydrazine hydrate, others prefer to reduce GO prior to its incorporation in composites [1].

In the present work reduced graphene oxide (rGO)/epoxy composites are produced in a facile, scalable and commercially-viable way. This involves dispersing freeze-dried GO in a diglycidyl ether of bisphenol-A (DGEBA) epoxy resin by shear mixing. The GO is then reduced in-situ (to rGO) by using a relatively high-temperature cure schedule for the epoxy resin system, after adding the hardener. The thermal and mechanical properties of the composites produced are characterized and the viability of the processing technique is demonstrated.

Experimental

A standard DGEBA resin (Araldite LY556; Huntsman, UK), having an epoxide equivalent weight (EEW) of 185 g/eq, was used. The curing agent was an accelerated methylhexahydrophthalic acid anhydride (Albidur HE600; Evonik, Germany),

* Corresponding Author: G. B. Olowojoba
Email: g.olowojoba@imperial.ac.uk

having an anhydride equivalent weight (AEW) of 170 g/eq.

A suspension of graphene oxide was prepared via a modified Tour et al. [6] synthesis in a custom-built rig, using natural graphite flakes (150 – 500 μm, Sigma-Aldrich). This was freeze-dried using a Powerdry LL1500 freeze dryer (Thermo Scientific, UK).

The freeze-dried GO, having an average lateral size of 33 ± 17 μm, was dispersed in the DGEBA epoxy resin using a three roll mill (80E; Exakt, Germany). A stoichiometric amount of the anhydride (Albidur HE600) was then added to the GO/DGEBA mixture (i.e. the ratio of DGEBA to anhydride was kept at 185:170, as according to their equivalent weights). The resulting mixture was stirred at 500 rpm for 15 mins at a temperature of 60 ºC under atmospheric pressure using an overhead stirrer. The mixture was degassed at -1000 mbar and 60 ºC for 15 mins to remove trapped air bubbles. The degassed mixture was poured into preheated rectangular steel moulds with internal dimensions of 150 x 80 x 3 mm^3 and cured at 90 ºC for 1 hr, and 160 ºC for 2 hrs. A post-cure step of 200 ºC for 30 mins was carried out to ensure sufficient in-situ thermal reduction of the GO, to rGO, in the composite [7].

Thermogravimetric analysis (TGA) was carried out on the composites and GO samples using a TGA/DSC 1 apparatus (Mettler Toledo, UK). A sample of the freeze-dried GO was thermally reduced according to the cure schedule employed for processing the composites (i.e. 90 ºC for 1 hr; 160 ºC for 2 hrs and 200 ºC for 30 mins). The GO and rGO samples were analysed in a nitrogen atmosphere using a heating rate of 5 ºC/min, while the composites were analysed in air using a heating rate of 10 ºC/min. All samples were analysed over the temperature range 30 to 800 ºC.

The thermo-mechanical properties of the rGO/epoxy composites were determined using a Q800 dynamic mechanical thermal analyser (DMTA) from TA Instruments, UK. Rectangular samples with dimensions 60 x 10 x 3 mm^3 were subjected to temperature sweeps from 30 to 200 ºC at a heating rate of 2 ºC/min in a dual-cantilever mode using a frequency of 1 Hz and an oscillation strain of 0.05%.

X-ray photoelectron spectroscopy (XPS) analyses were performed using a Theta Probe spectrometer (ThermoFisher Scientific; UK). The instrument was operated at a base pressure of 1 x 10^{-9} mbar. XPS spectra were acquired using a MXR1 monochromated Al Kα X-ray source (hυ = 1486.6 eV). An X-ray spot of ~400 μm radius was employed. High resolution, core level C1s spectra were acquired using a pass energy of 20 eV. The GO sample spectra were charge-referenced against the C1s peak at 284.4 eV to correct for charging effects during acquisition.

Uniaxial tensile tests were conducted on the rGO/epoxy composites at room temperature using a universal tensile testing machine (5584; Instron, UK). Dumbbell specimens having a gauge length of 25 mm were used. A displacement rate of 1 mm/min was adopted. The tensile properties were averaged from the results obtained from a minimum of five specimens. The strain was measured using a clip-on extensometer.

The thermal conductivities of the rGO/epoxy composites was determined from their thermal diffusivities measured by the laser-flash technique using an LFA-427 Nanoflash (Netzsch, Germany). Three shots each were made on 10 x 10 mm^2 samples which were 2 mm thick. A temperature range of 30 to 60 ºC was used, at 10 ºC intervals, with a laser voltage of 450 V and a pulse width of 0.8 ms. The samples were coated with a thin layer of graphite prior to testing to increase absorption and transmission of the infrared radiation energy.

The morphology of the fracture surfaces of the composites was examined using a Leo 1525 (Carl Zeiss, Germany) scanning electron microscope equipped with a field emission gun (FEG-SEM). An accelerating voltage of 5 kV was used, the samples being sputter-coated with a thin layer of chromium prior to examination.

Results and discussion

Fig. 1a shows the thermograms of the pristine GO and of the rGO reduced according to the temperature schedule adopted for curing the composites. In both thermograms, the weight loss at 100 ºC, of 15% in the case of GO and 7% in the case of rGO, may be attributed to the evaporation of adsorbed water. A further 30% weight loss at 200 ºC can be observed in the case of GO. This has been attributed to the thermal decomposition of oxygen-containing functional groups (OCFGs) on the surface of the GO. It has previously been shown that most of the OCFGs, which are attached to the basal aromatic plane of a GO sheet (i.e. hydroxyl and epoxy groups), can be removed by annealing at 200 ºC [8], thus partially restoring the thermal, electrical and optical properties of graphene.

Fig. 1b shows the C1s XPS spectra of GO and rGO, as well as the associated four-component fit which quantitatively represents the bonds between the carbon atoms on the GO and other moieties. A significant reduction in the OCFGs bonded to carbon atoms can be observed upon reduction of the GO to rGO, in agreement with the

TGA results discussed above. These techniques clearly demonstrate the effectiveness of the GO reduction strategy adopted in this work for the preparation of the rGO/epoxy composites.

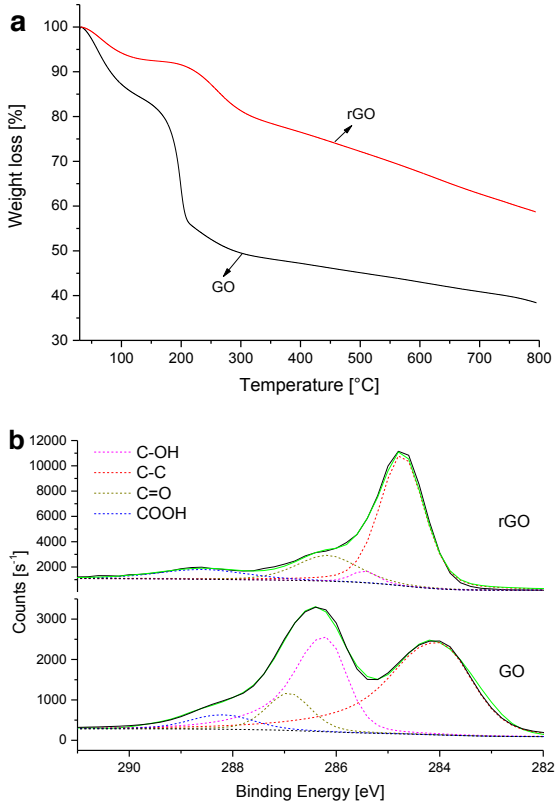

Fig. 1. (a) Thermograms of GO and rGO in a nitrogen atmosphere with a heating rate of 5 °C/min; (b) XPS of GO before and after reduction showing a decrease in the concentrations of functional groups present after reduction to rGO.

The morphologies of the fracture surfaces of the composites are shown in Fig. 2. Although the surface morphology of the neat epoxy (Fig. 2a) appears relatively smooth, those of the composites (Figs. 2b–e) exhibit increasing surface roughness with increasing rGO content.

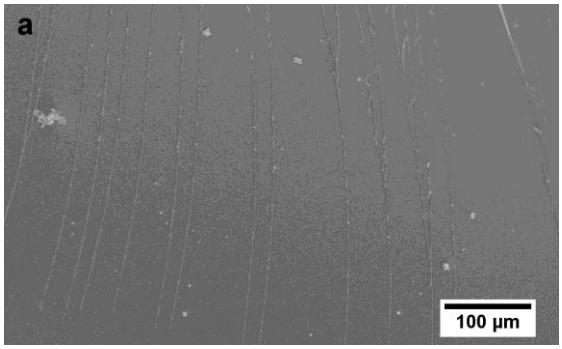

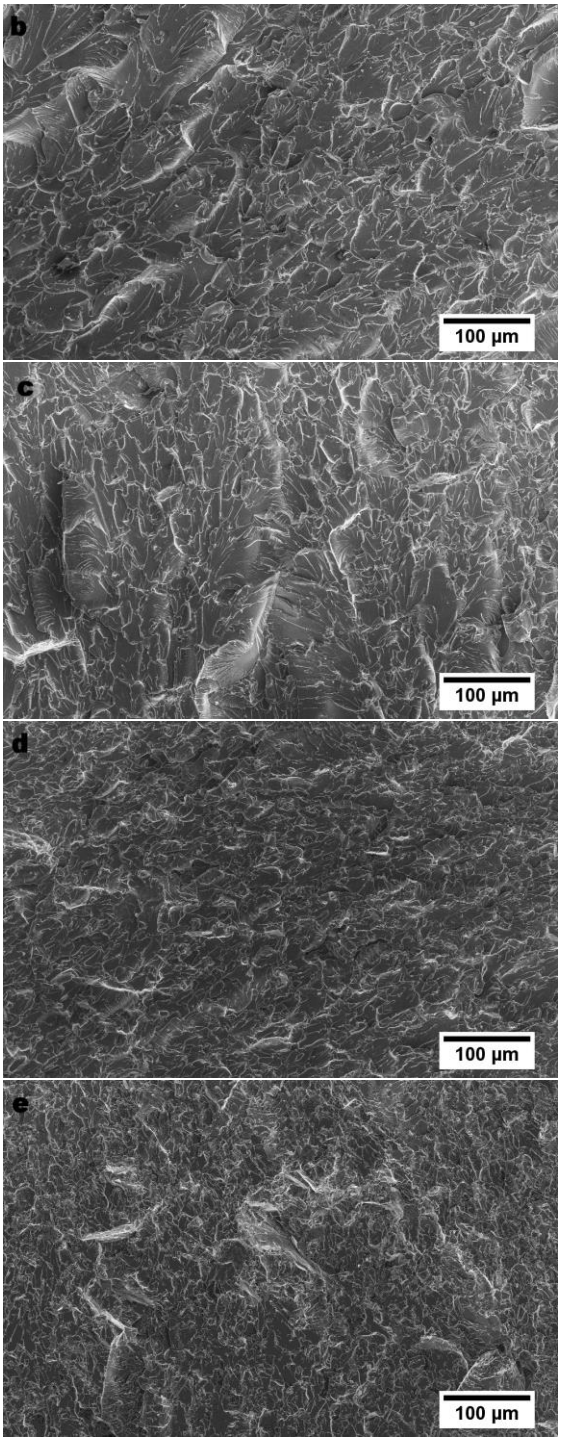

Fig. 2. Fracture surface morphology of rGO/epoxy composites examined by FEG-SEM. (a) Neat epoxy, (b) 0.1 wt%, (c) 0.5 wt%, (d) 1 wt%, (e) 2 wt% rGO.

It can also be seen in Figs. 2b–e that the rGO appears to be evenly dispersed throughout the composite. This is to be expected due to the fact that the GO contains epoxy groups which would impart good compatibility with the DGEBA resin and improve dispersion during mixing. Furthermore, since significant reduction of the GO takes place at

200 °C, the epoxy matrix would have already gelled at this temperature, therefore preventing re-agglomeration of any unattached rGO during reduction.

The thermo-mechanical properties of the in-situ thermally-reduced rGO/epoxy composites are shown in Fig. 3.

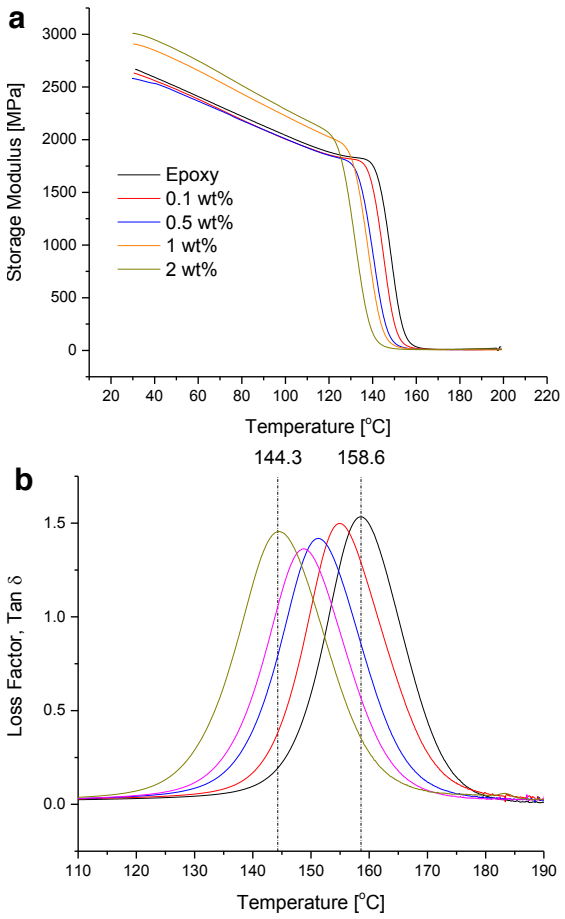

Fig. 3. Thermo-mechanical properties of the rGO/epoxy composites.

From Fig. 3a, the storage moduli of the composites at 35 °C can be seen to increase with increasing rGO content; rising from 2640 MPa for the neat epoxy polymer to 2990 MPa in the epoxy composite filled with 2 wt% rGO. The glass transition temperature of the composites, as shown in Fig. 3b, decrease with increasing rGO content, from 158.6 °C for the neat epoxy to 144.3 °C for the epoxy matrix in the composite with 2 wt% rGO (i.e. a decrease of nearly 15 °C). As discussed elsewhere [9], the increase in the storage modulus may be attributed to good interfacial adhesion between the rGO and the epoxy matrix due to the chemical interaction between the functional groups on the GO and epoxy during the in-situ reduction. This chemical interaction between the GO and epoxy may also lead to an increase in the molecular weight between crosslinks of the cured epoxy matrix. For this reason, the glass transition temperature may decrease as the rGO concentration increases.

Fig. 4 shows the thermal stability of the rGO/epoxy composites in air as measured by TGA. The thermal stabilities of the composites appear to decrease somewhat with increasing rGO content. This can be seen more clearly in Fig. 4b where the rate of thermal degradation of the composites at around 400 °C increases with increasing rGO content. Since the GO is only partially reduced in the composite, the oxygen content of the cured composite may therefore be expected to increase with increasing rGO content. This will lead to an increase in the rate of thermal degradation, as confirmed in Fig. 4b.

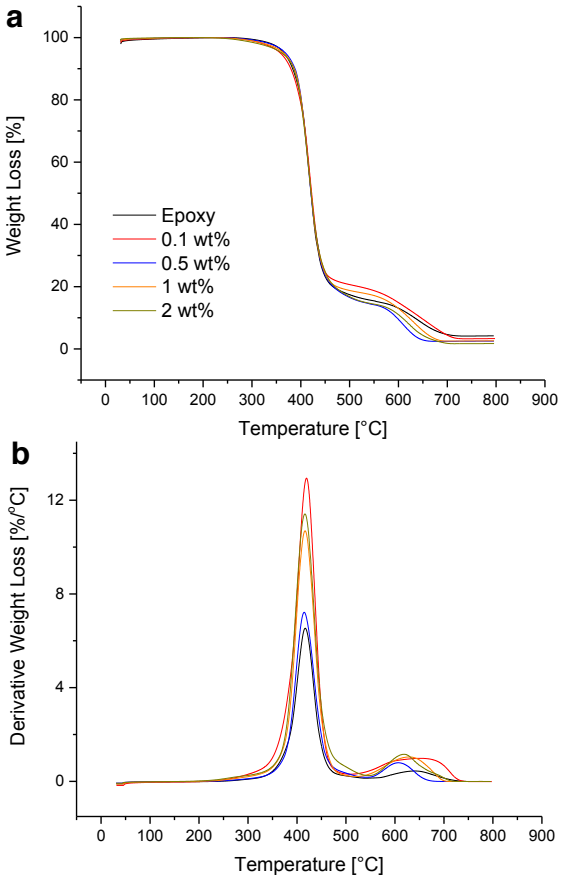

Fig. 4. Thermogravimetric analysis of the rGO/epoxy composites.

Fig. 5a shows the tensile moduli of the composites. The moduli increase from 2900 ± 70 MPa for the neat epoxy to 3290 ± 60 MPa for the 2wt% rGO/epoxy composite. This increase in modulus may be ascribed to the relatively high modulus of the rGO filler and to the good interfacial adhesion between the rGO and the epoxy matrix. The good interfacial adhesion may arise from surface chemistry interactions, as well as from

mechanical interlocking of the wavy rGO sheets with the epoxy matrix. As Fig. 5b shows, the tensile strengths of the composites tend to decrease with increasing rGO content. The tensile strength decreases from 68.7 ± 10.6 MPa in the neat epoxy to 44.1 ± 5.0 MPa in the composite with 2 wt% rGO. Such a decrease has been attributed to the change in molecular weight between crosslinks of the epoxy matrix, as mentioned above. Zaman et al. [10] obtained similar results with 4,4'-Methylene diphenyl diisocyanate (MDI)-functionalized graphene nanoplatelet (GNP)/epoxy composites.

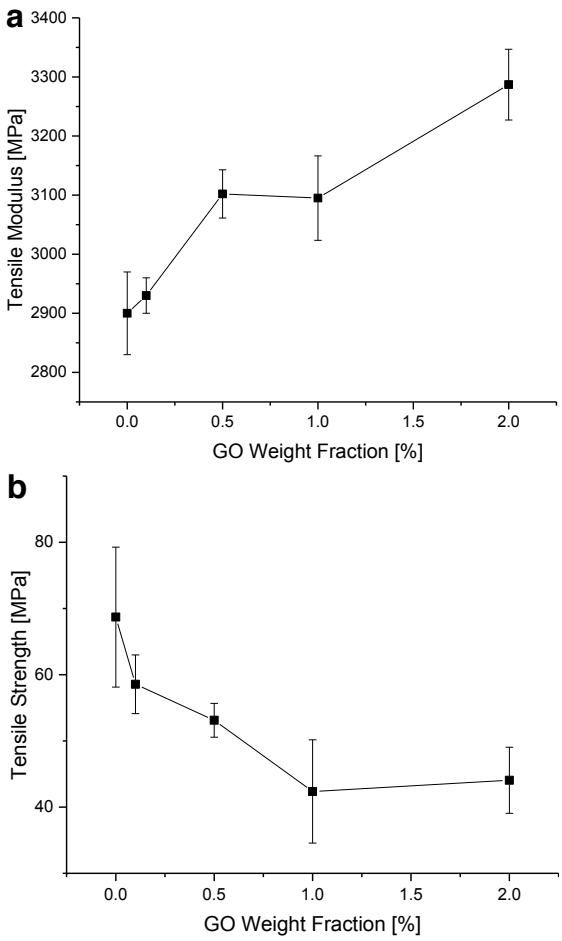

Fig. 5. Mechanical properties of the rGO/epoxy composites (a) Young's modulus, (b) tensile strength.

Fig. 6 shows the thermal conductivities of the rGO/epoxy composites. The thermal conductivities tend to increase with increasing rGO content and also with increasing temperature, as expected. The maximum thermal conductivity recorded was 0.264 W/mK for the 2wt% rGO/epoxy composite at 60 °C. The corresponding thermal conductivity of the neat epoxy polymer is 0.190 W/mK. At 30 °C, the corresponding values are 0.243 W/mK and 0.179 W/mK for the 2 wt% rGO/epoxy composite and neat epoxy respectively (i.e. an increase of about 36%). The measured thermal conductivities exhibited by these composites are relatively high when compared to the value of 0.21 W/mK reported in the literature for a GNP/epoxy composite [11]. This may be attributed to the excellent dispersion of the rGO in the epoxy resulting from the processing technique adopted in this work.

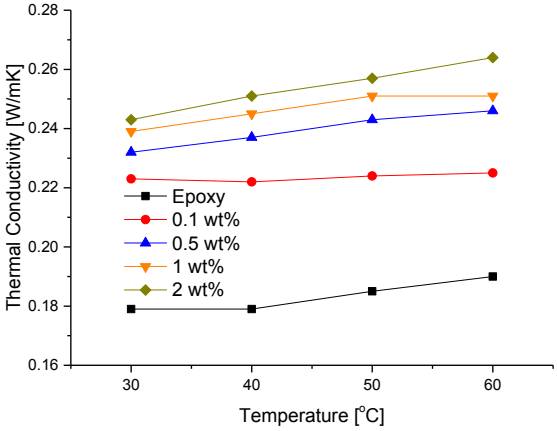

Fig. 6. Thermal conductivities of neat epoxy and rGO/epoxy composites at different temperatures.

Conclusions

A facile, scalable and commercially-viable method has been developed to prepare polymeric composites of DGEBA epoxy resin with varying rGO content, having improved thermal conductivities. It consists of dispersing freeze-dried GO in a DGEBA epoxy resin using a three-roll mill and subsequently curing at a relatively high temperature with an anhydride curing agent, thereby both partially reducing the GO to rGO in-situ and curing the epoxy matrix. The rGO/epoxy composites so produced exhibit a good dispersion of rGO, as observed by electron microscopy, which ensures significant improvements in the thermal conductivity, storage modulus, and tensile modulus. Other properties are however slightly weakened such as the thermal stability, glass transition temperature, and tensile strength, probably due to remaining oxygen groups in the embedded rGO and higher molecular weights between crosslinks. These results, taken together, show that it is possible to tune the properties of an epoxy polymer with a simple and viable method of GO addition.

Acknowledgements

This work was funded by the UK Engineering and Physical Sciences Research Council (EPSRC), Grant Number: EP/K016792/1. The authors wish to thank the Department of Mechanical Engineering Sciences, University of Surrey, UK, for the X-ray

photoelectron spectroscopy measurements. V. G. Rocha. would like to acknowledge the European Commission (FP7 Marie Curie Intra-European Fellowships GRAPES).

References

[1] Potts JR, Dreyer DR, Bielawski CW, Ruoff RS. Graphene-based polymer nanocomposites. Polymer 2011;52(1):5–25.
[2] Geim AK, Novoselov KS. The rise of graphene. Nature Materials 2007;6:183–91.
[3] Kuilla T, Bhadra S, Yao D, Kim NH, Bose S, Lee JH. Recent advances in graphene based polymer composites. Progress in Polymer Science 2010;35(11):1350–75.
[4] Pei S, Cheng H. The reduction of graphene oxide. Carbon 2012;50(9):3210–28.
[5] Hummers WS, Offeman RE. Preparation of graphitic oxide. Journal of the American Chemical Society 1958;80(6):1339.
[6] Marcano DC, Kosynkin DV, Berlin JM, Sinitskii A, Sun Z, Slesarev A et al. Improved synthesis of graphene oxide. ACS Nano 2010;4(8):4806–14.
[7] Tang H, Ehlert GJ, Lin Y, Sodano HA. Highly efficient synthesis of graphene nanocomposites. Nano Letters 2012;12(1):84–90.
[8] Jeong H, Lee YP, Jin MH, Kim ES, Bae JJ, Lee YH. Thermal stability of graphite oxide. Chemical Physics Letters 2009;470(4-6):255–8.
[9] Yang H, Shan C, Li F, Zhang Q, Han D, Niu L. Convenient preparation of tunably loaded chemically converted graphene oxide/epoxy resin nanocomposites from graphene oxide sheets through two-phase extraction. Journal of Materials Chemistry 2009;19(46):8856–60.
[10] Zaman I, Phan TT, Kuan H, Meng Q, La LTB, Luong L et al. Epoxy/graphene platelets nanocomposites with two levels of interface strength. Polymer 2011;52(7):1603–11.
[11] Chandrasekaran S, Seidel C, Schulte K. Preparation and characterization of graphite nano-platelet (GNP)/epoxy nano-composite: Mechanical, electrical and thermal properties. European Polymer Journal 2013;49(12):3878–88.

Tribological behaviors of yttria-stabilized zirconia (YSZ) nanoparticles as lubricant additives

A Sert[1] and D Yılmaz Çakta[2]

[1] Eskisehir Osmangazi University, Department of Mechanical Engineering, Eskisehir, Turkey

[2] Eskisehir Osmangazi University, Department of Metallurgical and Materials Engineering, Eskisehir, Turkey, E-mail: asert@ogu.edu.tr

Abstract

The aim of this work is to enhance lubrication with different amount of YSZ nanoparticles (size<200nm) and characterization of tribological properties of AISI 4140 steel material in the lubricating system. Synthesized YSZ nanoparticles are dispersed with different concentration (0.1%, 0.5% and 1.0% wt.) in synthetic engine oil (SAE10W40) and tribological tests are conducted using ball-on-disc geometry. The coefficients of friction is decreased about 12.6% using of nanoparticles as an oil additive.

1. Introduction

Nanoparticles are used as additives in coatings or lubrication systems in order to prevent friction and wear of materials in industry. The new interest area of nanotribology shows that the lubricants with nanoparticles have novel property in tribology, such as wear resistance, low friction coefficient, and high load capacity [1][2]. ZrO_2 is one of the nanoparticles used for tribological consideration such as coatings [3] and lubricant additives [4]. When zirconia doped with yttria, yttria-stabilized zirconia (YSZ) has good mechanical properties at high temperature and good chemical stability up to 1200 °C [5]. Y_2O_3 stabilized cubic zirconia is one of the key material for the development of high temperature zirconia ceramics as well as thermal barrier and wear resistant ceramic coatings. The objective of this study is to evaluate the effect of addition YSZ nanoparticles on the tribological properties of engine oil.

2. Experimental Details

Y_2O_3 (8% mole) stabilized ZrO_2 (8YSZ) powders were synthesized via high energy milling (HEM) which have been processed for 24 h with 1200 rpm. After HEM, heat treatment was carried at 900 °C for 2 hours for stabilization. Specific surface area value of 8YSZ was measured by BET as 32,8 m^2/g. SEM image and XRD profile of YSZ was given figure 1 and figure 2, respectively.

The prepared YSZ nanoparticles were dispersed in engine oil (SAE10W40, with a density of 0.88 g/cm^3 and a viscosity of 97 cSt at 40 °C). Lubricant samples were prepared using mechanical stirring and an ultrasonic probe with four different amount of YSZ nanoparticles were varied from 0 to 1% by weight.

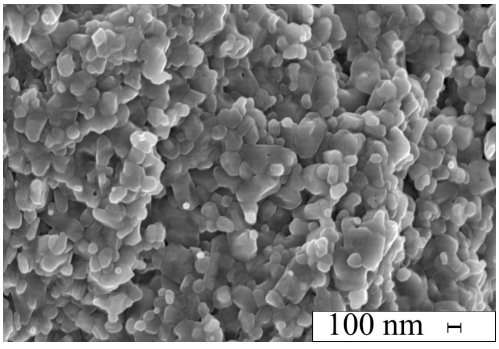

Figure 1. SEM image of YSZ nanoparticles

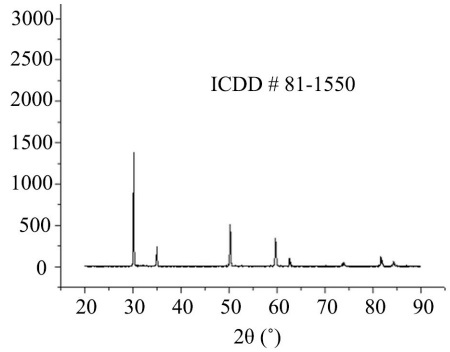

Figure 2. XRD profile of YSZ nanoparticles

[1] Corresponding author. Tel.:+90 2222393750; fax:
E-mail address: asert@ogu.edu.tr (A Sert)

The tribological properties of the lubrication with YSZ additives were evaluated using CSM ball-on-disc tribometer (Figure 3). The balls (3 mm in diameter) used in our experiment were made of WC-6% Co. The tribological tests were conducted at room temperature under a load of 10 N with a speed of 5 cm/s. AISI 4140 steel samples were austenitized at 860 ˚C for 1 h, quenched and tempered at 280 ˚C for 20 min. Hardness of the steel samples and the balls were 56.1 HRC and 91.5 HRA, respectively. The worn surfaces of the samples were examined with a scanning electron microscope (SEM, Zeiss Supra 50VP).

3. Results and discussion

Figure 4 shows the variation of friction coefficient as a function of sliding distance during the tribological tests. Lubrication oil with YSZ nanoparticles can form a protective layer between friction pairs. The friction coefficient was reduced with addition of the YSZ nanoparticles in amount of 0.1 and 0.5 %. When the base oil and 1 wt. % addition YSZ with base oil were used, the coefficient of friction shows high value also shows fluctuation in the condition of base oil and 0.1 wt. % addition YSZ with base oil. It was considered that dry contact between steel and ball could not prevent in the low amounts of YSZ additive and the base oil conditions. During the tribological tests, steel and ball were in contact with their asperities of their surfaces. Thus, the sliding motion was prevent by asperities so the friction coefficient was increased. When higher concentration of YSZ is added into base oil, nanoparticles can pile up between friction pairs, so protective layer may blocked [6]. As the nanoparticles concentration was higher than optimum, the nanoparticles acted as a abrasive. Therefore, the friction coefficient was increased when 1 wt. % was added. For the suspension with 0.5 wt. % the best tribological behaviour was of YSZ exhibiting 12.6% of friction reduction.

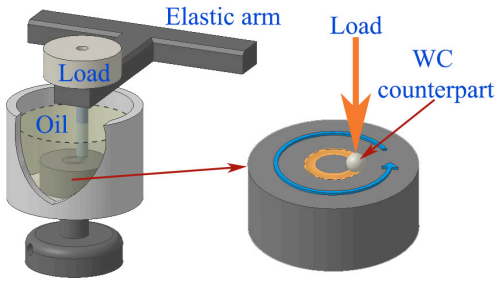

Figure 3. Figure illustrating the wear test device and the wear geometry

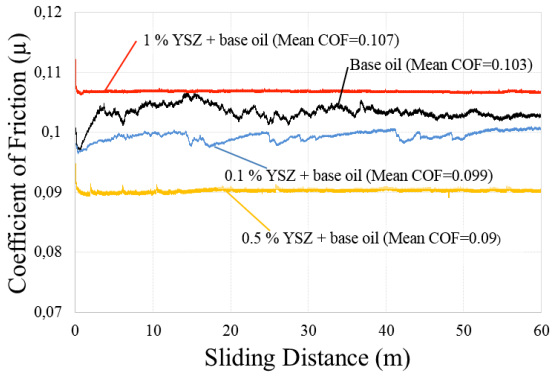

Figure 4. Coefficients of friction as functions of the sliding distance

Figure 5 shows the surface morphologies of the wear tracks. The measured wear track wides were 71.5, 72.3, 58.7 and 78.8 μm of base oil, 0.1 wt. %, 0.5 wt. % and 1 wt. %, respectively. The major reason for the increased wear track length in comparison to the base oil in 0.1 wt. % is probably the lack of YSZ nanoparticles and discontinuity in the oil film. A possible reason of increasing the wear track length in the 1 wt. % concentration, nanoparticles accumulate around asperities and act like abrasive also prevent the protective oil film. As shown in figure 5 (a) the rubbed surface obtained in base oil is rough with many wide, parallel and deep grooves. Addition of 0.1 wt. % YSZ the wear track length and grooves were decreased according to base oil (Figure 5b). Addition of 0.5 wt. % YSZ significantly smoothed the wear track zone (Figure 5c). In contrast, when 1wt. % was added, the nanoparticles caused the many deep scratches on the surface also the wear track length was increased (Figure 5d).

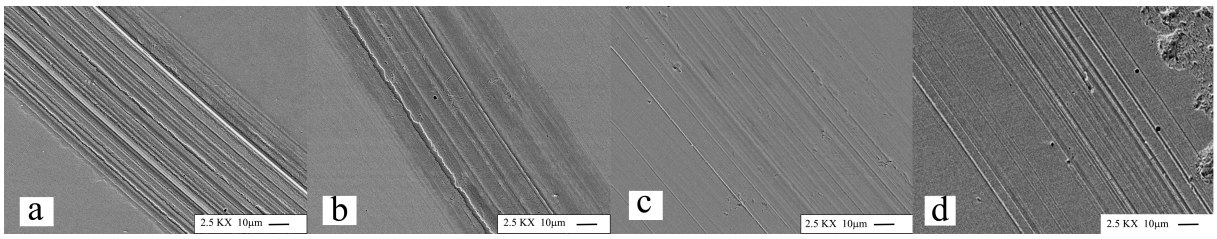

Figure 5. SEM images of worn surfaces of AISI 4140 steel using different lubricants: (a) base oil, (b) 0.1%, (c) 0.5% and (d) 1% YSZ additive

4. Conclusions

The addition of YSZ nanoparticles to engine oil performed a difference in the coefficient of friction. The highest coefficient of friction value was obtained with 1 wt. % because of it was agglomerated and acted like abrasive. For 0.5 wt. % YSZ concentration of engine oil, friction coefficient and wear track length were reduced by 12.6 and 17.9%, respectively. This study suggests a promising application of YSZ as lubricant additives and represents a first step towards fundamental understanding of tribological properties of YSZ.

References

[1] Jiao D, Zheng S, Wang Y, Guan R and Cao B 2011 *Appl. Surf. Sci.* The tribology properties of alumina/silica composite nanoparticles as lubricant additives 257 5720

[2] Zhenglin T and Shaohui L 2014 *Curr Opin Solid ST M* A review of recent developments of friction modifiers for liquid lubricants (2007-present) 18 119

[3] Yang Y, Chen W, Zhou C, Xu H and Gao W 2011 *Appl. Nanosci* Fabrication and characterization of electroless Ni-P-ZrO_2 nano-composite coatings **1** 19

[4] Ma S, Zheng S, Cao D and Guo H 2010 *Particuology* Anti-wear and friction performance of ZrO_2 nanoparticles as lubricant additive **8** 468

[5] Carpio P, Borrell A, Salvador MD, Gómez A, Martínez E and Sánchez E 2015 *Ceram. Int.* Microstructure and mechanical properties of plasma spraying coatings from YSZ feedstocks comprising nano- and submicron-sized particles **41** 4108

[6] Wei Z, Ming Z, Hongwei Z, Yu T, Kunlin W, Jinquan W, Fei J, Xiao L, Zhen L, Peng Z and Dehai W 2011 J. Phys. D: Appl. Phys. **44** 205303

An In Vitro Study of Osteoblast Behaviors on Graphene Oxide Eletrodeposited on Anodized Titanium

P Tanurat and S Sirivisoot

Biological Engineering Program , Faculty of Engineering, King Mongkut's University of Technology Thonburi, Bangkok 10140, Thailand

E-mail: phtanurat@gmail.com

Abstract: Surface modification of titanium mimicking a nanoscale hierarchical structure was widely studied. Anodization is a method has been used to frabication titanium dioxide (TiO_2) nanotube arrays on titanium surface in order to increase osteointegration. Using graphene oxide (GO) coating on biomaterial surfaces is a great potential for long-term use of orthopaedic implants due to its biocompatibility and antibacterial property. The aim of this study is to frabicate anodized titanium coated with graphene oxide (ATiGO) using anodization and electrodeposition of graphene oxide, respectively. Scanning electron microscopy (SEM) were used to investigate surface morphology. Their physiochemical properties were evaluated by energy-dispersive X-ray spectroscopy (EDX) and X-ray diffractrometer (XRD). Furthermore, cell proliferation of mouse osteoblastic cell line (MC3T3-E1) was investigated using MTT assay. The results from ATiGO, GO coated on titanium (TiGO), anodized titanium (ATi), and pure titanium (Ti) were compared and discussed. The results in the present study suggest that graphene oxide can promote osteoblast behaviors when compared with anodized titanium and pure titanium without GO coating.

1. Introduction

Currently, many people lost their lives or parts of body because disorders of bone [1]. The surgical intervention is only method for treating symptomatic. Artificial bone is chosen for replacement of bone diseased or damaged part. Titanium is one of the most popular light-weight metals used for orthopedic implant. Because their physical property and excellent biocompatibility [2]. Titanium can be resistant to corrosion due to their surface is protected by two to ten nm of titanium dioxide (TiO_2) layer which spontaneously formed when exposing to oxygen in the air. Corrosion resistance of titanium can prevent its surface and its biocompatibility [3]. However, its thin oxide layer is unable to prevent corrosion for long-term implants that caused to a metal ion release. When titanium inserted into body for long-time replacement over than 5 years, the thin oxide layer is not enough for protecting a metal ion release. Therefore, a corrosion of titanium can lead to a failure of implants. A surface modification of titanium becomes necessary subject to reduce on [4].

Anodization is alternative to modify titanium surface in order to increase its resistance corrosion property. This method can fabricate TiO_2 nanotube arrays on its surface. In addition, process of anodization can be controlled the building of oxide thickness, crystal structure, and diameter of oxide nanotubes by manipulating electrochemical parameters [5]. S. Sirivisoot *et al*.[6] fabricated TiO_2

nanotube arrays via anodization in hydrofluoric acid solution as an electrolyte and 20 volts were applied for 15 minutes. As a result, TiO_2 nanotube has 50-60 nm diameters and 200 nm lengths.

A modification of surface titanium with coating as carbon-base materials has been interestied. For example, Mulltiwalled carbon nanotube, fullerol and graphene are carbon-base nanomaterials which have been widely used for biomaterial surface coating [7]. K. Brammer *et al*. [8] studied the effect of carbon-coated on titanium oxide nanotube (C-TiONT) to titanium oxide nanotube (TiONT). Anodizations were frabicated TiONT at 20 V for 30 minutes. 0.5% w/v hydrofluoric acid to acetic acid. Carbon film was deposited onto TiONT substrates from a pyrolytic graphite wafer (99.999% purity) in sputtering system. They found that both of TiONT and C-TiONT enhance osteoblasts growth over smooth Titanium. On the other hand, alkaline phosphatase activity on TiONT was higher than on C-TiONT. Moreover, they observed that mechenchyma stem cells on C-TiONT had higher amount of osteocalcin and osteoponin when compared to TiONT. Additionally, they indicated that surface chemistry of carbon coating did not have effect on adhesion, growth or morphology but had a major influence on osteogenic differentiation. Oh S. *et al* [9] studied the response of MC3T3-E1 osteoblast cells on TiO_2 nanotube array. They reported that significantly by 300–400% as compared to cell proliferation on unanodized titanium which is in micro-scale roughness. Nanoscaled structure gives larger surface area than micro-scaled structure leading to higher protein adsorptions and cell adhesion. They recommended that anodization could be useful as an excellent treatment of titanium surface for orthopedic applications [10].

Graphene is a single layer of graphite, two dimensional atomic sheets which compose carbon atoms arranged in a flat honeycomb structure. Graphene is biocompatible due to their physical and chemical properties [11]. Graphene oxide is produced by chemical oxidation of graphene. Its structure is similar to graphene but theirs having oxygen functional groups. Graphene oxide have a hydroxyl and epoxide on basal planes. Carboxyl and carbonyl functional groups are present on edges [12].Depan *et al*. [13] studied effect of GO to cell proliferation in chitosan polymer-base scaffolds. MC3T3-E1 mouse pre-osteoblast cell line was used for cell proliferation evaluation. They reported that GO could success fully interpromoted osteoblast proliferation and gave an assumption that the negatively charge and hydrophilic (polar) of GO in this study, or carboxyl group, could be an important factor to promote a higher interaction between osteoblast cells and material.

Graphene oxide is a popular material which is also used for surface modifications. An electrodeposition of graphene oxide on metal surfaces has been very popular among several techniques because of its easily controlable process and inexpensiveness [14]. A several authors were studied eletrodeposition of graphen oxide on titanuim surface for orthopedic applications. For example, M. Li *et al* [15] used MG63 human osteosarcoma cells and L929 fibroblast cells for evaluating the effect of graphene oxide and hyrdoxyapatite (GO/HA) coating by a electrodeposition on pure titanium surface. A both of L929 and MG63 cells have a healthy morphology on the GO/HA composite materials. The result can indicate that GO/HA coatings on pure titanium as a composite material has a possibility of using as implants for load-bearing hard tissue replacements. Y. Phacharoen *et al*.[16] studied antibacterial properties of a composite of graphene oxide and hydroxyapatite which were elctrodeposited on anodized titanium surface. As a result, graphene oxide and hydroxyapatite could reduce cell survival of bacteria. Morover, sharpe edges of graphene oxide can lead to damage cell membrane of bacteria.

The surface modifications of titanium were performed by anodization of titanium and then electrodeposited of graphene oxide on its surface, and analysed. The aim of this study is study behaviors of mouse pre-osteoblast cell (MC3T3-E1) on difference surfaces of titanium: commercially pure titanium (Ti); anodized titanium (ATi); graphene oxide electrodeposied on pure titanium (TiGO) ; and graphene oxide electrodeposied on anodized titanium (ATiGO).

2. Materials and Methods

2.1 Anodization of titanium

The commercially titanium foils (99.2 % purity; Alfa Aesar, USA) with 100 x100 mm and 0.025 mm of thickness were used in the present study. The samples were mechanically cut into size of 10 mm x10 mm. Then, the samples washed twice with acetone and cleaned in ultrasonic sonicator for 15 minutes before use. The samples were etched for 10 second in acid solution (1.5wt% nitric acid: 1.5 wt% hydrofluoric acid = 1:1) in order to remove oxide layer. Ti samples were used as anode, while platinum wire was used as cathode. The distance between anode and cathode was 10 mm. Electrolyte for anodization was 1.5wt% hydrofluoric acid solution (HF) and polyethylene beaker was used as electrolyte container. All solutions were prepared from reagent grade chemicals and deionized (DI) water. Anodization was carried out at 20 V using a DC power supply (APS-3005D ATTEN DC power supply digital, China) for 15 minutes. Electrolyte was stirred using a magnetic stirrer during anodization. After anodization, the samples were rinsed with DI water and dried in room temperature [6].

2.2 Electrodeposition of graphene oxide

About 150 or 200 μg/ml of graphene oxide solution (GO) (Graphen Square Inc, South Korea) was used as an electrolyte. Isopropyl alcohol and DI water were used as a solvent. Titanium (Ti) or anodized titanium (ATi) were used as anode, while platinum was used as cathode. The electrodeposition of graphene oxide on samples was carried out at a constant potential of 10 V (APS-3005D ATTEN DC power supply digital, China) for 10 minutes and electrolyte was stirred using a magnetic stirrer. After electrodeposition, the samples were dried in room temperature. The samples define as about 150 μg/ml graphene oxide electrodeposied on pure titanium (TiGO150) and anodized titanium (ATiGO150) and 200 μg/ml graphene oxide electrodeposied on pure titanium (TiGO200) and anodized titanium (ATiGO200) [16].

2.3 Characterization

The surface morphology of sample was observed after gold coating by scanning electron microscopy (SEM-EDS, Bruker, USA). The diameters of TiO_2 nanotube were analyzed using image analysis solfware (ImageJ version 1.32, Montgomery) In order to investigate the elemental composition of graphen oxide coating, the samples were investigated by an energy dispersive X-ray spectrometer (SEM-EDS, Bruker, USA). The phase of electrodepositing was evaluated by using X-ray diffraction (XRD, BRUKER AXS : D8DISCOVER, USA) at a scanning rate of 1°/min.

2.4 Cell culture

Mouse pre-osteoblasts ((MC3T3-E, population number = 13-15, MTEC, Thailand)) were cultured in alpha-modified minimal essential medium (alpha-MEM, Hyclone, USA) supplemented with 10 vol% fetal bovine serum (FBS, Gibco, USA), and 1 vol% penicillin/streptomycin (Invitrogen Corporation) at 37˚C in a humidified atmosphere of 5% CO_2 in air. The culture media were replenished every 48 hours.

2.5. Cell seeding

MC3T3-E1 cells were subcultured when 80-85% confluence through trypsinization (0.25% trypsin and 0.25 EDTA; Invitrogen Corporation). Cells were seeded onto the samples and plastic polystyrene as control at a density of $5x10^4$ cells/cm^2 into 24-well culture plates (Corning, USA).

2.6 Cell proliferation assay

After cultured for 1, 3 and 5 days, the culture media were removed and the samples were rinsed three times with 1x phosphate saline buffer. About 150 μl of 3-(4,5-dimethylthiazol-2-yl)-2,5-diphenyltetrazolium bromide (MTT) working solution was added onto the cell-culture samples in order to allow the formations of formazan crystals. Then, 24-well culture plates were incubated at 37º C in a humidified atmosphere of 5% CO_2 in air for two hours. Then, 85 µl of MTT working solution were removed and using 50 µl of dimethyl sulfoxide (DMSO) for dissolve purple formazan crystals. About 100 µl of the mixed solution was tranfered to 96-well culture plates and incubated about 10 minutes at 37º C. The absorbance of solution was analyzed at a wavelength of 540 nm using spectrophotometer (Synergy Mx Multi-mode Reader, USA). The percentages of viable cells were calculated as in a following equation [16].

Cell viability (%) = (Absorbance of solution incubated with samples /Absorbance of solution incubated with control) ×100%

3. Results and discussion

3.1 surface morphology

Top sectional scanning electron microscope (SEM) images of the samples. Smooth surface of commercially pure titanium surface, Ti shown in figure 1(a). After anodization, TiO_2 nanotubes were fabricated on titanium surface with 50 nm diameters, as shown in figure 1(b). Morover, a smooth surface of Ti became to a nano-porous surface of TiO_2 nanotube arrays. In present study, anodization was carried out S. Sirivisoot *et al*.[6]. They fabricated TiO_2 nanotubes with 200 nm in a length and 50-60 nm in a dimensional. Therefore, a length of TiO2 in present study is similar to period work.

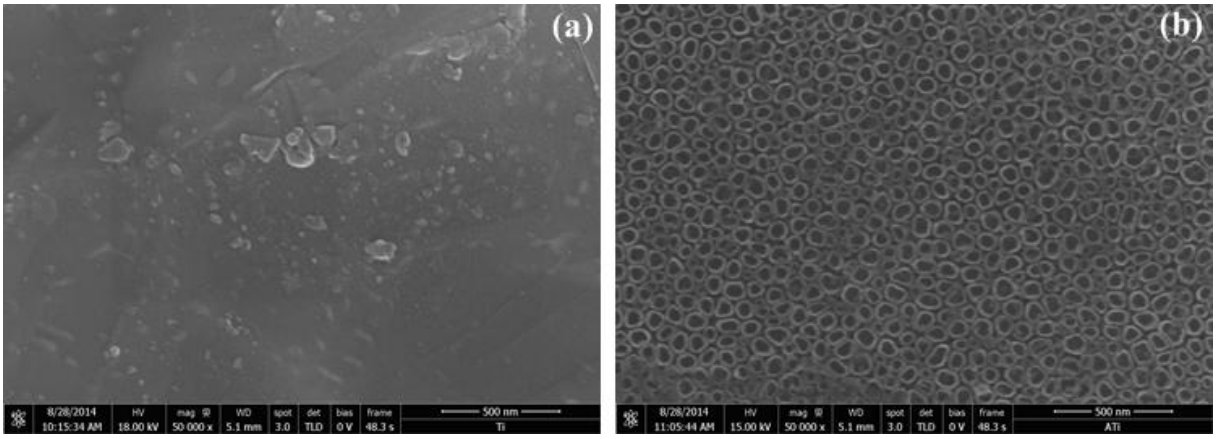

Figure1. Top sectional scanning electron microscope (SEM) images of: (a) commercially pure titanium, Ti; and anodized titanium, ATi (scale bar: 500nm).

After graphene oxide electrodeposition, SEM images show a thin layer of graphene covering on samples. About 150 µg/ml graphene oxide electrodeposied on Ti (TiGO150) and ATi (ATiGO150), shown in figure 2 (a) and 2 (b), respectively. About 200 µg/ml graphene oxide electrodeposied on Ti, (TiGO200) and ATi, (ATiGO200), shown in figure 2 (c) and 2(d), respectively

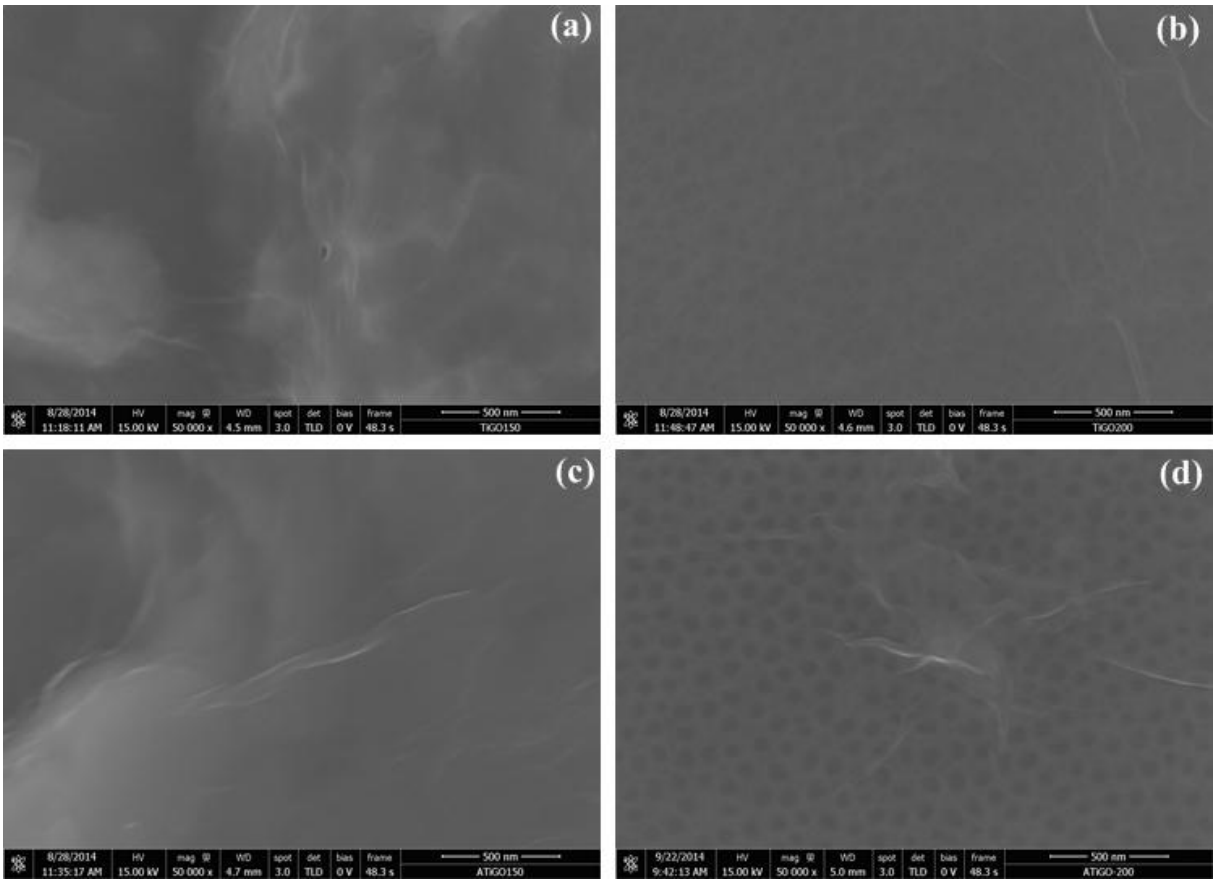

Figure2. SEM images of: (a) TiGO150; (b) ATiGO150; (c) TiGO200; and (d) ATiGO200 (scale bar: 500nm).

SEM images use for physical analysis that show a surface morphology of samples. A necessary confirm a chemical characterize of Ti, ATi and GO electrodeposition. Energy dispersive X-ray (EDX) was used to chemical analysis.

3.2 Energy dispersive X-ray (EDX) analysis

The EDX analysis has shown the atomic of elements in each sample: Ti; ATi; TiGO150; ATiGO150; TiGO200 and ATiGO200, respectively. Oxygen component of ATi is significantly increasing when compare to Ti. On the other hand, titanium component of ATi is significantly decreasing when compare to Ti. The reasonable of TiO_2 is fabricated by anodization. The fabrication of TiO_2 nanotube arrays in fluoride containing electrolyte is involve of two reactions. TiO_2 layer occurs according to the oxidation of Ti by the following the equation (1).

$$Ti + 2H_2O \rightarrow TiO_2 + 4H^+ + 4e^- \qquad (1)$$

The pits formation of TiO_2 by the following the reaction

$$TiO_2 + 4H_6F^- \rightarrow {}^1/_2\,[TiF_6]^{2-} + H_2O \qquad (2)$$

The applied potential drives Ti^{4+} ion from Ti migrates to the electrolyte. Ti^{4+} is combines with fluoride ion (F^-) to form a titanium hexafluoride complex ($[TiF_6]^{2-}$), which is stable in water.It believed the competition between the formations of TiO_2 in equation (1) and the dissolution in equation (2), is leading to the anodized titanium dioxide nanotube arrays produced [17]

Table1. , The carbon component of samples then electrodeposited with graphene oxide is approximately to 9.70%, 9.80% 17.00%, and 22.02% as TiGO150, ATiGO150, TiGO200, and ATiGO200, respectively. The elemental percentage of carbon is significantly increasing as the concentration of graphene oxide increased. Therefore, the elemental percentage of oxygen and titanium are significantly difference when compare with each samples; TiGO150; ATiGO150; TiGO20; and ATiGO200, respectively. To understand the reaction after electrodeposited of graphene oxide onto Ti and ATi surface. The X-ray diffraction (XRD) analysis is used for study structure of the crystal.

Table1. EDX analysis, the elemental percentage of carbon (C), titanium (Ti), and oxygen (O) on TiGO150, ATiGO150, TiGO200, and ATiGO200. Data analysis is mean ± standard deviation (N=3; n=1). Statistical analysis was used one-way ANOVA: $*p < 0.05$ when compared O of Ti with ATi. $**p < 0.05$ when compared Ti of Ti with ATi. $\#p < 0.05$ when compared C of each samples: TiGO150; ATiGO150; TiGO200; and ATiGO200. $\#\#p < 0.05$ when compared O of each samples: TiGO150; ATiGO150; TiGO200; and ATiGO200. $+p < 0.05$ when compared T of each samples: TiGO150; ATiGO150; TiGO200; and ATiGO200.

	Ti		ATi		TiGO150			ATiGO150			TiGO200			ATiGO200		
	Atom.{at%]		Atom.[at.%]		Atom.[at.%]			Atom.[at.%]			Atom.[at.%]			Atom.[at.%]		
	O	Ti	O	Ti	C	O	Ti	C	O	Ti	C	O	Ti	C	O	Ti
1	18.18	81.82	27.99	72.01	10.95	27.62	61.43	8.55	48.04	43.42	19.09	35.16	45.76	16.16	33.66	50.18
2	17.24	82.76	32.56	67.44	11.23	36.16	52.61	10.02	45.2	44.78	14.29	21.99	63.73	23.61	25.24	51.15
3	20.58	79.42	40.91	59.09	6.93	24.17	68.9	10.83	47.41	41.76	17.62	30.5	51.88	26.3	24.12	49.58
MEAN	18.67^{*}	81.33^{**}	33.82^{*}	66.18^{**}	$9.70^{\#}$	$29.32^{\#\#}$	60.98^{+}	$9.80^{\#}$	$46.88^{\#\#}$	43.32^{+}	$17.00^{\#}$	$29.22^{\#\#}$	53.79^{+}	$22.02^{\#}$	$27.67^{\#\#}$	50.30^{+}
SD	1.72	1.72	6.55	6.55	2.41	6.17	8.15	1.16	1.49	1.51	2.46	6.68	9.14	5.25	5.21	0.79

3.3 X-ray diffraction (XRD) analysis

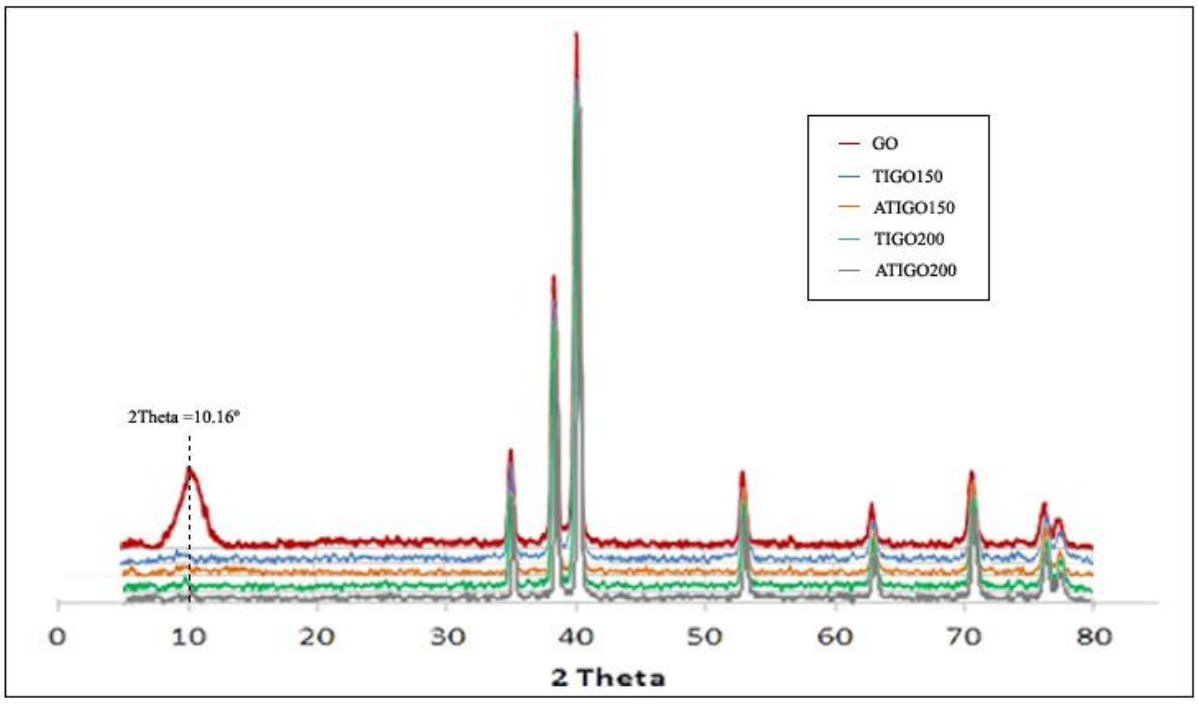

Figure3. The XRD patterns of: TiGO150; ATiGO150; TiGO200; ATiGO200; and graphene oxide (GO).

Graphene oxide was drop onto the ATi surface and dried in room temperature as uses for GO analysis. The sharp peak appears at 2 Theta = 10.16º as GO. On the other hand, XRD patterns of of: TiGO150; ATiGO150; TiGO200; and ATiGO200 absence the peak at 10-12º. Electrodeposition of graphene oxide leads to absence of peak at 2Theta approximately to 10-12º. [14]. Graphene oxide is a plane structure of graphite. Grophene oxide have a many oxygen functional groups such as, carboxyl (C−OOH), hydroxyl (C−OH), and epoxy (C−O−C).After a potential was applied GO migrated to the positive electrode (anode). In electrodeposition process, oxidation occurs at the anode. Some oxygen functional groups of GO could be remove during this process. These oxygen-containing groups become covalently attached to its coating surfaces. For example, when GO reacted with anodized titanium that presence of TiO_2, functional group on the GO surface such as, hydroxyl and carboxyl were removed. Then, some unpaired electrons bonded with the free electrons on the surface TiO_2 to form a Ti–O–C structure [18].

3.4 Cell proliferation using the MTT assay

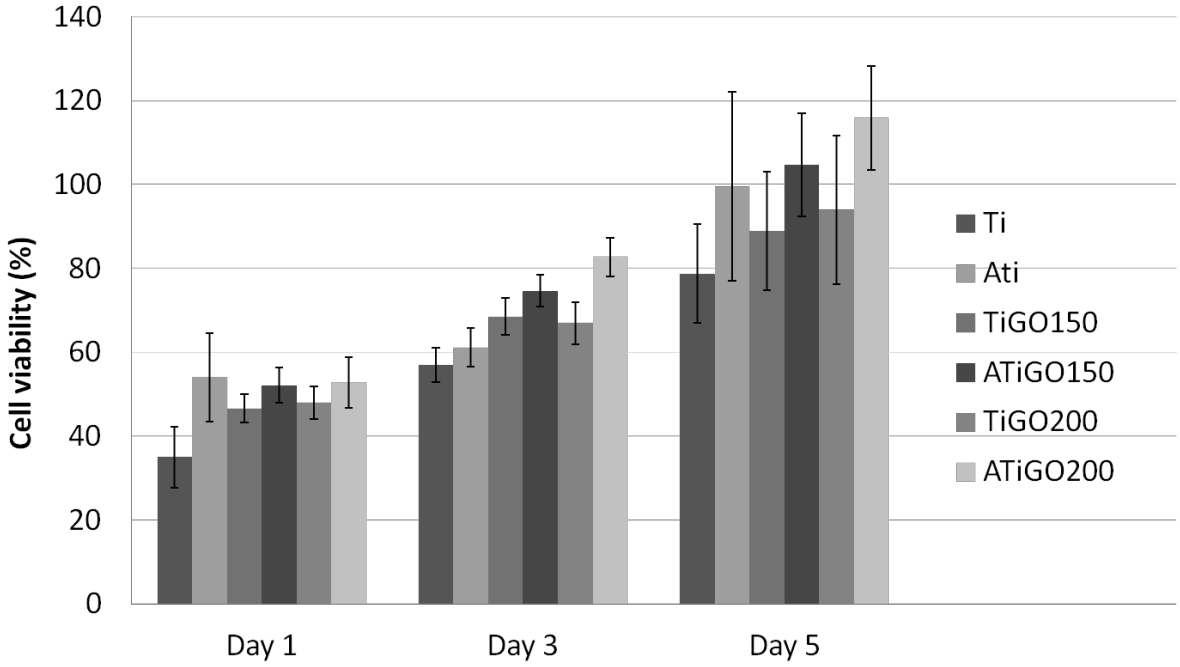

Figure 4. Cell viability of MC3T3-E1 pre-osteoblast cells evaluated at day 1, 3, and 5of cultivation. . Data analysis is mean ± standard deviation (N=3; n=3). Statistical analysis was used one-way ANOVA : $p < 0.05$

The MTT assay was used to determine the level of mitochondrial function of osteoblasts culturing on the surfaces of the Ti, ATi, TiGO150, ATiGO150, TiGO200, and ATiGO200. The percentages of cell viability after 1, 3 and 5 days of cultivation are showed in Figure 4. Ti had the lowest cell proliferation when compare with each samples of day 1, 3, and 5. Nanoscaled structure surface of ATi give a larger surface area than flat structure leading to higher protein adsorptions and cell adhesions [10]. Therefore, oxgen compononent of ATi is significant increase because TiO_2 nanotube arrays were fabricated on Ti surface after anodization. An experiment showed significant higher of cell proliferation on ATiGO than TiGO substrates when compare to each samples at day 1, 3, and 5 of cultivation. Moreover, ATiGO200 had significant higher cell proliferation than ATiGO150. The elemental percentage of carbon is significantly increasing as the concentration of graphene oxide increased. The present of high carbon and oxygen elements are play a major role to promotes cell proliferation.

4. Conclusions

TiO_2 nanotube arrays fabricated on Ti substrate by anodization process in hydrofluoric acid electrolyte and GO were successfully electrodeposited onto the samples. The EDX results indicate the presence of carbon element on the samples with confirmed GO electrodeposition. The XRD results indicate GO became to lose some oxygen functional group via electrodeposition process. Cell proliferation was tested by MTT assay. The results show that

ATiGO had significantly difference higher promote pre-osteoblast cell when compare to TiGO as the same concentration of graphene oxide electrodeposited. The results show that graphene oxide coating onto TiO_2 nanotube surface can promote cell proliperation of pre-osteoblast cells.

5. Acknowledgment

This research is funded by A Research Strengthening Project of the Faulty of Engineering, King Mongkut's University of Thonburi.

6. **References**

1. Temenoff, J.S. and Mikos A.G., 2008, Biomaterials The Inter section of Biology and Materials Science, 1st ed., Pearson Education International, New Jersey, pp.279-389.2

2. Park, S.H., Adolfo, L., Vijay, K.G. and John, C.K., 2003, "Hard Tissue Replacements" In Biomaterials Principles and Applications, Joon, B.P. and Joseph, D.B. (Ed.), CRC Press, Florida, pp.73-206.

3. Eillingsen, J.E. and Lyngstadass S.P., 2000, Bio-implant interface: improving biomaterials and tissue reactions, 1st ed., CRC Press, Florida.

4. Joon, B.P. and Young, K.K., 2003, "Metallic Biomaterials" In Biomaterials Principles and Applications, Joon B.P. and Joseph D.B. (Ed.), CRC Press, Florida, pp.1-20.

5. Minagar, S., Chris, T.C., Berndt, J.W., Elena, I. and Cuie, W., 2012, "A review of the application of anodization for the fabrication of nanotubes on metal implant surfaces", **Acta Biomaterials**, Vol.8, No. 4, pp. 2875-2888.

6. Sirivisoot, S. and Thomas J.W., 2008, "Multiwalled carbon nanotube enhance electrochemical properties of titanium to determine *in situ* bone formation" **Nanotechnology**, Vol.19, No.295110,pp. 1-12.

7. Pinto, A.M., Ines, C.G. and Ferno, D.M., 2013, "Graphene-based materials biocompatibility: A review", **Colloids and Surfaces B: Biointerfaces** , Vol. 111, No.1, pp. 188-202.

8. Brammer, K.S, Choi, C., Frandsen, C.J., Oh , S., Johnston, G, and Jin , S., 2011, "Comparative cell behavior on carbon-coated TiO2 nanotube surfaces for osteoblasts vs. osteo-progenitor cells", **Acta Biomaterialia**, Vol. 7, No. 4, pp. 2679–2703.

9. Oh, S., Chiara, D., Li-Han, C., Thomas, R.P., Rita, R. and Sungho Jin., 2010, "Significantly accelerated osteoblast cell growth on aligned TiO2 nanotubes", **Journal of biomedicine Material** , Vol. 73, No.1, pp. 97-103.

10. Zhang, W.,Qingfeng H., Ling, X., Jinhua L., Yuqin, J., Guifang, L., Xuanyong, L. and Xinquan, J.., 2013, "Effects of a hybrid micro/ nanorod topography-modified titanium implant on adhesion and osteogenic differentiation in rat bone marrow mesenchymal stem cells", **International Jounal of Nanomedicine**, Vol. 8, No. 1295, pp. 257-265.

11. Pinto, A.M., Ines, C.G. and Ferno, D.M., 2013, “Graphene-based materials biocompatibility: A review”, **Colloids and Surfaces B: Biointerfaces** , Vol. 111, No.1, pp. 188-202.

12. Zhu, Y., Shanthi, M., Weiwei, C., Xuesong, L., Ji, W.S., Jeffrey, R. P., and Rodney, S. R., 2010, “Graphene and Graphene Oxide: Synthesis, Properties,and Applications”, **Journal of Advance Material**, Vol. 12, pp. 1–19.

13. Depan, D., Girase, B., Shah, J.S. and R.D.K. Misra., 2011, “Structure process property relationship of the polar graphene oxide-mediated cellular response and stimulated growth of osteoblasts on hybrid chitosan network structure nanocomposite scaffolds”, **Acta Biomaterialia**, No. 7, pp. 3432-3445.

14. kaveri S. and Ramasamy J., 2013, “Synthesis and electrochemical properties of reduce graphene oxide via chemical reduction using thiourea as a reducing agent”, ,**Materails Letters**, Vol.113, pp.5-8.

15. Li, M., Qian, L., Zhaojun, J., Xuchen, X., Yan, C., Yufeng Z., Tingfei, X. and Shicheng W., 2013, “Electrophoretic deposition and electrochemical behavior of novel graphene oxide hyaluronic acid hydroxyapatite nanocomposite coatings”, **Applied Surface Science**, Vol. 284, pp. 804-810.

16. Parcharoen, Y., 2013, Electrophoric deposition of graphene oxide hydroxyapatite composits for orthopedic application, Degree of doctor of philosophy a thesis, Biological Engineering, Faculty of Engineering, King Mongkut's University of Technology Thonburi, pp. 1-19.

17. Al-Mobarak, N.A.,and Al-swayih A.A.,2014, “Development oftitanium surgery implants for improving ossteointegration through formation of a titanium nanotube layer”,**International Journal of Electrochemical Science**, Vol. 9,pp. 32-45.

18. Václav, Š., Snejana, B., Tomáš, M.G., Jana, B. and Martin, K., 2013, “TiO_2-graphene oxide nanocomposite as advanced photocatalytic materials”, ***Chemistry Central Journal***, Vol. 7, No. 41, pp. 1-12.

SETCOR The International Nanotechnology & NanoScience Conference & Exhibition
NANOTECH 2015 – Paris, France
15-17 June 2015, Paris - France

Some design and integration considerations for piezoelectric sensors based on individually contacted vertical ZnO nanowires

E. León Pérez[1], M. Mouis[2], E. Pauliac-Vaujour[1*]
[1]CEA-LETI, Systems Department, F-38054 Grenoble, France
[2]IMEP-LAHC, Minatec, 3 Parvis Néel, 38016 Grenoble, France
[*]Corresponding author :emmanuelle.pauliac-vaujour@cea.fr

Abstract : We report our last progress about the concept of collecting piezoelectric charges from vertical zinc oxide (ZnO) nanowires (NWs) for development of force-displacement sensor. Finite element (FE) modeling of NW pixels achievable through realistic microfabrication processes showed that piezopotential collection efficiencies of about 60% could be obtained by proper design. ZnO seed-layer thickness is an important parameter. The presence of a gap between NWs and contacting electrodes, which could be caused by process variability, was found to result in a sustainable 30 % drop in piezoelectric signal. Heterogeneous integration issues were also addressed, with selective growth of ZnO NWs as part of the microfabrication process. Arrays of µm-long single NWs with diameters in the 150 nm range were obtained by the hydrothermal method on patterned substrates. These simulation and experimental results are providing useful guidelines for the design and integration of high resolution and high sensitivity NW-based force-displacement sensors.

Keywords: *heterogeneous integration, nanowires, piezoelectricity, zinc oxide, sensor, simulation*.

1. Introduction

One-dimensional nanostructures offer a large range of potential applications in nanoelectronic devices. For instance, ZnO piezoelectric nanowires are promising elements for chip functionality enhancement [1]. In this context we are working on the implementation of ZnO NW arrays (Fig. 1) for high sensitivity and high spatial resolution sensor applications [2]. This paper discusses some aspects of the heterogeneous integration of these NWs within conventionnal silicon technologies.

The device exploits the piezoelectric polarization and the resulting change of the I-V characteristics of a semiconductive ZnO NW under bending. In order to integrate such a device, a certain number of issues must be addressed: (i) define a suitable NW-based "pixel" geometry based on the in-depth understanding of pixel piezoelectric behaviour and on technological considerations, (ii) develop specific microfabrication processes such as seed-layer growth and patterning and (iii) implement controlled NW growth on processed chips as part of the fabrication flow.

On one hand, a simulation study of the full contacted pixel of Fig. 1 was carried out. With heterogeneous integration in view, we analyzed the piezo-response of one pixel as a function of ZnO seed-layer thickness and of contact distance to the NW, in order to evaluate the influence of these parameters and account for process variability. On the other hand, the nature of the seed layer is another tunable parameter. Its impact on NW features (namely average diameter, length and tilt angle) was investigated experimentally. Low temperature processes such as hydrothermal growth [3] are the only ones that enable chip post-processing without damage to the underlying layers. Thus, this technique was used to grow ZnO NWs on different clean-room processed polycrystalline layers, both template-free and patterned into arrays.

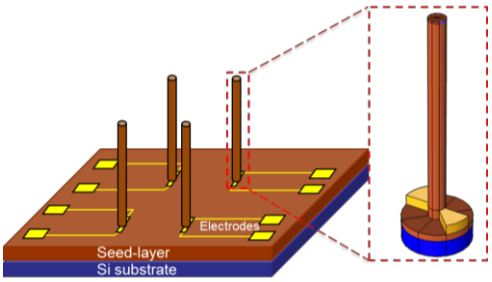

Figure 1: Schematic of the arrayed-NW sensor. Inset: one pixel constituted of an individually contacted vertical NW, with its two electrodes, a ZnO seed-layer (brown) and an Si substrate (blue).

2. Simulation and experimental conditions

A. Finite Element Model

The unit-cell is composed of a 50-nm thick silicon substrate, a piezoelectric ZnO seed-layer of variable thickness, a single vertical piezoelectric ZnO NW (diameter D_{NW}=50nm and length L_{NW}=600nm) and two, 30 nm thick, gold electrodes placed at the NW base, where the piezopotential generated by NW bending is maximum. A clamped edge condition is imposed on the bottom surface of the silicon substrate, and a lateral force of 80nN is applied at the free-end of the NW. Symmetrical contacts were considered. The electrode on the side where the force is applied is grounded, whereas the second one has a floating potential. Simulations were carried out using COMSOL multiphysics®. For the sake of simplicity, and because we were only concerned with general trends, we used linear mechanical parameters and bulk linear piezoelectric coefficients for ZnO. We assumed undoped ZnO with no free charges. The piezopotential attenuation, i.e. the ratio of the piezopotentials in the floating electrode and within the NW, was analyzed as a function of seed-layer thickness (t) and contact to NW distance (d).

B. Nanowire growth

ZnO NWs were synthesized by the hydrothermal method on different ZnO polycrystalline layers. The aqueous solution was prepared with zinc nitrate hexahydrate $Zn(NO_3)_2{\cdot}6H_2O$ and hexamethylene tetramine $(CH_2)_6N_4$ with an equimolar concentration of 30 mM and 10 mM for template-free and patterned substrates, respectively. To promote the growth of nanowires of suitable dimensions, the solutions were heated at 90°C for 16 hours and 5 hours, respectively. For patterned substrates, a triangular lattice of square holes (150 nm × 150 nm with variable spacing) was defined by e-beam lithography and dry-etched through a 100nm-thick SiN_x layer deposited on top of the ZnO seed-layer

3. Results and Discussion

FEM simulations show that the bottom region of the NW is featuring the highest piezopotential (Fig. 2a). Potential inversion in this region is a known effect due to clamping [4], [5]. A parametric analysis of the seed-layer thickness (t) demonstrated that collection efficiency increases as seed-layer thickness decreases. For a realistic thickness of 20 nm, i.e. a technologically achievable thickness, and for perfect contact between electrode and NW contact (d = 0 nm), piezopotential attenuation was about 60% (Fig. 2b). This value droped to 30% with a few nm gap between contact and NW, and remains quite stable for larger gaps, giving an order of magnitude of what can be expected accounting process variability.

A choice of suitable seed layer of appropriate thickness was then carried out among 13 different cleanroom processed ZnO layers. Deposition techniques included atomic layer deposition (ALD), chemical vapor deposition (CVD) and sputtering. The characteristics of hydrothermally grown ZnO NWs on these layers showed that Gallium-doped ZnO layers deposited at 450°C by CVD yielded low densities of nanowires with targeted dimensions, with µm-long NWs of diameters 85 ± 23 nm and 165 ± 40 nm on template-free and patterned substrates (through 150nm holes spaced by 750nm), respectively (Fig 3a and b). Next steps will include electrode deposition and the characterization of the NW-electrode contact.

4. Conclusion and Perpectives

The simulation results provided insight into device tolerance regarding process variability associated to microfabrication. Regarding heterogeneous integration, a silicon-technology-compatible NW growth process was implemented which yielded controlled-density NW growth on pre-patterned chips, using a low-temperature process that prevents damage of the underlying layers. NW-electrode contacting remains to be validated but these primary results are very encouraging.

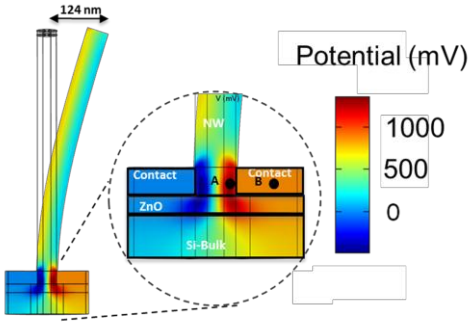

(a)

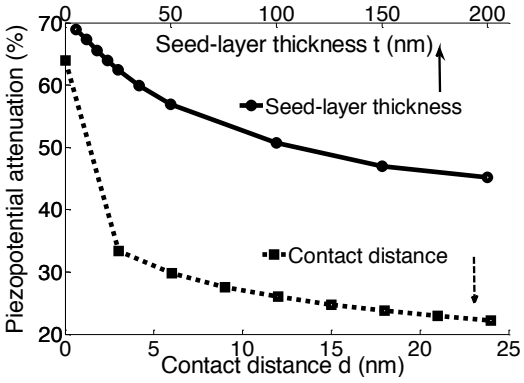

(b)

Figure 2: a) Simulated piezopotential profile within one pixel where points A and B show the maximum potential location within the NW and in the right electrode, respectively; and b) evolution of the piezopotential attenuation as a function of t (full line, d=0nm) and as function of d (dashed line, t=20nm).

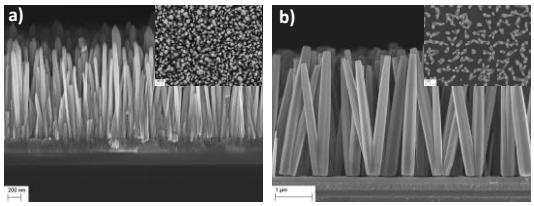

Figure 3: SEM cross-section views of vertical ZnO NWs on Gallium-doped ZnO layers: a) template-free; and b) patterned. The insets are the corresponding top views.

5. Acknowledgments

Authors acknowledge technical support from PIEZOMAT EU Project No. 611019.

6.References:

[1] Z. L. Wang, "Piezopotential gated nanowire devices: Piezotronics and piezo-phototronics," *Nano Today*, vol. 5, no. 6, pp. 540–552, Dec. 2010.

[2] R. Hinchet, J. Ferreira, J. Kera, G. Ardila, M. Mouis, and L. Montès, "Scaling rules of piezoelectric nanowires in view of sensor and energy harvester integration," in *Electron Devices Meeting (IEDM), IEEE International*, 2012, pp. 6.2.2–6.2.4

[3] D. Lincot, "Solution growth of functional zinc oxide films and nanostructures," *MRS Bull.*, vol. 35, no. October, pp. 778–790, 2010.

[4] Y. Gao and Z. L. Wang, "Electrostatic potential in a bent piezoelectric nanowire. The fundamental theory of nanogenerator and nanopiezotronics.," *Nano Lett.*, vol. 7, no. 8, pp. 2499–2505, 2007.

[5] Y. Gao and Z. L. Wang, "Equilibrium potential of free charge carriers in a bent piezoelectric semiconductive nanowire.," *Nano Lett.*, vol. 9, no. 3, pp. 1103–10, Mar. 2009.

A Comparison of Various Patch Sizes and Feed Point Positions of Graphene Microstrip Antenna

N Fugto[1], R Kaewon[2] and S Sirivisoot[1]

[1]Biological Engineering, Faculty of Engineering, King Mongkut University of Technology Thonburi, Bangkok 10140, Thailand.

[2]Department of Electrical Engineering, Faculty of Engineering and Industrial Technology, Silpakorn University, Nakornprathom 73000, Thailand.

Abstract: Antenna is used in many wireless communication devices, such as mobile phone and radar, as well as in medical devices, such as sensor or transmitter. In the present study, graphene was used as a patch material, of antenna because of mechanical, electrical and biocompatible properties. Thus, it is replaced the metallic patch-material in simulation. Titanium dioxide was used as a dielectric substrate because of it has light-weight, corrosion resistance and shape memory. The antenna was designed as microstrip with graphene as patch and titanium dioxide as dielectric substrate. The simulation results showed an early test of antenna size variation and various positions of feed point. The result of size variation showed that the width variation was more effective than length, moreover, better than a theoretical size obtained from a mathematical model. Each position of feed point gave an unique reflection coefficient of input and output electromagnetic signal wave.

Keywords: Antenna, Biomedical Devices, Feed Point, Graphene, Size Variation, Microstrip, Titanium Dioxide.

Introduction

Wireless technology has been an important part of developments in communication, education, business, and biomedical device telemetry. Orthopaedic implantation is a medical treatment of bones by a use of medical devices such as plates and screws. For example, a shoulder endoprosthesis is composed of endplate, transmitter circuit, strain gauge, cables, circuit, power coil, and antenna [1]. Antenna is a receiving and transmitting electrical signal instrument [2] and can be modified to be specific for a source of signal or target [3]. In biomedical telemetry, it is used in implant surgery and real-time monitor of blood pressure and glucose [4]. It is classified into three types, including wired, slot and patch antennas. Each type has different physical and electrical characteristics. Wired antenna is a common antenna that always used in low frequency wave range and its radiation pattern is omni-directional [5]. Slot antenna is an antenna that has slots or holes on itself and is used in a high frequency wave range (such as cell phone base station). It has a radiation characteristic as bidirectional radiation pattern [6, 7]. Patch antenna can be found in mobile phone because it has a small size, low cost and light weight and used in a wide range of frequency from 100 MHZ to 100 GHZ. Its radiation characteristic is omnidirectional [8]. Patch antenna is more suitable to be used in orthopaedic medical devices than wire and slot antennas because of its versatile working range, and a smaller size when compared to wire and slot antennas. Moreover, Costa et al. reported that the round shape antenna

had an absorbing cross section smaller than the edged shape antenna such as rectangular one [9]. Therefore, in the present study, a rectangular shape of graphene microstrip antenna was studied. Each patch antenna is composed of three components, including patch, dielectric substrate and ground plane. The patch part is used to radiate electromagnetic energy or signal. The dielectric substrate is the main mechanical and electrical characteristic of antenna. The ground plane is related to radiation pattern of antenna but it is not yet very important in the beginning of antenna design. The patch and dielectric substrate are fabricated from different materials. The materials for patch part should have a low resistance and high stability to environmental condition and chemical reaction, which is usually metallic materials such as copper and aluminum. The material for dielectric substrate should have a low relative dielectric constant in order to possess high efficiency in energy radiation of antenna [10]. However, the metallic material can cause a burden when its size is shrunk. Such antenna can lead to serious drawbacks, such as reductions of effective electron movement and resonance in high range frequency [11]. Therefore, metallic material is replaced by graphene in the present study, because graphene has a good electric conductivity and mechanical properties [12]. Moreover, graphene is a biocompatible material that do not cause harm in the human body and it can support and promote cell attachment and growth [13]. Graphene is an atomic-scale honeycomb shape of carbon atom that stronger than steel 100-300 times and has very high stiffness [12, 14, 15]. Titanium is widely used in orthopaedic implants. Titanium dioxide (TiO_2) is an oxide of titanium, which is occurred upon a contact with air and water. TiO_2 has a dielectric constant at 100 farad/meter [16] and is used in many applications including sensor and solar cell. Moreover, titanium has light weight, corrosion resistance, and shape memory effect when combined with other materials such as nickel [17]. Thus, the material for dielectric substrate of graphene microstrip antenna is TiO_2. Furthermore, when graphene and TiO_2 were combined together as the antenna, it could induce a lower resonance frequency from Terahertz to Gigahertz and was assured that the antenna is biocompatible with human healthy tissues [11]. In the present study, antenna performance in the term of reflection coefficient from mathematical model and simulation of graphene microstrip antenna was reported with various patch sizes (width and length) and positions of feed point on antenna.

Theoretical Backgrounds

First, the size of graphene microstrip antenna was designed with a theory calculation. The geometry of graphene antenna in the present study is a rectangular shape, because the previous study reported that the rectangular shape of antenna had better ability to absorb the electromagnetic radiation and can transform to the energy in the cross section of material better than the round shape [9], [18]. The mathematical model for a basic design of rectangular antennas is firstly introduced by Balanis [19]. The constant parameters used in the mathematical model include the dielectrical constant ($\mathcal{E}_r$) which is 100 farad/meter, the speed of light (c) which is 3×10^8m/s, the height of antenna (h) which is 2 mm, and the middle of frequency range (f_c) which is 2.5 GHz. The rectangular antenna dimensions were calculated for both patch and dielectric substrate. The mathematical model for each compartment is used to determine an appropriate size of that compartment, which is width and length. First, the width and length of graphene patch were calculated. Then, width and length of dielectric substrate were determined. The first equation used to calculate the width of graphene patch is shown in Equation (1).

$$W_p = \frac{c}{2f_c\sqrt{\frac{\varepsilon_r+1}{2}}} \quad (1)$$

In Equation (1), the parameter (W_p), which is the width of patch, can be calculated by substituting all constants (c, f_c and ε_r). Then, W_p was found to be 8.4 mm. The next mathematic equation uses the value of W_p to calculate the length of patch, as shown in Equation (2).

$$L_{eff} = \frac{c}{2f_c\sqrt{\varepsilon_{eff}}} \quad (2)$$

The effective length of patch (L_{eff}) in Equation (2) can be further calculated and is also used to calculate the real length of patch (L_p) in Equation (4). The efficiency value of dielectric constant (ε_{eff}) can be calculated from Equation (3).

$$\varepsilon_{eff} = \frac{\varepsilon_r+1}{2} + \frac{\varepsilon_r-1}{2}\left[1 + 12\frac{h}{W_p}\right]^{-\frac{1}{2}} \quad (3)$$

The height of antenna (h) is assigned to be 2 mm in the present study. From Equation (1), the width of patch (W_p) is known. The value of ε_{eff} was found to be 75.704. Then, ε_{eff} was replaced in Equation (2), therefore, it became Equation (4).

$$L_p = \frac{c}{2f_c\sqrt{75.704}} \quad (4)$$

When c and f_c were replaced in Equation (4), L_p was found to be 6.9 mm. Next, the most effective length or the real patch length (L_p) is calculated, as shown in Equation (5).

$$L_p = L_{eff} - 2\Delta L$$

In Equation (5), ΔL is an extension length of patch antenna that can affect to the effective length of patch (L_{eff}). The extension length (ΔL) can be calculated from Equation (6).

$$\Delta L = 0.412h\frac{(\varepsilon_{reff}+0.3)(\frac{W}{h}+0.264)}{(\varepsilon_{reff}-0.264)(\frac{W}{h}+0.8)} \quad (6)$$

The values of W_p from Equation (1) and ε_{eff} from Equation (3) were substituted in Equation (6). The ΔL was found to be 0.742 mm, and then replaced in Equation (5) to find the L_p, as shown in Equation (7).

$$L_p = L_{eff} - 2(0.742) \quad (7)$$

The L_p was found to be 5.417 mm. Thus, the size of patch part was 8.4 mm in width and 5.414 mm in length from the theoretically mathematical model.

At this point, the dimension of patch part is completed. The next part is the dimension of dielectric substrate. The mathematical equations to calculate the width and length of dielectric substrate are shown in Equations (8) and (9).

$$W_{sd} = 6h + W_p \quad (8)$$

$$L_{sd} = 6h + L_{eff} \quad (9)$$

The Equation (8) is used to find the width of dielectric substrate by substituting the previously calculated parameters from the patch design. Since h was set as 2 mm in the present study and W_p was found to be 8.4 mm, the value of W_{sd} was found to be 20.4 mm from Equation (8). And the equation (9) is same as equation (8) but use to find the length of dielectric substrate, the value of L_{sd} was found to be 18.9 mm.

After deriving parameters from Equations (1)-(9), the dimensions of patch antenna and dielectric substrate were summarized in Figure (1). Then, this theoretical geometry of the graphene microstrip antenna was used further in software simulation to determine the reflection coefficient of input and output signal wave.

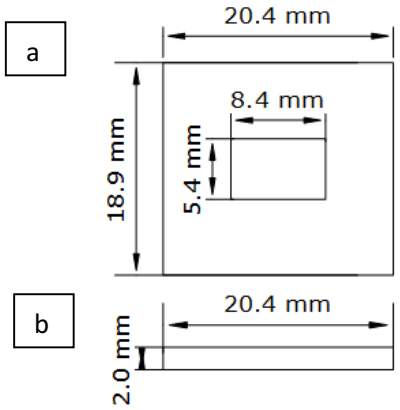

Figure (1). A diagram represents the theoretically-calculated dimension of graphene microstrip antenna. (A) The top view of microstrip shows the inner rectangle, which is the patch part (width=8.4 mm and length=5.417 mm), and the outer rectangle, which is the dielectric substrate. (B) The side view of microstrip shows the dielectric substrate (width=20.4 mm, length=18.89 mm, and height=2 mm).

Simulation Result

The present study used an EMCoS Antenna VLab software (EMCoS Ltd., Tbilisi, Georgia) for a mathematical simulation of graphene microstrip antenna on titanium dioxide substrate. A three-dimensional antenna is shown in Figure (1) with its theoretically calculated width and length. The antenna in Figure (1) was used as a beginning model in software simulation of antenna performance. The interested parameter in the present study is a reflection coefficient of input and output signal wave, or S_{11}. The simulated result of theoretically designed antenna is shown in Figure (2).

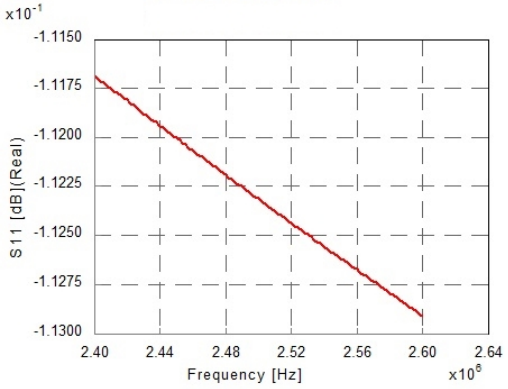

Figure (2). Reflection coefficients (S_{11}) of theoretically-designed graphene antenna in a frequency range of 2.4-2.6 GHz. The values of S_{11} are between -1.1175 × 10^{-1} dB and -1.130 × 10^{-1} dB.

Therefore, the next step is to vary width and length of graphene patch to find the appropriate value of S_{11} to be close to -10dB. The values of width and length were varied in simulation software. The simulated results from length and width variation are showed in Figures (3A) and (3B), respectively. The Figure (3A) shows the result from the simulation of length variation, when the theoretical length (L) is 5.417 mm and the range of variation is between 4.417 mm and 11.717 mm. The result suggests that the length of patch at 10.417 mm (dot line at the bottom of the figure) has the most approached value to -10 dB. At L=10.417 mm, S_{11} is between -1.543×10^{-1} dB and -1.554×10^{-1} dB. The length of patch at 5.417 mm, which is the theoretical value, has the most distant value to -10 dB. At the theoretical length, S_{11} is between -0.013×10^{-1} dB and -0.016×10^{-1} dB. The Figure (3B) shows the result from the simulation of width variation, when the theoretical width (W) is 8.4 mm and the range of variation is between 7.4 mm and 13.0 mm. At the width of 9.6 mm (cross line at the bottom of the figure), the most approached value to -10 dB is found and S11 is between -1.622×10^{-1} dB and -1.653×10^{-1} dB. The width that has the most distant value of S11 from -10 dB is at 10 mm (dot line at the top of the figure), which has S11 between -0.013 × 10^{-1} dB and -0.016 × 10^{-1} dB.

From the Figure (3), the results suggest that the width and length variation of graphene patch has a direct effect to the reflection coefficients (S_{11}) and antenna performance. The width that has the most approached value of S11 to -10 dB is at W=9.6 mm and the most distant value of S_{11} is at 8.2 mm. The S_{11} values were varied from 0 dB to -1.653 × 10^{-1}dB. The results of S_{11} from the length variation were close to each other at -1.2 × 10^{-1} dB to -1.6 × 10^{-1} dB. The mathematical simulation of the graphene patch was also performed when changing the location of feed point on the antenna. Feed point is where the components of antenna feed the electromagnetic waves to antenna [20]. The results showed that the location of feed point also affected to the reflection coefficients (S_{11}). The simulation result of S_{11} with various feed point positions of designed antenna (Figure (1)) is shown in the Figure (4).

From the Figure (4), the feed point that has the most approached value of S_{11} to -10 dB was at the point 'h', which has the position of x=0.0042, y=0.0027, and z=0.002. The result of S_{11} at the point 'h' is between -7.00 × 10^{-4} dB and -8.00 × 10^{-4} dB. Although at the 'h' position S_{11} is the most approached to -10 dB, this simulation was tested after the width and length variation to observe the effect of position of feed point to the antenna efficiency.

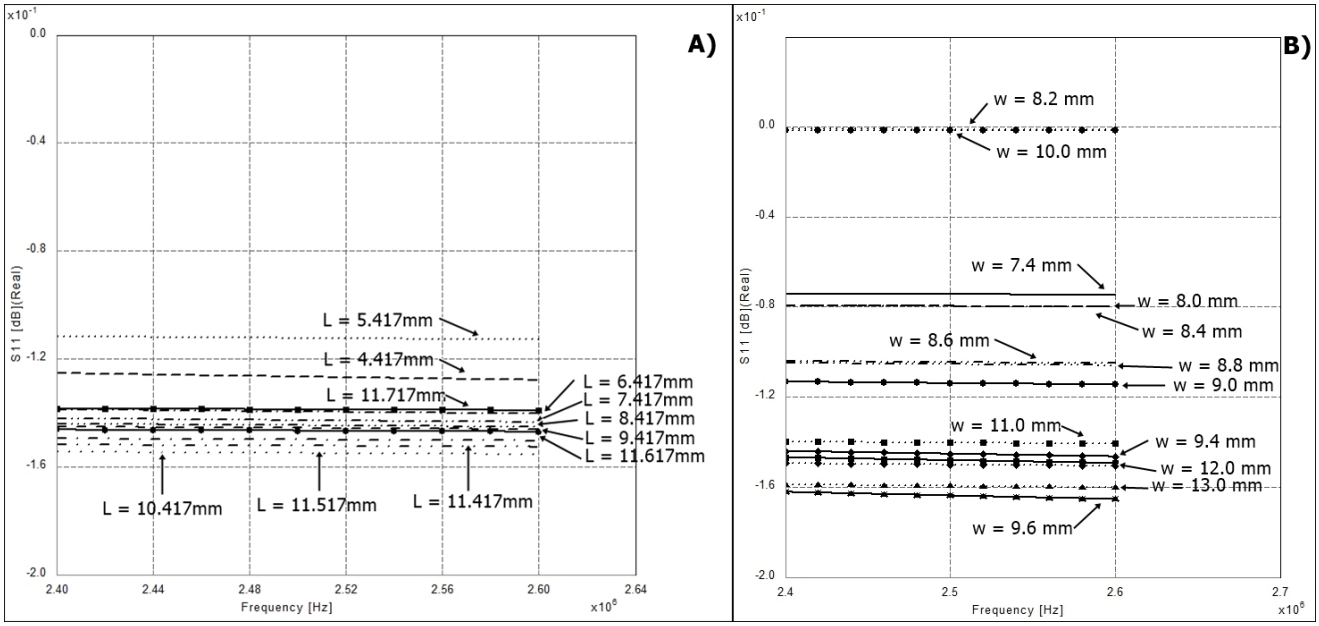

Figure (3). Reflection coefficients (S_{11}) of graphene microstrip antenna in a frequency range of 2.4-2.6 GHz: (A) length variation; and (B) width variation from the theoretical value

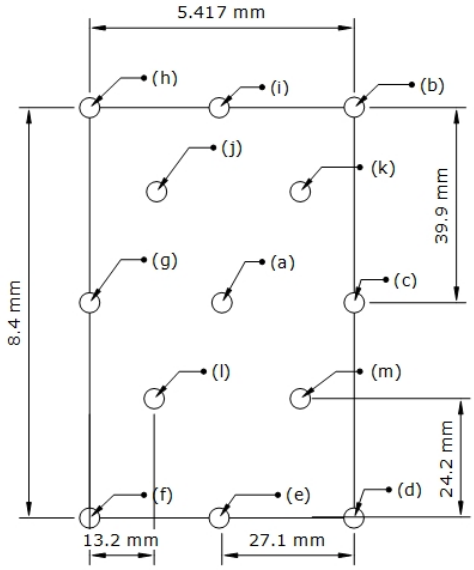

Figure (4). A diagram shows various positions of feed point on the antenna that used in mathematical simulation. The results of reflection coefficient (S_{11}) for each feed point are: a) -3.30×10^{-4} dB to -4.00×10^{-4} dB; b) -5.50×10^{-4} dB to $-6.40 \times \times 10^{-4}$ dB; c) -2.95×10^{-4} dB to $-3.40 \times \times 10^{-4}$ dB; d) 0 dB; e) 0 dB; f) 0 dB; g) -2.70×10^{-4} dB to -3.20×10^{-4} dB; h) -7.00×10^{-4} dB to -8.00×10^{-4} dB; i) -3.30×10^{-4} dB to $-3.90 \times$

10^{-4} dB; j) -2.80 × 10^{-4} dB to -3.30 × 10^{-4} dB; k) -1.90 × 10^{-4} dB to -2.25 × 10^{-4} dB; l) -2.40 × 10^{-4} dB to -2.90 × 10^{-4} dB; and m) -2.40 × 10^{-4} dB to -2.90 × 10^{-4} dB.

Discussion

The width and length variation of the patch part had a strong effect on graphene antenna radiation in term of reflection coefficient (S_{11}). The result of S_{11} suggested that the width variation was stronger effect to the antenna than the length variation. The results of S_{11} from the width variation were between 0 dB to -0.165 dB. The value of S_{11} was close to -10 dB the most at the width of 9.6 mm (S_{11}=-0162 dB to -0.165 dB), whereas, at the width of 10.0 mm the value of S_{11} was between -0.001 dB and -0.002 dB. For the length variation, the results of S_{11} were mostly close to each other from -0.120 dB to -0.160 dB. At the length of 10.417 mm, the value of S_{11} was between -0.154 dB and -0.155 dB, which was close to -10 dB the most among other lengths. However, the best value of S_{11} from the length variation was less than the best value of S_{11} from the width variation. The highest value of S_{11} (-0.011 dB) at the L=5.417 mm (the theoretical length). The results suggested that effect of the length variation to the graphene antenna radiation was less than the width variation. In a previous study of copper microstrip antenna used for medical devices which works in frequency ranges of 2-2.8 GHz and 5.3-6 GHz, the S_{11} was less than -10 dB [21]. It is probably because the size of that antenna is much larger than our antenna. Moreover, graphene patch has different electrical property and could affect the S_{11} rather than using the copper patch.

Conclusion

The theoretical design of microstrip did not give an appropriate result of return loss. Size variation of antenna was simulated and showed better results than the theoretical one. The width variation had a most approached result of S_{11} (reflection coefficient of input and output signal wave) to -10 dB when compared to the length variation. The length variation showed the similar results of S_{11} which suggested that the microstrip was stable to the length variation more than the width variation. The result in the present study is different from the previous study which reported that the graphene antenna was sensitive when changed the size of length [9]. It is also probably because the define of direction dimension is different in each work. Each position of feed point gave an unique result of return loss. In the future work, we will find an appropriate way to optimize the microstrip to exhibit the return loss at -10 dB and will observe simulated radiation characteristics of the microstrip in the human body. The work in optimizing the size antenna to exhibit the better return loss (close to -10 dB), and test the new design of antenna to compare with the theoretical design is still in progress.

Acknowledgements

The authors thank the funding from A New Researcher Scholarship of Coordinating Center for Thai Government Science and Technology Scholarship Students (CSTS), National Science and Technology

Development Agency (NSTDA), and the support of student license program of EMCoS Antenna VLab from EMCoS Ltd., Tbilisi, Georgia.

References

1. Graichen, F., et al., *Implantable 9-Channel Telemetry System for <emphasis>In Vivo</emphasis> Load Measurements With Orthopedic Implants.* Biomedical Engineering, IEEE Transactions on, 2007. **54**(2): p. 253-261.
2. Stover, H.H., *Antenna for miniature implanted medical device*. 2004, Google Patents.
3. Waiyapattanakorn, C., *The Analysi of Antenna*. Vol. 1. 2004, Bangkok: Chulalongkorn University Press.
4. Chinanupakorn, M., Thosdee, P., Thongsopa, C., *Dual Band Quasi-Rhomboid Antenna for Bio-medical Monitoring Applications.*
5. Fung, C., *Basic Antenna Theory and Application*. 2011.
6. Author, U., *OZ2OE Technical Home Page - 10 GHz waveguide slot antenna.*
7. Author, U., *Slot antenna.*
8. Roblin, P., *Past 682R Wireless Design Course Projects.* 1998.
9. Costa, K.Q., et al. *Graphene nanoantennas with different shapes*. in *Microwave & Optoelectronics Conference (IMOC), 2013 SBMO/IEEE MTT-S International*. 2013.
10. Pornchaloempong, P., Nunak, N., Rattanapaon, N. *Dielectric constant* Available from: http://www.foodnetworksolution.com/wiki/word/0645/dielectric-constant-%E0%B8%84%E0%B9%88%E0%B8%B2%E0%B8%84%E0%B8%87%E0%B8%97%E0%B8%B5%E0%B9%88%E0%B9%84%E0%B8%94%E0%B8%AD%E0%B8%B4%E0%B9%80%E0%B8%A5%E0%B9%87%E0%B8%81%E0%B8%97%E0%B8%A3%E0%B8%B4%E0%B8%81.
11. Llatser, I., et al., *Graphene-based nano-patch antenna for terahertz radiation.* Photonics and Nanostructures - Fundamentals and Applications, 2012. **10**(4): p. 353-358.
12. Fatikow, S., V. Eichhorn, and M. Bartenwerfer, *Nanomaterials Enter the Silicon-Based CMOS Era: Nanorobotic Technologies for Nanoelectronic Devices.* Nanotechnology Magazine, IEEE, 2012. **6**(1): p. 14-18.
13. Marimuthu, M., et al., *Sodium functionalized graphene oxide coated titanium plates for improved corrosion resistance and cell viability.* Applied Surface Science, 2014. **293**(0): p. 124-131.
14. Hamilton, C., & Barron, A. . *Graphene*. 2012 [cited 2014 23]; Available from: http://cnx.org/content/m29187/1.4/.
15. Fuente, J. *Graphene - What is it?* ; Available from: http://www.graphenea.com/pages/graphene#.U1c_zvmSziM.
16. Lundstrom, J.M., et al. *Measurement of the dielectric strength of titanium dioxide ceramics*. in *Pulsed Power Conference, 1999. Digest of Technical Papers. 12th IEEE International*. 1999.
17. Hermawan, H., D. Ramdan, and J.R.P. Djuansjah, *Metals for Biomedical Applications*. Biomedical Engineering - From Theory to Applications. 2011.
18. West, W., *Absorption of electromagnetic radiation*.
19. Balanis, C.A., *Antenna Theory: Analysis and Design*, ed. T. edition. 2005: Wiley.
20. Reviews, C.T., *e-Study Guide for: Modern Electronic Communication by Jeff Beasley, ISBN 9780132251136*. 2012: Cram101.

21. Soontornpipit, P., C.M. Furse, and C. You Chung, *Design of implantable microstrip antenna for communication with medical implants.* Microwave Theory and Techniques, IEEE Transactions on, 2004. **52**(8): p. 1944-1951.

Photovoltaic response of non toxic $CuInS_2$ quantum dot doped poly(3-hexylthiophene) film.

Inderpreet Singh[1,2,a)], J. Singh[2], A. Kumari[2], P.K. Rao[2] and P.K. Bhatnagar[2]

[1] Department of Electronics, SGTB Khalsa College, University of Delhi, Delhi - 110007, India
[2] Department of Electronic Science, University of Delhi South Campus, New Delhi - 110021, India

Abstract

The photovoltaic activity in the poly(3-hexylthiophene) (P3HT) and non-toxic $CuInS_2$ (CIS) quantum dot (QD) composite films has been studied. The photoluminescence (PL) spectrum of the P3HT is found to be strongly influenced by the presence of CIS molecules. Their presence quenches the PL emission from polymer, which is an evidence of the charge transfer from P3HT to CIS QDs. The electrical characterization also showed that CIS doping induces a major enhancement in the J-V characteristics at illumination. The power conversion efficiency of the solar structure containing 50 % w/w content of CIS is observed to be ~ 0.39 %, which is about an order of magnitude higher as compared with that of pristine P3HT device.

Keywords: Conducting polymer, non toxic quantum dots, photovoltaic applications, thin films.

I. INTRODUCTION

I-III-VI_2 ternary compound non-toxic quantum dots (QDs) have recently attracted the scientific community for their application in various fields of nano-electronics [1-3]. Their non-toxic nature in conjunction with semiconductor like electrical and optical properties has been the driving force behind this [4]. Although, the technology for II-VI compound semiconductor QDs has already progressed but their commercialization in various regions of

[a)] Author to whom correspondence should be addressed. Electronic mail: inderpreetsingh_05@rediffmail.com. Tel.: +91-11-24116718. Fax: +91-11-24115270.

the world has been banned. This is due to the presence of toxic heavy metals such as Cd, Pb, Te, Se, As etc. in their composition, which pollutes the environment.

$CuInS_2$ (CIS) is the most extensively studied form among various I-III-VI_2 ternary compositions. It has a small direct band gap of 1.5 eV, high absorption coefficient ($>10^5$ cm^{-1}), high photoconductivity and long term electronic stability [5-7]. The Bohr exciton radius for CIS QDs is ~4 nm hence nanopaticles having size less than ~ 8 nm can show quantum confinement effects [1]. In the present work, we have developed a composite of $CuInS_2$ QDs with the conjugated polymer poly(3-hexylthiophene) (P3HT) and studied its photovoltaic response. Polymer matrix is chosen because of its well established processing technology. Also, the cost of energy conversion in polymer based devices is much lower as compared to that in inorganic semiconductor based devices. The novelty of introducing QDs into the polymer matrix is that the exciting properties of QDs can be exploited by a simple and economic spin cast technique. Polymers, also act as a capping agent that passivate the surface states of QDs leading to reduction in their coagulation [8, 9].

II. EXPERIMENTAL DETAILS

The conducting polymers, P3HT and poly(3,4-ethylenedioxythiophene):poly (styrenesulfonate) (PEDOT:PSS) were commercially procured from Sigma Aldrich, USA. The CIS QDs were synthesized in the lab itself using indium acetate ($In(OAc)_3$), copper iodide (CuI) and 1-dodecanethiol (1-DDT) by solvothermal route as explained in our earlier communication [10]. The so formed CIS QDs were dispersed in a P3HT solution, already dissolved in toluene 10 mg/ml. Two different P3HT:CIS composite solutions were made keeping concentration of CIS as 25 and 50 % w/w. These composite solutions were then homogenised by ultrasonication for ~30 minutes and their PL spectra were recorded using Shimadzu UV-VIS spectrofluorophotometer (Model RF 5310PC). For SEM measurements

the composite film was coated on a glass substrate and the imaging was done using Zeiss EVO MA 15. Finally, the solar cell structure ITO/PEDOT:PSS/composite/Al was fabricated [11] and its dark and illuminated J-V characteristics were measured using Keithley Sourcemeter 2400 under NEWPORT-MD69907with an irradiance of 100 mW/cm^2.

III. RESULTS AND DISCUSSIONS

Fig. 1 shows a typical SEM image of P3HT:CIS composite film. It can be observed that QDs are homogeneously distributed in the polymer matrix, which is utmost required for the dissociation of photogenerated excitons throughout the film. The average size of the QD clusters is observed to be ~ 40 nm.

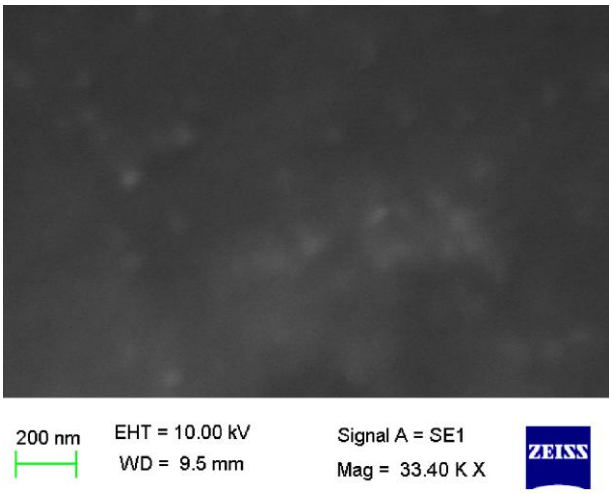

Fig. 1: A typical SEM image of P3HT:CIS (50 % w/w) composite film.

The PL spectra of P3HT:CIS composite with different CIS concentrations are shown in Fig. 2. A very high PL emission is observed from pristine P3HT, which is an evidence of the formation of excitons in the polymer. The so generated excitons have tendency to relax to ground state within a timescale of a few femto seconds. This is undesirable because if all of the excitons decay then there will be no charge carriers for the flow of current in the photovoltaic device. These excitons, therefore, have to be dissociated into free charge carriers

before they can decay to emit PL. The PL spectra also ensures that CIS QDs, due to their low lying LUMO level and high electron affinity, have capability to dissociate the photogenerated excitons in the closely lying polymer chains. The intensity of PL emission due to polymer is found to decrease as the content of CIS increases in the composite. At 50 % doping content the emission from P3HT is almost completely quenched. However, an additional peak at 670 nm in PL spectrum of the composite film is also observed. This is due to the radiative decay of excitons, which are either transferred from polymer or generated in the QDs itself. The intensity of PL emission at 670 nm is also observed to increase as the concentration of CIS increases from 25 to 50 % w/w.. The suppression of PL due to P3HT and enhancement in PL emission of CIS with increasing CIS concentration is a strong evidence of intermolecular coupling between the two species, leading to efficient charge transfer from former to later.

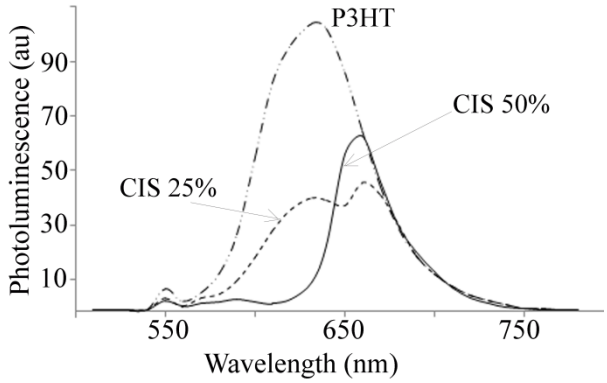

Fig. 2: Effect of CIS QDs on the PL spectrum of P3HT polymer.

The dark and illuminated J-V characteristics of the solar cell structures are shown in Fig. 3. It is observed that under illumination there is a down ward shift in the J-V curve of both the cells. The down ward shift is an evidence of the generation and flow of free charge carriers in the solar cell structure. The larger will be the current flow more will be the shift.

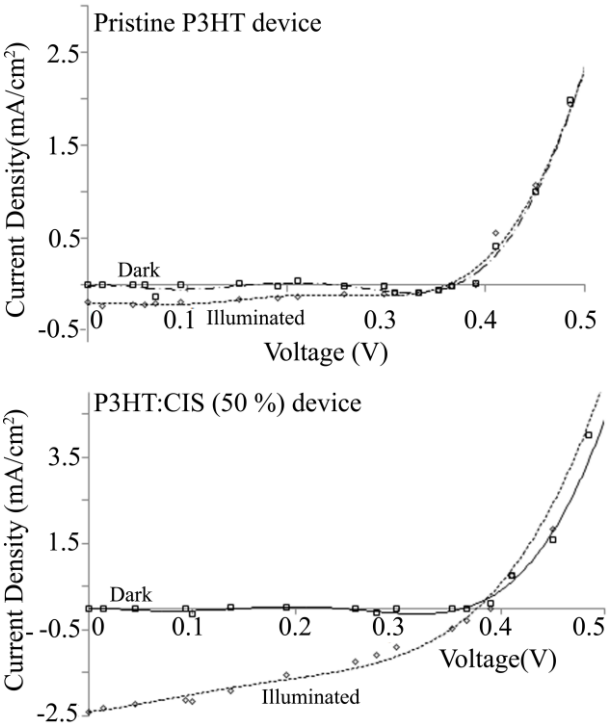

Fig. 3: J-V characteristics of P3HT and P3HT:CIS solar cells.

The inclusion of CIS QDs at 50 % w/w concentration induces a larger down ward shift as compared with that of pristine P3HT device. This is due to the fact that CIS QDs owing to their high electron affinity are able to dissociate the photogenerated excitons in the polymer chains, which increases the number of charge carriers in the photoactive film. The free electrons, so generated, are dragged by the QDs and are transferred to the cathode via hopping. The photo conversion efficiency of pristine P3HT cell was calculated to be 0.03 % and for P3HT:CIS cell (at 50 % w/w concentration) the value is 0.39 %. This enhancement, although, is not substantial for commercialization of this structure but it can be further improved by controlling other fabrication parameters that control the device efficiency. These are donor to acceptor ratio, annealing temperature, choice of solvent, morphology and film thickness. Apart from this, the presence of numerous defects in the CIS QDs also limit the device performance. It may also be noted that the PL emission at 670 nm is due to decay of excitons in QDs, which is again undesirable in the interest of developing high efficiency

device. This problem can be resolved by doping P3HT:CIS composite films with carbon materials like carbon nanotubes and graphene. These nanofillers have high electron affinity and large surface area by which, they are able to dissociate almost all the excitons generated in their vicinity [11]. They also have tendency to develop highly conducting interconnected percolation pathways in the polymer matrix which enhances the charge transport towards the electrodes.

IV. CONCLUSIONS

It can be concluded that addition of CIS QDs in the P3HT enhances the dissociation of excitons into free charge carriers. The photo conversion efficiency of P3HT:CIS composite cell is found to be ~ 0.39 %, which is more than about an order of magnitude as compared with that of pristine P3HT cells.

ACKNOWLEDGMENTS

Authors wish to thank Department of Science and Technology (DST), India for financial assistance. The financial assistance from Delhi University under Cluster innovation projects is also gratefully acknowledged.

REFERENCES

1. C. Czekelius, M. Hilgendorff, L. Spanhel, I. Bedja, M. Lerch, G. Muller, U. Bloeck, D.S. Su, and M. Giersig, Adv. Mater. **11(8)** 643 (1999).
2. E. Arici, A. Reuning, N.S. Sariciftci, and D. Meissner in Proceedings of the 17th European Photovoltaic Solar Energy Conference Munich (2001).
3. R. Xie, M. Rutherford, and X. Peng, J. Am. Chem. Soc. **131** 5691 (2009).
4. P.M. Allen and M.G. Bawendi, J. Am. Chem. Soc. **130** 9240 (2008).

5. H.J. Lewerenz, Sol. Energy Mater. Sol. Cells **83(4)** 395 (2004).
6. H.W. Schock, in Solarzellen (Ed: D. Meissner), Vieweg and Sohn, Wiesbaden. Ch 2 (1993).
7. G. Saygili, C. Ozsoy, I. Oner, C. Zafer, C. Varlikli, and C. Lcli, Synth. Met. **161(1-2)** 196 (2011).
8. Y.A. Badr, K.M. Abd Ei-Kader, and M. Khafagy, J. Appl. Polym. Sci. **92** 1984 (2003).
9. P.A. Kurian, C. Vijayan, K. Sathiyamoorthy, C.S.S. Sandeep, and R. Philip, Nanoscale. Res. Lett. **2** 561 (2007).
10. I. Singh, S. Madan, A. Kaur, J. Kumar, P.K. Bhatnagar and P.C. Mathur, MRS Comm. **4** 1 (2005).
11. I. Singh, P.K. Bhatnagar, P.C. Mathur, I. Kaur, L.M. Bharadwaj, and R. Pandey, Carbon **46(8)** 1141 (2008).

Computer microscopy of biological liquid dry patterns for medical diagnostics and modeling of their properties by dissipative dynamics methods

P. Lebedev-Stepanov ,[1,2,*] M. Buzoverya,[3] I. Shishpor[3], K. Vlasov[2]
[1]Photochemistry Center RAS, Moscow, Russia
[2]National Research Nuclear University MEPhI, Moscow, Russia
[3] Sarov State Physics Technical Institute, Sarov, Russia
*E-mail: petrls@yandex.ru

Keywords: microstructural bio-liquids' analysis, quantitative microscopy, cracks, concretions, hardware-software complex, biomedical applications, dissipative particle dynamics (DPD), self-assembly, computer modeling, nanoparticles.

Introduction

It is important to develop the high-precision computerized methods for medical rapid diagnostic which is generalizing the unique clinical experience obtained in the past decade as specialized solutions for diagnostic problems of control of specific diseases and, potentially, for a wide health monitoring of virtually healthy population, identify the reserves of human health and take the actions to prevent of these reserves depletion. Problem-solving of the complex and mass rapid diagnosis is, on the one hand, the creation of multi-function, multi-parameter stationary systems, and on the other one, in the field of mobile medicine, i.e. in the creation of mobile diagnostic units, through which the patients take the information about their health and then send to the diagnostic center through the Internet or the telephone network [1].

Diagnostic methods based on the analysis of biological liquid drying spot (pattern, facies) have all these advantages. Applications and techniques of dried blood spot (DBS) sampling (DBS-based polymerase chain reaction technologies, LC-MS/MS methods for quantitative analysis of small molecules, digital microfluidics platform for DBS diagnostics, etc) are reviewing in Ref. [2].

In addition, by today there has been accumulated a large amount of actual data on specific features of structure formation of different bio-liquids of human body in the normal state and during the pathological state development. A study of mechanisms for bio-liquids' structure formation by a method of optical microscopy is of specific interest [3-7]. Dry pattern (facies, spot) is formed by evaporation of small drop of the biological liquid on a flat substrate. Such a pattern can be used for the diagnosis of various diseases.

Materials and Methods

We demonstrate some capabilities of the hardware-software complex *Morfo* in the field of solving the diagnostics problems of the human body in normal state, and when pathology states are being developed (Fig.1) [5,6].

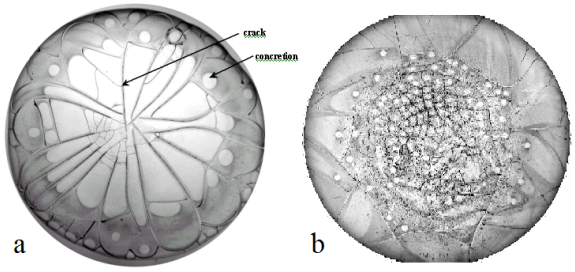

Figure 1: Blood serum facies: a – norm; b – pathology.

Formation of cracks and concretions occurs in the process of bio-liquid dehydration. Due to a complex component composition this process occurs phase-by-phase accompanied by formation of solid phase concentration zones, which are formed through corresponding bio-liquid components with definite physicochemical parameters. After evaporation of free water, a bio-liquid drop fully goes over into a solid phase and forms a facies. As a result of bound water evaporation being continued, in the facies structure there are developed rather powerful processes of stretching and compression of material, also due to protein molecules' coagulation, what causes the facies cracking and structural elements formation – *cracks*. *Concretions* are formed as a result of homogeneous substance accumulation in different facies zones, as a rule, surrounded by cracks.

In the course of experimental and clinical studies it has been shown that cracks and concretions possess a well-defined interrelation with definite physiological and pathological states of the human body [8-10]. Therefore the study of quantitative characteristics of cracks and concretions (a form, distribution homogeneity over the facies area, a size, a number and et al.) provides information on the microstructural facies inhomogeneity.

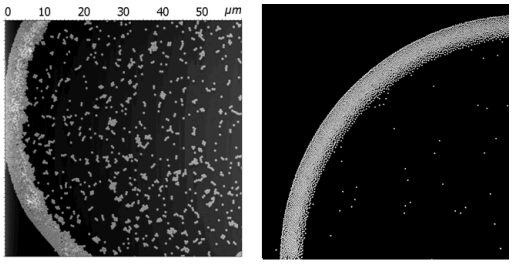

a b

Figire 2: a - ASM image of inkjet droplet pattern which consists of monodisperse colloidal particles. b –DPD numerically modeling pattern. The calculation visualization was performed via VMD 1.8.

Also we are elaborating the useful software complex to predictive modeling of setup, spreading, evaporation of liquid droplet of inkjet size, as well as self-assembly of solvated monodisperse nanoparticles from the drop during evaporation (Fig. 2), [7]. The most difficult case for modeling is a drop of biological liquid (such as blood serum, tear, saliva et al.) which consists of many different components of solution and forms the complex dry pattern onto substrate as a final stage of solvent evaporation process.

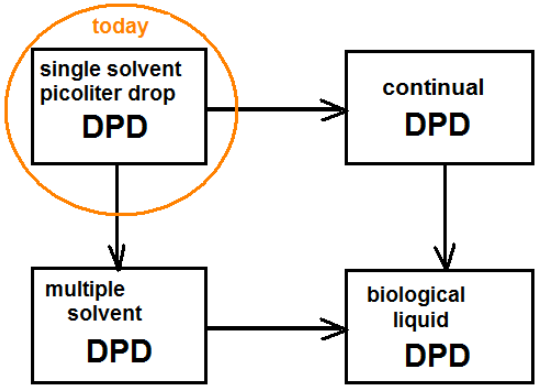

Figure 3: Running status and perspectives in modelling by dissipative particle dynamics (DPD)

The modern computer methods are not yet able to model such a system in details. Our current investigations suppose further development of DPD methods to describing the formation of the dry pattern (Fig.3) and search for new interpretation of this process and pattern diagnostics optimization.

Conclusion

A possibility for employing the complex's software for processing of bio-liquid images and specifying the most informative quantitative criteria is shown. The complex's application has allowed obtaining of interesting results not only in biomedical applications, but also acquisition of interesting data on the processes of facies structure formation**.** Theoretical interpretation and computer modeling of such a system is an actual problem of modern science and technologies.

This work was partially supported by grants of Russian Foundation for Basic Research # 15-03-08050.

References:

1. Topol E. How the Digital Revolution Will Create Better Health Care, Basic Books 2012, 303 P.

2. Li W., Lee M.S. Dried Blood Spots: Applications and Techniques. John Wiley & Sons. 2014, 364 P.

3. Brutin D. Droplet Wetting and Evaporation. From Pure to Complex Fluids. Academic Press. 2015, 464 P.

4. Tarasevich Y.Y., Pravoslavnova D.M. Segregation in desiccated sessile drops of biological fluids. Eur.Phys.J.E22(4)(2007)311–314.

5. Shabalin, V., Shatokhina, S. (2001), The human being bio-liquids' morphology, Moscow, Khrizostom. 304 P.

6. Buzoverya, M, Shishpor, I., Potekhina, Yu., Shcherbak, Yu. (2012), The bio-liquids' microstructural analysis, Journal of Technical Physics, 82, 7, 123-128.

7. Lebedev-Stepanov, P., Vlasov K. (2013), Simulation of self-assembly in an evaporating droplet of colloidal solution by dissipative particle dynamics, Colloids and Surfaces A: Physicochem. Eng. Aspects, 432, 132–138.

8. Buzoverya M.E., Shcherbak Yu.P., Sadovoy S.A., Shabalin V.N., Shatokhina S.N. Bio-liquids' morphometry «Markerblood 1.0». Certification on official registration of computer program No2005611510 dated by 20.06.2005.

9. Buzoverya M.E., Shishpor I.V., Yermakov P.V., Korzeneva I.B. Data base of bio-liquids' morphograms «Morfotest» (Data Base «Morfotest»). Certification on official registration of computer program DB No2005620026 dated by 21.01.2005.

10. Buzoverya M.E., Shishpor I.V., Sadovoy S.A. Quantitative microscopy of images of dendrite structure objects. Certification on official registration of computer program No2013610336 dated by 09.01.2013.

Carboxymethyl-nanocellulose: a versatile raw-material in coating industry

A Reis,[1]* R Duarte,[1] A Caetano[2], J Tedim[2], AP Mendes de Sousa[3], J Ataíde[3], DV Evtuguin[1]

[1]CICECO-Aveiro Institute of Materials, Department of Chemistry, University of Aveiro, 3810-193 Portugal

[2]CICECO-Aveiro Institute of Materials, Department of Materials and Ceramic Engineering, University of Aveiro, 3810-193 Portugal

[3]RAIZ, grupo PORTUCEL/SOPORCEL, Quinta de S.Francisco, 3801-501 Eixo, Portugal

*Corresponding author: anareis@ua.pt

Abstract. In a technological eco-friendly society the use of cellulosic wood pulp for papermaking needs is rapidly declining. The use of wood pulps towards the development of valuable composite biomaterials is a challenging goal and an alternative to papermaking applications. The mechanical defibrillation of cellulose fibers to nanoscale dimensions (5-10 nm) to produce nanofibrillated cellulose (NFC) offers an alternative route to drain the excess in pulp production and an attractive option to the development of innovative smart biomaterials. Currently, the development of NC-based raw materials is limited by the high production costs and the full potential of these materials in food, paper, biotechnological industries is still being explored. In this study, and benefiting from the strategic partnership between industry and academia, we describe the production of CMC nanocellulose suspensions and the properties of these raw materials for the development of controlled release systems in air-water interfaces.

1. Introduction

Cellulose is the most abundant polysaccharide and widespread biopolymer in nature. For this reason, cellulose is an attractive source for the manufacture of sustainable bio-based materials. Alternatives to the use of cellulosic pulp are emerging, particularly in the form of nanocellulose (NC) obtained by mechanical defibrillation of pulp. NC are produced as aqueous suspensions of nanometric cellulose fibrils (5-20 nm diameters) with market expectations estimating that given the current range of potential applications the production of NC could reach 35million tonnes/year by 2020 [1]. At present, the high NC production costs are delaying the full portrayal of potential applications.

Chemical and enzymatic pre-treatments performed to wood pulp facilitate the mechanical defibrillation process modification, reducing the energy input during mechanical defibrillation and costs associated. Enzymatically and chemically TEMPO-oxidized NC's are commercially available, though the yield of nanofibrils in suspension is poor. Other cellulose derivatives such as carboxymethyl groups (CMC) have been attempted though the effect of degree of substitution on the

NC suspensions and film properties is not fully characterized. So, the mechanical and water retention properties, the biocompatibility of commercial CMC are promising characteristics to use CMC as a support of biomolecules though the high degrees of substitution (DS) ranging between 0.5-1.2 and high density of anionic charged groups have a deleterious impact on the stability of the incorporated biomolecules [2] and even affecting the release behavior of incorporated drug [3].

In this study, we describe the modification of cellulosic pulp with low DS for the production of nanocellulose suspensions. The results obtained of differently modified carboxymethyl-NC are discussed and enable to evaluate the effect of degree of substitution on the properties of NC suspensions and NC films as potential eco-sustainable materials for the controlled release of bioactive components in air-water interfaces.

2. Experimental methods

Characterized *E. globulus* wood pulp was chemically modified with different degrees of carboxymethyl groups. Modified and unmodified wood pulps were submitted to mechanical defibrillation for the production of nanocellulose (NC) suspensions. NC suspensions and films produced were characterized for their chemical, physical, optical, barrier and mechanical properties. The conditions used are described below.

2.1. Wood pulp sample

E. globulus bleached kraft cellulosic pulp with 65° SR value composed of 5 mol% of xylans and cristalinity index of (CrI) of 77 was used throughout this study for chemical modification and nanocellulose production.

2.2. Functionalization of wood pulp and chemical characterization

Modification of bleached kraft *E. globulus* pulp was performed under alkali conditions (20% (w/v)) by reaction with sodium chloroacetate (0.04moles) at 65°C for 4 hours with constant stirring. Presence of carboxymethyl groups was confirmed by FTIR analyses carried out on a Perkin Elmer spectrometer under controlled moisture (35% RH) and temperature conditions (23°C). Spectral absorbance of 5 replicates for each sample was acquired at $2cm^{-1}$ spectral resolution in the $600\text{-}4000cm^{-1}$ frequency range. Absorption spectra were baseline corrected, smoothed using a Savitzky-Golay filter using Opus software (Bruker Optics). Quantification of carboxymethyl groups was done by solid state ^{13}C NMR analyses on a Bruker Avance 400MHz (magnetic field 9.4T) operating at frequencies of 100.61 MHz using a 4mm Bruker double resonance probe using the ratio of signals of carboxylic substitution (at 177ppm) and C-1 signal (at 105ppm) in the cross-polarization magic angle spinning (CPMAS) experiments as described elsewhere [4]. Acquisition parameters were as follows: contact time of 2ms, recovery delay of 4s accumulated for 7000scans.

2.3. Production of nanocellulose by ultra-homogenization

E. globulus pulp and modified pulp were prepared at 3% consistency and submitted to ultra-homogenization (GEA Panther NS3006L) in 8 passes, namely 1@500bar, 1@750bar, 1@1000bar, and 5@1500bar.

2.4. Characterisation of nanocellulose suspensions

Relative humidity and solids of nanocellulosic suspensions were determined by gravimetry. Qualitative evaluation of NC suspensions was done by spectrophotometric measurements (transmittance) in the range 200-800nm as described elsewhere [5].

2.4.1. Viscosity measurements. Dynamic viscosity measurements were done on NC suspensions using CED solution in accordance to ISO 5351 (2009) using a glass viscosimeter at constant temperature (25°C).

2.4.2. Electrochemical properties. Electrochemical impedance spectroscopy (EIS) was used to evaluate the protective performance of nanocellulose additives against corrosion of 2024 aluminium alloys in saline solutions (in a 5 mM NaCl aqueous solution). Aluminium alloy 2024-T3 with the following composition was used: Cu 3.8-4.9 %, Mg 1.2-1.8 %, Mn 0.3-0.9 %, Fe 0.5 %, Si 0.5 %, Zn 0.25%, Ti 0.15 %, Cr 0.1 %, other 0.15 %, balance Al. All the alloy panels were chemically etched prior to coating applications by a two-step cleaning procedure described previously [6]. Electrochemical impedance spectroscopy (EIS) measurements were carried out with a Gamry FAS2 Femtostat coupled with a PCI4 controller at open circuit potential with an applied 10 mV sinusoidal perturbation in the 100 kHz to 10 mHz frequency range, taking 7 points per decade. For this purpose, a conventional three-electrode cell was used, composed of a saturated calomel reference electrode, a platinum foil as the counter electrode, and AA2024 substrates as the working electrodes, with a surface area of 3.3 cm^2.

2.4.3. Incorporation of acetylsalicylic acid. NC suspensions (~45mg) were mixed with acid acetylsalicylic (15mg) and left at constant stirring at room temperature for 24hours. Aliquots of mixed suspensions were centrifuged at 4000rpm and further diluted (5 fold) before measuring absorbance values between 200-350nm.

2.5. Production of nanocellulose films

NC films (~ 20g/m^2) were produced by solvent-casting in a plexiglass support at constant temperature (25°C) in fan oven. Film thickness (μm) was measured using a Loretzen & Wettre equipment randomly across the 4 quadrants of the film. Films were characterized according to their optical and barrier properties.

2.5.1. Optical properties. Light transmission and film transparency were spectrophotometrically measured using a UV-1601 spectrophotometer (Shimadzu, Kyoto, Japan). Transparency of films was calculated considering the transmittance value at 600nm and the film thickness [7].

2.5.2. Barrier properties. Water vapour transmission rate (WVTR) of films were measured in triplicate using a ASTME96-95 standard procedure through the dessicant method (gravimetry). Circular film samples were sealed to the open mouth of the test-cups (area 19.6cm^2; internal depth 2.0cm) containing a anhydrous calcium chloride (desiccant). The sealed test-cups were weighed and placed in a test chamber with forced circulation of air (using an air-fan), at 26 ± 1°C and 42%RH (obtained with a saturated aqueous solution of magnesium nitrate hexahydrate). The test-cups were periodically weighed over a three day period, to determine the amount of water transferred through the paperboard sample into the test cup. Water vapour transmission rate (WVTR, $g.m^{-2}.day^{-1}$) were obtained from the linear representation of the experimental data, namely sample weight gain $\Delta w = (w - w0)$ versus time (t). Oil barrier properties were determined by contact angle using mineral (Silicon-based) and vegetable (sunflower-based) oils.

3. Results

Eucalyptus globulus bleached kraft wood pulp with 65°SR value and 75% relative humidity was chemically modified under aqueous eco-friendly conditions. Modified and unmodified pulps were used to produce nanocellulose suspensions. The results obtained are described below.

Chemical modification of *E. globulus* wood pulp was confirmed by the presence of absorbance bands at 1590cm-1 (**Figure 1A**). Quantification of carboxymethyl groups conducted by NMR measurements using the ratio of bands 178ppm/105ppm (shown in **Figure 1B**) reveals pulps contained a low degree of substitution (DS 0.1) with one glucose residue modified in every 10 glucose residues.

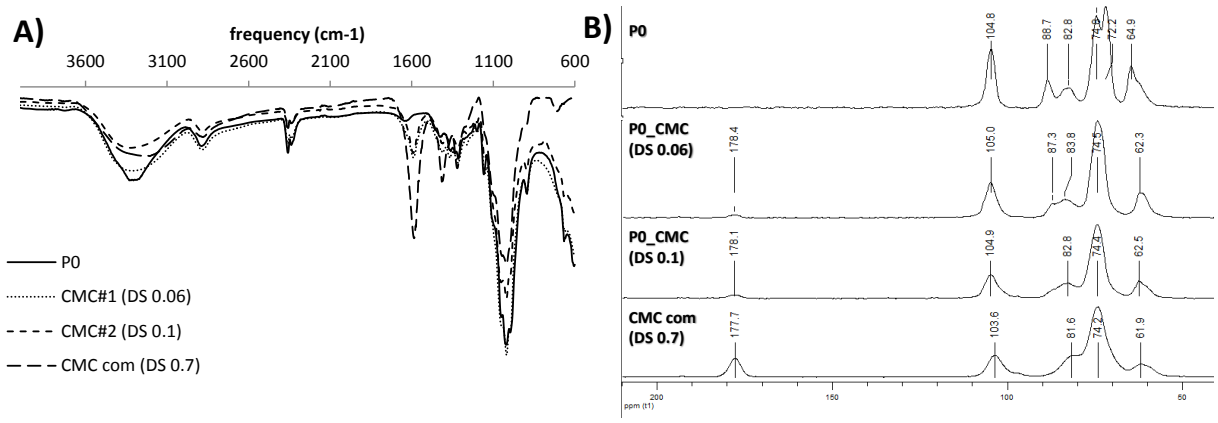

Figure 1. Characterization of prepared modified *E. globulus* pulps by FTIR analyses (A) and ^{13}C NMR (B) for quantification of degree of substitution.

Modified and unmodified pulps submitted to mechanical defibrillation process for the production of nanocellulose suspensions were qualitatively evaluated [5]. Nanocellulose suspensions of unmodified pulp exhibited low transmittance value (5%) suggesting the presence of an heterogeneous population of micro and nanofibrils in suspensions, while suspensions obtained with modified pulps exhibited larger transmittance values (>85%) suggesting a more homogeneous population of nanofibrils.

Viscosity measurements (**Figure 2A**) conducted on NC suspensions revealed that modified pulps exhibited lower viscosity values around 200cm^3/g when compared to unmodified pulp suspensions, and well above the value exhibited by the commercial TEMPO modified suspension (used as reference).

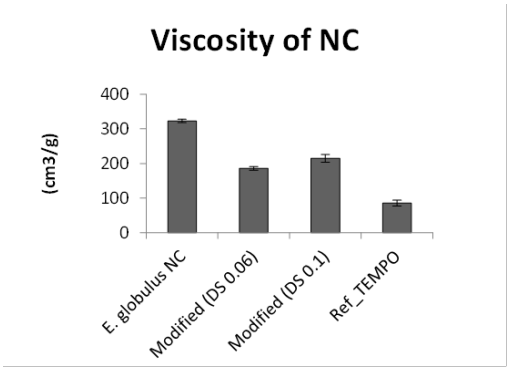

Figure 2A. Intrinsic viscosity measurements of modified and unmodified NC suspensions compared to commercial TEMPO-modified NC sample

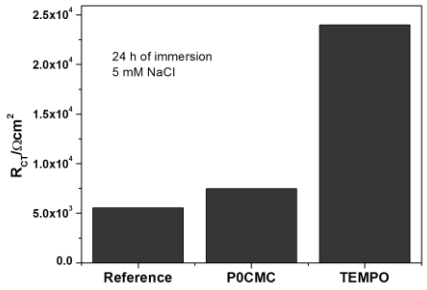

Figure 2B. Electrochemical impedance readings performed in electrolyte reference sample, CMC modified and TEMPO-modified NC suspensions.

Electrochemical impedance spectroscopy (EIS) measurements and subsequent fitting of obtained EIS spectra using equivalent circuits, allowed the estimation of charge-transfer resistance for nanocellulose-based formulations, tested directly in 0.005 M NaCl solution for corrosion protection of AA2024 (**Figure 2B**). After 24 h of immersion, the carboxymethyl-modified NC (DS 0.1) behaves similarly to the bare (reference) electrolyte, though the TEMPO NC sample performed better than the previous 2.

Additional experiments conducted on NC suspensions by incubation with acetyl-salicylic acid to study the effect of charge density on the stability of aspirin were carried out and monitored by

spectrophotometry (shown in **Figure 3**). Results obtained show the decrease of absorbance at 256nm with increasing degree of substitution.

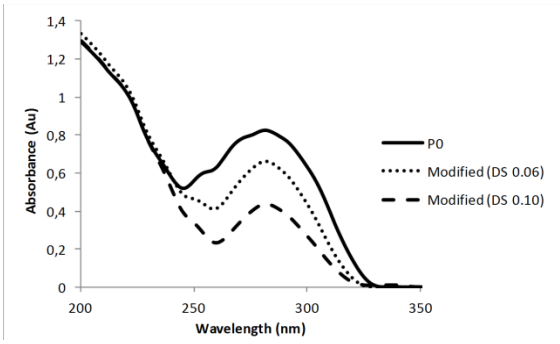

Figure 3. Absorbance measurements (200-350nm) of NC suspensions incubated with acetyl salicylic acid (aspirin).

Films (~20g/m^2) from modified and unmodified NC suspensions by solvent casting protocol were characterized regarding their optical, mechanical and barrier properties. Results obtained showed that films produced with NC suspensions from modified pulps exhibited lower transparency values and improved optical properties with increasing DS (**Figure 4A**), similar to the value obtained for the reference sample (TEMPO-modified). Films prepared with modified-NC suspensions were tested for their oil-barrier properties. As can be seen in Figure 4B, deposition of an oil drop onto the carboxymethyl-modified film retains the passage of oil up to 4 hours, whereas the oil drop deposited onto the unmodified film is not retained and soaks the paperboard sheet. Moreover, the lower water vapor transmission rate (WVTR) observed in modified films (data not shown) and improved oil-based properties (**Figure 4B**) suggest and improvement of barrier properties with modification.

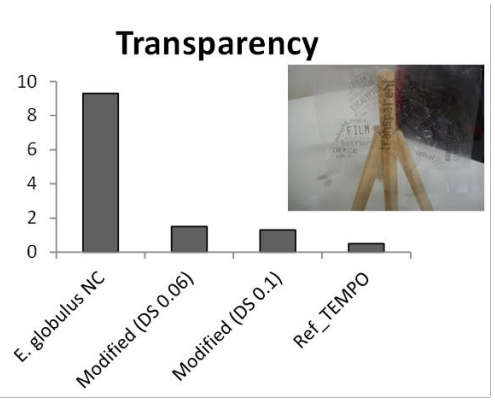

Figure 4A. Transparency values of NC films calculated using transmittance at 600nm and film thickness.

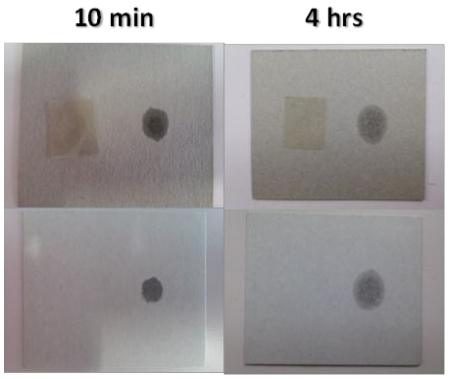

Figure 4B. Oil-based barrier properties to vegetable oils of carboxymethyl-modified films at 10min and 4hours.

The insertion of carboxymethyl groups to cellulose polymers resulted in improved optical and barrier properties, however the modification had no impact on the mechanical properties of films with high elastic modulus (~1.0x10^{10}) when compared to elastic modulus (~5x10^9) obtained for unmodified pulp films in the range -50°C to 200°C (data not shown).

4. Discussion

Currently, the development of cellulosic-based materials is highly valued as a sustainable alternative to fuel-based materials in food, cosmetic, electronic and biopharmaceutical industries. However, the high energy inputs and costs associated with the production of nanocellulose is hindering expansion of research with these raw materials and the full commercial exploitation.

Benefiting from the strategic partnership between academia and industry, we have prepared carboxymethyl-modified nanocellulose suspensions. Characterization of NC suspensions revealed that carboxymethyl groups improved defibrillation process with formation of a homogeneous network of nanofibrils, as suggested by transmittance values obtained, when compared to the heterogenous fibril population from unmodified pulps. In consequence, the NC suspensions obtained from modified pulps exhibited lower viscosity values when compared to unmodified *E. globulus* suspensions though still more viscous than the observed for the commercially TEMPO-modified suspensions (Figure 2A). The lower viscosity values observed for the commercial sample may be related to the oxidative conditions involved during TEMPO-modification reaction, suggesting carboxymethyl NC suspensions with improved rheological properties may be considered as potential additives (thickeners) in food industry. Moreover, electrochemical impedance readings obtained for modified-NC suspensions (Figure 2B) were within the same range as those obtained for the electrolyte reference sample, and a potential biodegradable alternative to the existing ones in paint industry. Incubation of acetyl salicylic acid in NC suspensions showed that the band at 256nm attributed to acetyl salicylic acid decreased with increase degree of substitution (Figure 3) suggesting that charge density of NC suspensions may affect the stability of the drug. These results reveal the crucial role of charge density in the incorporation of drug for the development of solutions tailored for wound healing.

Characterization of films produced with NC suspensions show that the increase of film transparency with increasing degree of substitution (Figure 4A), and improved oil-barrier properties to vegetable oils, as observed in Figure 4B. These properties allied with the observed lower water vapour transmission rates in carboxymethyl-modified films and oil-barrier properties (Figure 4A) together with the good mechanical properties, when compared to unmodified-films, suggest this raw material as valuable alternatives for film packaging in food industry.

Our findings suggest that modification of cellulose for the production of NC results in a raw material with improved physical, optical, and barrier characteristics valuable in the development of sustainable and versatile bio-based materials to be used as alternative to petroleum-based products in air-water interfaces.

Acknowledgements

This work was funded by ERDF Funds through Operational Competitiveness Programme – COMPETE in the frame of the project NMC – FCOMP-01-0124-FEDER-34169.

References

[1] Cellulose Nanomaterials – a path towards commercialization (workshop Report)- Aug 2014. USDA Forest Service, National Nanotechnology Initiative, Washington DC.

[2] Carlsson, D.O., Hua, K., Forsgren, J., Mihranyan, A. (2014), Aspirin degradation in surface-charged TEMPO-oxidized mesoporous crystalline nanocellu-lose. Int. J. Pharma. 461, 74-81.

[3] Valo, H., Arola, S., Laaksonen, P., Torkkeli, M., Peltonen, L., Linder, M.B., Serimaa, R., Kuga, S., Hirvonen, J., Laaksonen, T. (2013), Drug release from nanoparticles embedded in four different nanofibrilar cellulose aerogels, Eur. J. Pharm Sci., 50, 69-77.

[4] Kumar V, Yang T. Int. J. Pharm. (1999) Analysis of carboxyl content in oxidized celluloses by solid-state 13C CP/MAS NMR spectroscopy, 184, 219-226.

[5] Kangas H, Lahtinen P, Sneck A, Saariaho A-M, Laitinen O, Hellen E. Characterization of fibrillated celluloses. A short review and evaluation of characteristics with a combination of methods. Nordic Pulp & Paper Res. J. 2014, 29, 129.

[6] J. Carneiro et al., RSC Adv., 2015, 5, 39916.

[7] Jridi M, Hajji S, Ayed HB, Lassoued I, Mbarek A, Kammoun M, Souissi N, Nasri M. Physical, structural, antioxidant and antimicrobial properties of gelatin-chitosan compositie edible films. Int. J. Biol. Macromol. 2014, 67, 373-379.

Raman SERS monitoring of Acetylcholinesterase activity for the detection of pesticides

Amal EL ALAMI [1,2*], Fabienne LAGARDE[1], Mimouna BAITOUL [2,] Philippe DANIEL[1]

1. Institut des Molécules et des Matériaux du Mans UMR CNRS 6283 (France) ; 2. Laboratory of Solid state physics, polymers and nanomaterials, USMBA, FSDM, Fès, Morocco;

*: amal.el_alami.etu@univ-lemans.fr

ABSTRACT

In this work, we present a new Raman SERS biosensing system for pesticides detection by measuring the Acetylcholinesterase (ACHE) activity. Gold nanoparticles (AuNP) were used as dynamic surface-enhanced Raman spectroscopy (SERS) for sensitive monitoring of ACHE activity in the presence of very low levels of Paraoxon (PO) pesticide. The limit detection of PO was determined at 10^{-2} nM. These results suggest that this methodology could be used for the non-selective detection of all ACHE inhibitors at low concentrations.

Keywords

Raman SERS, Biosensor, Pesticides, AuNP, ACHE.

1. INTRODUCTION

ACHE is one important enzyme in the brain. It hydrolyzes the neurotransmitter acetylcholine (ATC) to choline and acetic acid [1,2]. ACHE can be inhibited by many types of neurotoxins and drugs and its inhibition can cause loss of memory and impairment of neuromuscular functions.[3, 4]

Paraoxon (PO) is an organophosphate pesticide, widely used in agriculture. It is known as a powerful ACHE inhibitor[5]. Therefore ACHE activity can be used as a biomarker of this pesticide exposure [6, 7]. There are already techniques for the detection of ACHE inhibitors but most of them are specific to each pollutant and they usually require long times of analysis. In recent years, SERS has been developed for many applications such as detection. Due to its sensitivity and ease to use, SERS protocols have been implemented in many research areas such as biology, material science, art, and analytical chemistry. The aim of this study is to provide a tool for the fast and sensitive detection of ACHE inhibitor pesticides using AuNP as active SERS substrate, without any functionalization step.

2. Materials and methods

2.1 Chemicals

ACHE from Electrophorus electricus (500U/mg), acetylcholine chloride was purchased from sigma-Aldrich. Phosphate Buffer (PB) was prepared at pH =8 as a mixture of KH_2PO_4 (1 M) and K_2HPO_4 (1M) solution in deionized water. $HAuCl_4$ and Paraoxon 97% were purchased from Sigma Aldrich. ATC (0.01 M) is added to the ACHE solution in PB as substrate for activity measurements.

2.2 Synthesis of gold nanoparticles

AuNP colloids were prepared according to the literature by citrate reducing method[8]. They were characterized by UV-Visible spectroscopy and TEM to examine their shapes and average size. The spherical AuNP showed one Plasmon band at 516nm with average size of 15nm. Before use the solution of synthesized AuNP was centrifuged.

2.3 Raman SERS measurements

To collect the SERS spectra, 5µL of the analyte solution and 5µL of AuNP solution were mixed before deposition on a glass slide. For each analysis, 6 SERS spectra were acquired at different position on the slide and an average of spectra was generated. SERS spectra were recorded with a Raman X-Plora spectrometer from HORIBA. The 638 nm excitation wave length was provided by a diode laser with an output power of 4mW with a 50x microscope objective from 400 to 2000cm^{-1}. The spectra were recorded with acquisition times of 10s with 5 accumulations. The SERS spectra were recorded. All spectra displayed here were baseline subtracted and normalized.

2.4 Detection principle for the proposed biosensor

2.4.1 In absence of pesticide (active ACHE)

The activity of ACHE was first monitored in the absence of pesticide. In this case, according to reaction (1), ATC added to the enzyme solution was totally hydrolyzed in choline and acetic acid.

$$ATC + H_2O \xrightarrow{ACHE} Choline + Acetic\ acid \quad (1)$$

2.4.2 In presence of pesticide (inhibited ACHE)

In the presence of pesticide, ACHE was inhibited and ATC cannot be totally transformed in choline and was still present in solution.

$$ATC + H_2O \xrightarrow{ACHE+Pesticide} ATC + choline + acetic\ acid \quad (2)$$

2. Results and discussion

In the absence of pesticide, after addition of AuNP to the analyte solution (ACHE + ATC), a very intense Raman signal is obtained (Figure 1a) corresponding to the SERS spectrum of choline with typical bands at 713, 960 and 1435cm^{-1}[9,10]. In Figure 1b, the SERS spectrum of the ATC solution is presented for comparison purpose. The bands at 639 and 1735 cm^{-1} are characteristic of the acetic acid part of the molecule. Their disappearance in the spectrum 1a is directly correlated to the ATC hydrolysis as evidence of the ACHE activity.

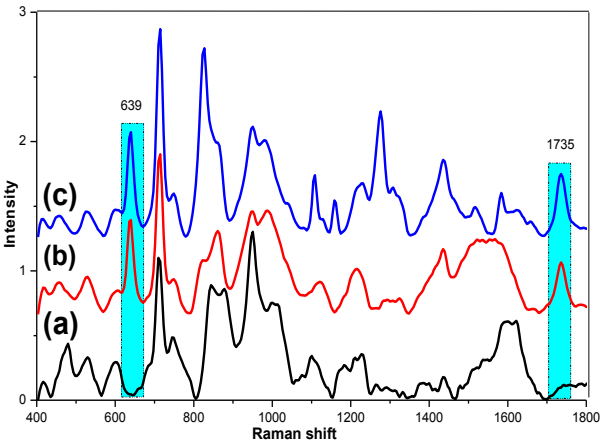

Fig.1 (a) SERS spectra of ACHE mixed with ATC (without pesticide Eq.1), (b) SERS spectra of ATC control (c) SERS spectra of ATC added to ACHE mixed with PO ($4*10^{-5}$ M)(presence of pesticide Eq.2).

In the presence of pesticides in the analyte solution, when AuNP are added, they bind to ATC molecules (eq. 2) that were not hydrolyzed by ACHE. In this case, the Raman signal (1c) which is observed is very close to the SERS spectra of pure ATC (1b) with the same characteristic bands of the molecule. This confirms that the inhibition of the ACHE activity in presence of paraoxon can be monitored by Raman spectrometry.

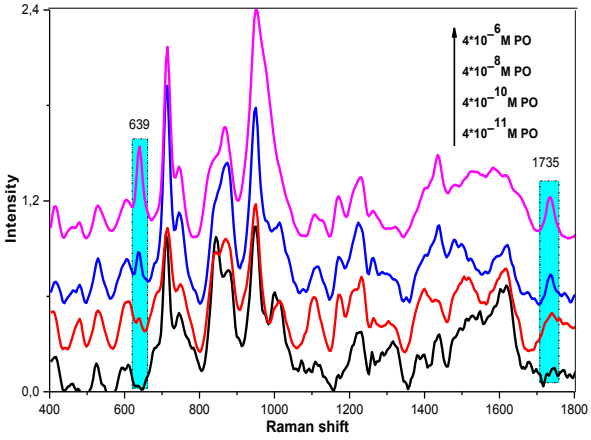

Fig.2. (a) SERS spectra of ATC after incubation with ACHE mixed with PO pesticide $4*10^{-6}$; $4*10^{-8}$; $4*10^{-10}$ and $4*10^{-11}$ M respectively.

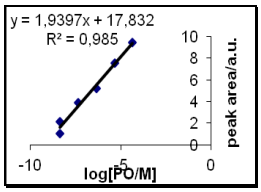

Fig.3. Calibration curve displays the effect of paraoxon on the Raman 639cm^{-1} peak intensity. ACHE was incubated with different concentrations of PO ($4.10^{-5}$to 4.10^{-10} M), before adding ATC.

Different concentrations of paraoxon were tested from 4.10^{-5} to 4.10^{-11} $mol.L^{-1}$. For each concentration, the pesticide solution was set at the contact with ACHE during an optimized duration of 3 hours before SERS analysis. As shown on Figure 2, the intensity of the 639 and 1735 cm^{-1} bands increase with pesticide concentration showing the progressive loss of ACHE activity for the transformation of ATC. The intensity of the 639 cm^{-1} band as a function of paraoxon concentration is plotted in Figure 3. It shows that this intensity is directly proportional to the PO concentration. These results demonstrate that this nanobiosensor can be used for the detection of all ACHE inhibitors and for measuring the ACHE activity.

3. Conclusion

A novel sensitive SERS nanobiosensor for detection of ACHE inhibitors and measuring ACHE activity was developed based on Raman spectroscopy using gold nanoparticles for SERS effect. This optimized protocol was found very sensitive for the monitoring of ACHE loss of activity in presence of very low paraoxon concentration. The response to paraoxon presence was found to be linearly correlated with its concentration. The resulting nanobiosensor could be used in the future for the detection of all types of ACHE inhibitor with excellent sensitivity and good reproducibility.

REFERENCES

1. Xia N, Zhang Y, Chang K, et al. Ferrocene-phenylalanine hydrogels for immobilization of acetylcholinesterase and detection of chlorpyrifos. 2015;746:68-74.

2. Fonnum F. Radiochemical micro assays for the determination of choline acetyltransferase and acetylcholinesterase activities. *Biochem J*. 1969;115(3):465-472.

3. Frank B, Gupta S. A review of antioxidants and Alzheimer's disease. *Ann Clin Psychiatry*. 2005;17(4):269-286. doi:10.1080/10401230500296428.

4. Hyeock S, Ho Y, Ho D, Jea D, Hyeon J. Mutation and duplication of arthropod acetylcholinesterase : Implications for pesticide resistance and tolerance. 2015;120:118-124.

5. Carvalho FP. Agriculture, pesticides, food security and food safety. *Environ Sci Policy*. 2006;9(7-8):685-692. doi:10.1016/j.envsci.2006.08.002.

6. Ma K, Lu L, Qi Z, Feng J, Zhuo C, Zhang Y. Biosensors and Bioelectronics In situ induced metal-enhanced fl uorescence : A new strategy for bio- sensing the total acetylcholinesterase activity in sub-microliter human whole blood. 2015;68:648-653.

7. Zheng Y, Liu Z, Jing Y, Li J, Zhan H. Sensors and Actuators B : Chemical An acetylcholinesterase biosensor based on ionic liquid functionalized graphene – gelatin-modified electrode for sensitive detection of pesticides. 2015;210:389-397.

8. Kimling J, Maier M, Okenve V, et al. Turkevitch method for gold nanoparticle synthesis revisited. *J Phys Chem B*. 2006;110(95 mL):15700-15707.

9. Siek M, Kaminska A, Kelm A, et al. Electrodeposition for preparation of efficient surface-enhanced Raman scattering-active silver nanoparticle substrates for neurotransmitter detection. *Electrochim Acta*. 2013;89:284-291. doi:10.1016/j.electacta.2012.11.037.

10. Gauthier S, Belin CGM. Pages 29-33 WITH ALUMINIUM OXIDE SURFACE STUDIED BY INELASTIC Copyright © 1980 by Academic Press , Inc . All rights o f reproduction in any form reserved . 1980;94(1):29-33.

Nanostructured Polymer Matrix Composites for High Performance Engineering Applications

T. Turcsán[1,*], L. Mészáros,[1,2]
[1]Budapest University of Technology and Economics, Department of Polymer Engineering, Muegyetem rkp. 3., H-1111 Budapest, Hungary
[2]MTA–BME Research Group for Composite Science and Technology, Muegyetem rkp. 3., H-1111 Budapest, Hungary
*corresponding author, e-mail: turcsan@pt.bme.hu

Abstract: The researchers and developers intend to obtain favourable mechanical and thermal properties on the field of polymer composites. The thermoset matrix polymer composites have great mechanical properties and relatively good thermal resistance, but they have not as good toughness as the thermoplastic polymer ones, ductile metals and alloys have. The high performance polymer composites usually give rigid reactions to the quickly forthcoming and cyclic loads. Rigidity could be caused by the pronouncedly rapid crack propagation and fracture velocity inside of the composite. This is the reason why it is important to improve their toughness without decrease the great strength properties (Karger-Kocsis, 2005).
Usually the matrix of the polymer composite is responsible for the toughness of the complete material. Improvement in the toughness of the thermoset resins can be reached by several ways. One of them is creating nanostructure in the material by modification its morphology. On one hand it is possible by incorporation of nano-sized additives, nanoparticles to the resin on the other hand there is an opportunity to interblend different type of resins. During the crosslinking process of different mixed resins the compound can be divided to at least two segments by phase separation processes. Because of this phase separation in case of optimal conditions it is possible that nanostructured hybrid resin come into being with co-continuous conformation. In this nanostructured material, there are lots of entanglements of the molecule chains of the components by the way they have lots of secondary bounds between them with additional flexibility and toughness. By reason of the mentioned phenomena the crack propagation of the hybrid resin is hampered because of lots of bounds and molecule entanglements in the material (Turcsán et al, 2014).
Using the mentioned phase separated hybrid resin as matrix material of fibre reinforced composite (Fig 1) it could result improved damping properties by the way enhanced toughness (Mészáros et al, 2014).
The main aim of our research work is to create nanostructured high performance fibre reinforced polymer composites for mechanical applications and to investigate their morphological and mechanical properties.

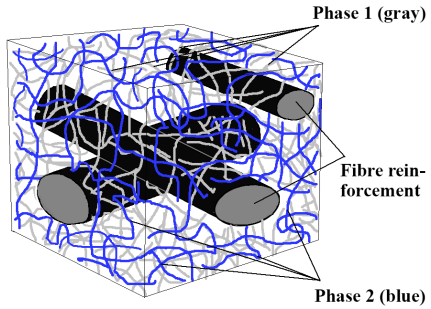

Figure 1: Theoretical structure of a co-continuous matrix hybrid composite

Materials: As matrix material epoxy (EP), and vinyl ester (VE) were used. The EP consisted of a bisphenol A diglycidyl ether (with 188 g/epoxy equivalent, 12000 mPa·s viscosity at 25°C, and 1.17 g/cm^3 densiy, Ipox ER 1010 product name, manufactured by Ipox Chemical Hungary) and isophorone diamine hardener (with 43 g/hydroxy equivalent, 5-25 mPa·s viscosity at 25°C, ~660 mg KOH/g amine value, Ipox EH 2293 product name, manufactured by Ipox Chemicals, Hungary). The VE resin (bisphenol based, with 1300 mPa·s Brookfield viscosity 5 rpm at 25°C, 35% styrene content, AME 6000 T 35 (product name), manufactured by Ashland Italia S.p.A., Italy was used. In case of VE resin 2 wt% amount of methyl-ethyl ketone peroxide accelerator (in diisobutyl phtalate dissolved), MEKP-LA-3 (product name), manufactured by Peroxide Chemicals, South Africa) was used. As reinforcing material unidirectional carbon fabric Panex 35 FB UD 300 was used (sized for epoxy, manufactured by Zoltek Zrt., Hungary).

Experimental: There were applied two different method for creating mixed resins. Both of them have 1:1 ratio of EP and VE. In the first method (#1) the EP and VE resins were stirred for ten minutes. Then the amine of EP was added in and stirred for two further minutes again. Finally the catalyst of VE was added also stirred for two minutes. For the second method (#2) the EP and its amine was mixed in stoichiometric ratio, stirred for two minutes. After that it had 30 minutes rest time at room temperature without stirring. Then the VE was added and stirred calmly for two minutes. Finally, exactly the same as the first method the catalyst of the VE was added and stirred for two minutes. Composites were made by simple hand lay-up method using 6 unidirectional carbon

fabric layers, the orientation of the layers was the same. After the hand lay-up the laminates were pressed between parallel steel plates by hydraulic press with 0.5 MPa compressive stress at room temperature. Beside the EP/VE matrix, reference composites with exactly the same reinforcement orientation and content were also prepared with EP and VE. After 24 hours of crosslinking all of the laminated composites were cured at 80°C for 4 hours. The interlaminar shear stregth tests (ILSS) of the composite materials were carried out in compressive mode with 1,3 mm/min test speed on a Zwick Z020 (Germany) universal testing machine at room temperature according to ASTM D3846-94. The specimens of the ILSS investigation were double-side notched to the middle layer of the composite plates, the direction of the reinforcement was along to the specimens. To avoid the buckling effect a special adapter was used during the ILSS tests. The images of the scanning electron microscopy (SEM) were produced by a JEOL JSM-6380 LA device. The samples were coated with a thin Au-Pd layer for the proper conduction of them and avoid overcharging.

Results and discussion:

The usefulness of the composites material can be characterized by their interlaminar properties because it can shead light to the quality of the matrix-reinfoircement connection and the toughness of the matrix material as well. The results of the ILSS investigation (fig 2) show that the hybrid resin matrix composites have higher average shear stress values than the others beside moderate standard deviations. It can be rooted in the spacial phase structure and entanglemented molecule chains of the mixed resins, which could indicate a proper connection between components of the mixed resin and maybe between the matrix and reinforcement as well.

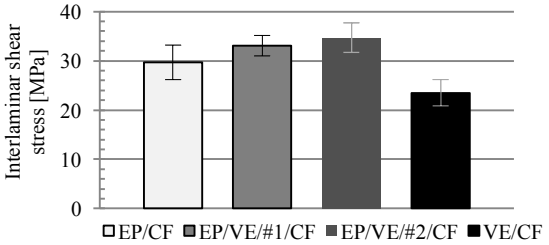

Figure 2: The interlaminar shear strength of the investigated CF reinforced composites

The SEM pictures of the fractured surface of ILSS specimens (fig 4) shows that the compatibility of the reinforcement and the matrix was proper in case of all investigated material but the cracking mechanisms of them were different. The EP composite (fig 3/a) shows typical fracture surface with good adhesion, the VE matrix composite have less good adhesion compared to the EP composite. The hybrid matrix composites have better reinforcement-matrix connection compared to the VE composite and their fracture surface shows hackle pattern effect, which demands more energy during the cracking process this is the reason of the higher level of interlaminar shear strength in case of hybrid resin matrix composites. The fracture mechanism of mixed resin matrix composites could be caused basically by the micro- or nanostructured phase boundary system of the hybrid resins. The lots of presumed entanglements of molecule chains results more toughen matrix and they may generate a better and tough connection between the matrix and fibre reinforcement.

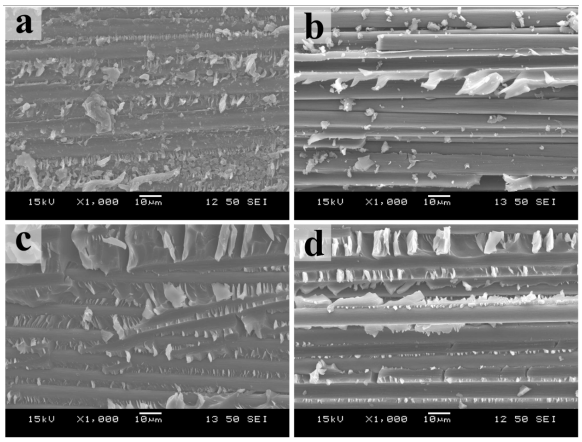

Figure 3: The SEM images on the fractured surface of the ILSS specimens, EP/CF (a), VE/CF (b), EP/VE/#1/CF (c), EP/VE/#2/CF (d)

Conclusions: In this study high performance hybrid matrix fibre reinforced composites were produced and their mechanical properties were characterized. The developed hybrid matrix composites have better toughness because the phase structure of the mixed resins. Another benefit of them is the lower styrene content compared to the neat VE and reduced cost compared to the initial EP resin.

Keywords: polymer composites, phase separation, high performance composites, epoxy, vinyl ester

Acknowledgement: This research was realized in the frames of TÁMOP 4.2.4.A/1-11-1-2012-0001 „National Excellence Program – Elaborating and operating an inland student and researcher personal support system" The project was subsidized by the European Union and co-financed by the European Social Fund. This research was also supported by the Hungarian Research Fund (OTKA PD105564).

References:

Karger-Kocsis J. (2005) Simultaneous interpenetrating network structured vinyl ester/epoxy hybrids and their use in composites, in 'Micro- and Nanostructured Multiphase Polymer Blend Systems: Phase Morphology and Interfaces' CRC Press, Boca Raton.

Mészáros L., Turcsán T. (2014), Development and mechanical properties of EP/VE hybrid composite systems, Periodica Polytechnica, Mechanical Engineering, 58, 127-133.

Turcsán T., Mészáros L (2014), Development of high-performance polymer composite with toughened matrix, The Fiber Society Spring 2014 Conference, May 21-23, 2014, Liberec, pp 69-70.

High Pressure Laminates containing Fluorinated Polyhedral Oligomeric Silsesquioxanes

S Magina[1]*, J Ferra[2], P Cruz[3], I Portugal[1] , D Evtuguin[1]

[1]CICECO – Aveiro Institute of Materials, Department of Chemistry, University of Aveiro, 3810-193 Aveiro, Portugal
[2]EuroResinas – Indústrias Químicas SA, 7520-064 Sines, Portugal
[3]SONAE Indústria de Revestimentos (SIR), 4470-177 Maia, Portugal

(*) E-mail: smagina@ua.pt

Abstract. High Pressure Laminates (HPLs) are durable, resistant, environment friendly and good cost-benefit decorative surface materials with special properties tailored to meet market demands. In the present work, Fluorinated Polyhedral Oligomeric Silsesquioxanes (F-POSS) particles were synthesized, characterized (by DSC, SEM and XRD) and incorporated in HPLs aiming the improvement of dirt-repellence and abrasion resistance. Promising results were obtained with F-POSS loads ranging from 0.25% up to 1.0% w/w of melamine-formaldehyde (MF) resin formulations.

1. Introduction

High Pressure Laminates (HPLs) are considered the most versatile and ubiquitous decorative materials used by the furnishing and building industries to produce furniture, countertops, flooring and wall paneling surfaces. They exhibit high durability and special surface properties including chemical, heat, stain and wear resistance. HPLs consist of an assembly of phenol-formaldehyde resin-saturated layers (5 to 50) of kraft-paper topped by a single decorative-paper layer and, in some cases, a finishing protective overlay (Figure 1), all cured during pressing at high temperature and pressure.

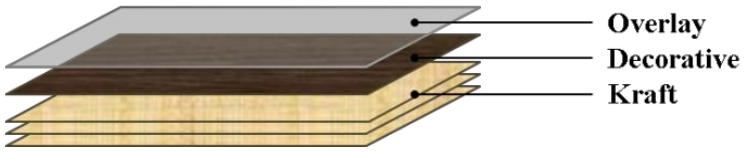

Figure 1. Scheme of a typical assembly of an HPL.

Considerable research has been carried out to improve the hydrophobicity and oleophobicity of surfaces. Promising results concerning the use of oxidized siloxane surfactants to improve cleanability of melamine-formaldehyde (MF) based decorative laminates have been recently reported [1].

It is well recognized that the development of hydrophobic surfaces is achieved by reducing the surface free energy (SFE) and/or by increasing the surface roughness [2,3]. It is also known that incorporating/grafting fluorinated or perfluorinated compounds reduces the SFE of a material [4,5] whereas surface roughness may be enhanced using bulky compounds such as Polyhedral Oligomeric

Silsesquioxanes (POSS), which have a general structure $(RSiO_{1.5})_8$ comprising a siloxane cage in a three-dimensional arrangement [6]. Both strategies can be combined using a fluorinated or perfluorinated POSS (F-POSS) [7] that can be incorporated into a resin formulation dissolved in a solvent or as dry powder by melt or mechanical blending.

F-POSS are synthesized via a simple single-step base-catalyzed sol-gel method [5,8]. Generally, F-POSS are white solid crystalline particles exhibiting a melting point between 120 - 140 ºC and low surface energy [8], therefore they are highly hydrophobic [5,8] and oleophobic [9] materials. Blending F-POSS into functional polymers, such as poly(methyl methacrylate) (PMMA), enhances the hydrophobicity and thus reduce the surface energy of the ensuing polymer composite [10,11]. Therefore, it is expected that F-POSS may be incorporated into other polymer mixtures, namely in melamine-formaldehyde (MF) resin formulations, in order to produce HPLs with improved surface properties, in particular, enhanced hydrophobicity.

In this work a promising route to improve the dirt repellence character of HPLs by reinforcing the MF resin formulation with F-POSS particles, is presented. In particular, this work concerns the synthesis and characterization of 1H,1H,2H,2H-nonafluorohexyl POSS (FH-POSS) particles and their incorporation in HPLs. Though flurodecyl POSS (FD-POSS) is more stable and hydrophobic than other F-POSS materials [5,8], several attempts to obtain solid (powder) FD-POSS particles failed since the product was persistently a gel-type material unsuitable for dispersion in the MF resin formulations.

2. Materials and Methods

2.1. FH-POSS synthesis and characterization

FH-POSS $(1H,1H,2H,2H\text{-nonafluorohexyl})_8Si_8O_{12}$, was synthesized by a sol-gel method [5,8]. FH-POSS particles (a fine powder) were characterized by Differential Scanning Calorimetry (DSC), Scanning Electron Microscopy (SEM) and Powder X-Ray Diffraction (XRD).

Decorative (deep brown color imitating wood texture) and overlay (semi-transparent) papers were impregnated with MF resin formulations containing different loads of FH-POSS particles (0.25%, 0.50%, 0.75% and 1.0% w/w MF resin formulation). The ensuing FH-POSS-HPLs were prepared as usual and tested by proven industrial procedures (EN 438-2:2005). Contact angle (CA) measurements were carried out using three probe liquids (water, formamide and diiodomethane) to assess the wettability of the FH-POSS-HPLs and to determine the optimal load of FH-POSS particles.

3. Results and discussion

3.1. FH-POSS characterization

Syntheses (4 replicas) of FH-POSS particles were carried out as described in the literature with consistently high yields (64% w/w product/silane) and a reproducible product. The final product consisted of a fine white powder with irregular size (0.5-5.0 μm) and shape particles (Figure 2). Furthermore, the FH-POSS particles are highly crystalline having a triclinic unit cell (Figure 3) and a melting point of 127.06 ± 0.28 ºC (four replicas, data ascertained by DSC).

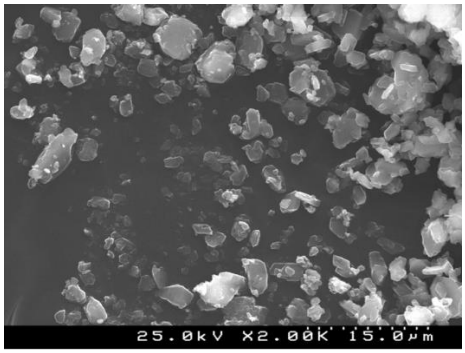

Figure 2. SEM image of FH-POSS particles.

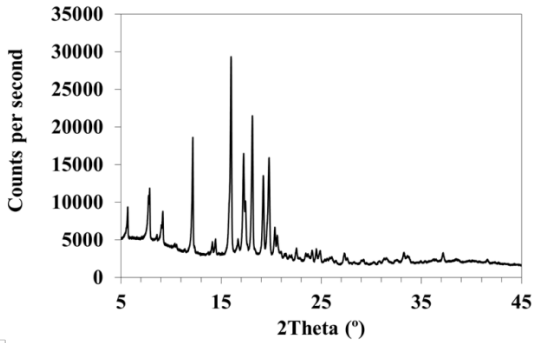

Figure 3. XRD pattern of FH-POSS particles.

3.2. HPLs characterization

The dispersion of FH-POSS particles within the MF resin formulation was satisfactory as observed by SEM-EDX images (Figure 4) of the FH-POSS-HPLs where the green spots correspond to Fluorine (F) and the red spots to Iron (Fe). The concentration of green spots indicates a regular distribution of FH-POSS and it increases with the particle load, as expected, since the presence of fluorine derives solely from the FH-POSS particles. The presence of iron (red spots) is abundant and cannot be neglected. The most plausible explanation for iron is its presence in the decorative paper, probably as part of a pigment, and not from the MF resin since iron-based compounds are not allowed in MF resin formulations. Noteworthy the abundance of red spots (Figure 4) decreases as the load of FH-POSS particles in the MF resin increases, thus confirming that the presence of iron is concealed by the fluorinated particles.

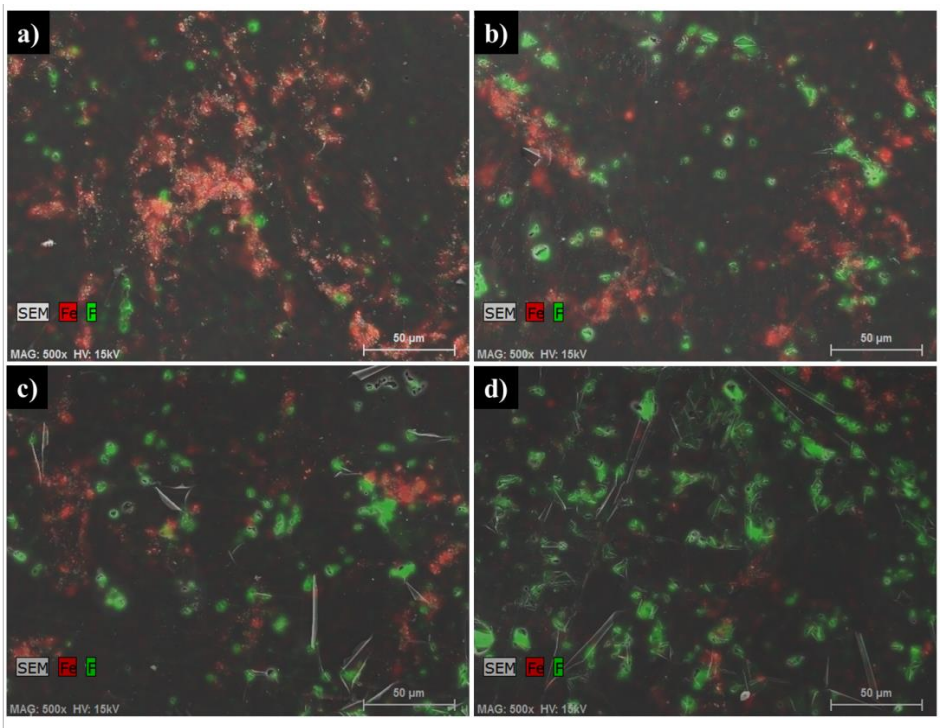

Figure 4. SEM-EDX images of FH-POSS-HPLs containing different loads (w/w) of particles in the resin formulation: a) 0.25%, b) 0.5%, c) 0.75% and d) 1.0%).

Contact angle (CA) measurements were used to calculate the dispersive and polar components of the surface free energy (SFE) of HPLs containing FH-POSS particles (FH-POSS-HPLs), prepared with and without overlay – Figure 5. In both cases, CA increases with the presence of FH-POSS particles in HPLs formulations even when using low particle loads (e.g. 0.25% w/w MF resin formulation), hence indicating higher hydrophobicity of FH-POSS-HPLs in comparison with the conventional HPL (without FH-POSS). No significant changes in CAs were detected while increasing the amount of FH-POSS particles in resin from 025 to 1.0%. This result can be explained by migration phenomena occurring after resin drying and subsequent curing processes. In fact, the low surface energy FH-POSS particles [12] might migrate from the bulk to the surface of HPLs and consequently the SFE of the ensuing HPLs was decreased.

Considering that the HPLs manufactured in the present work are of high gloss products with smooth surfaces it seems that FH-POSS particles do not interfere with the HPLs surface roughness and, therefore one may conclude that the decrease in SFE of HPLs is predetermined by chemical nature of FH-POSS particles. Furthermore, since the water CA on smooth surfaces turned hydrophobic by chemical transformations cannot be increased beyond 120° [13], FH-POSS loads should have been higher than 1% (w/w resin formulation) in order to accomplish a CA circa 120º. However, high loads of FH-POSS particles confer an undesirable whitish appearance to dark surface caused by decor paper, already visible with a load of 1.0%, interfering with the final aspect of the HPLs produced. Finally, comparing the two sets of results (Figure 5, a and b), it is clear that HPLs with and without overlay display similar values of CA and SFE.

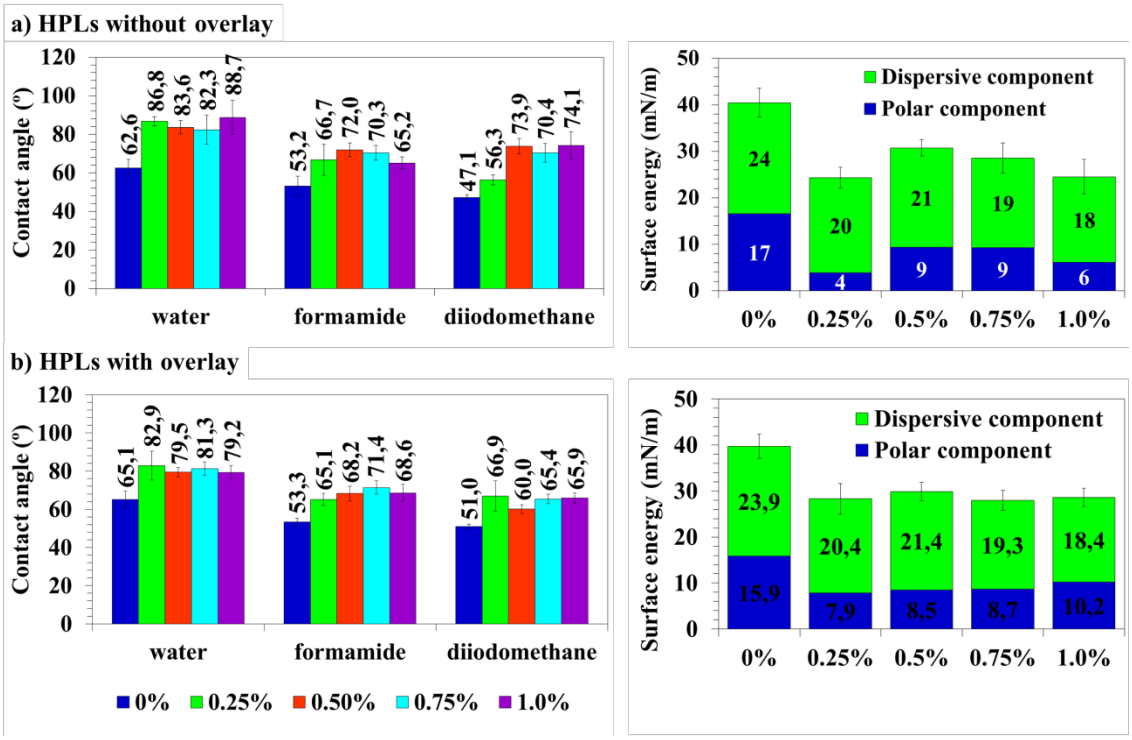

Figure 5. Measured CA (and respective error bars) and polar and dispersive components of SFE (including the total SFE error bars), for FH-POSS-HPLs containing different loads (wt %) of particles and prepared (a) without overlay and (b) with overlay.

Recalling that the overlay is a finishing protective layer, CA measurements on HPLs without overlay were taken systematically over a three-month period, to examine the evolution of HPLs surface properties. The results (Figure 6) reveal that HPLs become more hydrophobic over time especially the FH-POSS-HPLs containing higher loads of particles (water CA around 100º were

observed for HPLs with 0.75% and 1.0% w/w MF resin). This significant enhancement in hydrophobicity is most likely due to the following two main reasons: (1) MF resin residual curing occurs over time after HPL production has ended (in fact, during the hot pressing process resins are seldomly fully cured leading to dimensional variations, i.e. shrinking [14]); and, (2) additional migration of FH-POSS particles continue to occur during the MF resin curing process enhancing the reduction of SFE.

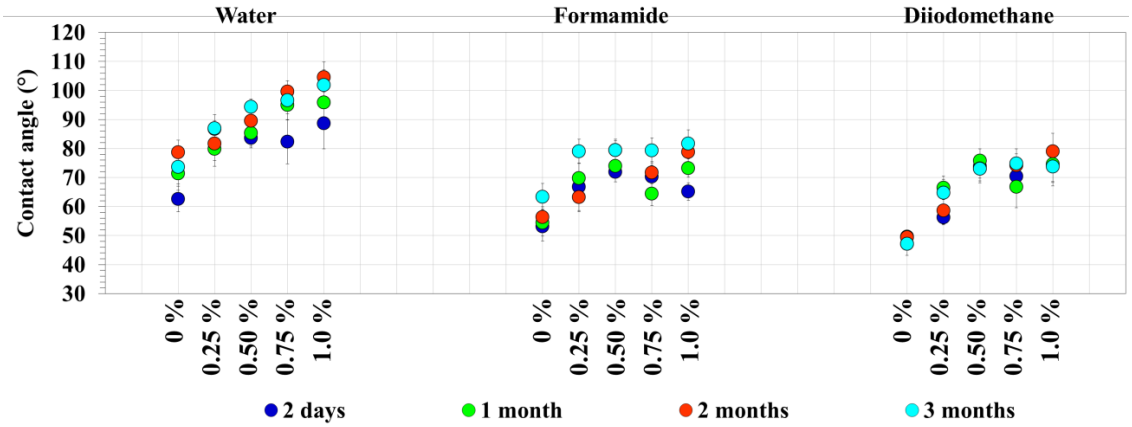

Figure 6. Evolution of CA on FH-POSS-HPLs containing different loads (wt %) of particles and prepared without overlay, over a 3-month period.

Given that a printed decorative paper was used for the production of FH-POSS-HPLs with overlay, these HPLs were further tested for abrasion/wear resistance (AR). This test measures the number of abrasion cycles the HPLs surface resists until wear-through of the decorative layer. The results presented in Figure 7 reveal that AR increases in the presence of FH-POSS, being directly proportional to the particle load. This confirms the overall contribution of the robust Si-O core of FH-POSS particles to the surface properties of HPLs.

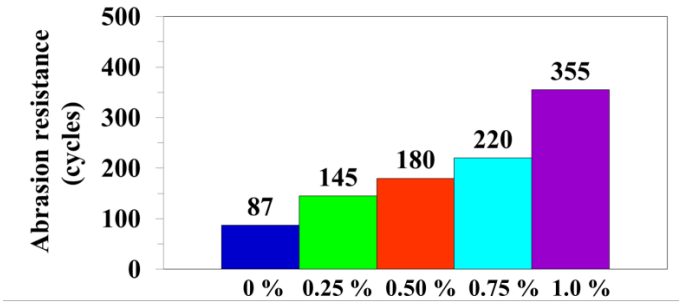

Figure 7. Abrasion resistance for FH-POSS-HPLs containing different loads (wt %) of particles and prepared with overlay.

4. Conclusions

FH-POSS particles were successfully synthesized in a reproducible manner with high yields (ca. 65%). The irregular shaped/sized small particles (fine powder) were characterized by SEM-EDS, DSC and XRD. These particles were satisfactorily dispersed into the MF formulation to produce HPLs containing F-POSS particles, namely FH-POSS-HPLs that present lower surface free energy comparing to standard HPLs (due to the fluorinated groups) and an increase of the abrasion resistance (due to the robust Si-O cages). Therefore, multifunctional HPL prototypes can be prepared to combine

enhanced hydrophobicity and abrasion resistance (achieved by using the FH-POSS particles). The measurement of contact angles over time revealed to be essential information to complete the characterization of the HPLs surface properties in order to evaluate and understand possible changes that these materials undergo, for instance, during storage.

Acknowledgments
This work was developed in CICECO – Aveiro Institute of Materials and is funded by ERDF Funds through Operational Competitiveness Programme – COMPETE in the frame of the project 2GLAM – FCOMP-01-0202-FEDER-23006. We acknowledge the collaboration of Margarida Nogueira during the production of HPLs at SIR.

References

[1] Badila M, Kohlmayr M, Zikulnig-Rusch E M, Dolezel-Horwath E and Kandelbaue A 2014 Improving the cleanability of melamine-formaldehyde-based decorative laminates *J. Appl. Polym. Sci*. **131** 40964
[2] Celia E, Darmanin T, Givenchy E T, Amigoni S and Guittard F 2013 Recent advances in designing superhydrophobic surfaces *J. Colloid Interface Sci*. **402** 1–18
[3] Ganesh V A, Raut H K, Nair A S and Ramakrishna S 2011 A review on self-cleaning coatings *J. Mater. Chem*. **21** 16304–22
[4] Hare E F, Shafrin E G and Zisman W 1954 Properties of films of adsorbed fluorinated acids *J. Phys. Chem*. **58** 236–9
[5] Tuteja A, Choi W, Ma M, Mabry J M, Mazzella S A, Rutledge G C, McKinley G H and Cohen R E 2007 Designing Superoleophobic Surfaces *Science* **318** 1618–22
[6] Cordes D B, Lickiss P D and Rataboul F 2010 Recent developments in the chemistry of cubic polyhedraloligosilsesquioxanes *Chem. Rev*. **110** 2081–173
[7] Ramirez S and Mabry J 2014 *Handbook of Fluoropolymer Science and Technology* ed D W Smith Jr., S T Iacono and S S Iyer (New Jersey: John Wiley & Sons Inc) chapter 23 pp. 545–63
[8] Mabry J M, Vij A, Iacono S T and Viers B D 2008 Fluorinated Polyhedral Oligomeric Silsesquioxanes (F-POSS) *Angew. Chem. Int. Ed*. **47** 4137–40
[9] Choi W, Tuteja A, Chhatre S, Mabry J M, Cohen R E and McKinley G H 2009 Fabrics with tunable oleophobicity *Adv. Mater*. **21** 2190–5
[10] Tuteja A, Choi W, Mabry J M, McKinley G H and Cohen R E 2008 Robust omniphobic surfaces *Proc. Natl. Acad. Sci. U.S.A*. **105** 18200–5
[11] Xu J, Wang X, Ye Q, Song J, Cho C M and He C 2015 Fluorinated polyhedral oligomeric Silsesquioxanes *RSC Adv*. **5** 4547–53
[12] Suk D E, Chowdhury G, Matsuura T, Narbaitz R M, Santerre P, Pleizier G and Deslandes Y 2002 Study on the kinetics of surface migration of surface modifying macromolecules in membrane preparation *Macromolecules* **35** 3017–21
[13] Mahadevan L 2001 Non-stick water *Nature* **411** 895–6
[14] Kandelbauer A, Wuzella G, Mahendran A, Taudes I and Widsten P 2009 Model-free kinetic analysis of melamine–formaldehyde resin cure *Chem. Eng. J*. **152** 556–65

Selective preconcentration within a nanoslit: one route for monitoring the biomolecule focusing front line.

F-D. Delapierre,[1*] A. Lafon,[1] A. Pallandre,[1] A-M Haghiri-Gosnet[1]
[1]Laboratoire de Photonique et de Nanostructures, LPN/UPR20 CNRS, route de Nozay, 91460 Marcoussis, France

Abstract: Due to the electrical double layer, a nanometric restriction in a glass microchannel acts as a selective filter for ions under specific electric field and ionic strength. The unbalanced transport between anionic and cationic species in the microsystem leads to a polarization of the ionic concentrations (Zangle *et al*., 2009). This polarization effect provokes variations of the local ionic flow which can be canceled at some specific locations where ions are collected. This phenomenon can be used to preconcentrate biomolecules before a separation step to improve the limit of detection. Numerical simulations (Plecis *et al*., 2008) have shown that the localization, the intensity and the stability of the preconcentration vary depending on several parameters such as the electrophoretic mobilities, the channel surface charge, the bulk composition, the ionic force, the voltage or the height of the nanochannel etc. Four different preconcentration regimes, stable or unstable, can thus be defined depending on the position of the preconcentration front line. Our experiments have demonstrated the existence of these regimes and our ability to travel in the electro-preconcentration diagram by varying the ionic force, the pressure or the voltage. Tuning these parameters, preconcentration rates of several hundreds of times have been reached. Moreover, by adding a hydrodynamic pressure flow (Louër *et al*., 2013), we find a way to stabilize unstable preconcentration regimes or to adjust the localization of the preconcentration front line.

Introduction: In a simple microchannel (fig. 1. Left) filled with an electrolyte with negatively charged walls (glass), cations concentrate at the interface between the glass and the solution. Under the influence of an electric field, a flow is driven by the motion of cations that are attracted by the electrode of opposite sign and carried along the whole solution: this flow is called Electro-Osmotic Flow (J_{EOF}). It coexists with the Electrophoretic Flow (J_{EP}) that depends on the charge and size of the analyte (i.e. in our case, fluorescein).

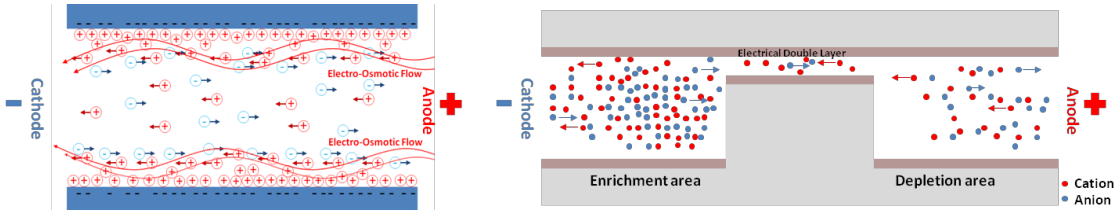

Figure 1: Left: In a glass microchannel, walls are usually negatively charged. An excess of cations concentrate close to the walls. The nearest ones from the walls cannot move at all, but the further ones migrate to the cathode and thus carry the whole liquid in the same direction. Right: view of the selective ionic transport in a MNM structure. The nanoslit acts as a selective ionic filter, blocking the anions because of the electrostatic repulsions from the wall of the nanoslit.

To induce electropreconcentration, the microchannel must include a restriction of nanometric scale, resulting in a straight micro/nano/micro (NMN) structure as described in fig.1 (right). External electric field induces a selective transport of ionic species through the nanochannel: the negatively charged surfaces of the nanoslit stand in the way of the negative charges. It results in a dissymmetry of the ionic concentration inside the MNM structure. This polarization of concentration induces local variation of the electric field. Thus the apparent flow has not the same velocity everywhere. For negative species, the electro-osmotic and electrophoretic velocities are opposed and thus can cancel each other out. The molecules can be stopped and preconcentrated in the MNM device at a specific location named focusing frontline. The depletion and enrichment volumes in the focusing regions can be static or propagate in the channel. A.Plecis *et al*. have developed a 1D computational simulation based on the competition between electro-osmotic and non-linear electrophoretic flow to predict the flow and concentration profile of the analyte in the MNM structure (fig. 2.). The total apparent flow profile (equal to the vectorial summation of J_{EOF} and J_{EP}) shifts towards low values when the electroosmotic flow decreases: thus, it can be cancelled at different points. The resulting focusing regimes are called **Anodic Stacking** (AS), **Anodic Focusing** (AF), **Cathodic Focusing** (CF) and **Cathodic Stacking** (CS)(see fig. 2). We have studied experimentally these theoretical predictions to show how the preconcentration phenomenon can be controlled.

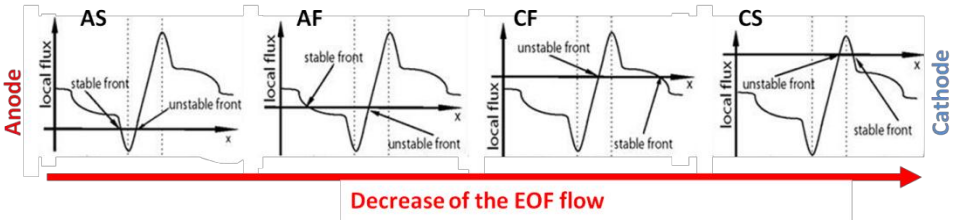

Figure 2: Comsol simulation (Plecis et al.) of the flux profile of fluorescein anion in a KCl solution. The profile moves up/down with the increase/ decrease of the electroosmotic flow.

Material and methods: Chips have been made in borosilicate glass. First, 300 nm of amorphous silicon (α-Si) is deposited by plasma-enhanced chemical vapor deposition. Then AZ-5214 reversible photoresist is spin-coated on the glass substrate and the microchannels are defined by UV lithography. In the regions that are not protected by the resin, the α-Si is etched by reactive-ion etching (SF_6).

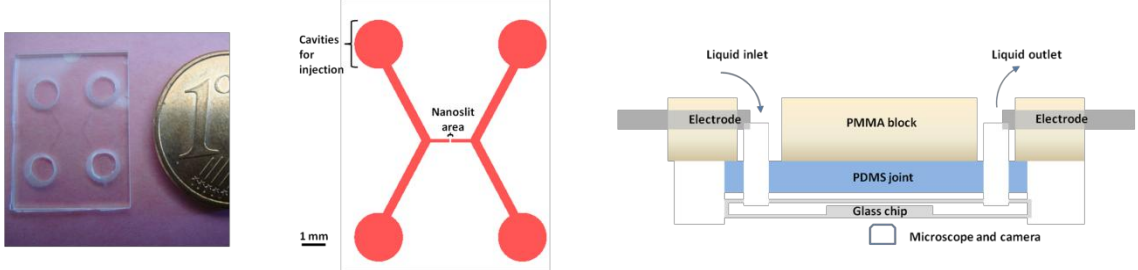

Figure 3: Left: Top view of the chip. Middle: Top view of the chip structure. Right: Side view of the system used to perform electropreconcentration experiments.

The microchannels are then etched, where α-Si does not protect the glass, using Ammonium fluoride – hydrofluoric acid etching mixture (Sigma-Aldrich®). The nanochannel is made using the same method after a second spin-coating and a lithography. The inlets/outlets, where

aqueous solutions are injected, are drilled by sandblasting. The glass chip is finally closed by thermal bonding with another glass wafer at 550°C under pressure (3-5 bars) during 2h. The chip is mounted on the experimental holder under, first, a PDMS layer containing fluidic injection holes and, secondly a PMMA block with reservoirs containing electrodes. Ionic solutions are injected using a pressure controller OB1 (Elvesys®). Voltage is applied using a Keithley 236 Source measure unit. Fluorescence images are taken using an inverted microscope and a Hamamatsu CCD camera. During experiments, the preconcentration of 10µM sodium fluorescein solutions have been studied in KCl solutions.

Results and discussion: Tuning pressure and voltage allows to preconcentrate fluorescein several hundreds of times (fig. 4). Since for one chip geometry, biomolecule, background solution and voltage, only one focusing point among the four AS, AF, CF and CS regimes can be reached, we have proposed an original way to choose the location of the preconcentration frontline: adding an additional hydrodynamic pressure to balance the competition between J_{EOF} and J_{EP} (Louër *et al*., 2013). Here we demonstrate that the two CS and CF regimes can be reached by adding a pressure applied from cathode to anode (Fig 5). In addition, since CF regime was shown to be more often propagating through analytical predictions (Zangle *et al*., 2009), we demonstrate that the application of an additional pressure allows to stabilize the CF regime in a transition region of the pressure - voltage diagram (fig. 6).

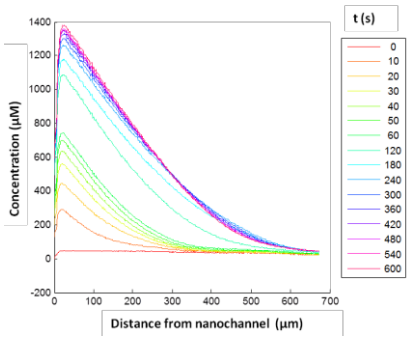

Figure 4: CS Fluorescein preconcentration. Here, a preconcentration rate of 140 has been reached. 15 V. 0.2 bar applied in the opposite direction of J_{EOF}. Nanochannel height and length: h=159 nm, l=100µm. Microchannel height: H=1.4µm.

By varying pressure and voltage, the existence of different predicted preconcentration regimes (propagating CF, stable CF and CS) has been confirmed for fluorescein (fig. 5.). At a given pressure, the behavior of the preconcentration pattern changes from a propagating CF to a stable CS when voltage decreases. By adding a hydrodynamic pressure, we can also reduce or increase the total bulk liquid flow without changing J_{EP}. At a given voltage, if the pressure flow is opposite to J_{EOF}, the local ionic flow curve performs a global translation to lower values of the apparent flow when pressure is increased: this corresponds to a transition from a CF regime towards a CS regime.

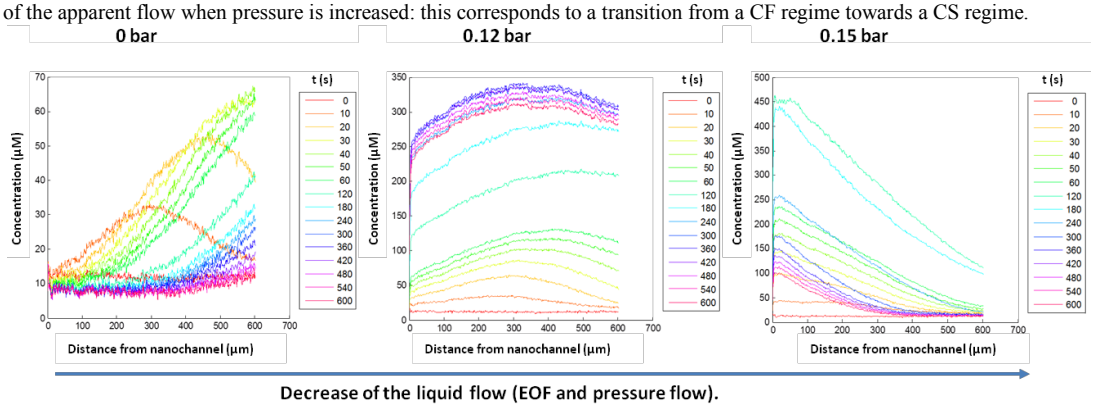

Figure 5: Cathodic preconcentration profiles of fluorescein in a MNM structure. Voltage: V=12.5V. Nanochannel height and length: h=159 nm, l=100µm. Microchannel height: H=1.4µm. The pressure flow is applied in the direction opposite to J_{EOF}, thus the bulk liquid flow is reduced when pressure increases.

At the boundary of those two regimes, a transition region corresponding to a stable CF regime has been observed. By adding a hydrodynamic pressure, it is, thus, possible to stabilize an unstable regime. This is of great interest since the CF regime has theoretical higher rates than the CS regime (Plecis *et al*., 2008). Schematic regimes diagrams for a 159 nm nanochannel glass chip are presented on fig. 6 for two different KCl solutions. By tuning the voltage or the applied additional pressure, the preconcentration regime can be precisely adjusted.

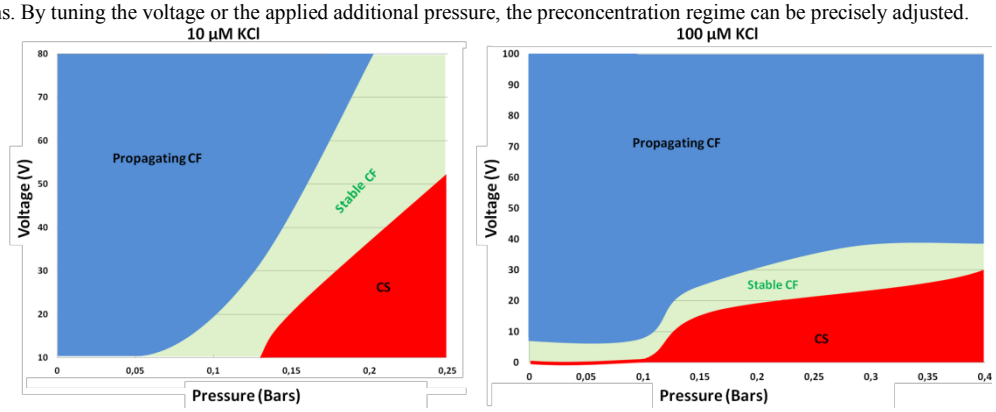

Figure 6: Pressure/Voltage diagram of 10µM fluorescein solution behavior. Fluorescein was diluted in KCl solution.

Conclusion: Different regimes of preconcentration predicted by previous computational simulations have been experimentally found. By adding an additional controllable pressure, the two CS and CF focusing regimes can be easily obtained. Especially, a stable CF focusing regime, useful for further step of analysis can be observed. We present for the first time experimental preconcentration regime diagrams that provide a universal way to perform stable enrichment experiments.

References:

Zangle, T. A., Mani, A., Santiago, J. G. (**2009**), *On the Propagation of Concentration Polarization from Microchannel-Nanochannel Interfaces Part II: Numerical and Experimental Study*, **Langmuir**, *25*, 3909-3916.

Plecis, A., Nanteuil, C., Haghiri-Gosnet, A. M., Chen, Y. (**2008**), *Electropreconcentration with Charge-Selective Nanochannels*, **Analytical Chemistry**, *80*, 9542-9550.

Louër, A-C., Plecis, A., Pallandre, A., Galas, J-C., Estevez-Torres, A., Haghiri-Gosnet, A-M. (**2013**), *Pressure-assisted selective preconcentration in a straight nanochannel*, **Analytical Chemistry**, *85, 7948-7956*.

Green Synthesis of Gold Nanoparticles by Using *Peltophorum pterocarpum* Flower Extracts

M. Balamurugan[1], S. Kaushik[2], S. Saravanan[1,*]

[1]*Centre for Photonics and Nanotechnology, Sona College of Technology, Salem - 636005, Tamilnadu, India*

[2] *The Indian Public School, Senapathipalayam, Erode – 638112, Tamilnadu, India*

Abstract

The gold nanoparticles have been prepared using *Peltophorum pterocarpum* flower extracts. The prepared gold nanoparticles were characterized by Ultra Violet-Visible spectroscopy and High Resolution Transmission Electron Microscope. The Ultra Violet-Visible spectroscopy shows the absorbance maximum around 560nm. HR-TEM shows that the mean sizes of the prepared gold nanoparticles were ranging from 10-30 nm.

Introduction

Noble metal nanoparticles such as gold, silver, and platinum are widely used in products that directly contact with the human body, such as shampoos, soaps, detergent, shoes, cosmetic products, and toothpaste, besides medical and pharmaceutical applications [1]. Among the noble metal nanoparticles, gold has enormous potential applications in various fields [2]. Already silver nanoparticles have been synthesized by PP lower extracts [3]. Currently, we are in the vital need to develop safe, reliable, clean and eco-friendly methods for the preparation of nanoparticles. In this present study the gold nanoparticles have been prepared using *Peltophorum pterocarpum* (PP) flower.

Experimental

The flower extract was prepared by heating 1g of PP flowers in 100 mL of DI water at 80º C for 30 min. 20 mL of PP flower extract was slowly dripped into 1 mM aqueous $HAuCl_4 \cdot xH_2O$ with constant stirring at RT as well as elevated temperatures (50, 60 and 70º C).

Results and Discussions

Figure 1 shows the digital photograph of aq. $HAuCl_4 \cdot xH_2O$ a) before adding the 20ml of flower extract and (b-d) after adding the flower extract a visible color appearance. UV-vis spectral analysis has been done in the range of 400 to 800nm with the periodic time intervals of 5, 30, 60, 90, 120 and 1200 min. The formation of Au NPs were influenced by the experimental parameters such as initial concentration of Gold (III) chloride hydrate, dosage of plant extract and temperatures.

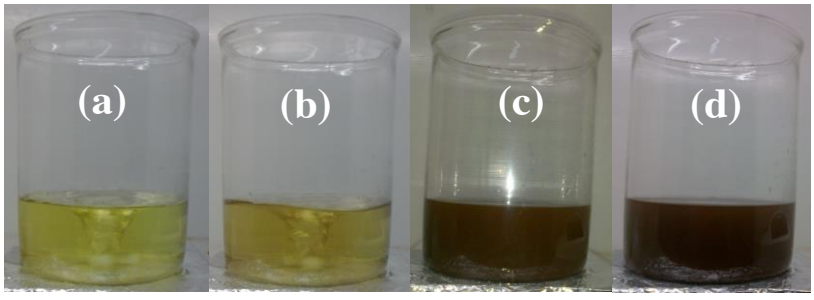

Figure 1

Figure 2 shows the UV-vis spectrum of Au NPs and illustrate the reduction of gold ions and the formation of nanoparticles. The spectrum shows the absorption maximum (λ_{max}) in the range of 530 to 550 nm and confirmed that the presence of Au NPs. It shows that the rate of the reaction/formation of Au NPs is higher in elevated experimental temperatures compare to room temperature. As shown in Figure 2 the UV-vis λ_{max} appeared around 557, 542, 532 and 532 nm for Au NPs prepared at room temperature, 50, 60 and 70° C respectively. It is clear that, when the experimental temperature is increased the UV-vis λ_{max} blue shifted. The blue shifting represents the size reduction of particles. Also, the full width at half maximum (FWHM) of UV-vis peak decreased. The lower FWHM in the absorbance peak depends on the size and uniformity of the synthesized nanoparticles.

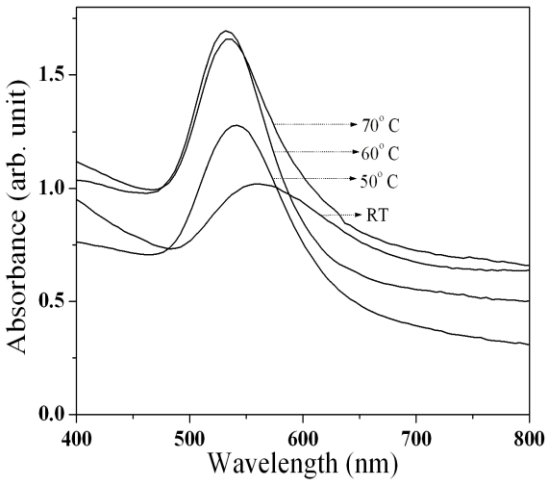

Figure 2

The size and morphology of nanoparticles were examined by HR-TEM. Figure 3 shows the TEM image of Au NPs prepared at room temperature. The image shows the nanostructure and morphology of Au NPs with good dispersion and the size of the NPs varied from 10-30 nm.

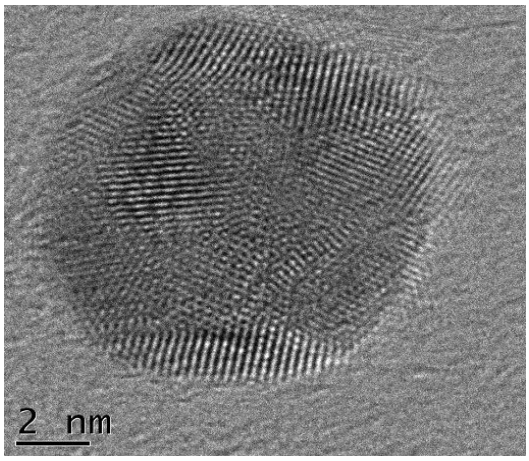

Figure 3

Conclusions

The gold nanoparticles were successfully synthesized by using PP flower extract. The nanoparticles were prepared at ambient as well as elevated temperatures. The prepared particle sizes varied from 10 to 30 nm. The results show that the temperature can significantly affect the formation of the nanoparticles and the higher temperature support the small size particle formation.

References

[1]. Song JY, Jang HK, Kim BS, Biological synthesis of gold nanoparticles using *Magnolia kobus* and *Diopyros kaki* leaf extracts, *Process Biochemistry* 2009; **44**: 1133–38.

[2]. Daniel MC, Astruc D, Gold nanoparticles: Assembly, supramolecular chemistry, quantum-size related properties and applications towards biology, catalysis and nanotechnology, *Chem*. *Rev*. 2004; **104**: 293−340.

[3]. Balamurugan M, Kandasamy N, Saravanan S, Ohtani N, Synthesis of uniform and high-density silver nanoparticles by using Peltophorum pterocarpum plant extract, Japanese Journal of Applied Physics 2014; 53: 05FB19.

Efficient Encapsulation of Carboplatin Anticancer Molecule into Boron Nitride Nanotube : a Promising Drug Nanovector

M. El Khalifi,[1] E. Duverger [2], T. Gharbi[1], H. Boulhadour[1] and F. Picaud[1]
[1]Laboratoire de Nanomédecine, Imagerie et Thérapeutique, EA 4662, Université Franche-Comté (UFR Sciences et Techniques), Centre Hospitalier Universitaire de Besançon, 16 route de Gray, 25030 Besançon, France
[2] Institut FEMTO-ST, 32 Avenue de l'Observatoire, 25044 Besançon, France

Abstract: Chemotherapy is frequently used to treat cancer patients. However, serious adverse effects are observed when drugs are systemically administered since they exhibit poor specificity in reaching tumor tissues(Yang, Hong et al. 2011). More, the efficacy of many potent and promising drug molecules is limited by their low water solubility, by the increased drug resistance and highly cytotoxic side effects (Samori, Ali-Boucetta et al. 2010). To circumvent such important drawbacks, an efficient way of systemic transportation needs to be developed. Many of the pharmacological properties of conventional drugs can be improved through the use of nanocarriers(TM Allen, Cullis et al. 2004). Anticancer drug transport is now become a central research since it would allow to localize the drug release near the tumor cell, avoiding secondary medical effect. We report a theoretical study based on molecular dynamics simulations to demonstrate that encapsulation of anticancer carboplatin molecule (CPT) is favored in boron nitride nanotube (BNNT). The ability of BNNT to vectorize CPT is improved since several drug molecules can be adsorbed inside the nanotube.
The insertion of CPT inside an armchair single walled (10,10) BNNT whose diameter is equal to 13.94 Å and length is 21.32 Å was studied step by step. To take advantage of the high surface area−volume ratio offered by the inner volume of the BNNT, we filled progressively the nanotube by CPT until completion. This is obtained when the total length of the vector is comparable to the sum of the encapsulated molecules size . We have estimated the diameter of the CPT to be 0.7 nm, and the length of the BNNT was about 2.1 nm. The capsule was thus filled by at least three drug molecules, corresponding to a encapsulation capacity of 1500 molecules per micrometer. The storage capacity of BNNT is thus very large due to high confinement effects and hydrophobic interactions, favoring its filling with drug molecules opening the way to a very efficient drug transportation (Figure 1).

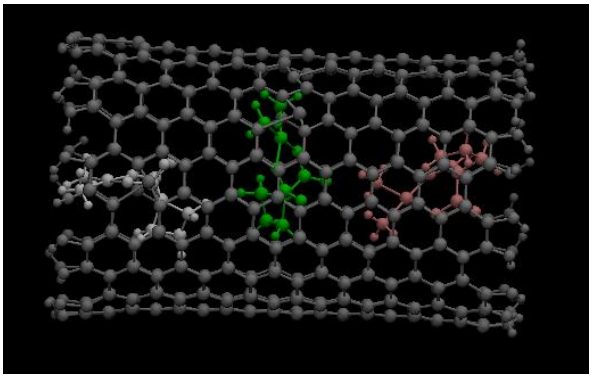

Figure 1: Encapsulation of thee CPT molecules in side BNNT

More precisely, CPT was placed in front of the BNNT entrance (at about 6 Å) and the total system was solvated in order to avoid periodic boundary interactions between each molecule. Then, the molecular dynamic simulations were launched without any constraint on the BNNT or the drug molecule. Figure 2 describes the energy path of the drug during the simulation, described as its interaction with the BNNT during time. As clearly showed in this figure, the drug molecule is rapidly catched by the nanopore (the beginning of the insertion is observed at 1 ns) and stays inside (from t = 2.5 ns) during all the remaining time of the simulations (at least 10 ns). This insertion is marked by a strong decrease of the interaction energy between the CPT and the BNNT nanopore of about 40 kcal/mol (around -1.7 eV, compared to -1.15 eV using DFT (El khalifi, Duverger et al., in press), a result which did not take into account the dispersion repulsion terms and the presence of solvent). Our result demonstrates a stable encapsulation of the CPT in the BNNT since it diffuses on the inner surface without escaping until the end of the simulations. Then a second molecule was placed behind the entrance of the BNNT and penetrated it rather rapidly (0.004 ns) because of the strong interaction with its encapsulated neighbor one. The third one also inserted and arranged with the

others forming very stable cluster inside the nanotube.

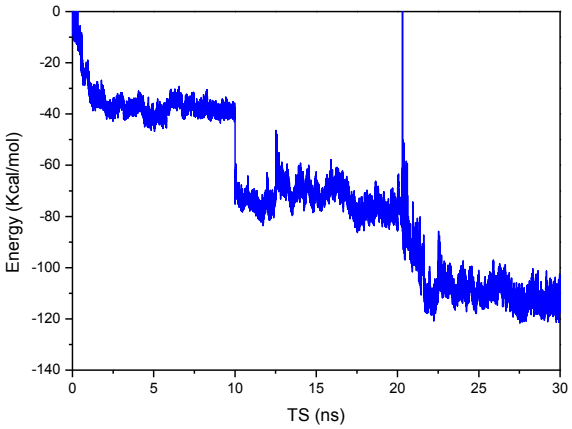

Figure 2: Interaction energy of CPT with BNNT molecular dynamic simulation in ns.

The last step of our study was the ability of BNNT to release the molecule near its target. However, before studying it, we first conducted the mechanism of stability and insertion of BNNT nanotube in lipid bilayers using MD simulations to analyze the affinity of BNNT with lipid cell. For this the nanotube was initially placed close to a lipid membrane made of POPC lipids bilayers with water reservoirs added to its both sides. The empty BNNT was positioned at 20 Å from the first atom of the POPC molecules, and the periodic box was chosen in order to leave more than 64 Å between the central simulation box and the periodically repeated one. The entire system is then minimized and equilibrated before running production of standard MD simulations. The diffusion path of the BNNT was very amazing since it rotated fastly to become approximately parallel to the lipid bilayers and, then inserted very rapidly in the membrane in around 200 ns of simulation. Then the nanotube remained confined in the lipid bilayers for the rest of the simulation. The filled BNNT-CPT system should follow the same behavior than the empty one and we could hope that the CPT molecules can extracted from the BNNT as showed in figure 3, due to the hydrophobic interaction between the nanotube and the water molecules. Indeed, CPT could be naturally and rapidly released as far as they approach the cell.

Keywords: boron nitride nanotube, therapeutic agents, cell membrane, all-atom molecular dynamic.

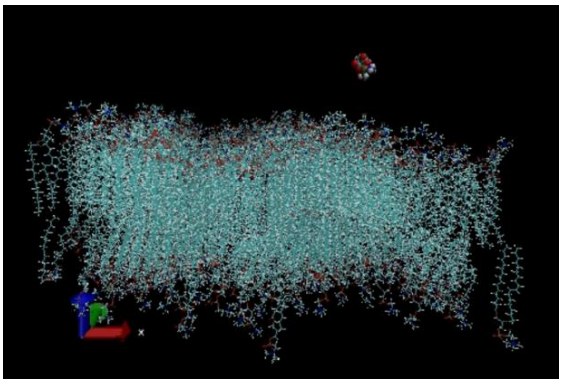

Figure 3 : Drug release

References:

Yang, X., H. Hong, et al. (2011). "cRGD-functionalized, DOX-conjugated, and (64)Cu-labeled superparamagnetic iron oxide nanoparticles for targeted anticancer drug delivery and PET/MR imaging." Biomaterials **32**(17): 4151-4160.

Samori, C., H. Ali-Boucetta, et al. (2010). "Enhanced anticancer activity of multi-walled carbon nanotube-methotrexate conjugates using cleavable linkers." Chemical Communications **46**(9): 1494-1496.

TM, Allen. and Cullis. PR (2004). "- Drug delivery systems: entering the mainstream." *Science* **303**(5665): 1818-22.

El khalifi, M., E. Duverger, et al. "Theoretical study of the interaction between carbon nanotubes and carboplatin anticancer molecules." Analytical Methods. *in press*

Performance study of Phase Change Memory in Different Crossbar Architectures

Nemat H. El-Hassan, T. Nandha Kumar and Haider A.F.Almurib

Department of Electrical and Electronic Engineering
The University of Nottingham
Selangor, Malaysia

E-mail: kecx2nha@nottingham.edu.my

Abstract. This work presents comparison between two Phase Change Memory (PCM) based memory architectures, namely standard crossbar architecture and a new architecture that was adapted for PCM operation. The performance of the two architectures was compared in terms of leakage energy, programming and reading delay, and reliability. It was found that the new crossbar architecture offers more than six orders of magnitude improvement in leakage energy and offers up to N times improvement in programming delay where N is a metric proportional to the size of the architecture, and more than an order of magnitude improvement in reading delay.

1. Introduction

Resistive nonvolatile memories (NVM) such as memristors, Magnetic Torque Junctions (MTJs) and Phase Change Memory (PCM) among others are considered as potential candidates for storage class memory and replacing SRAM [1], since NVM capture the desired qualities to fulfill the growing demands of consumer electronics market. PCM in particular poses most of desirable properties; including high density and scalability, high operating speed, endurance and full CMOS compatibility [2]. Non-volatility of PCMs comes from the fact that the material exhibits a thermally induced phase change between at least two resistive states, and that the phase does not spontaneously reverse; therefore the material resistance is considered a memory element.

When the programming pulse applied across the PCM cell is sufficient to raise its temperature to crystallizing temperature for duration adequate for crystallization to take place, the material rearranges into long atomically ordered low resistance state. On the other hand, if the applied pulse was sufficient to raise the temperature of the material above melting temperature, and steep the material will quench into highly disordered architecture, which exhibits high resistance at least two orders of magnitude larger than that of crystalline state.

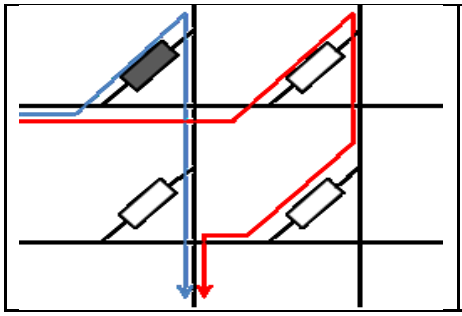

Figure 1. Leakage currents in standard crossbar architecture, the blue line is the current passing through the targeted cell (shaded), the red line is a possible leakage current path.

By placing PCM cells in standard crossbar architecture very high density memory system can be achieved, where PCM storage elements are placed in intersection points of a wires grid (figure 1). Although the standard crossbar architecture shown in figure 1 offers a high density storage medium; it undergoes multiple performance issues ranging from stray capacitances caused by memory peripheral circuitry [3], to thermal crosstalk [4], connecting wire resistances [5], and leakage currents [6]. This work focuses on the leakage currents and how they add up to the dissipated energy in the memory system and affect the programmed resistance. The paper compares leakage effects in two different architectures, namely the standard nano-wire crossbar architecture and a novel architecture suggested in [7] to mitigate sneak path leakage current effects. The studied leakage characteristics include delay, power and energy dissipation and programming errors. Simulation results showed that the novel architecture demonstrates superior behavior in comparison to the standard architecture, in terms of delay energy and reliability.

The layout of the rest of this paper is as follows, section 2 describes the compared crossbar architectures, while section 3 shows and discusses the simulation results, and the paper is concluded in section 4.

2. Crossbar architectures description

In this work two architectures were studied, a standard crossbar architecture where the memory elements are placed at each intersection point of Word lines (rows) and Bit lines (columns) as shown in figure 2. The second tested architecture of figure 3 is a new architecture presented in [7]; it was designed for the purpose of mitigating the leakage effects in the standard crossbar. This architecture was originally intended for memristor based memory architecture. In this work the key feature "i.e. individual cells Word lines" of the architecture is maintained, and the architecture was adapted to entertain a PCM cell as the memory element, where the PCM model from [8] was the used model.

2.1. Standard Architecture

The standard architecture is constructed of an intersecting grid of Word lines and Bit lines; at each intersection point a memory element is placed. To access a cell for either programming or reading, the address lines A0 and A1 provided at the input of the controller will decide which row and column to be activated accordingly. The write enable signal $WE/\overline{RE}$ dictates whether the cell is to be programmed or read. If the cell is to be programmed DATA controller input decides the programming voltage applied, i.e. V_{P0} and V_{P1} program into logic 0 and 1 respectively.

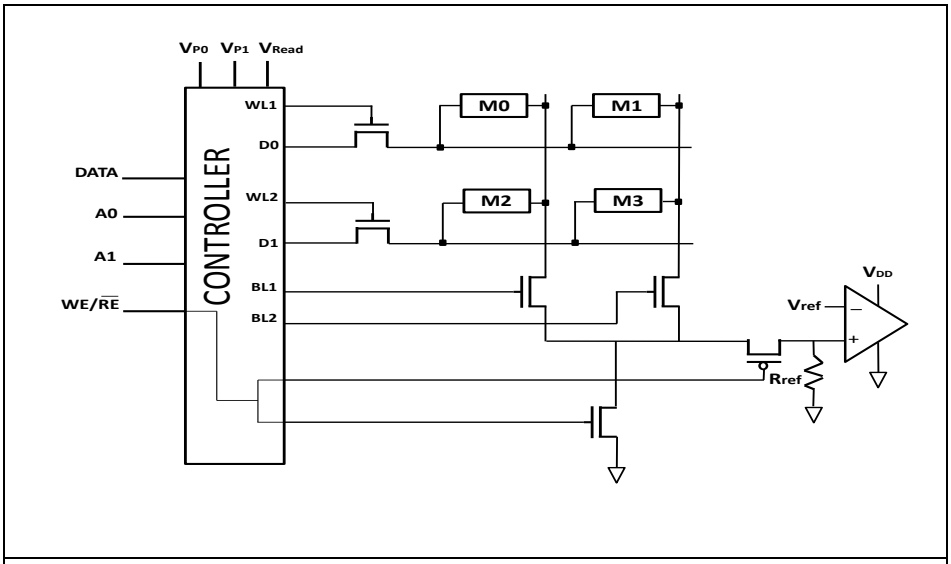

Figure 2. Standard crossbar architecture

On the other hand, to perform reading operation on an accessed cell the reading voltage V_{Read} will be supplied to the selected cell. An external reading circuit consisted of a comparator operational amplifier and a series resistance that forms a voltage divider with the PCM cell is utilized. When the cell is at ON state the voltage at the positive input of the comparator would be higher than the voltage when the PCM cell is at the OFF state. By selecting a proper reference voltage between these two values at the negative comparator output; the output of the comparator will fully swing between GND and V_{DD} (1V) according to the PCM state thus indicating the stored bit value. Table 1 shows the truth table of the controller unit in the standard architecture.

Table 1. Truth table of standard architecture controller unit (x indicate don't care)

Operation	WE/$\overline{RE}$	A0	A1	DATA	D0	D1	WL1	WL2	BL1	BL2
Write	1	0	0	0/1	VP0/VP1	*Floating*	1	0	1	0
	1	0	1	0/1	VP0/VP1	*Floating*	1	0	0	1
	1	1	0	0/1	*Floating*	VP0/VP1	0	1	1	0
	1	1	1	0/1	*Floating*	VP0/VP1	0	1	0	1
Read	0	0	0	x	VRead	*Floating*	1	0	1	0
	0	0	1	x	VRead	*Floating*	1	0	0	1
	0	1	0	x	*Floating*	VRead	0	1	1	0
	0	1	1	x	*Floating*	VRead	0	1	0	1

2.2. New Architecture

The other tested architecture in this work is an advanced novel architecture presented in [7]; the architecture was designed for a Memristor based crossbar and aimed to eliminate leakage. This architecture was adapted to suit a PCM memory element, by adjusting the voltage supplied to program and read the cells, and the read circuitry. The main feature of the novel architecture i.e. the separate Word line for each memory element was retained as well as the ability to program the cells sharing the same Bit line simultaneously.

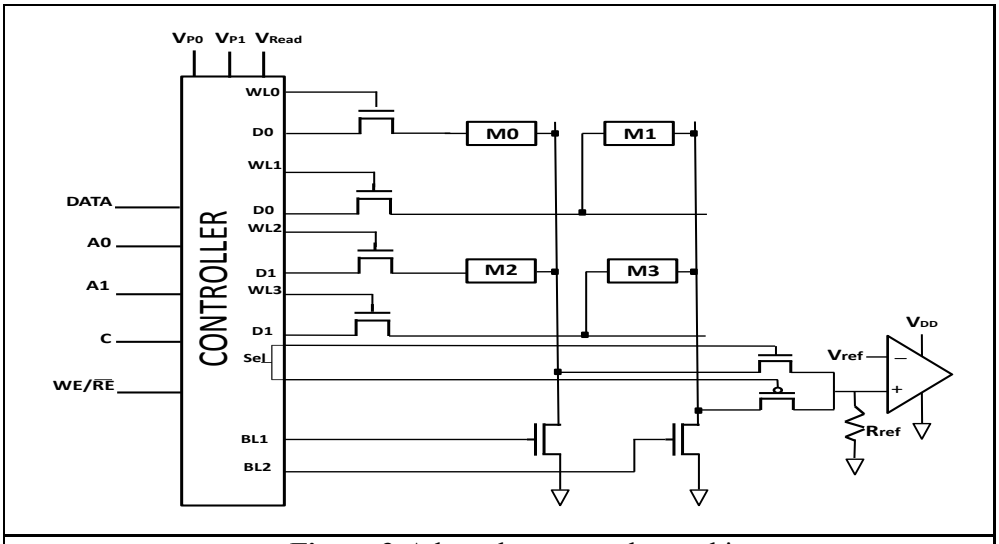

Figure 3. Adapted new crossbar architecture

To program cells; the write enable signal $WE/\overline{RE}$ is set to high, and regardless of the value at the address lines, the cells at the selected Bit line according to C will be programmed. While in read operation the cells are addressed in a similar manner as in the standard architecture using A0 and A1; the accessed cell is supplied VRead and a similar comparator as the one described in the standard architecture is used. The truth table of the novel architecture is presented in table 2.

Table 2. Truth table of novel architecture controller unit

Operation	WE/-RE	A0	A1	C	DATA	D0	D1	WL0	WL1	WL2	WL3	BL1	BL2	Sel
Write	**1**	**x**	**x**	**0**	**0/1**	V_{P0}/V_{P1}	V_{P0}/V_{P1}	**1**	**0**	**1**	**0**	**1**	**0**	*Floating*
	1	**x**	**x**	**1**	**0/1**	V_{P0}/V_{P1}	V_{P0}/V_{P1}	**0**	**1**	**0**	**1**	**0**	**1**	***Floating***
Read	**0**	**0**	**0**	**x**	**x**	V_{Read}	V_{Read}	**1**	**0**	**0**	**0**	**1**	**0**	**1**
	0	**0**	**1**	**x**	**x**	V_{Read}	V_{Read}	**0**	**1**	**0**	**0**	**0**	**1**	**0**
	0	**1**	**0**	**x**	**x**	V_{Read}	V_{Read}	**0**	**0**	**1**	**0**	**1**	**0**	**1**
	0	**1**	**1**	**x**	**x**	V_{Read}	V_{Read}	**0**	**0**	**0**	**1**	**0**	**1**	**0**

3. Simulation results and discussion

The two crossbar architectures described in section 2 were constructed and simulated using LTSpice IV. The architectures were tested for both reading and writing operations, the operations were tested for both 0 and 1, i.e. the high and low resistance states R_{OFF} and R_{ON} respectively, where the untargeted cells are at R_{ON} when the addressed cell is R_{OFF} and vice versa.

Leaked energy during the programming and reading i.e. the energy dissipated in untargeted cells shows a great variation between the two architectures as expected and shown in figure 4. The novel architecture showed more than six orders of magnitude less leaked energy, this is directly tied to the elimination of leakage paths in this architecture by utilizing separate Word lines for each memory cell. It was also noted as shown in figure 4 that the leakage of reading process in the novel architecture is the least of all, due to the fact that in addition to eliminating leakage paths, V_{Read} is much smaller than V_P.

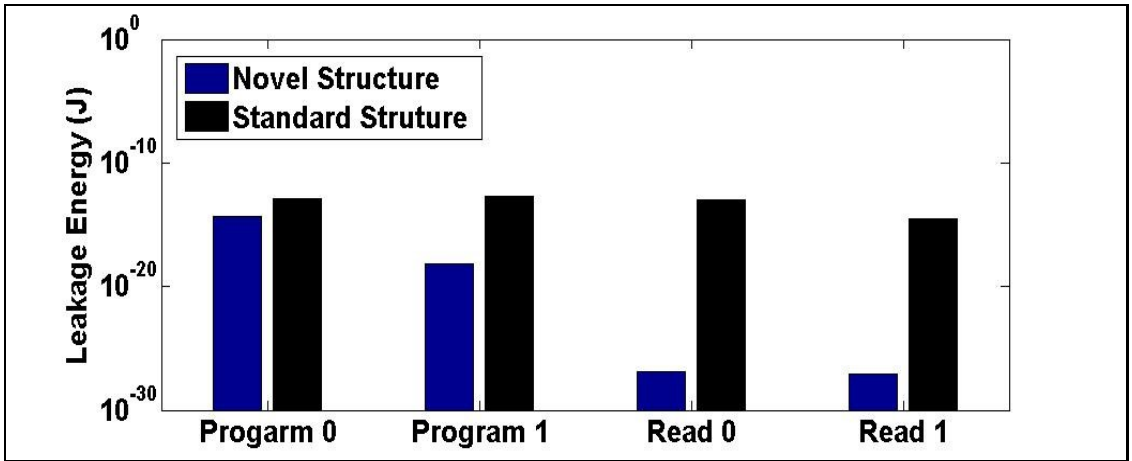

Figure 4. Summary of simulation results of leaked energy during reading and programming.

While for the dissipated energy during programming pulse; it was found that programming energy i.e. the energy dissipated in all memory cells (M0 – M3) is the same in both architectures, as shown in figure 5. This is explained by the fact that the voltage applied to the grid during programming operation is the same regardless of the architecture. While for the reading process the novel architecture showed better performance as expected due to elimination of leakage paths, resulting in most of the applied current to pass through the targeted cell rather than untargeted ones.

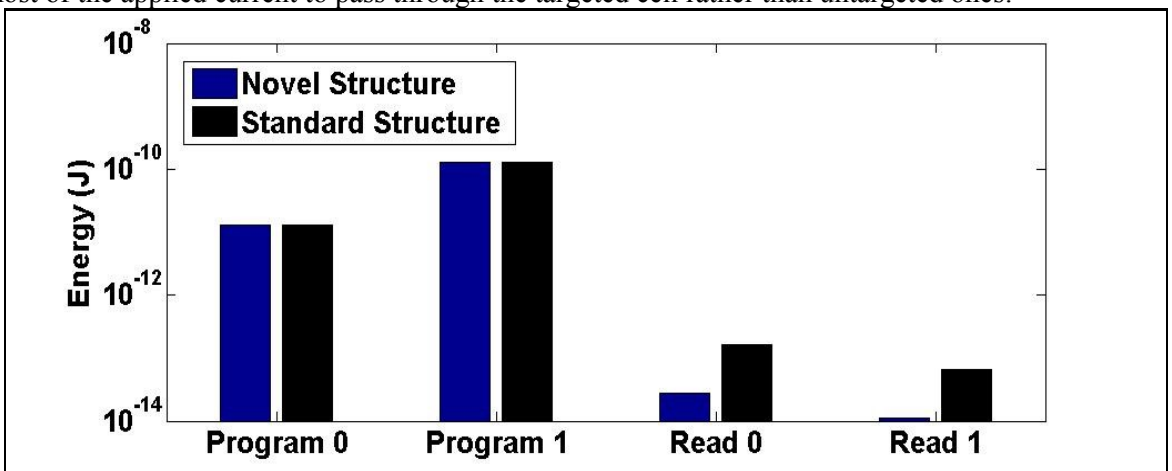

Figure 5. Summary of simulation results of dissipated energy during reading and programming.

Moreover, the programming duration for both architectures was set to a constant value in order to evaluate the effect of underlying architecture on the final resistance state, the built in capability to program all cells sharing a Bit line in the novel architecture thus showed a superior performance in terms of programming delay per cell as shown in table 3, this particular improvement in programming time is an architectural advantage rather than an advance of cell behaviour.

Furthermore, the reading delay was measured as the time for the output to fully swing to 0 or 1 from the moment the address lines and the read signal were propped. It was found that the novel architecture demonstrated almost three times less delay to read a stored 0 and more than an order of magnitude less time to read a stored 1 bit. This is due to larger current supplied to the comparator due to less leakage, resulting in a faster voltage swing.

The last tested metric was the programmed state; it was found that when programming to high resistive state R_{OFF} i.e. storing binary 0; both architectures cells were fully programmed to maximum R_{OFF} of 200KΩ. While when programming to R_{ON} the standard architecture demonstrated higher R_{ON} compared to the novel architecture as shown in table 3, this is a direct effect of leakage, since less

power is fed to the targeted cell, the phase of the material does not fully change resulting in a higher programmed ON resistance. This could jeopardize the reliability of memory operation as well as limit multilevel operation potential.

Table 3. Delay and programmed level simulation results summary (N≈ No. of cells in a Bit line)

Operation	Novel Architecture	Standard Architecture
Programming 0 Delay (s)	10n/N	10n/cell
Programming 1 Delay (s)	200n/N	200n
Reading 0 Delay (s)	1.23E-06	3.31E-06
Reading 1 Delay (s)	9.29E-07	1.41E-06
Programmed ON resistance (Ω)	16.3213E03	30E03
Programmed OFF resistance (Ω)	200E03	200E03

4. Conclusion

In this work a PCM based memory crossbar architecture comparison was carried out. A novel architecture that was originally designed for memristor based architecture was adapted to entertain a PCM storage element instead. The novel architecture showed superior performance compared to the standard architecture, in terms of leakage energy and delay in both programming and reading processes.

The extracted results can be further extended to crossbars with larger sizes, given that for a standard architecture leakage would be directly proportional to the crossbar size, while in the novel architecture the leakage is limited regardless of the architecture's size.

References

[1] H. Li , and Y. Chen, "Emerging nonvolatile memory technologies: Frommaterials, to device, circuit, and architecture," IEEE International Midwest Symposium on Circuits and Systems (MWSCAS), pp.1-4, 2010

[2] A. Pronin, "Phase Change Memory: Fundamentals and Measurement Techniques", *Keithley Instruments Inc*., March 2010.

[3] E. G. Yeo, L. P. Shi, R. Zhao, K. G. Lim, T. C. Chong, and I. Adesida, "Parasitic capacitance effect on programming performance of phase change random access memory devices," Applied Physics Letters 96, 2010

[4] M. Gh. Mohammad, L. Terkawi, M. Albasman, "Phase Change Memory Faults," 19th International Conference on VLSI Design, 2006.

[5] M. Dong and L. Zhong, "Challenges to Crossbar Integration of Nanoscale Two-Terminal Symmetric Memory Devices," IEEE Conference on Nanotechnology, 2008

[6] S. Kannan, J. Rajendran, R. Karri, and O. Sinanoglu, "Sneak-Path Testing of Crossbar-Based Nonvolatile Random Access Memories," IEEE Transactions On Nanotechnology, VOL. 12, NO. 3, pp. 413 – 426, May 2013.

[7] T. Nandha Kumar, Haider A.F Almurib, Fabrizio Lombardi. (2014), A Novel Design of a Memristor-Based Look-Up Table (LUT) for FPGA In: IEEE Asia Pacific Conference on Circuits & Systems, 703-706.

[8] N. H. El-Hassan, T. Nandha Kumar, and H. Abbas F. Almurib. (2014), Improved SPICE Model for Phase Change Memory Cell, 5th IEEE International Conference on Intelligent and Advanced Systems, 1- 6.

Synthesis and Cytocompatibility of Functionalized Multi-Walled Carbon Nanotubes Derivatives

Ahmed A. Haroun
Chemical Industries Research Division, National Research Centre (affiliation ID: 60014618), 33 Bohouth Str., Dokki, Giza, Egypt, *email: haroun68_2000@yahoo.com*

Abstract
Innovative functionalized multi-walled carbon nanotubes (MWCNTs) are emerging tool in the nanobiotechnology applications. However, thier toxic effects on environment and health have become an issue of strong concern. In the present study, we address the impact of functionalized MWCNTs on breast carcinoma (MCF7) cell line. Moreover, the prepared nanomaterials were characterized using different analytical tools; Fourier transform infrared spectroscopy (FTIR), X-ray diffraction patterns (XRD), scanning and transmission electron microscopes (SEM and TEM). The results showed that the functionalized MWCNTs with 2-glucosyloxyethyl methacrylate (GEMA) and coaed with gelatin exhibited low cytotoxic effects in comparison with the standard doxorubicin. Also, gelatin was grafted with GEMA *via* their amino groups using Michael addition reaction.

Keywords: nanobiotechnology, multi-walled carbon nanotubes, cytotoxicity, cell growth, cell adhesion, grafting copolymerization.

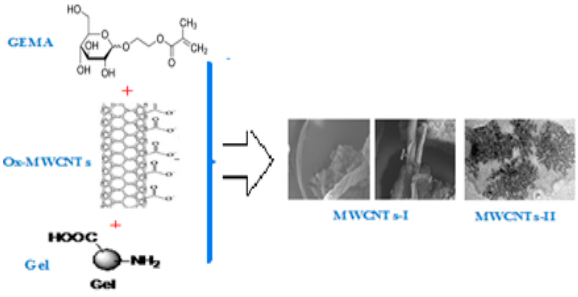

Figure 1: illustrating schematic representation of the prepared functionalized multi-walled carbon nanotubes using (Gel) gelatin and 2-glycosyloxyethyl methacrylate (GEMA).

1. Introduction

CNTs showed low solubility, poor wettability and bad dispersibility in common solvents and solid matrices.This major drawback is particularly relevant to their compatibility with biologicalsystems [1]. Except the dispersing and wetting of CNTs, chemical functionalization may result in other effects such as: introduction of reactive functional groups on their surfaces, grafting of polymer chains on CNTs and tuning the intrinsic properties of CNTs like biocompatibility, toxicity and conductivity [2]. Recently, glucosyloxyethyl acrylate (GEA) was used to modifiy chitosan through Michael addition reaction. Acrylic monomers and polymers bearing a monosaccharide residue have unique properties to be used as pharmacological or biomedical materials and play important roles in the intercellular recognition process [3]. This work deals with preparation and characterization of some functionalized MWCNTs with 2-glucosyloxyethyl methacrylate (GEMA) and coaed with gelatin. Moreover, the potential *in vitro* cytotoxic study of the prepared materials with breast carcinoma cell line (MCF7) using SBR assay was investigated.

2. Materials and methods

Multi-walled carbon nanotubes (MWCNTs), carbon > 95%, O.D L 6-9 nm 5 µm obtained from Aldrich. 2-Glucosyloxyethyl methacrylate (GEMA), a monomer having a pendant glucose moiety, was supplied as an aqueous solution of 5 w/v % by Aldrich. Edible Gelatin, Mw~40000 (Gel) was purchased from Davis Gelatin NZ Limited, Christchurch, NZ. All chemicals and other reagents were used as received without further purification.

2.1. Oxidation and purification of MWCNTs [4]

Pristine MWCNTs (300 mg) were dispersed in mixed concentrated sulphuric and nitric acids (3:1, v/v) at ratio of 50 mL acid mixture per 10 mg of CNTs. The resulted mixture was then refluxed at 110°C overnight with continuous stirring to produce oxidized mutli-walled carbon nanotubes (MWCNTs-COOH). The samples

were washed with ultrapure water until the filtrate is neutral (pH 7.0). The collected solid was dried under vacuum at 70°C for 12 hr. The resulted materials denoted MWCNTs-COOH and kept for further modification and analysis.

2.2. Preparation of MWCNTs-based nanocomposites

2.2.1. Synthesis of Gel-GEMA through Michael addition reaction [5]

2 gm of gelatin (Gel) was dissolved in 80 mL deionized water (pH ~ 5.5). Then, 0.01 mol GEMA dissolved in 20 mL of deionized water were added, stirred for 48 hr at 50°C. Subsequently, the pH value of reaction mixture was adjusted to 8-9 by adding saturated sodium biocarbonate solution. The solution was poured into 1L of acetone to remove the unreacted reactant, filtrate to collect solid, dialyzed for 5 days and freeze-dried to obtain pure Gel-GEMA. The aforementioned steps were repeated in presence of ox-MWCNTs to prepare the derivatives I and I (Table 1).

Table 1. Chemical compositions of the prepared nanocomposites

Sample code (w/w%)	Chemical compostion	
	MWCNTs	Gel
GEMA		
GEMA 100	0	0
Gel/GEMA 50	0	50
MWCNTs-I 50	50	0
MWCNTs-II 25	50	25

2.3. *In vitro* cytotoxicity examination of some promising prepared materials, using SBR assay: Potential cytotoxicity of the prepared nanomaterials was tested using the method of Skehan *et al.* [6] as follows: Different human normal cell lines (HFB4, and/or fibroblasts) were plated separately in 96-multiwell plate (10 cells/well) for 24 hr before treatment with the prepared nanomaterials to allow attachment of cell to the wall of the plate. Different concentrations of the prepared nanomaterials under investigation (0, 5, 12, 25 and 50) µg/mL were prepared for each individual dose. Monolayer cells were incubated with the prepared materials for 48 hr in 5% carbon dioxide atmosphere at 37°C. After 48 hr, cells were fixed, washed and stained with Sulpho-Rhodamine-B stain. Excess stain was washed with acetic acid and attached stain was recovered with Tris-EDTA buffer. Colour intensity was measured in an ELISA reader.

3. Results and discussion

Characterization of the prepared materials

Fig 1 shows FTIR spectra of ox-MWCNTs, MWCNTs-I and MWCNT-II. Typically the absorption peaks assigned to the O-H groups was observed at range 3400-3700 cm^{-1} in both spectra of MWCNT-I and II different from that of ox-MWCNTs. This indicates that the prepared derivatives I and II had many OH groups based on GEMA structure. Obviously, in case of the derivatives I and II, the appearance of new peaks at 1720 cm^{-1} assigned to the carbonyl ester new bonding between Ox-MWCNTs s and gel/GEMA. Fig 2 shows TEM images of the prepared materials gel/GEMA and MWCNTs-II before and after swelling in aqueous medium. Gel/GEMA exhibited aggregation spherical-like particles (Fig 2a). While, the nanotubes have been cut into short ones, and the grafted MWCNTs can entangle with neighboring ones like brush hair (Fig 2b). On the other hand, the grafted and coated MWCNTs were aggregated into a cluster form after swelling in aqueous medium. Fig 3 shows SEM micrographs of MWCNTs derivatives I and II. As can be seen, the increased in diameter of the grafted carbon tubes (Fig.3a). This indicates that the grafting reaction with GEMA took place over the whole surface of the MWCNTs. While the tubes were completely coated with gelatin in the case of MWCNTs-II (Fig 3b).

In vitro cytotoxicity study of the prepared materials using SBR assay

Fig 4 shows *in vitro* cytotoxicity study of the prepared materials I and II using SBR assay. It was observed that the prepared MWCNTs derivatives I and II exhibited low cytotoxicity against MCF7 cells in comparison with standard

doxorubicin at different concentrations. Moreover, all the prepared materials have high IC50 values relative to the standard. In other words, at high concentration (50 µg/ml) suggesting the relatively non-toxic nature of these materials on the cancer cells (MCF7). As indicated in Fig. 4, treatment of the cancer cells with various concentrations (5, 12, 25, and 50µg/ml) of the prepared materials caused a dose-dependent decrease in cell viability relative to the control culture.

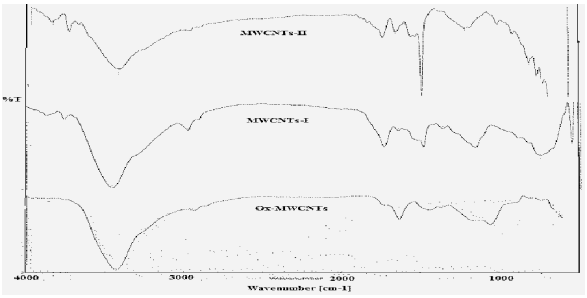

Fig.1

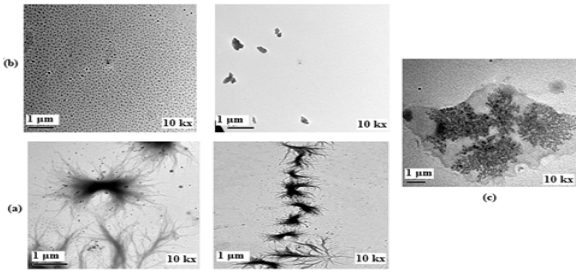

Fig 2.

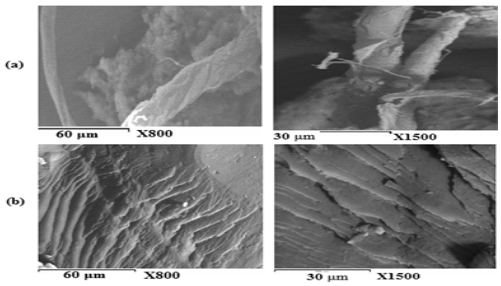

Fig 3.

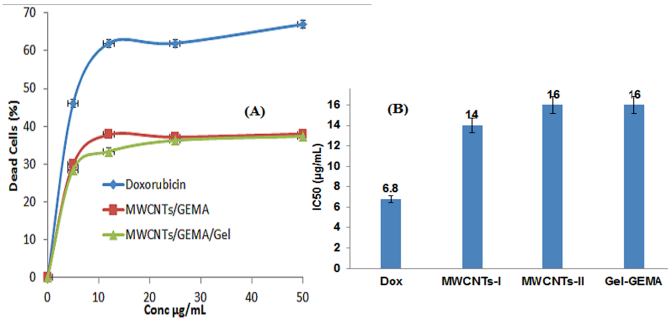

Fig 4.

References

[1] Bianco A., Kostarelos K., Partidos CD., Parto M. *Chem Commun* (2005) 571.

[2] Han J., Gao C. *Nano-Micro Letters* 2 (2010) 213.

[3] Takashi M., Atsushi J., Katsuhiko N., Allan S.H. *Macromol. Chem. Phys.* 197 (1996) 1135.

[4] Marshall MW, Popa-Nita S, Shapter JG. *Carbon* 44(2006) 1137.

[5] Wang K, Yin R, Tong Z, Yu Q, Nie J. *Int. J. Biol Macromol* 48 (2011) 753.

[6] Skehan P., Storeng R. et al. *J. Natl. Cancer Inst.*82 (1990) 1107.

Acknowledgement

This work was a part from the project which financially supported by National Research Centre, Cairo, Egypt.

A novel method for the preparation of poly(aminoacid) capped ultrasmall gold nanoclusters

I. Guryanov,[1,2,*] F. Polo,[3] S. Antonello,[3] F. Maran,[3] E. V. Ubyivovk,[4] E. Vlakh,[1,2] T. Tennikova,[1,2]
[1]St.-Petersburg State University, Laboratory of Biomedical Chemistry, St.-Petersburg, Russia
[2]Institute of Macromolecular Compounds RAS, St.-Petersburg, Russia
[3]University of Padova, Padova, Italy
[4]St.-Petersburg State University, Department of Physics, St.-Petersburg, Russia

Nanoparticles (NPs) have an enormous potential for the construction and study of systems suitable for molecular recognition and self-assembly at the nanoscale. This is particularly true for possible applications in biomedicine, such as tissue engineering, drug delivery and medical diagnostics. Due to their excellent biocompatibility and unique physicochemical properties, gold nanoparticles (AuNPs) are emerging as one of the most promising platforms for possible applications in various therapeutic strategies. We have recently found that monolayer-protected Au_{144} nanoclusters (MPCs), which have a gold core of only 1.6 nm, easily undergo cellular uptake, show no toxicity, and once loaded with drugs display excellent properties as drug carriers (unpublished results). On the other hand, the presence in the protective monolayer of small ligands with only restricted amount of binding groups facilitates their desorption and may lead to aggregation and disruption of the nanoparticle itself, particularly because of the presence of thiol-containing molecules in physiological environment.[1] In this contest, hybrid core/shell nanosystems based on gold MPCs capped with poly(aminoacids) could be particularly useful owing to their relatively easy preparation and functionalization, and the possibility of displaying bioactive molecular moieties in a controlled manner.[2] Very few examples describe direct polymer formation trough polymerization on the AuNP surface.[3] In particular, there are no reports concerning direct polymerization approaches for the preparation of AuNP/poly(amino acids) nanostructures. In this work, we describe a novel method for assembling poly(amino acids) on Au_{144} MPCs.

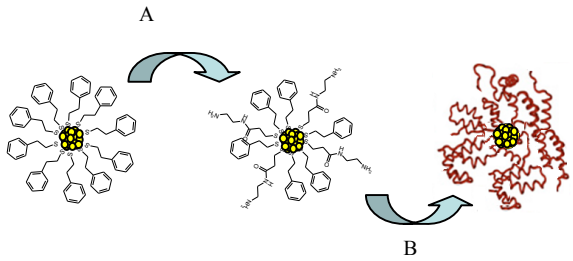

Scheme 1: Synthesis of core/shell star-like nanoparticles. (A) Ligand exchange reaction and preparation of the initiator of polymerization. (B) N-carboxyanhydride polymerization and polymer deprotection.

The method we used consists in the direct polymerization of N-carboxyanhydrides (NCA) directly on Au_{144} MPCs, which serve as both supports and initiators of polymerization, and allows creating core/shell star-like platform as possible nanocarrier for bioactive molecules. To prepare gold MPCs containing free amino groups suitable to act as polymerization sites, the monolayer of preformed phenylethanethiolate protected clusters, $Au_{144}(SCH_2CH_2Ph)_{60}$, was modified via ligand place exchange using thiolated ligands carrying a Fmoc-protected amino-group (Scheme 1, A).

The average number of exchanged ligands was calculated by oxidatively decomposing the MPCs with excess iodine and analyzing the molar ratio between the liberated ligands through a comparison between the integrals of conveniently separated peaks. The so-obtained mixed monolayer nanoclusters were Fmoc-deprotected and fully characterized by STEM, TGA and UV, allowing us to verify that the gold core size was not affected by the above chemical steps (Fig. 1).

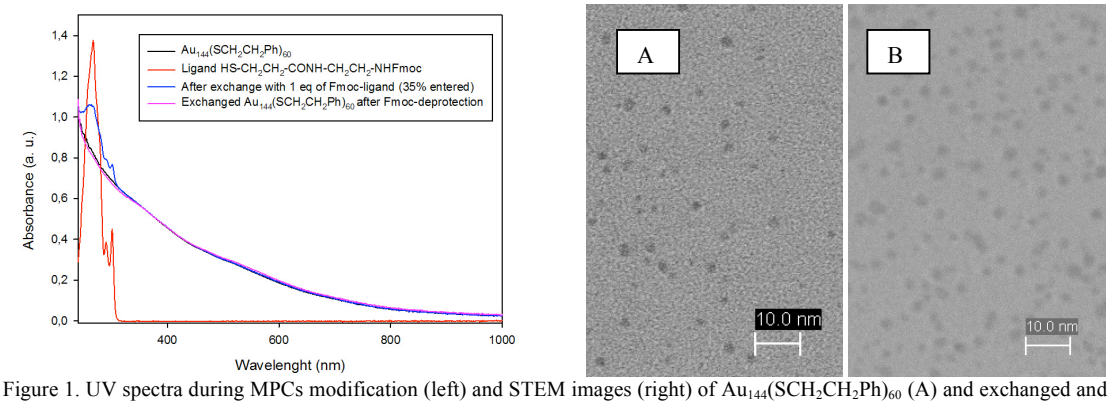

Figure 1. UV spectra during MPCs modification (left) and STEM images (right) of $Au_{144}(SCH_2CH_2Ph)_{60}$ (A) and exchanged and deprotected MPCs (B)

The polymerization of NCA was carried out at different temperatures, monomer/initiator ratios, and concentrations of monomer and initiator (Table 1).

Table 1. Polymwrization conditions and characterization of core/shell nanoparticles after Fmoc-deprotection.

Sample	T, °C	Molar ratio NCA/NH_2	C_{NH2}, mM	C_{NCA}, mM	pLys, % (TGA)	M_{pLys}, kDa (TGA)	D, nm (DLS)
4-Au50	4	50	3	150	-	-	-
Au50-1	30	50	3	150	84,7	160	29
Au100-1	30	100	1,5	150	87,9	200	28
Au150-1	30	150	1	150	93,4	400	29
Au50-2	30	50	0,15	7,5	75,2	85	24
Au100-2	30	100	0,15	15	79,5	110	Aggregation
Au150-2	30	150	0,15	22,5	84,7	150	Aggregation

At low temperature the polymerization leads to the formation of low molecular weight products, whereas at 30 °C the MPC-induced polymerization of NCA takes place promptly and yields products whose molecular weights strongly depend on the ratio monomer/initiator and the concentrations of the reagents (Table 1). After Fmoc-deprotection, the initial brown color typical for Au_{144} MPCs turns pink, a color generally associated with the presence of larger AuNPs (Fig. 2). Moreover, a low intensity plasmon resonance band, seen also in the Fmoc-protected NPs, was found to increase in time and is visible even after dilution. The presence of the plasmon resonance band in the UV spectra was observed also in the samples obtained by using diluted solutions of the initiator, which prevented its clustering during polymerization. No pH-induced shift of its maximum (530 nm) was observed, which was shown to occur upon aggregation.[4] STEM images confirmed the mantainance of the gold core dimension and the absence of large aggregates. This plasmon resonance band appears to be caused by cooperative long-range interactions between gold nanoclusters mediated by polylysine chains, rather than induced by aggregation of nanoparticles. To the best of our knowledge, this phenomenon has never been observed.

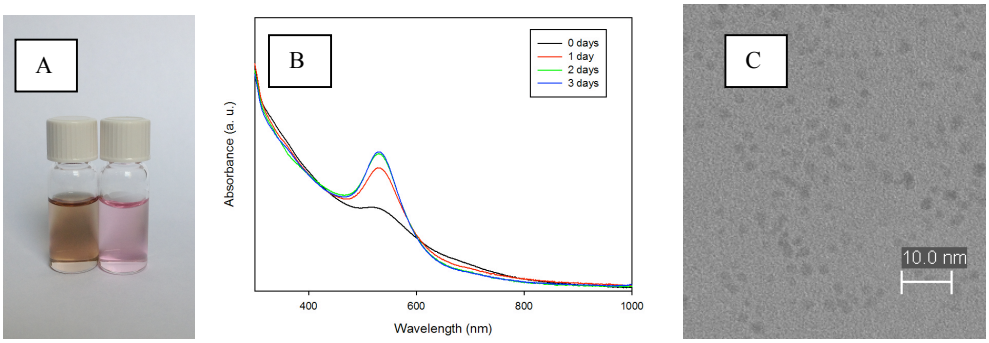

Figure 2. Au50-1: (A) Polymer coated AuNPs before (left) and after (right) Fmoc-deprotection; (B) Increase of the plasmon resonance band with time after Fmoc-deprotection; (C) STEM image of the Fmoc-deprotected core/shell AuNPs.

The lysine N-carboxyanhydride polymerization reaction leads to the formation of a robust polylysine protective shell, stable in the conditions of chemical etching (presence of thiols at high concentrations) and at different pH. This method can be easily extended to prepare core/shell nanosystems with other mono- and co-poly(amino acids).

References:

1. Chen, H. *et al. Nano Res.* 5 (2012) 815–825
2. Perego, D. *et al. Nanotechnol.* 24 (2013) 075102
3. Nuß, S. *et al. Angew. Chem. Int. Ed.* 40 (2001) 4016–4018
4. Guo, Y. *et al. J. Phys. Chem. C.*111 (2007) 9172–9176

Dynamic Characteristics of Carbon Nanotube Based Nanocomposites with Atomic Vacancy and Stone-Wales Defects

Sachin O. Gajbhiye[1*] S. P. Singh[1]
[1]Department of Mechanical Engineering, Indian Institute of Technology Delhi,
Hauz Khas, New Delhi 110016, India

Abstract: A unique atomic structure of carbon nanotube unveils outstanding properties. This makes it potentially highly valued reinforcing material to strengthen composite materials. But, the presence of defects in the nanostructure substantially alters the material's properties. So, the static and dynamic characteristics of carbon nanotube based nanocomposites subjected to atomic vacancy and Stone-Wales defects are studied using nonlinear representative volume element. The carbon-carbon bond of nanotube is modeled using Tersoff-Brenner potential. The H110MA grade polypropylene is used as matrix material and its properties are tested in the laboratory which are further used to model it. The interaction between nanotube and polymer matrix is modeled using nonlinear spring elements in the presence of defects in reinforcing material.

Keywords: Carbon nanotube, Nanocomposites, Representative volume element, Atomistic vacancy defect, Stone-Wales defect, Tersoff-Brenner potential.

1. Introduction

Shokrieh et al [1] investigated the tensile behavior of the carbon nanotube embedded polymer matrix. They have assumed the linear behavior of polymer matrix and carbon-carbon bond. Joshi et al [2] analyzed the elastic properties of carbon nanotube reinforced polypropylene with pinhole defects. They have represented the polypropylene and carbon nanotube using continuum elements with linear material properties. Wernik et al [3] proposed the multiscale modeling of the nonlinear response of nano-reinforced polymers. They have used the spring elements to simulate carbon nanotubes and vdW interactions. They used the Morse potential to represent carbon-carbon bond and Lennard-Jones potential to represent vdW interactions. Joshi et al [4] studied the chirality effects in carbon nanotube reinforced composites. They considered the length of carbon nanotube equal to the length of matrix material in the (representative volume element) RVE and investigated the effects of different elastic properties, length of carbon nanotube, material of matrix. Researchers have assumed the linear material behavior for carbon-carbon bond. While modeling the interface between polymer and nanotube, they have assumed the interaction only between the nearest carbon atoms of these two materials.

2. Modeling Procedure

In the design of RVE as shown in Fig. 1, the carbon-carbon bond of nanotube is modelled using its nonlinear material model [5]. The nonlinear interactions between the nanotube and matrix material (interface) is modelled using "Lennard-Jones 6-12" potential [5]. In the designed RVE, the nanotube is considered as surrounded by the matrix material from all sides with clearance equal to the equilibrium distance between the nanotube atoms and the polymer atoms. This equilibrium distance is taken as 0.3282 nm [6]. To simulate the matrix material (H110MA polypropylene), SOLID186 element of Ansys is used in the computation. It is a higher order 3-D 20-Node Structural Solid element that exhibits quadratic displacement behaviour and is capable to model the nonlinear material behaviour.

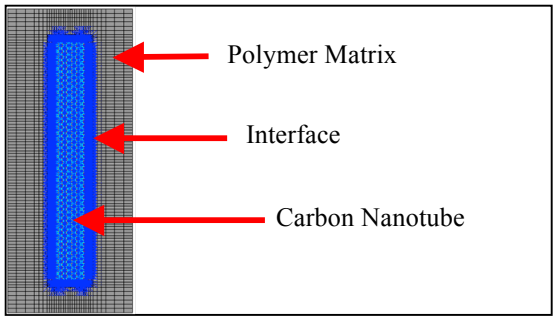

Fig. 1. Representative volume element

3. Results and discussion

3.1. Static characteristics

The representative volume element is made by adding 5 % by volume of nanotube with H110MA grade polypropylene. It is then subjected to the cantilevered boundary condition where one end is clamped and the strain is applied at the other end. Armchair (9, 9) and zigzag (16, 0) nanotubes are considered in the RVE both of approximately same diameter to investigate the effect of chirality on the static characteristics of nanocomposite. Atomic vacancy and Stone-Wales defects of nanotube are considered to investigate its effect on the static characteristics of nanocomposite material. Eight number of equally spaced vacancy defects are created in the nanotube of RVE along its length. Similarly, ten number of equally spaced Stone-Wales defects are also created. Before investigating its effects on the nanocomposite material, its effects are studied on the carbon nanotubes. Fig. 2 shows the nonlinear stress-strain curve of the defect-free and defective SWCNT under cantilevered boundary condition. It is observed that the presence of defects in nanotube reduce its stress and strain carrying capacity. It is also observed that vacancy defect affects more to the static characteristics of the nanotube compared to the Stone-Wales defect. These

defective nanotubes are then used in the RVE such that their percentage volume is 5 % of the total volume of RVE. Fig. 3 shows the nonlinear stress-strain curve of the RVE under cantilevered boundary condition. It is seen that the defect-free and the defective RVE shows the same static characteristics. Though the vacancy and Stone-Wales defect alter the mechanical properties of the nanotube but once they are mixed with the matrix material then their effect on the overall static characteristics of the nanocomposite material is negligible.

3.2. Dynamic characteristics

Effect on natural frequencies of the matrix material by addition of 5 % of nanotube (by volume) is studied in this section. The variation of natural frequencies of the neat polypropylene and nanocomposite material under cantilevered boundary condition is shown in Fig. 4. It is observed that addition of nanotube significantly improves the natural frequencies of matrix material. At higher modes, there relative increase in the values of natural frequencies is more. The reason for this is, the higher modes of the RVE are the higher flexural modes and the added nanotube restricts this motion by providing extra stiffness to the RVE, as a result the natural frequencies also increase. Next, to study the effect of defects of nanotube on the vibration of nanocomposite material, the defect-free nanotube of RVE is replaced by the defective nanotube. In this case also, vacancy and Stone-Wales defects are considered. After extracting the natural frequencies of RVE with defective nanotube under cantilevered boundary conditions, it is observed that effect of defects on the natural frequencies is negligible, though their role is significant when nanotubes are used alone.

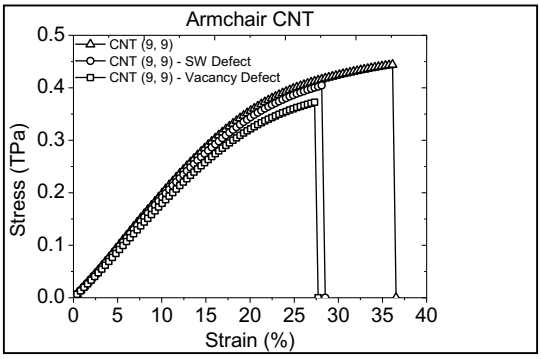

Fig. 2. Nonlinear stress-strain curve of Armchair CNT with defects

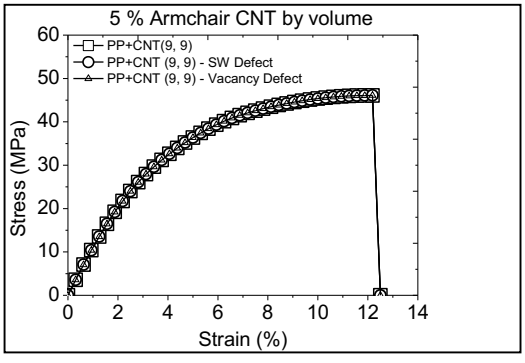

Fig. 3. Nonlinear stress-strain curve of RVE with Armchair nanotube with defects

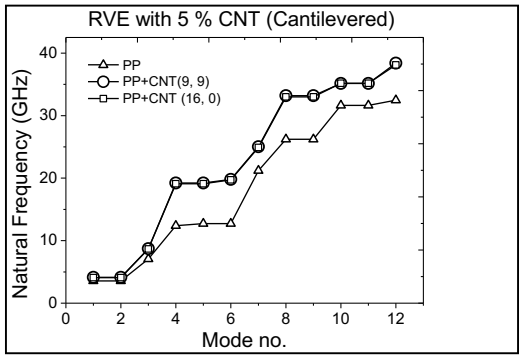

Fig. 4. Natural frequencies of RVE for (a) Cantilevered and (b) Clamped boundary condition

4. Conclusions

The static and dynamic characteristics of the nanocomposites material with and without presence of defects are studied using the concept of RVE. A nonlinear RVE is proposed to carry out this task. Though, the enhancement of the strength of the neat polypropylene is observed by adding CNT to it, but the effect of defects is negligible on the static and dynamic characteristics of nanocomposite material. The stress-strain curve of the RVE encompassing vacancy and Stone-Wales defective nanotube under the application of external strain shows same behaviour. Similarly, the natural frequencies of the RVE are also approximately same in case of defect-free and defective condition.

References

[1] M. M. Shokrieh and R. Rafiee, "On the tensile behavior of an embedded carbon nanotube in polymer matrix with non-bonded interphase region," *Composite Structures,* vol. 92, pp. 647-652, 2010.

[2] U. A. Joshi, S. C. Sharma, and S. P. Harsha, "Analysis of elastic properties of carbon nanotube reinforced nanocomposites with pinhole defects," Computational Materials Science, vol. 50, pp. 3245-3256, 2011.

[3] J. M. Wernik and S. A. Meguid, "Multiscale modeling of the nonlinear response of nano-reinforced polymers," Acta Mechanica, vol. 217, pp. 1-16, 2011.

[4] U. A. Joshi, S. C. Sharma, and S. P. Harsha, "A multiscale approach for estimating the chirality effects in carbon nanotube reinforced composites," Physica E: Low-dimensional Systems and Nanostructures, vol. 45, pp. 28-35, 2012.

[5] S. O. Gajbhiye and S. P. Singh, "Multiscale nonlinear frequency response analysis of single-layered graphene sheet under impulse and harmonic excitation using the atomistic finite element method," Journal of Physics D: Applied Physics, vol. 48, pp. 1-16, 2015.

[6] L. Y. Jiang, Y. Huang, H. Jiang, G. Ravichandran, H. Gao, K. C. Hwang, et al., "A cohesive law for carbon nanotube/polymer interfaces based on the van der Waals force," Journal of the Mechanics

and Physics of Solids, vol. 54, pp. 2436-2452, 2006.

Hybrid gold nanoparticles modified by oligopeptides for lead (II) ions interaction monitoring

Jane Politi[1,2], Jolanda Spadavecchia[*3,4], Mario Iodice[1], Luca de Stefano[1]

[1]Institute for Microelectronics and Microsystems, Unit of Naples-National Research Council, Italy
[2]Department of Chemical Sciences, University of Naples "Federico II", Naples Italy
[3]Sorbonne Universités, UPMC Univ Paris VI, Laboratoire de Réactivité de Surface, Paris, France.
[4]CNRS, UMR 7244, Laboratoire de Chimie, Structures et Propriétés de Biomateriaux et d'Agents Therapeutiques, Paris, France

Abstract

In this paper we report the interaction monitoring between lead (II) ions in aqueous solution and Phytochelatin 6 oligopeptides bioconjugated onto pegylated gold nanorods (PEG-AuNr). Phytochelatins are small peptides, found in different organisms such as plants and fungi for detoxification mechanisms. This study is the first step towards a high sensitive label free optical biosensor to quantify heavy metals pollution in water using nanostructured hybrid materials as PEG-AuNr.

Introduction

Nanostructured materials have become increasingly popular due to their unique properties in development of novel biosensors. Therefore, more attention should be paid to find efficient synthesis methods to match the enlarging demand of gold nanoparticles. Several different solution synthesis methods have been employed to prepare gold nanoparticles, including biomolecule reduction of $HAuCl_4$, seed mediated synthesis at room temperature and polymer-assisted synthesis. Recently, the utility of nanomaterials for any application is strongly dependent upon their physicochemical characteristics and their interactions with surfaces modifiers (Spadavecchia *et al.*; 2014). Exchange of organic molecules on Au nanoparticles with PEG can indeed be performed to prepare biocompatible PEG-stabilized Au nanoparticles. Gold nanoparticles can interact with specifically sequenced peptides that can self-assemble on their surface. The polypeptides could induce or prevent aggregation of nanoparticles causing consequently the change of absorbance and, moreover, allow to interact with other metal ions i.e. Cd^{2+}, Ni^{2+}, Co^{2+}, Zn^{2+} etc. Lead is a widely used heavy metal and has a large number of industrial applications, such as battery manufacture, paint, gasoline, alloys, radiation shielding, piping and so on. Lead content in paints and gasoline represents a severe risk of environment pollution and, consequently, for human health. Moreover, bioprobes play an important role in heavy metal detection. Phytochelatins (PCs) oligopeptides have been widely studied because of their ability to chelate heavy metal ions in plants and fungi for detoxification mechanisms (Cobbett, 2000). We report here synthesis to prepare polymer-modified gold nanoparticles and gold nanorods using dycarboxylic PEG (DPEG) as stabilizer. We have thus implemented and evaluated a simple and reproducible method for labeling biomolecules with PEG gold nanostructures without utilizing organic solvents and surfactants. A new kind of pegylated gold nanorods based assay to quantify lead-Phytochelatin 6 (PC_6) interactions in aqueous solution by using the proteins as bioprobes was developed. Ultraviolet-visible (UV-Vis) spectroscopy and Fourier transform surface plasmon resonance (FT-SPR) has been used for monitoring the formation of metal-biological complexes at different concentration lead.

Discussion

In order to improve the biointerfacial properties of AuNPs, we coated them with a bifunctional PEG linker carrying two carboxylic groups. The synthesis of PEG-capped gold nanoparticles (DPEG-AuNPs) was achieved by reducing-tetrachloroauric acid ($HAuCl_4$) with sodium borohydride ($NaBH_4$) in the presence of PEG-diacid as a capping agent. The main difference with other synthesis procedures of DPEG-AuNPs is that PEG-diacid is used in the same way as the citrate for the stabilization of the particles through electrostatic interactions between the carboxylic acid groups and the gold surface [28]. Particle formation and growth were tuned by the amphiphilic character of the PEG-diacid polymer and include three steps: (1) reduction of $HAuCl_4$ facilitated by dicarboxylic acid-terminated PEG to form gold clusters; (2) adsorption of PEG diacid molecules on the surface of the gold clusters and reduction of metal ions in that vicinity; and (3) growth of gold particles and colloidal stabilization by PEG polymers. Interaction of PC_6 biomolecules and PEG-AuNPs or nanorods PEG-AuNr was monitored by observing the Localized Surface Plasmon (LSP) band in the UV–Vis spectrum. Figure 1 displays the LSP bands of AuNPs before and during interaction with PC_6 molecules at equal concentrations of AuNPs in aqueous solution (10^{-4} M). It is well visible that AuNPs before bioconjugation show one peak at 530nm, while after 2 minutes of mixing with PC_6 proteins appears a second LSP peak around 650nm. A decrease of the plasmon absorption can be attributed to the change of localized refractive index near the AuNr surface indicating that PC6 were attached to the AuNr surface. From UV-Vis recorded spectra, it is clear that AuNr bind PC6 molecules and the resulting complexes are stable since there is not any degradation of the absorption peak.

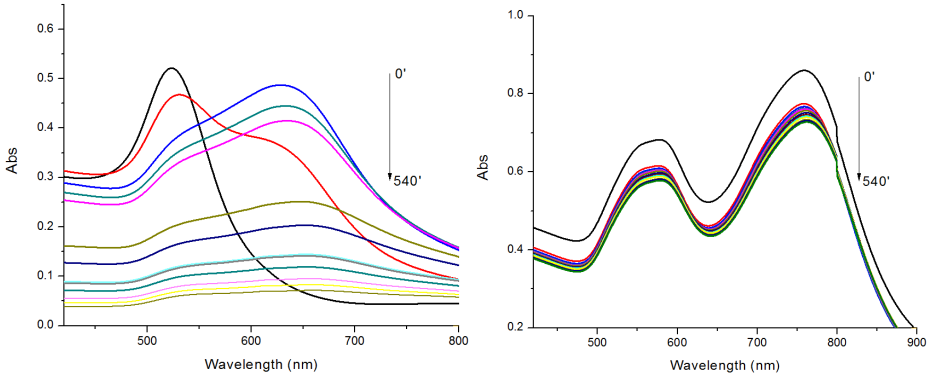

Figure 1: UV-Vis spectra of PEG-AuNPs (left) and PEG-AuNr (right) before and after bio-conjugation wih PC6 protein.

Planar gold surfaces were functionalized by a cysteamine self-assembled monolayer, which could strongly bound, under EDC/NHS chemistry activation the PC6-AuNr in order to perform Fourier Trasform Surface Plasmon Resonance (FT-SPR) measurenments (Figure 2).

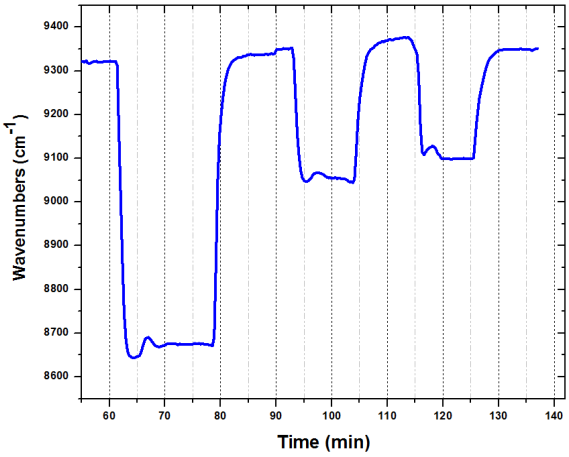

Figure 2. FT-SPR response as function of Lead (II) solutions concentration (respectively 100, 50 and 25ppb) during 3 cycles of binding followed by rinsing.

The real-time monitoring of all Pb (II) solutions with different concentrations tested shows important wavenumer change. It is of particular interest that after rinsing the signal restores its initial value since this means that interaction between nanocomplexes and metal ions is reversible. These wavenumber shifts indicate that lead (II) ions in solution significantly bind to phytochelatin modified AuNr even if the hybrid probes are conjugated to the analysis surface of FT-SPR. These wavenumber shifts indicate that lead (II) ions in solution significantly bind to phytochelatin modified AuNr even if the hybrid probes are conjugated to the analysis surface of FT-SPR (Politi et al. 2015).

Conclusions

In this work, we have characterized by optical, label free techniques the interaction between small peptides, namely PC6, and Pb (II) in aqueous solutions based on proteins bioconjugated gold nanorods. These hybrids nanocomplexes are stable and biologically active: even if linked by adsorbed-gold interaction on the nanorods surface, the peptides are able to strongly bind the heavy metal ions. These results are very promising for development of sensitive and effective nanoparticle-based biosensor for quantifying Pb (II) ions concentration in water.

References:

1. Cobbett, C.S.; (2000) Phytochelatin biosynthesis and function in heavy-metal detoxification. Current opinion in plant biology, 3, 211–216.
2. Politi, J., Spadavecchia, J.; Iodice, M.; De Stefano, L.; (2015**)** Oligopeptide–heavy metal interaction monitoring by hybrid gold nanoparticle based assay, *Analyst*, , 140, 149-155.
3. Spadavecchia, J.; Perumal, R.; Barras, A.; Lyskawa, J.; Woisel, P.; Laure, W., Pradier, C.M., Boukherroub R., Szunerits S., Amplified plasmonic detection of DNA hybridization using doxorubicin-capped gold particles Analyst, 2014,139, 157-164.

Ammonia gas sensing properties of ZnO nanowires synthesized by thermal oxidation of Zn film

B. Behera and S. Chandra*
Centre for Applied Research in Electronics
Indian Institute of Technology Delhi, Hauz Khas, New Delhi 110016, INDIA
*E-mail: sudhirchandra1950@gmail.com

Abstract

In this work, long, dense and uniformly distributed ZnO nanowires have been synthesized and studied as the sensing element for the detection of ammonia gas. 130 nm thick Zn film was deposited on oxidized Si substrate by RF magnetron sputtering at the rate of 4.5 nm/min in Ar ambient. The film was subsequently oxidized at 600 ^{o}C in moist environment for 1 hr. The structural phase of post oxidized sample indicates that sample is completely oxidized and morphology indicates that surface is covered by nanowires. These nanowires diameters are about 40-50 nm and length is few tens of micron. The resistance of nanowires was measured through Cr-Au IDE (inter digital electrode) of 30 μm gap in air and test gas (ammonia) atmospheres.

Introduction

Ammonia (NH_3) is a toxic gas and needs to be detected in industrial units and other places. Till date, various semiconducting metal oxides such as SnO_2, ZnO, In_2O_3, CuO, WO_3 and V_2O_5 have been used for detection of various gases [1]. ZnO is a highly sensitive, thermally and chemically stable material [2]. Though various forms of ZnO such as thick film, thin film and nanostructures have been used in gas sensing application, still nanostructured ZnO is reported to be an excellent material because of its high surface area to volume ratio resulting in enhancement in physical and chemical properties at the surface. Nanostructured ZnO such as nanowires, nanorods, nanoribbons, nanoflakes and nanobelts have been synthesized by thermal evaporation, CVD, pulsed lased deposition, hydrothermal and thermal oxidation technique. The thermal oxidation technique is quite simple, cost effective and catalysis free and mass productive method [3].

In this paper, we report Zn film deposition by RF magnetron sputtering and its subsequent oxidation in moist environment to grow long, dense and uniformly distributed ZnO nanowires. These nanowires were synthesized on inter digital electrode (IDE) structure and its change in resistance was measured on exposure to NH_3 gas.

Experimental work

Zn film was deposited on oxidized Si substrate using RF magnetron sputtering at the deposition rate 4.5 nm/min to achieve 130 nm. This deposited Zn film was oxidized in a tube furnace in moist ambient. The heating temperature and time were 600 ^{o}C and 1 h respectively. Post oxidized samples were characterized using scanning electron microscopy (SEM) and X-ray diffraction (XRD). These nanowire syntheses were synthesized on Cr-Au IDE to fabricate a device. The device was heated using a small hot plate and nanowires resistance was measured using IDE. The gas sensing properties of the fabricated device were analyzed for 5-50 ppm of ammonia at different operating temperatures. The sensitivity "S" is defined as: $S= [(R_a - R_g)/R_g]\times 100\%$, where R_a and R_g are the resistances of the gas sensor in air and gas ambient.

Results and Discussion

The 130 nm Zn film, oxidized at 600 ^{o}C in moist air for 1 h resulted in long, dense and uniformly distributed nanowire growth. The corresponding SEM image is shown in Fig. 1(a). The SEM image reveals that, nanowire diameter is around 40-50 nm and length of few tens of micron. The XRD pattern was analyzed for the post-oxidized sample and material was indexed as hexagonal ZnO. The peak positions corresponding to (200) and (101) have maximum intensity. Also, it is observed that ZnO nanowires are high crystalline, since peaks are narrow. The resistance of nanowires was measured through Cr-Au IDE (30 μm gap). The resistances decreases upon heating and it is a clear proof that synthesized material is a semiconducting metal oxide. Upon exposure to reducing gases such as NH_3, the resistance further decreases (Fig 1(c)) clearly shows that ZnO is an n-type semiconductor. When ZnO is exposed to air, available oxygen molecules capture electrons from conduction band and convert to ions (O_2^-, O^-, O^{2-}). When ammonia gas is introduced to chamber, absorbed oxygen ions react in the following manner:

These donated electrons increases total charge carrier concentration and so the resistance decreases. The interaction between ZnO nanowires and gases (O_2/NH_3) is enhanced by thermal activation. Thus ZnO nanowires were heated for better response. Fig 1(c) shows the change in resistance of ZnO nanowires at 200 ^oC when exposed to 50 ppm of NH_3 gas. The sensitivity for above case is 53.5% and it is clear that synthesized ZnO nanowires are excellent material for gas sensing application. The response and recovery (90% of total change in resistance) time was measured to be 43 and 108 s. At this temperature, the sensor was tested for different concentrations. Sensitivity versus concentration graph is shown in Fig. 1(d) and it is found that the sensitivity is quite linear. The sensor shows excellent sensing performance which can be explained with quantum size effect. The diameters of nanowires are 40-50 nm. From XRD data, the calculated grain size from optimum peak is 27 nm. According to Kolmakov et al. the typical Debye length of ZnO nanowire is 30nm [4]. Thus we can presume that all available atoms of ZnO nanowires participate in the reaction to increase the sensitivity.

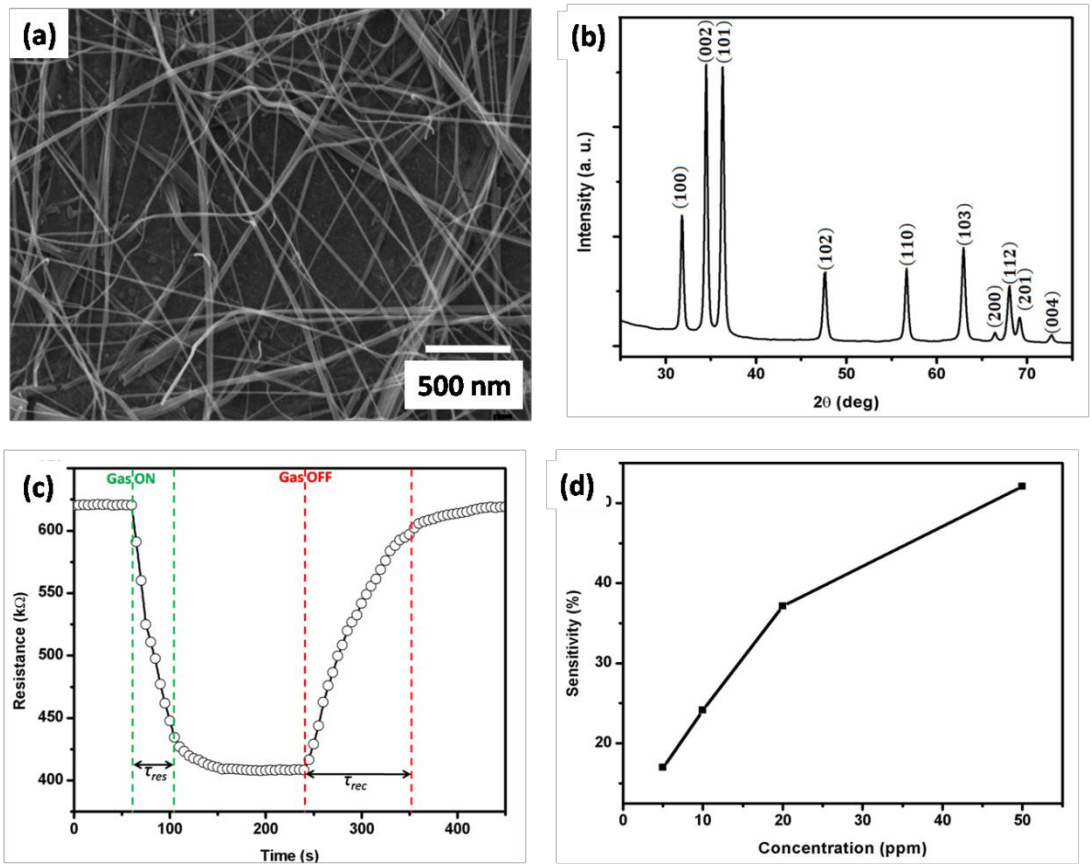

Fig. 1(a) SEM image (b) XRD pattern of ZnO nanowires (c) Change in resistance of ZnO nanowire upon exposure of 50 ppm of ammonia gas (d) Sensitivity v/s concentration plot

References

[1] G. Eranna, Metal Oxide Nanostructures as Gas Sensing Devices, 1 edition, CRC Press, Boca Raton, FL, 2011.

[2] Chang, Shoou Jinn, Wen Yin Weng, Cheng Liang Hsu, and Ting Jen Hsueh. (2010) High Sensitivity of a ZnO Nanowire-based Ammonia Gas Sensor with Pt Nano-particles., Nano Communication Networks, 1, 4: 283–88.

[3] B. Behera, S. Chandra, Catalyst-Free Synthesis of ZnO Nanowires on Oxidized Silicon Substrate for Gas Sensing Applications, J. Nanosci. Nanotechnol. 15 (2015) 4534–4542

[4] Kolmakov, A.; Moskovits, M. Annu. Rev. Mater. Res. 2004, 34, 151-180.

Ultrasensitive magnetic particles/DNAzymes based biosensors for clinical applications.

Stefano Persano[§‡†], Giuseppe Vecchio[§], Paola Valentini[§], Pier Paolo Pompa[§]*.
[§] Istituto Italiano di Tecnologia, Center for Bio-Molecular Nanotechnologies@UniLe, Via Barsanti, 73010 Arnesano (Lecce), Italy.
[‡] Università del Salento, Via Provinciale Monteroni, 73100 Lecce, Italy.
[†] Houston Methodist Research Institute, 6670 Bertner Avenue, Houston, 77030 Houston (TX), United States of America (USA).

Traditional *in vitro* diagnostic is based on assays and procedures optimized for modern clinical laboratories, equipped with all the necessary instrumentation. However, these high-tech and costly tests are not suitable to address the current diagnostic challenges of preventive medicine, ultra-early diagnosis, and large-scale population screenings. To address these issues, innovative diagnostic tests need more simplified procedures, resulting in cheap, rapid, instrument-free analyses that can be performed also in non-specialized settings, at the point-of-care (POC). In this framework, we show here two hybrid strategies for the sensitive detection of Human Papilloma Virus (HPV)[1] and RNases activity[2]. HPV is a very important analytical target, due to its broad diffusion and clinically relevant association with cervical cancer. Generally, the main obstacle for developing simplified testing for nucleic acid targets is their rather low concentration in clinical samples that does not match the sensitivity of most common assays; usually, the target needs to be amplified by PCR (Polymerase Chain Reaction), which requires dedicated instrumentation. In this context, we developed a polymerase reaction free, low-cost and sensitive assay for the colorimetric detection of HPV, based on the use of a smart design exploiting magnetic microparticles (MMPs), chimeric RNA/DNAzyme oligonucleotides, and double signal amplification (Fig. 1).

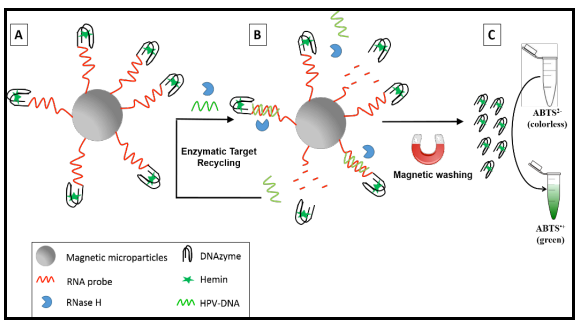

Figure 1. Schematic representation of the colorimetric detection platform based on RNase H-assisted target DNA recycling and generation of the colorimetric signal catalyzed by the peroxidase-mimicking DNAzyme. (A) DNAzyme-hemin complexes are immobilized onto MMPs via streptavidin-biotin interactions. (B) HPV DNA target recycling in the presence of RNase H. (C) DNAzyme-catalyzed oxidation of the ABTS substrate and generation of the colorimetric signal.

We exploited this system for the colorimetric detection of HPV-16, which is the most diffuse oncogenic HPV worldwide. We probed a broad range of target concentrations from 1 mM to 10 pM. Fig. 2A
shows the typical time-dependent absorbance changes in samples containing different concentrations of target DNA during the DNAzyme-catalyzed oxidation of ABTS.
The results show that the reaction is quite rapid, reaching the plateau in short time, and allowing us to record the maximum signal after about 3 min. Fig. 2B shows the quantitative response of our assay at different target concentrations. The signal can still be clearly distinguished from the background at 10 pM of target DNA.This sensitivity is significantly better than those of previously reported methods based on peroxidase-mimicking DNAzymes.[3–13]

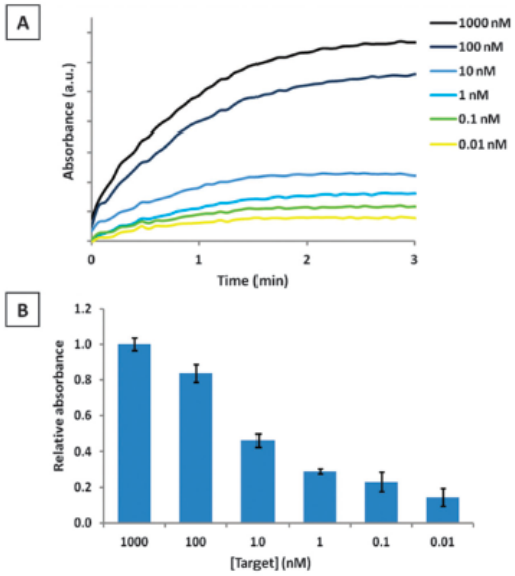

Figure 2. (A) Time-dependent absorbance changes at l = 414 nm in the presence of different amounts of target DNA ranging from 0.01 to 1000 nM. (B) Absorbance changes upon analyzing different concentrations of HPV–DNA. Error bars represent the standard deviation (SD) of three independent experiments. Absorbance data represent background subtracted values.

On the other side, the detection of RNases activity has also great importance in a wide range of biomedical applications, including assessment of RNase con

tamination in molecular biology and screening of new antiviral drugs and RNase inhibitors. In this regard, we proposed a new versatile strategy that allows the detection of several classes of RNases with better sensitivity then existing assays. Our two-step approach consists of a DNA-RNA-DNA chimeric Hairpin Probe (cHP) conjugated to MMP, a DNAzyme sequence and molecular beacons (see Fig. 3).

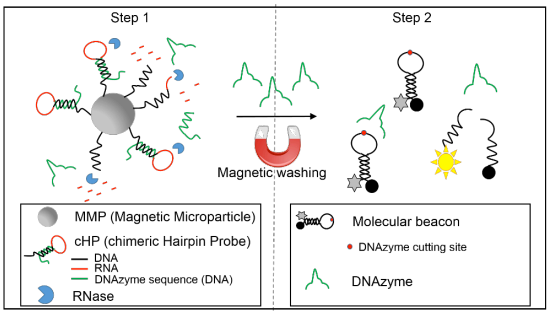

Figure 3. Schematic illustration of the two-step RNase assay. The DNA-RNA-DNA chimeric Hairpin Probe (cHP) is immobilized by biotin-streptavidin interaction onto Magnetic Microparticles (MMP) in order to obtain the MMP-cHPs complex. In the first step, the digestion of the RNA portion of cHPs by RNase allows the release of DNAzyme. After magnetic washing, the released DNAzyme is added to FAM/Dabcyl molecular beacon. In the second step, the catalytic activity of the DNAzyme on the molecular beacons generates fluorescence signal.

We used our assay to detect RNase A, a well-established model to evaluate the sensitivity of RNase assays[14], and largely used as positive control in commercial RNase contamination detection kits. As reported in Figure 4, the experimental results show that our strategy allows sensitive detection of RNase A down to 0.85 pg after just 30 min of DNAzyme activity.
However, using a longer incubation time (2 h), the sensitivity increases to 0.017 pg (corresponding to~3 X 10^{-7} U/mL) of RNase A (Figure 2, inset).

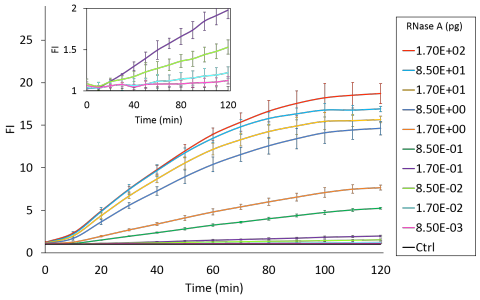

Figure 4. Time-dependent normalized fluorescence intensity (F/F0) at 522 nm upon incubation of our hybrid probe with different RNase A amounts (0.0085–170 pg) for 30 min at 37°C. The first step duration was fixed at 30 min. Inset shows a zoom of the kinetic curves at the lowest en

zyme amounts. Error bars represent the standard deviation (SD) calculated from triplicate experiments.

Our assays permit the detection of low amount of analyte by the use of an amplification step exploiting the catalytic activity of DNAzyme molecules. These characteristics, coupled with the small volume of samples needed by our approaches, make our assays suitable for future implementations, such as low cost Lab-On-a-

Chip and high-throughput screening applications.

Keywords: HPV, DNAzymes, Magnetic microparticles, RNase, chimeric DNA-RNA.

References:

[1] S. Persano, P. Valentini, J.H. Kim, and P.P. Pompa, *Chem. Comm.* 49, 10605 (2013).

[2] S. Persano, G. Vecchio, and P.P. Pompa Scientific Reports 5 : 9558

[3] J. H. Kim, R. A. Estabrook, G. Braun, B. R. Lee and N. O. Reich, Chem. Commun., 2007, 4342–4344.

[4] K. Schlosser and Y. Li, Chem. Biol., 2009, 16, 311–322.

[5] S. K. Silverman, Angew. Chem., Int. Ed., 2010, 49, 7180–7201.

[6] S. K. Silverman, Org. Biomol. Chem., 2004, 2, 2701–2706.

[7] K. Tram, P. Kanda and Y. Li, J. Nucleic Acids, 2012, 2012, 958683.

[8] H. Asanuma, H. Hayashi, J. Zhao, X. Liang, A. Yamazawa, T. Kuramochi, D. Matsunaga, Y. Aiba, H. Kashida and M. Komiyama, Chem. Commun., 2006, 5062–5064.

[9] M. Chandra, A. Sachdeva and S. K. Silverman, Nat. Chem. Biol., 2009, 5, 718–720.

[10] N. Carmi and R. R. Breaker, Bioorg. Med. Chem., 2001, 9, 2589–2600.

[11] B. Cuenoud and J. W. Szostak, Nature, 1995, 375, 611–614.

[12] J. Liu and Y. Lu, Chem. Commun., 2007, 4872–4874.

[13] T. L. Sheppard, P. Ordoukhanian and G. F. Joyce, Proc. Natl. Acad. Sci. U. S. A., 2000, 97, 7802–7807.

[14] Raines, R. T. Ribonuclease A. Chemical reviews 98, 1045–1066 (1998).

Efficiency Improvement in Dye Sensitized Solar Cells by Plasmonic Effect of Green Synthesized Silver Nanoparticles

S. Saravanan[1,*], R. Kato[2], M. Balamurugan[1], S. Kaushik[3], T. Soga[2]

[1]*Centre for Photonics and Nanotechnology, Sona College of Technology, Salem – 636 005, Tamilnadu, India*
[2]*Department of Frontier Materials, Nagoya Institute of Technology, Nagoya 466-8555, Japan*
[3]*The Indian Public School, Senapathipalayam, Erode – 638 112, Tamilnadu, India*

Abstract

Remarkably increased power conversion efficiency (PCE) of dye-sensitized solar cells has been achieved by addition of small quantities of silver nanoparticles into TiO_2 photo anodes. In this report, the uniform silver nanoparticle were developed by treating silver ions with *Peltophorum pterocarpum* flower extract. The X-ray diffraction analysis confirmed that the synthesized silver nanoparticles are single crystalline in nature with face centered cubic. Silver nanoparticles, with an approximate size of 15-30nm were observed in the Transmission Electron Microscopy image. A Plasmonic effect of silver nanoparticles in dye-sensitized solar cells is studied. Our investigations show that, the Ag NPs improves the power conversion efficiency of the solar cell from 2.83% to 3.62% with increment around 28% that takes place after incorporation the 2 wt% of the Ag NPs in P25-TiO_2 NPs.

1. Introduction: The third generation solar cells such as dye-sensitized solar cell (DSSC) and organic solar cell (OSC) have received great attention as promising technology for renewable energy production. DSSC have inspired enormous research interest due to several advantages such as flexibility, relatively high power conversion efficiency, low toxicity to environment, and easy fabrication with low cost. From the time of DSSC fabricated by Gratzel et al., [1] significant attempt has been put into the design of photoanodes in addition to dyes, [2] electrolytes [3] counter electrodes photo anode semiconducting material and redox shuttle for improve the efficiency of DSSC. Among these, the photoanode plays a crucial role in the determining the cell performance. In this study, the DSSCs have been fabricated by green synthesized Ag NPs mixed with photo anode TiO_2 and studied the plasmonic effect of Ag NPs on DSSC.

2. Experiments: Silver nanoparticles were prepared according to previous report [4]. 3 grams of fresh PP flowers were immersed in 300 mL boiling distilled water for 30 minutes and then filtered. The obtained extract dripped into 100 mL of 0.01 M aqueous silver nitrate solution in a flask with constant stirring. The appearance of the yellowish brown indicated the formation of the Ag NPs and then continued stirring for another 1 hour. The product dried in an oven at 60° C.

The above prepared Ag NPs were mixed with purchased P25 TiO_2 nanoparticles with different weight percentages of 1, 2 and 3. Also, a reference sample without Ag NPs are also prepared. The P25 TiO_2 layers without/with Ag NPs have been immersed in an ethanol solution of a 0.5 mM of Ruthenium complex based dye for 18 hrs at room temperature. DSSCs were assembled by sandwiching a platinum glass counter electrode and photoanode, by inserting polymer film (50 μm) between two electrodes, and injecting the redox iodide electrolyte into the space between two electrodes. The J/V characteristics of the devices were studied.

3. Results and Discussions: Structural and phase formation of the synthesized Ag NPs were characterized by X-ray diffraction ((XRD; SEIFERT, Cu Kα radiation, λ=1.540598 Å). Figure 1 shows XRD and it exhibits four main characteristic diffraction peaks for Ag at 2θ angle of 38.1, 44.3, 64.7, 77.7, which correspond to (111), (200), (220), and (311). It explains the prepared Ag NPs were face centered cubic crystal structure.

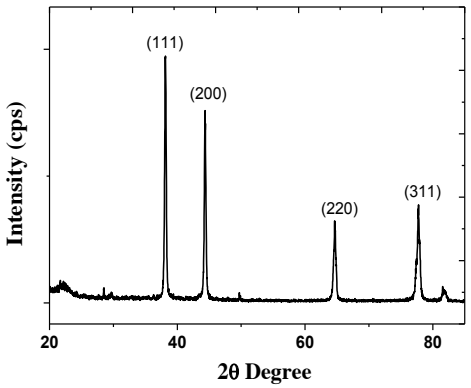

Figure 1

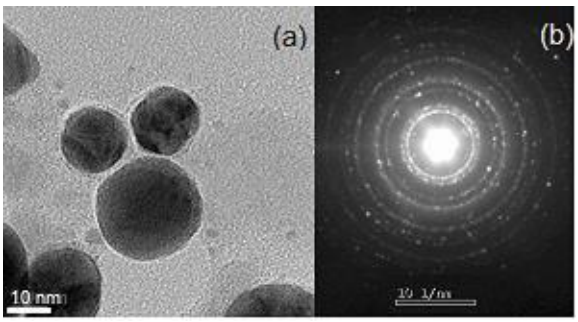

The surface morphology and size of Ag NPs were investigated using High Resolution Transmission Electron Microscopy (HR-TEM). Figure 2 (a) and (b) depicts the TEM and SAED pictures of Ag NPs respectively. As shown in the figure the obtained Ag NPs were predominantly spherical and the size was determined as 15-30 nm. Figure 4 shows the HR-SEM image of purchased P25 TiO_2 NPs. From the image the P25 TiO_2 NPs were spherical in shape with uniform sizes about 30-40 nm.

Figure 2

The J/V characteristics of of DSSCs without and with 1, 2, 3 wt% of Ag NPs were measured. Short-circuit current density (Jsc) and conversion efficiency are shown in Figure 3 (a). As shown in the figure the efficiency of 2 wt% of Ag doped increased from 2.83% to 3.62% (nearly 28% when compared to the non doped sample). Also the Jsc has increased for 2, 3 wt% of Ag doped sample. The FF and V_{oc} were also increased nearly 7.2% and 12.1% respectively for 2 wt% compared to the non doped sample as shown in the Figure 3 (b).

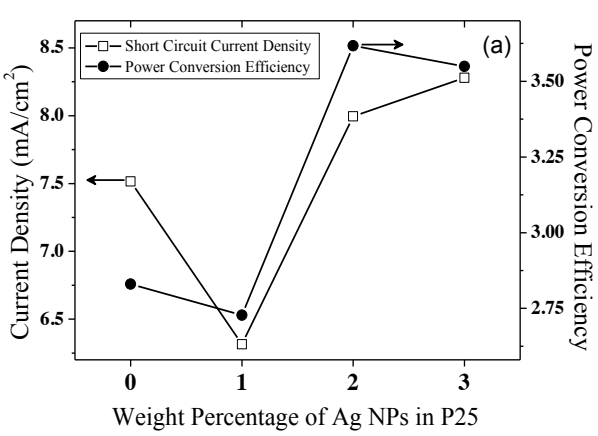

Figure 3 (a)

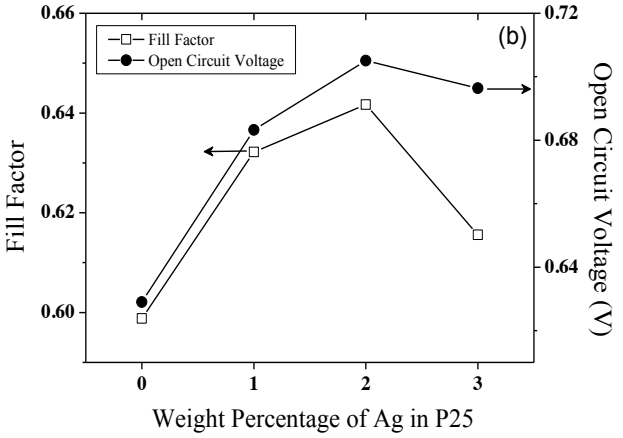

Figure 3 (b)

Conclusions: In this study, the Ag NPs have been prepared by green method and DSSCs were fabricated with different wt% doping of green synthesized Ag NPs in TiO_2. The 2 wt% of Ag doping in TiO_2 significantly increased the efficiency of DSSC around 28% due to the Plasmon effect. The FF and V_{oc} increased as the doping concentration increased up to 2 wt% of Ag NPs doping and reached to a maximum of nearly 7.2% and 12.1% for 2 wt% of Ag doped samples respectively when compared to the non-doped sample.

References:

[1]. Oregan, B. and Gratzel, M. (1991) 'A low-cost, high-efficiency solar cell based on dye-sensitized colloidal TiO_2 films', *Nature*, Vol. 353, pp.737–740.

[2]. Yella, A., Lee, H.W., Tsao, H.N., Yi, C., Chandiran, A.K., Nazeeruddin, M.K., Diau, E.W.G., Yeh, C.Y., Zakeeruddin, S.M. and Gratzel, M. (2011) 'Porphyrin-sensitized solar cells with cobalt (II/III)-based redox electrolyte exceed 12 percent efficiency', *Science*, Vol. 334, pp.629–634.

[3]. Chung, I., Lee, B., He, J., Chang, R.P.H. and Kanatzidis, M.G. (2012) 'All-solid-state dye-sensitized solar cells with high efficiency', *Nature*, Vol. 485, pp.486–489.

[4]. Balamurugan, M., Kandasamy, M., Saravanan, S. and Ohtani, N. (2014) 'Synthesis of uniform and high-density silver nanoparticles by using *Peltophorum pterocarpum* plant extract', *Japanese Journal of Applied Physics*, Vol. 53, pp.05FB19.

Advantages and Obstacles of Using Microfluidic Based Immunoassay for the Detection of Cancer Biomarkers from Biofluids

Ruba Khnouf[1*], Dina Karasneh[1], Ahmad Elbetieha[2], & Borhan Aldin Albiss [3]
[1]Department of Biomedical Engineering, Jordan University of Science and Technology, Irbid, Jordan
[2]Department of Applied Biological Sciences, Jordan University of Science and Technology, Irbid, Jordan
[3]Department of Applied Physics, Jordan University of Science and Technology, Irbid, Jordan

Abstract:
Microfluidic devices also known as lab-on-chip devices have been a prime candidate for replacing popular biomarker detection techniques such as Enzyme-Linked- Immunoassays (ELISA) for advantages they provide such as reduced reagent and sample consumption, reduced time required, and reduced cost [1]. In addition, microfluidic devices provide the potential of incorporating more than one process on the same device, one of which is filtration of biofluids such as blood before analyte detection [2]. In this work we present the design optimization process of a lab-on-chip device for the detection of Alphafetoprotein (a liver cancer biomarker) from blood. We have found that the presence of blood reduces the fluorescence signal of the detected protein, we have also favored a blood filtration technique that is dependent on red blood sedimentation rather on flow differences, and finally we were successful at detecting AFP at a limit of detection of 0.03 ng/ml.

Introduction
One of the major advantages of using microfluidic devices in the field of diagnostics, is thier' capability of integrating multiple sample processing steps on the same device providing the promise of biofluids pretreatment such blood purification or urine preconcentration before the detection of the target analyte. However, the complexity of biofluids and especially the presence of red blood cells (RBC) makes the implementation and commercialization of these devices a challenge because of problems such as clotting and assay hindrance.[3]

Many techniques and designs have attempted taking advantage of microfluidic structures and phenomena to separate RBCs from plasma. The techniques included centrifugation in CD on chip device formats , embedding microfliters in the device, using microfluidic phenomena such as the Zweifach-Fung effect which depends on the attraction of RBCs towards the higher flow rate branch at a microscale bifurcation. Finally, RBC sedimentation depending on RBCs' higher sedimentation rates than other blood components including the analyte of interest was used to separate blood components.[4]

On the other hand, the detection of the analyte itself requires a separate mechanism. Methods used for such a purpose range from immunosensors, to impidometric mechaisms and nanosensors. The most prevalent method in microfluidics has been the miniaturized immonobased sensor which requires the binding of the analyte of interest (the antigen) to its specific antibody and the detection of the binding event. [5]

Here we present the design optimization of a microfluidic device that integrates red blood cell filtration with miniaturized immune detection for the detection of Alphafetoprotein – a liver cancer biomarker. Two main blood filtration techniques were investigated mainly using a trench pattern that takes advantage of sedimentation and a device design that takes advantage of the Zweifach-Fung effect, the detection region of the device was fuctionalized with antibodies for the detection of AFP.

Methods:
As described above two different designs were tested for blood filtration, the first design shown in figure 1 a depends on the Zweifach-Fung effect while the second design depends in having a series of trenches within the microfluidic device, with the channel having a 150 µm depth and the trenches a 500 µm and the length of each trench was 1 mm with a 4 mm distance between trenches. (figure 1 b and inset)

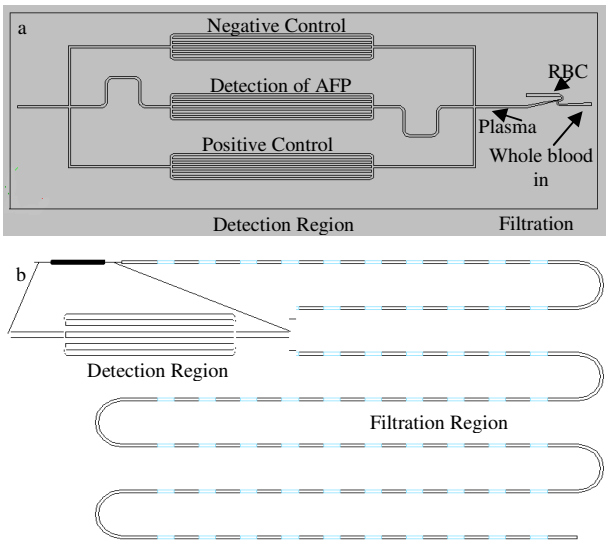

Figure 1: Device designs a) the device design using the ZF effect for blood filtration. b) the device design using trnenches for filtration

* Corresponding author email: rekhnouf@just.edu.jo

The polydimehtyl siloxane (PDMS) devices were fabricated using soft lithography. In short, polymethylmathcrylate (PMMA) molds were fabricated using high-precision milling. Afterwards, the molds were cleaned using ultrasonication and dried using a nitrogen stream, PDMS was mixed with its curing agent at a 10:1 ratio, then the mixture was dessicated for 30 minutes, poured into a mold and cured for 4 hours at 70^{o} C in an isothermal oven.

Antibodies were immobilized in the detection region using APTES and then the antibody was added to the surface and incubated for an hour. To conduct the experiments, sheep's blood was collected in EDTA coated tubes, spiked with fluorescently tagged AFP, then it was diluted in Phosphate Buffer Saline (PBS) at a ration of 1:20, afterwards it was pumped through the devices using a syringe pump and serum was collected to evaluate its purity in some experiments (figure2) or it was passed through the detection area to measure AFP concentration. This was accomplished by measuring fluorescence intensityusing a fluorescence microscope and relating the fluorescence intesntiy to a calibration curve.

Results and Discussion:

Blood filtration was more successful in terms of purity and consistency when using the trenches design (figure 2). This design yielded the best purity when pumping blood through the channel intermittently with pauses to allow RBCs to sediment into the trenches. The drawbacks of using this design were that blood filtration required a longer period of time and a relatively larger blood volume – 40 µl vs 10 µl.

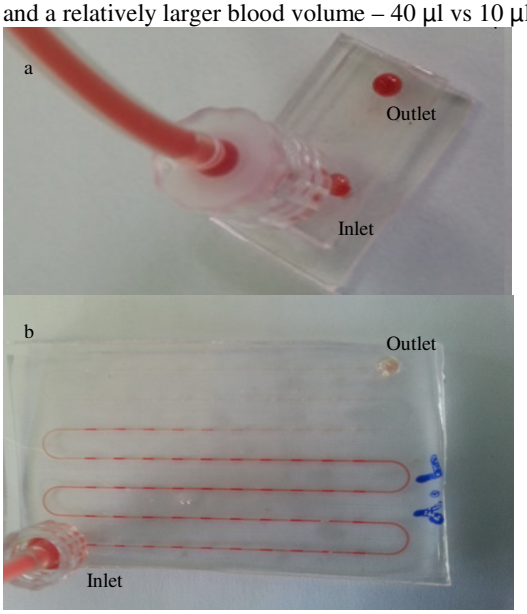

Figure 2: Filter tests. a) the filter based on the ZF effect. b) The filter with trenches.

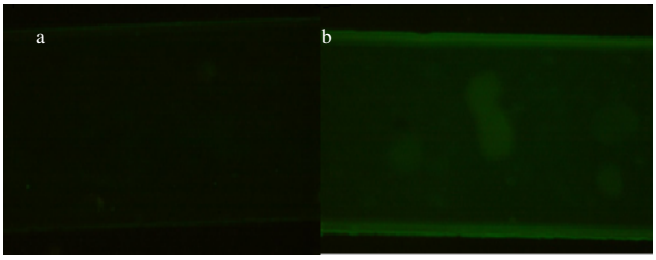

Figure 3: Difference in fluorescence signal for the same AFP concentration (1 ng/ml) with the presence of whole blood (a) and with the use of the filtration device (b)

Alphafetoprotein was detected from plasma with a limit of detection of 0.03 ng/ml, it was observed that the detection's signal was reduced when spiking with the same AFP concentration in whole blood (figure 3), this is probably due to the interference of the blood cells with the fluorescence signal in addition to the destructive effect that RBCs and their components have on proteins highlighting the significance of blood filtration before biomarker detection.

Acknowledgements: This work is supported by the Scientific Research Support Fund (SRSF) in the Hashemite Kingdom of Jordan.

References:

(1) Ng, A. H. C.; Uddayasankar, U.; Wheeler, A. R. *Anal. Bioanal. Chem.* **2010**, *397* (3), 991–1007.

(2) Sollier, E.; Rostaing, H.; Pouteau, P.; Fouillet, Y.; Achard, J.-L. *Sens. Actuators B Chem.* **2009**, *141* (2), 617–624.

(3) Barbosa, A. I.; Castanheira, A. P.; Edwards, A. D.; Reis, N. M. *Lab. Chip* **2014**, *14* (16), 2918–2928.

(4) Kersaudy-Kerhoas, M.; Sollier, E. *Lab. Chip* **2013**, *13* (17), 3323–3346.

(5) Jenko, K. L.; Zhang, Y.; Kostenko, Y.; Fan, Y.; Garcia-Rodriguez, C.; Lou, J.; Marks, J. D.; Varnum, S. M. *Analyst* **2014**, *139* (20), 5093–5102.

Preparation and *in vivo* investigation of Perchlozone©-loaded polylactide nanoparticles using mice model of tuberculosis

L.P. Churilov[1], V.A. Korzhikov[2], O.N. Darashkevich[3], M.D. Poida[1], G.A. Platonova[4], G.V. Papayan[5], E. Sinitsyna[4], T.N. Vinogradova[6], V.J. Utekhin[1] V.A. Zinserling[1,6], P.K. Yablonsky[1,6], T.B. Tennikova[2*]

[1] *St. Petersburg State University, Faculty of Medicine, 21st Line 8a, 199106 St. Petersburg, Russia*

[2] *St. Petersburg State University, Institute of Chemistry, Universitetskii Pr. 26, 198504 Peterhoff, St. Petersburg, Russia*

[3] *Republican Center for Innovative and Technical Creativity, Slavinskogo Ul. 12220086, Minsk, Belarus*

[4] *Institute of Macromolecular Compounds, Russian Academy of Sciences, Bolshoy Pr. 31, 199004, St. Petersburg, Russia*

[5] *St. Petersburg I.P. Pavlov 1st State Medical University, L. Tolstoy Ul. 6-8, 197022 St. Petersburg, Russia*

[6] *St. Petersburg Research Institute of Phthisiopulmonology, Ligovsky Pr. 2-4, 191036 St. Petersburg, Russia*

Perchlozone© (PCZ; Pharmasyntez OJSC, Russia) is a novel antituberculosis drug active in multiple drug resistance, but hepatotoxic [1, 2]. To decrease systemic load and to achieve targeting, the drug was encapsulated into biocompatible polylactic acid nanoparticles and injected into mice with experimental tuberculosis to investigate phenomena of phagocyte mediated delivery. The survival of control animals was compared to those treated by daily oral or single intraperitoneal administration of drug-loaded particles (**Fig. 1**). Some mice were treated by drug-loaded particles modified with polyclonal camel IgGs containing antimycobacterial fraction. The distribution of particles and their accumulation in infectious foci was tracked with double immunofluorescent labeling (Indocyanine green and Platinum(II)-coproporphyrin). Tuberculosis changes, deposition of particles and drug-related toxic changes were registered morphologically. Phagocytes interiorized particles and transported them to foci of tuberculosis in inner organs. Nanoparticle-based drug formulation, especially modified with camel IgGs, demonstrated significantly better survival and lower degree of lung involvement comparatively to other ways of treatment.

In present research it was clearly shown that PCZ-loaded nanoparticles injected intraperitoneally are interiorized by phagocytes and transported into foci of TB inflammation in lungs (**Fig. 1**) and other organs. The application of nanoparticle-based formulation of PCZ, especially when modified with camel IgGs, results in much lower total doses and significantly

better mice survival rate comparatively to oral PCZ treatment. Lower degree of lung involvement in survived mice as compared to intraperitoneal treatment with free PCZ was observed. Phagocyte mediated delivery of antituberculosis drugs to the sites of infection exhibits promising prospects to increase effectiveness of treatment and reduce drug toxicity.

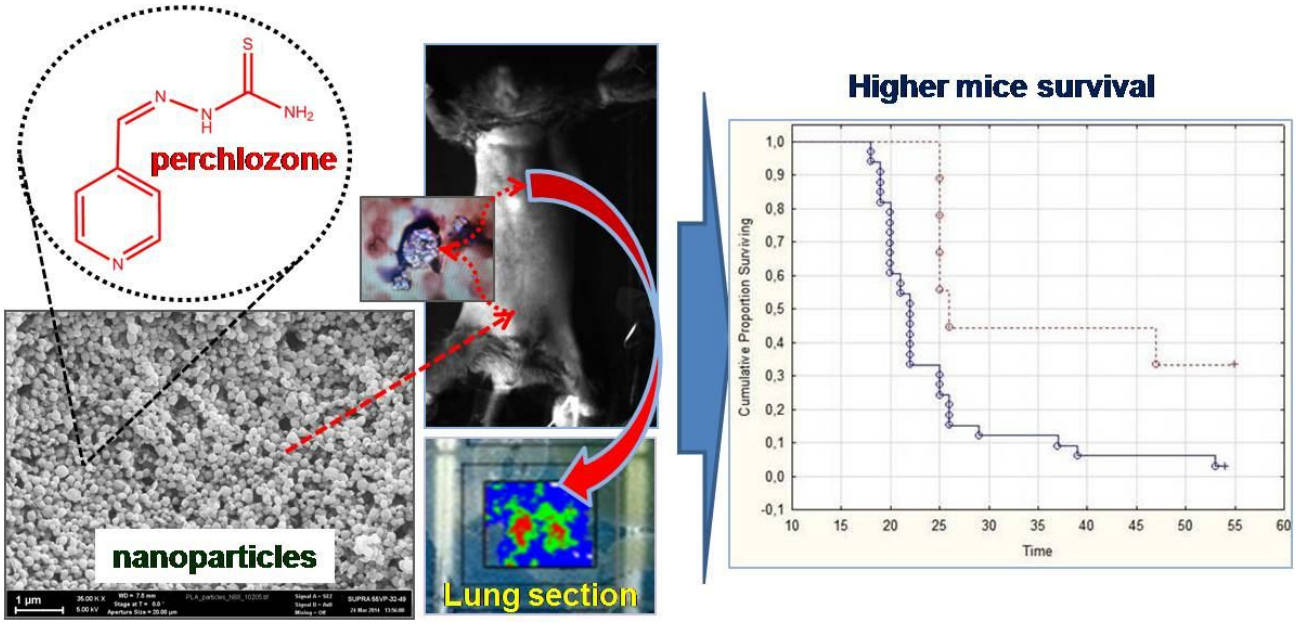

Figure 1. The scheme of experiment: nanoparticles injected intraperitoneally into mice tuberculosis model are effectively captured by phagocytes, which deliver them to the foci in the lung. This was proved by highly intensive fluorescence of platinum(II)-coproporphyrin in lung section. The application of such approach results in the higher mice model survival.

References

[1] Pavlova M, Vinogradova T, Starshinova A, Yablonskii P. et al. Confirmation of preclinical studies data on tioureidoiminomethylpyridinium perchlorate (Perchlozon) in clinic. *Int. J. Curr. Res.* 2015; **7:** 14501-14505.

[2] Chernokhaeva I, Pavlova M, Starshinova A., Yablonskii P. et al. Therapy of pulmonary tuberculosis with multidrug-resistant Mycobacterium tuberculosis using tioureidoiminomethylpyridinium perchlorate (Perchlozon) *Int. J. Techn. Res. & Applicat.* 2015; **3:** 59-62.

Molecular dynamics simulation of glass formation and crystallization in binary PdNi and CuNi alloys.

Muhammad Faruq,[a] Antoine Villesuzanne,[a,b] and Guosheng Shao [a,c]

[a] Institute for Renewable Energy and Environmental Technologies, University of Bolton, Bolton BL35AB, UK

[b] CNRS, ICMCB, University of Bordeaux, F-33600 Pessac, France

[c] UK-China Centre for Multi-functional Nanomaterials, Zhengzhou University, Zhengzhou 450001, People's Republic of China

Abstract

Molecular dynamics (MD) using Quantum Sutton-Chen potentials were used to obtain an atomistic description of melting, glass formation and crystallization processes for Cu, Ni and Pd metals to study the PdNi and CuNi alloys. The thermodynamic and mechanical properties were calculated in the 0-2000K temperature range from the MD trajectories. The formation of amorphous Cu, Ni and Pd and their equimolar alloys by rapid quenching was investigated from MD at constant pressure and temperature (TPN ensemble). The structural properties were analyzed by means of pair distribution functions and volume *vs* temperature, at cooling rates ranging from 40 K/ps to 0.4K/ps. The relation between the cooling rate and glass transition temperature, or crystallization, was investigated. The radial distribution function agrees well with experimental results for amorphous phases. Upon cooling rates in the range from 5K/ps to 0.4K/ps, Cu, Ni, Pd metals and CuNi alloy form a crystalline structure while the PdNi alloy form a glass. A mismatch in atomic size (1.02 vs 1.134 ratio for CuNi and PdNi, respectively) appears to favor the glass formation.

Keywords: Molecular dynamics, Quantum Sutton-Chen potentials,Cu-Ni alloys, Pd-Ni alloys, Quenching rate,Glass formation.

I. Introduction

Inoue proposed three empirical rules to evaluate the glass forming ability (GFA) of an alloy system. One of them is the significant difference in atomic size ratio that gives a good guidance for the bulk metallic glasses (BMG). However, the fundamental theories on the glass formation, are still not clear. A further research on the formation mechanisms of the metallic glasses is still necessary. MD are currently one of the most powerful tools for investigating the glass formation and crystallization processes of liquids. Many studies have been conducted using classical MD (CMD) methods on inorganic glass former materials, such as palladium[1], Copper[2], nickel[3] and binary alloys such as $Ni_{80}P_{20}$,[4] Pd-Si,[5–7] , Pd-Ni,[3,8,9] Cu-Zr[10,11] and Cu-Ni[12–15] systems.

II. Q-SC potentials

Çağin et al.[12] were the first to introduce quantum corrections of SC type potentials by fitting with DFT. Q-SC potential parameters for palladium, copper (Cu) and nickel (Ni) were shown in table 1.

Table 1. Q-SC potential parameters for Pd , Ni and Cu

Element	ε (eV)	a (Å)	n	m	c
Pd-Pd	0.003967	3.9382	12	7	113.14
Ni-Ni	0.0073767	3.5157	10	5	84.745
Cu-Cu	0.0057921	3.6030	10	5	84.843

III. Results and Discussion

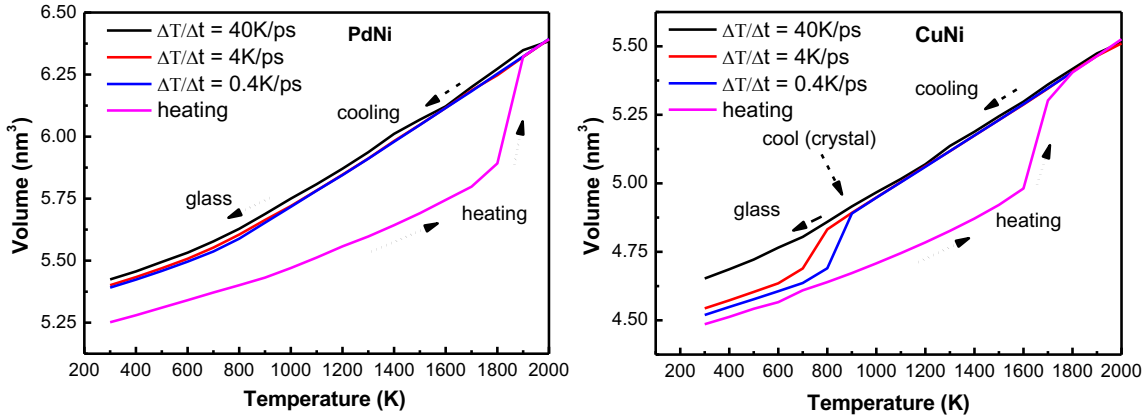

Figure 1: Changes in cell volume during heating and cooling of (a)PdNi and (b) CuNi alloys

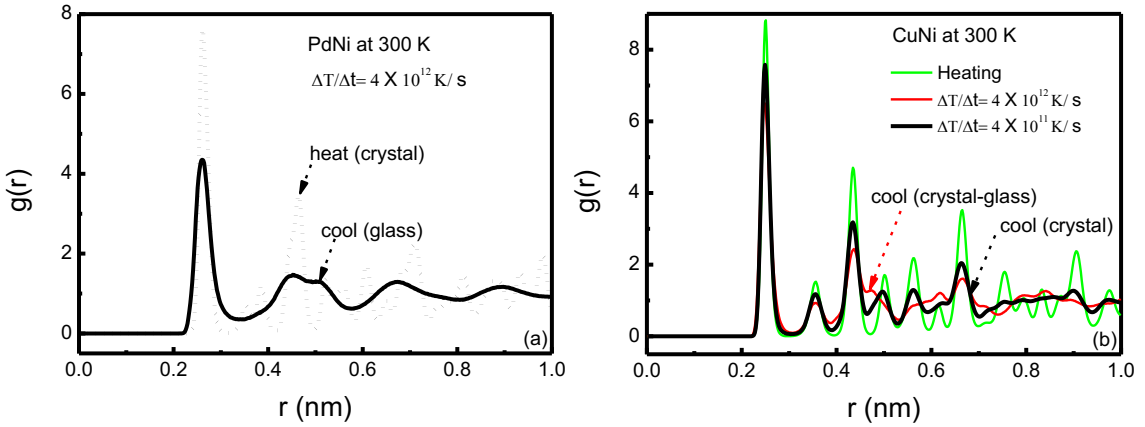

Figure 2:Pair correlation function of a) PdNi and b) CuNi alloys during heating and cooling process at room temperature.

IV. Conclusion

In this work, molecular dynamics simulations applied using Q-SC potentials to investigate the phase transformation in PdNi and CuNi alloys. We observe that PdNi forms a metallic glass for all quenching rates while CuNi form an fcc crystal for all quenching rates. The result shows that changing the radius ratio from 1.02 to 1.134 has a dramatic effect on the propensity for glass formation. The observed glass transition temperature and crystallization temperature depend on the quenching rate.

V. References

1 S. Ö. Kart, M. Tomak, M. Uludo\uGan and T. Ça\uG\in, *Mater. Sci. Eng. A*, 2006, **435**, 736–744.
2 J. Liu, J. Z. Zhao and Z. Q. Hu, *Mater. Sci. Eng. A*, 2007, **452–453**, 103–109.
3 S. Özdemir Kart, M. Tomak, M. Uludoğan and T. Çağın, *J. Non. Cryst. Solids*, 2004, **337**, 101–108.
4 T. A. Weber and F. H. Stillinger, *Phys. Rev. B*, 1985, **31**, 1954.
5 R. Takagi, A. K. Adya and K. Kawamura, *Trans. Japan Inst. Met.*, 1987, **28**, 761–764.
6 T. Ohkubo and Y. Hirotsu, *Mater. Sci. Eng. A*, 1996, **217**, 388–391.
7 P. H. Gaskell, *J. Non. Cryst. Solids*, 1979, **32**, 207–224.
8 L. Qi, H. F. Zhang, Z. Q. Hu and P. K. Liaw, *Phys. Lett. A*, 2004, **327**, 506–511.
9 S. Ö. Kart, M. TOMAK, M. ULUDOGAN and T. CAGIN, *Turkish J. Phys.*, 2006, **30**, 319–327.
10 C. Valencia-Balvín, C. Loyola, J. Osorio-Guillén and G. Gutiérrez, *Phys. B Condens. Matter*, 2010, **405**, 4970–4977.
11 M. I. Mendelev, M. J. Kramer, R. T. Ott and D. J. Sordelet, *Philos. Mag.*, 2009, **89**, 109–126.
12 Y. Qi, T. Çağın, Y. Kimura and W. A. Goddard III, *Phys. Rev. B*, 1999, **59**, 3527.
13 B.-J. Lee and J.-H. Shim, *Calphad*, 2004, **28**, 125–132.
14 B. Onat and S. Durukano\uglu, *J. Phys. Condens. Matter*, 2014, **26**, 35404.
15 J. Teeriniemi, P. Taskinen and K. Laasonen, *Intermetallics*, 2015, **57**, 41–50.

Influence of TiO_2 and Al_2O_3 Addition on Mechanical Properties of Dental Zirconia

Ozlem AGAC[1], Abdullah OZTURK[2], Jongee PARK[1]

[1]Atilim University, Metallurgical and Materials Engineering Department, Incek Ankara 06836, Turkey

[2]Middle East Technical University, Metallurgical and Materials Engineering Department, Ankara 06531, Turkey

Abstract:

Zirconia-based ceramics have generated considerable interest in the dental community as restorative materials due to their high mechanical and chemical properties (Kaya *et al.*, 2012). This study is conducted to produce dental zirconia ceramics by adding titania and alumina as dopants. Mechanical ball milling is used to add the additives into zirconia. The shaped samples are sintered at 1450 °C for 2 hrs. Bulk density and shrinkage was calculated to investigate the effect of these additives, the mechanical property was determined after sintering using the method of Vickers indentation. SEM (Scanning Electron Microscope) was used to analyze of grain size and surface morphology. Also, XRD (X-Ray Diffraction) was operated to examine the crystalline phases in the titania-added zirconia ceramics during heat treatment.

Keywords: zirconia dental ceramics, TiO_2, Al_2O_3, Vicker's hardness, fracture toughness

I. INTRODUCTION

Recently, important progress in dental restoration techniques has been thanks to ceramic materials and 3 mol % yttria stabilised zirconia (Y-TZP) has become popular in the dental community. Pure zirconia (ZrO_2) has three polymorphs: monoclinic, tetragonal and cubic phases. Due to the large volume change associated with the tetragonal to monoclinic phase transformation, pure zirconia has no practical applications for engineering components [1], but it can be stabilised with various additives, among which yttria and cerium are the most useful ones. The tetragonal structure of zirconia can be retained in a metastable phase at room temperature. In particular, yttria-stabilized zirconia is known to be both hard and tough at room temperature [2]; it also possesses a notably high corrosion resistance in biological environments.

Titania (TiO_2) is a ceramic material, which is generally used as a white pigment or catalyst in manufacturing industries. Fine TiO_2 particles with a narrow size distribution are desirable for producing advanced ceramics with enhanced reliability. Titania has promising biological and physico-chemical properties. Metals coated with titania layers show superior biocompatibility [3]. Although TiO_2 is inferior to apatite in terms of bone apposition rate and bone bonding strength, titania is relatively stable in a biological environment and is sufficiently capable of providing long-term bonding. TiO_2 addition also influences sintering behaviour and mechanical properties. It has been reported that small amounts of titania addition reduces sintering temperature and increases the mechanical properties in alumina ceramics [4]. However, the effect of TiO_2 addition on dental zirconia ceramic by mechanical milling has not been explored yet. Alumina ceramics are most widely used as manufacturing components in dental industries because of their low cost and satisfactory mechanical features. Al_2O_3 addition also reduces sintering temperature and increases such properties of dental zirconia. With this in mind, the purpose of this experiment is to investigate the effects of TiO_2 and Al_2O_3 on the mechanical properties of zirconia.

II. EXPERIMENTAL PROCEDURE

A. Powder preparation and sintering

The starting powder was 3mol% yttria stabilized tetragonal ZrO_2 (3Y-Z, AMS) with an average particle size of 150 nm. TiO_2 (P-25, Degussa) and Al_2O_3 (Merck) were used as received form. Various amount of TiO_2 (0, 0.5, and 1 wt%) and Al_2O_3 (0, 0.5, 1, and 2 wt%) were used as a dopant. Doped zirconia powders were prepared by mechanical ball milling. Each batch of 20 g was wet-milled in a zirconia jar at 500 rpm for 3 hours. The prepared powders were then dried and uniaxially pressed under 23 MPa in order to

achieve the disk-shaped compacts of 10 mm in diameter and 4 mm in thickness. Later, all disks were pressureless sintered at 1450ºC at a heating rate of 5ºC/min for 2 hours. The densities were determined using the Archimedes' Method with distilled water as the immersion medium. The microstructural morphology of surface was observed by SEM. An X-Ray diffractometer with the Cu Kα radiation was also used to examine the change throughout the crystalline phases.

B. Hardness and toughness measurements

Hardness was measured using Vicker's indentation method by pressing Vicker's indenter into the test specimen to generate cracks around the indentation. The loading condition was 10 kg 10 sec. and the diagonals of the indented area and the length of the cracks were measured by optical microscopy. Fracture toughness was calculating by using Evans y Charles equation as below;

$$K_c = 0{,}16(\frac{c}{a})^{-1{,}5} Ha^{1/2}$$

where K_c is the fracture toughness (MPa.m$^{1/2}$), H is the Vicker's hardness (MPa), c is the average length of the cracks obtained in the tips of the Vicker's marks (microns), and *a* is the half average length of the diagonal of the Vicker's marks (microns).

III. RESULTS & DISCUSSIONS

Table I shows the densification behavior of various zirconia ceramics containing different amounts of TiO_2 and Al_2O_3. It can be seen that the addition of TiO_2 has been effective in lowering the sintering temperature, even though the density increased with increasing sintering temperature. The density of the 0 wt%TiO_2 is 5.91 g/cm^3 at 1450°C while the 0.5 wt% TiO_2 added zirconia has 5.88 g/cm^3 at the same sintering temperature. However, as the amount of addition is increased up to 1.0 wt%, the densities decrease with increasing the percentage of titania. Al_2O_3 shows similar density behaviour as titania added zirconia while that amount of alumina addition increases upto 2.0 wt%, densities decreased with increasing of sintering

The XRD patterns of each sample sintered at 1450 °C for 2 h with different TiO_2 and Al_2O_3 contents are shown in Fig.2. All peaks possess the characteristics of tetragonal zirconia structure. The addition of titania and alumina up to 1.0 wt % and 2.0 wt% didn't affect the phase separation of zirconia.

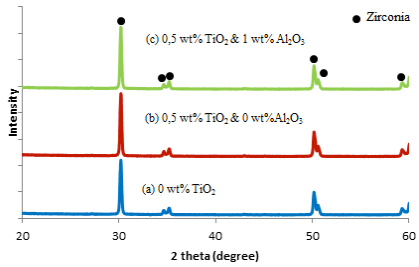

Fig.2: X-ray diffraction pattern of zirconia sintered at 1450 °C with various titania and alumina contents.

IV. CONCLUSION

Within the limitation of this study, the following conclusions can be made:

1. TiO_2 and Al_2O_3 containing dental zirconia ceramics were successfully prepared by mechanical milling, and the effects of titania & alumina contents were investigated as to density, hardness, and fracture toughness.
2. TiO_2 and Al_2O_3 addition enhanced the mechanical properties of zirconia. Maximum hardness and toughness were seen at 0.5 wt% TiO_2 at 1450ºC. Adding titania or alumina decreases the density, but it increases fracture toughness and hardness. 1 wt% Al_2O_3 and 0,5 wt% TiO_2 marks the highest mechanical properties in dental zirconia.

REFERENCES

[1]. T. Miyazaki, T. Nakamura, H. Matsumura, S. Ban, T. Kobayashi, "Current status of zirconia restoration", *J. Prosthod. Res.*, vol. 57, pp: 236-261, October 2013.

[2]. P. Kohorst, L. Borchers, J. Strempel, M. Stiesch, T. Hassel, F.-W. Bach, C. Hubsch, "Low-temperature degradation of different zirconia ceramics for dental applications", *Acta Biomater*, vol. 8, pp: 1213-1220, March 2012.

[3]. P. Amaravathy, S. Sathyanarayanan, S. Sowndarya, N. Rajendran "Bioactive HA/TiO_2 coating on magnesium alloy for biomedical applications", *Ceram. Int.,* vol. 40, pp: 6617-6630, June 2014.

[4]. C.-J. Wang, C.-Y Huang, "Effect of TiO_2 addition on the sintering behavior, hardness and fracture toughness of an ultrafine alumina", *Mater. Sci. Eng. A*, vol. 492, pp: 306-310, September 2008.

temperature. However, Al_2O_3 addition is better for increasing the mechanical properties of zirconia. When the mechanical properties are compared as to the alumina contents, 0.5 wt%TiO_2 & 1 wt% Al_2O_3 is shown the maximum hardness and toughness values at 1360±9 and 5.32±0.20, respectively.

Table I: Density, hardness, and toughness values of zirconia with different titania and alumina content.

Sample	**Density (g/cm^3)**	**Hardness (H_v)**	**Toughness ($MPam^{1/2}$)**
0 wt% TiO_2	5.91	1220±4	4.55±0.40
0.5 wt% TiO_2	5.88	1331±22	4.74±0.30
1 wt% TiO_2	5.79	1215±11	4.63±0.25
0.5 wt% TiO_2 & 0.5 wt% Al_2O_3	5.85	1339±5	4.96±0.24
0.5 wt% TiO_2 & 1 wt% Al_2O_3	5.81	1360±9	5.32±0.20
0.5 wt% TiO_2 & 2 wt% Al_2O_3	5.71	1296±3	4.61±0.05

Fig.1 shows the SEM micrograph of the fractured surface of the zirconia with 0.5, wt% TiO_2 were sintered at 1450 °C for 2 h. Other doped specimens have submicro-sized grains; however, the 0.5 wt% titania-added zirconia sample showed relatively clear grain shape and boundary.

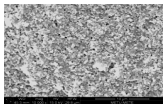

Fig.1: SEM micrograph of the fractured surface of 0.5wt% TiO_2

Textured fabrication of Cadmium sulphide (CdS)/ Cadmium telluride (CdTe) thin film Photovoltaic (PV) cell with back contacts using electron beam lithography

Murugaiya Sridar Ilango[1, 2], Sheela K Ramasesha[1,*]
[1]Indian Institute of Science, Divecha Centre for Climate Change, Bangalore, Karnataka, India
*sheela@caos.iisc.ernet.in

Abstract

Textured fabrication of CdS/CdTe thin film PV with back contacts is fabricated. Thin film materials are deposited using sputter deposition process. n-CdS and p-CdTe are having bandgap of 2.44 and 1.45 eV respectively, which is measured using UV-visible spectroscopy. The metallic contact used for CdS/CdTe is gold (Au). The sample after deposition of CdS/CdTe is annealed at 430° C for 1 min. This paper aims about bringing a novel design to place both the front and rear contacts at the bottom. The physical and optical properties of the sputter

Introduction

CdTe based thin film solar cells possess high optical absorption coefficient (5×10^5 cm^{-1}) with a direct band gap of 1.45 eV [1]. n-CdS is used as the widow layer traditionally for most of the CdTe solar cell applications. The bandgap of CdS thin film is 2.4 eV [2].

Nanostructuring of silicon has been the topic of extensive research in solar cell application because of its low reflectance and enhanced light trapping technique [3]. Nanotextured solar cells exhibited relatively high power conversion efficiency, short circuit current, open circuit voltage and power outputs [4] [5]. Along with the texturing of junction area, the concept of back contact is taken into interpretation. As the front contact in a solar cell transmits only 50% of the solar radiation [6], back contact research started after the publication of R.J Schwartz in 1975 as a substitute for cells which has front and rear contacts.

In this paper we present the studies on the sputter deposited CdS/CdTe thin film heterojunction. In addition, a novel design for assigning the front and rear contacts at the bottom of the solar cell is investigated. Texturing of nanowall structure on the substrate is completed using e-beam lithography technique. Hence by texturing, the surface area of the solar cell increases which in turn allows more absorption of photons.

Experimental:

Figure 1 shows the complete experimental process flow for fabrication textured PV using e-beam lithography.

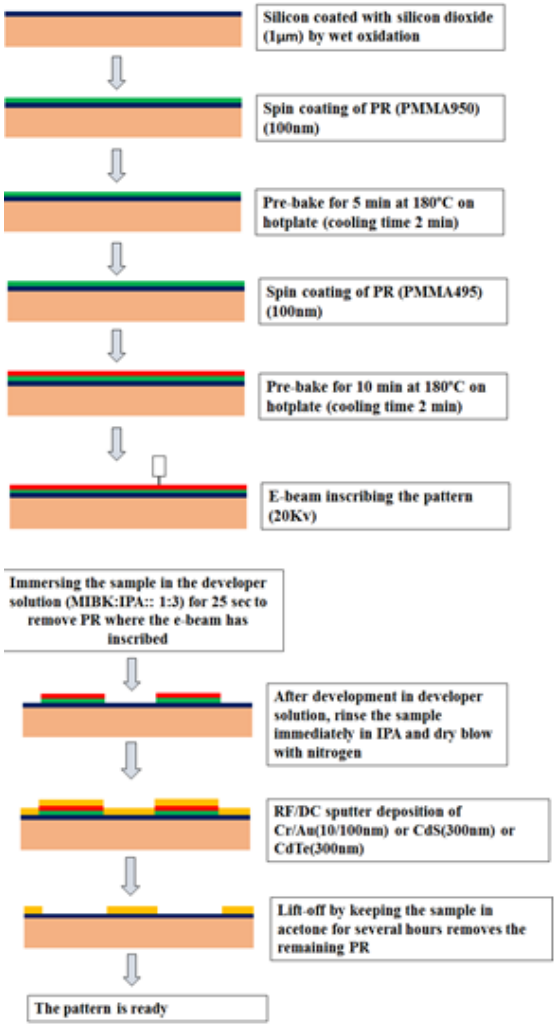

Figure 1: Schematic representation of process flow for fabrication of textured thin film PV.

Results and discussion

For a planar cell which has CdTe on top of CdS, the area in this case will be length (60μm) multiplied with the breadth (50μm). The total area is calculated

as 3 mm^2. Let us calculate in 3D approach, nanowall breath '50 µm', displace gap of '200 nm', height of the wall '200 nm' and length of each wall is '100nm'. The total area of nanotextured cell is 5 mm^2. It is evident from the calculation that there is a 66.67 % increase in the surface area by texturing the surface. The grain size of CdS/CdTe are in the range of 50-70 nm. Figure 2 shows the height and width of the fabricated nanowall.

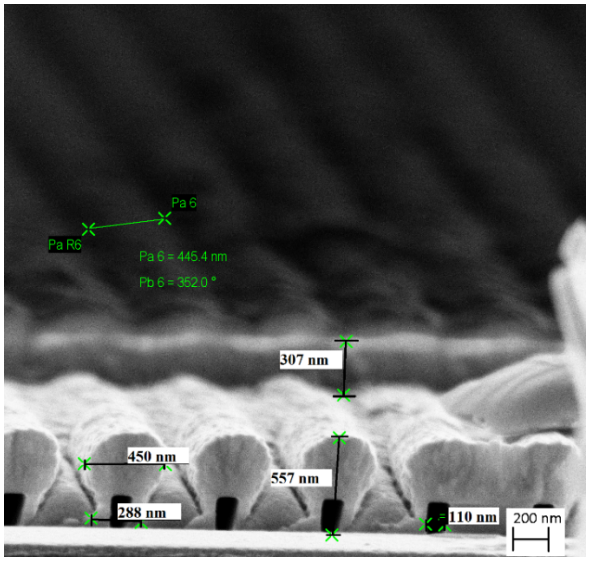

Figure 2: Correctional FE-SEM image of CdS/CdTe nanowall structure

CdTe sputtered and annealed (in air) sample is showing the XRD peaks conforming the hexagonal CdTe structure (JCPDS file No. 00-019-0193). The other XRD peaks are from orthorhombic CdS structures (JCPDS file No. 47-1179).

The surface roughness (Ra) seems to be similar on both the CdS and CdTe thin films which is measured using non-contact optical profiler. Ra for CdS and CdTe are ± 12 and ± 10 nm respectively.

Optical Bandgap:

Absorbance and bandgap are related by the equation,

$$(\alpha h\nu)^2 = A(h\nu - E_{gap}) \qquad (1)$$

Where α is the absorption coefficient as derived by Beer-Lambert's law ($\alpha = \frac{2.303 \times Abs(\lambda)}{d}$), where Abs and d are film absorbance and film thickness respectively. A, E_{gap}, hν are the constant, bandgap of the thin film material, incident photon energy respectively. Value of n in this case of CdS/CdTe thin films the transition is direct hence the value of n is kept as 0.5. The optical bandgaps are observed to be 1.40 and 2.44 eV for CdTe and CdS respectively.

Conclusion:

The novel design of placing both the front and rear metallic contacts at the bottom is fabricated using e-beam lithography. SEM images verified dense and uniform grain growth with grain size of 50-70 nm for CdS and CdTe films. XRD results showed orthorhombic and hexagonal crystal orientation for CdS and CdTe respectively. Non-contact optical profiler measured the surface roughness of CdS and CdTe to be ± 12 and ± 10 nm respectively. With the help of UV-visible spectrometer the optical bandgap of the thin films are calculated as 2.44 and 1.4 eV. Thus by further optimising the post deposition treatments, the efficiency of CdTe solar cell can be raised.

References

[1] A. Morales-Acevedo, "Can we improve the record efficiency of CdS/CdTe solar cells?," *Solar Energy Materials & Solar cells,* vol. 90, no. 15, pp. 2213-2220, 2006.

[2] I. O. Oladeji, L. Chow, C. S. Ferekides, V. Viswanathan and Z. Zhao, "Metal/CdTe/CdS/Cd 1~x Zn x S/TCO/glass: A new CdTe thin film solar cell structure," vol. 61, pp. 203-211, 2000.

[3] P. Oelhafen and A. Schuler, "Nanostructured materials for solar energy conversion," *Solar Energy,* vol. 79, pp. 110-121, 2005.

[4] J. D. Beach and B. E. McCandless, "Materials Challenges for CdTe and CuInSe2 Photovoltaics," *MRS bulletin,* vol. 32, no. 3, pp. 225-229, 2007.

[5] A. K. Srivastava, R. S. Singh, K. E. Sampson, V. P. Singh and R. V. Ramanujan, "Templated Assembly of Magnetic Cobalt Nanowire Arrays," *The Minerals, Metals & Materials Society and ASM International,* vol. 38, no. 4, pp. 717-724, 2007.

[6] Z. Fan, H. Razavi, J.-w. Do, A. Moriwaki, O. Ergen, Y.-L. Chueh, P. W. Leu, J. C. Ho, T. Takahashi, L. A. Reichertz, G. F. Brown, S. Neale, K. Yu, M. Wu, J. Wu, J. W. Ager and A. Javey, "Three dimensional nanopillar array photovoltaics on low cost and flexible substrates," *Nature Materials,* vol. 8, pp. 648-653, 2009.

Fatigue properties of basalt fibre and carbon nanotube reinforced hybridcomposites

J. Szakács[1,*], L. Mészáros PhD[1,2]
[1] Budapest University of Technology and Economics, Department of Polymer Engineering, Muegyetem rkp. 3., H-1111 Budapest, Hungary
[2] MTA-BME Research Group for Composite Science and Technology, Muegyetem rkp. 3., H-1111 Budapest, Hungary
[*] corresponding author, e-mail: szakacs@pt.bme.hu

Abstract:
More and more researchers think that using an additional third phase might be an effective way to enhance the mechanical performance of a polymer matrix composite or endow it with new properties. This third phase can be another polymer or a reinforcing material, too. In the first case the main goal is often to create a co-continuous phase system and this way the energy consumption during the fracture process could be increased (Turcsán *et al.*, 2014). In the second case where two different reinforcing materials are present usually the aim is to increase the strength and the stiffness of the material (Figure 1.). Beside microfibres nanoparticles are also widely used as secondary reinforcing materials like nanoclays, carbon nanotubes and graphene.
Carbon nanotubes have unique electrical, thermal and mechanical properties. These nanoparticles have another great property what is the extremely high aspect ratio.

Figure 1. Figure illustrating the base concept of hybrid composites in case of well dispersed nanoparticles (blue cylindrical body as fibres and yellow disks as particles)

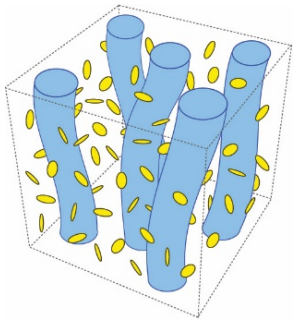

In one of our previous study (Mészáros *et al*, 2013) positive effect of the nanoparticles on the polymers elasticity was presented. It was showed that the presence of graphene or carbon nanotube efficiently can decrease the residual deformation of hybrid composites after different tensile loads. This behaviour refers to these materials could also have higher fatigue life.
However the positive effect of fibre reinforcement on the fatigue properties are well known and deeply investigated but the fatigue properties of hybrid reinforced composites are not revealed yet. There are only a few studies that displays the positive effects of the hybridization. Grimmer *et al* (2010) investigated fatigue life of carbon nanotube and glass fibre reinforced epoxy matrix hybrid composites. The presence of a relatively low amount of carbon nanotube reduced the cyclic delamination and crack propagation in the material significantly. This effect was more remarkable at lower levels of cyclic stress.
In this study carbon nanotube containing basalt fibre reinforced polyamide 6 matrix hybrid composites were produced and their quasi-static and fatigue behaviour were investigated.

Materials and methods

Materials

Schulamid 6 MV 13 type polyamide 6 (PA 6) from A. Schulman GmbH (Germany) was used as matrix. For micro-sized reinforcement, BCS KV12 type basalt fibre (BF) from Kamenny Vek Ltd (Russia) was applied. Nanocyl NC 7000 multiwalled carbon nanotube (MWCNT) supplied by Nanocyl s.a. (Belgium) were used as nano-sized reinforcement.

Sample preparation

For the composites, 30 wt% BF and different amount of carbon nanotubes (0.25; 0.50; 0.75 1.00 wt%) were used. The dried PA 6 granulates (80°C; 4 hours) were mechanically mixed with the reinforcing materials then extruded and granulated. For continuous melt mixing a Labtech Scientific type twin screw extruder (L/D=44; D=26 mm) was used. The screw speed was 12 $^{1}/_{min}$ and the extrusion temperature was 250°C. Dumbbell type specimens (4x10 mm of cross section) were injection moulded on an Aurburg Allrounder Advance 370S 700-290 injection moulding machine, the process temperature was 275°C and the temperature of mould was 80°C. Before the injection moulding the materials were dried at 80°C for 4 hours, too.

Characterization methods

Before the mechanical tests, the specimens were conditioned at 50% relative humidity and 25°C for a week. Tensile tests were performed on a Zwick Z020 universal testing machine according to EN ISO 527. The crosshead speed was 5 mm/min during tensile tests.
Fatigue tests were carried out on an Instron 8872 hydraulic tensile testing machine equipped by Instron 2742-301 type hydraulic grips. The load-controlled fatigue tests were performed under tension-tension load with sinusoidal waveform. The frequency was 2 Hz and the load factor was R=0.1 (R=maximum stress/ minimum stress). The test lasted until the specimen break or the necking started. The elongations for

the cyclic creep curves was registered during the fatigue test at the median of the load in every cycle.

Results and discussion

The basalt fibre notably increased the tensile strength and Young's moduli of the PA 6 as it was excepted. The presence of nanotubes did not change the tensile strength significantly, howwever in case of lower nanoparticle contents moderate increment can be observed (table 1.). The same tendency was observed for the Young's moduli.

Table 1. Mechanical porperties of BF reinforced and hybrid composites (the numbers in material name shows quantity of reinforcers in wt%)

Materials	Tensile strength [MPa]	Young's moduli [GPa]
PA6	68 ± 0.7	2.7 ± 0.2
PA6 / 30BF	135 ± 1.3	6.2 ± 0.3
PA6 / 30BF / 0.25CNT	136 ± 1.3	6.2 ± 0.1
PA6 / 30BF / 0.5CNT	137 ± 1.1	5.8 ± 0.1
PA6 / 30BF / 0.75CNT	135 ± 2.0	5.7 ± 0.3
PA6 / 30BF / 1CNT	131 ± 1.5	5.2 ± 0.2

To determine the fatigue test loads high speed quasi-static tensile tests were carried out (200 mm/min). The applied loads for fatigue tests are shown in Table 2.

2. Table. The applied forces during fatigue tests

	Fmax 90% [N]	Fmax 80% [N]	Fmax 70% [N]
Load	5580	4960	4340

At high loads the number of cycles connected to fracture were nearly the same for each composites (Figure 2.). At lower loads the effect of MWCNT can observed already, morover 0.5 wt% MWCNT content made a slightly increasment in fatigue life of hybrid-composite. At higher MWCNT contents the lower fatigue lifes were observed for the hybrid composites. At higher MWCNT content the Young's moduli were lower, that means the deformation during the fatigue test was higher at the same loads. This higher deformation may have increased the disspated heat in every cycle, that lead to fater fracture process.

Figure 2. Stress-Number of cycles curves of basalt fibre reinforced composites and hybrid composites.

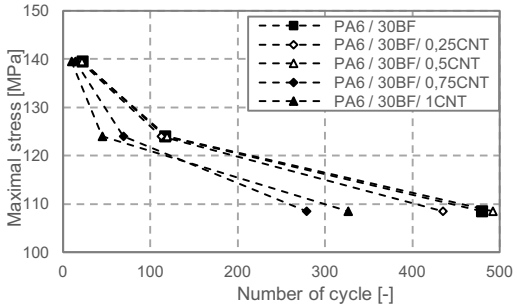

During the fatigue tests the cyclic creeping was measured, too. The phenomena is similar to the creeping behavior in case of static loads and the curves are the affinitive to each other. The creeping behavior of low CNT content materials were faintly changed (figure 3.). Hybrid composite with 0.5 wt% MWCNT was slightly decreased the deformation at higher cyclic numbers, the curve has lover slope. That means the MWCNT may decreased the residual deformation of the composie.

Figure 3. cyclic creep curves of composites during fatigue test

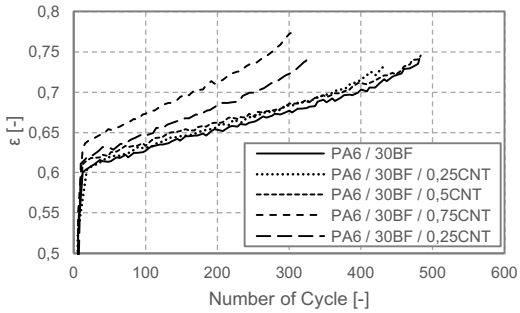

Conclusion

In this study polyamide matrix basalt and carbon nanotube reinforced hybrid composites were mechannicaly investigated. The tensile strength of the composites were not changed significantly at low MWCNT contents but higher nanoparticle contents resulted lower mechanical properties compared to the just basalt fibre containing one. The 0.5 wt% MWCNT containing hybrid seams to be good choice because the strength and moduli increased and it has positive effect on the fatigue properties.

Keywords: nanoparticles, carbon nanotube, polyamide, fatigue, hybrid composite

References:

Turcsán, T., Mészáros, L. (2014), Development and mechanical properties of carbon fibre reinforced EP/VE hybrid composite systems, *Periodica Polytechnica,* 58, 127-133.

Mészáros, L., Szakács, J. (2013), Elastic recovery at graphene reinforced PA 6 nanocomposites. *5th International Nanocon Conference*, Brno, Czech Republic, pp. 1-5. Paper nr. 1955

Grimmer, C. S., Dharan, C. K. H. (2010), Enhancement of delamination fatigue resistance in carbon nanotube reinforced, *Composites Science and Technology*, 70, 901-908.

Acknowlwdgement

This research was realized in the frames of TÁMOP 4.2.4.A/1-11-1-2012-0001 „National Excellence Program – Elaborating and operating an inland student and researcher personal support system" The project was subsidized by the European Union and co-financed by the European Social Fund. This research was also supported by the Hungarian Research Fund (OTKA PD105564).

New Synthesis of Cobalt Nanoparticles With Tunable Size in Ionic Liquids

Bishoy Morcos,[1,2,*] P.-H. Haumesser,[2] C. C. Santini[1]
[1] Université de Lyon, CNRS-UMR 5265, 43 Bd du 11 Novembre 1918, 69616, Villeurbanne Cedex, France.
[2] CEA–LETI-Minatec Campus, 17 rue des Martyrs, 38054 Grenoble Cedex 9, France.
bishoy.morcos@cea.fr

Abstract: Progress in the comprehension in the formation of metallic nanoparticles (NPs) is central due to their great potential in the development of new and innovative materials for microelectronics, data storage and magnetic fluids. Indeed; the controlled synthesis of metallic nanoparticles (NPs) in the range of 1 to 10 nm is still an on-going challenge, as is the understanding of their stabilization and agglomeration. Unlike traditional solvents, ionic liquids (ILs) can be used to generate metallic NPs and stabilize them in the absence of further additives. Using imidazolium-based ILs, monodisperse zero-valent cobalt nanoparticles (CoNPs) have been successfully synthesized by reduction of the organometallic precursor (1,5-cyclooctadiene) (cyclooctadienyl) cobalt(I), Co(COD)(COE).

Introduction: Nanoparticles exhibiting dimensions less than 10 nm possess unique physicochemical properties inbetween the bulk and molecular states owing to their high surface-to-volume ratio. Such properties vary greatly with small changes in size. CoNPs represent one of the most interesting metallic NPs owing to their magnetic properties and their potential applications in catalysis, data storage, and in the field of medication and diagnosis. They are typically produced using physical methods such as the arc plasma evaporation with a limited NP size control.(Meng, Zhao *et al*. 2012) Chemical methods usually provide accurate control on NP sizes that are very small up to 1 or 2 nm, *e.g*. the CoNP synthesis by chemical reduction of a selected Co organometallic precursor, Co(COD)(COE) in the presence of ligand or polymer or by thermal decomposition of Co carbonyl compounds requiring high temperature.(Chaudret and Philippot 2007, Comesana-Hermo, Estivill *et al*. 2014) In a more straightforward approach, stabilized NPs are directly generated in ionic liquids (ILs) which act both as solvents and as stabilizer.(Gutel, Santini *et al*. 2009) In this work, an insight on the mechanism of formation of CoNPs through the decomposition of Co(COD)(COE) under H_2 in imidazolium IL is presented. On this basis, the experimental conditions are optimized in order to get reproducible small and monodispersed metallic CoNPs.

Experimental section: 1-butyl-3-methylimidazolium bis(trifluoromethane)sulfonimide $C_1C_4ImNTf_2$ was prepared and dried as reported.(Gutel, Santini *et al*. 2009) Co(COD)(COE) (NanoMePS) kept at -30°C in a glove box is used without further purification.
In a typical synthesis of CoNPs, under argon, Co(COD)(COE) (27.9 mg) was dissolved in 2 mL of $C_1C_4ImNTf_2$ using 0.1 mL of dry degased pentane till complete dissolution to give a dark brown solution. The pentane was removed under vacuum for 10 min. The autoclave was pressurized under 2 bars of H_2 then heated up to the reaction temperature. The H_2 pressure was then increased to 3 bars. At the end of the reaction, the volatile by-products were condensed under vacuum and the resulting black suspension was kept at room temperature under argon in a glove box.
Thermogravimetric Analysis (TGA) was performed using a Mettler Toledo TGA DSC1. For the GC-MS measurements, a 20 m CP-PoraBOND Q column was used to separate the products that were then analyzed using a GC-MS equipment (Agilent GC 6850 MS 5975C). The suspensions of NPs in IL were deposited on a TEM grid and analyzed by TEM/HRTEM using a MET JEOL 2100FEF (field effect gun energy filtering) microscope at the "Centre Technologiques des Microstructures", CTμ, Villeurbanne, France.

Results and discussion: As Co(COD)(COE) is thermally unstable, a systematic study of its thermal stability under different atmospheres has been conducted in order to determine the optimal conditions to decompose it into CoNPs.
a) Thermal stability of Co(COD)(COE): Under N_2 atmosphere , TGA results show that the decomposition of Co(COD)(COE) occurs above 60 °C meaning that Co(COD)(COE) could be dissolved in IL at room temperature without significant decomposition. Conversely, the decomposition of solid Co(COD)(COE) under 3 bars of H_2 at 20 °C is complete after 5.5 h only, as revealed by coupled DRIFT- GC-mass analysis. Similar to the (1,5-cyclooctadiene)(1,3,5-cyclooctatriene)ruthenium(0), the main decomposition product is cyclooctane.(Gutel, Santini et al. 2009) However, traces of cyclooctene and pentalene have also been detected.
As in the solid state, the decomposition of a solution of Co(COD)(COE) in $C_1C_4ImNTf_2$ under H_2 affords cyclooctane as main decomposition product together with traces of cyclooctene and pentalene (Fig. 1-a). This indicates that the IL does not perturb the Co(COD)(COE) decomposition mechanism. It should be noted that the amount of cyclooctane corresponding to the total decomposition of Co(COD)(COE) is evolved after 8 h. This duration does not correspond to the sole decomposition, but includes the time needed to vaporize C_8H_{16} (boiling point, 149°C) from the IL.
The Co(COD)(COE) decomposition was consecutively studied under Ar atmosphere (20 min), then under H_2 atmosphere (3 bars). The GC-mass analyses were performed both before and after applying H_2 (Fig. 1-b). Before applying H_2, only unsaturated derivatives - cyclooctene, 1,3-cyclooctadiene ,1,5-cyclooctadiene - were detected. When H_2 is applied, mainly cyclooctane

and small amount of pentalene appear. Concomitantly, the intensity of the peaks of the unsaturated derivatives decreases. The formation of pentalene could result from a series of isomerization reactions of cyclooctadiene under H_2. (Otsuka and Taketomi 1972) The fact that pentalene concentration is still much lower compared to the cyclooctane suggests a slower kinetics of this side reaction as compared to the main H_2 reduction reaction.

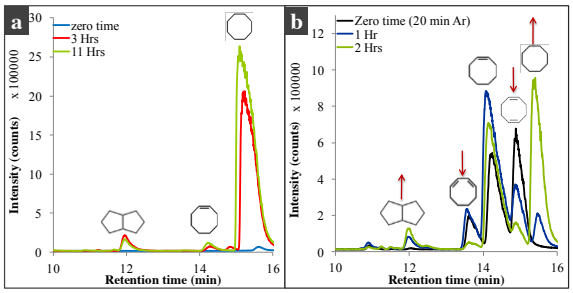

Figure 1: GC-mass chromatograms for the Co(COD)(COE) decomposition in IL, under (a) 3 bars of H_2, (b) Ar then 3 bars H_2

b) Formation of CoNPs from Co(COD)(COE): On the basis of these observations, we investigated the formation of monometallic CoNPs from Co(COD)(COE) in imidazolium-based ILs. The effect of several experimental parameters on CoNPs size, crystal structure and size distribution were studied.

In $C_1C_4ImNTf_2$, the CoNP size increases from 3.6±0.7 nm to 7.0±0.8 nm when the temperature rises from 65 °C to 150 °C in agreement with tendencies reported for RuNPs. This could be attributed to the high degree of self-organization at the nano scale of ILs. (de Caro, Ely *et al*. 1996) HRTEM pictures were analyzed and compared with all metallic, oxide, hydride, carbide, carbonate and oxalate forms of cobalt found in literature. The experimental angle values from different particles in both samples were in excellent agreement with the theoretical values of metallic Co possessing either cubic (Co - 04-017-5578) or hexagonal (Co - 04-007-2107) crystalline structures. The hexagonal form showed higher occurrence when the NPs were prepared at high temperatures (100 °C) compared to those obtained at 65 °C.

Contrary to RuNPs, the mean size of CoNPs was found to be almost identical whatever the chain length of $C_1C_nImNTf_2$ (n = 4; 8; 12; 14) was, (Table 1). Interestingly, regularly interspaced NP arrays were also observed with long chain ILs (n>10). This separating distance was sharply distributed (1.7±0.3 nm for n=14). This suggests that NPs are surrounded by a layer of IL that keeps them apart. Finally, the decomposition of Co(COD)(COE) in $C_1C_4ImNTf_2$, at 100 °C under 3 bars of H_2 was further investigated using different reaction durations. It seems that the reaction is almost completed after 0.5 h since there is no noticeable increase in the size of NPs prepared after 0.5, 4 or 24 hours (4.1±0.4, 4.1±0.5 and 4.1±0.4 nm respectively). This indicates also that the NPs are stable in IL under H_2 atmosphere like Ru NPs, (de Caro, Ely *et al*. 1996) and contrary to Cu NPs. (Arquillière, Haumesser *et al*. 2012) This could be attributed to the possible presence of surface hydride on CoNPs. (de Caro, Ely *et al*. 1996) This point is still under investigation.

Table 1 : CoNPs size as function of alkyl chain length of $C_1C_nImNTf_2$

Alkyl chain length (n)	Mean size (nm)
4	4.1±0.5
8	4.0 ± 0.3
12	4.4 ± 0.3
14	5.3 ± 0.5

Conclusion: We have demonstrated that small and monodisperse CoNPs may be generated under mild conditions by decomposition of Co(COD)(COE) under H_2 in imidazolium derived ionic liquids. Their lower size when the reaction is run at low temperature could be linked to the high degree of self-organization of ILs at the nano-scale. HRTEM pictures prove that these metallic Co possess either cubic or hexagonal crystalline structures with higher occurrence of the later at higher temperatures. The CoNPs mean size does not vary with the IL chain length in $C_1C_nImNTf_2$. Moreover, they are regularly interspaced with the long chain ILs (n>10) suggesting that the NPs are surrounded by a layer of IL keeping them apart. Finally the stability of CoNPs under H_2 atmosphere after 24 h, suggests the presence of surface hydrides as already reported for RuNPs.

References:

Arquillière, P., et al. (2012) Copper nanoparticles generated in situ in imidazolium based ionic liquids, *Microelectronic Engineering* 92 (0): 149-151.

Chaudret, B., et al. (2007) Organometallic Nanoparticles of Metals or Metal Oxides, *Oil & Gas Science and Technology* - Rev. IFP 62 (6): 799-817.

Comesana-Hermo, M., et al (2014) Effect of a Side Reaction Involving Structural Changes of the Surfactants on the Shape Control of Cobalt Nanoparticles, *Langmuir* 30 (15): 4474-4482.

de Caro, D., et al. (1996) Synthesis, Characterization, and Magnetic Studies of Nonagglomerated Zerovalent Iron Particles. Unexpected Size Dependence of the Structure, *Chemistry of Materials* 8 (8): 1987-1991.

Gutel, T., et al. (2009) Organized 3D-alkyl imidazolium ionic liquids could be used to control the size of in situ generated ruthenium nanoparticles?, *Journal of Materials Chemistry* 19 (22): 3624-3631.

Meng, H., et al. (2012) Preparation of cobalt nanoparticles by direct current arc plasma evaporation method, *International Journal of Refractory Metals and Hard Materials* 31(0): 224-229.

Otsuka, S., et al. (1972) Bicyclo[3,3,0]octa-2,4-dien-1-yl(cyclo-octa-1,5-diene)cobalt, *Journal of the Chemical Society, Dalton Transactions*(17): 1879-1882.

Materials aspects of AlSi + SiC Composites Foams Joining

J. Nowacki
Institute of Materials Science and Engineering
West Pomeranian University of Technology, Szczecin, Poland

Abstract: The cellular structure and unique properties of aluminum foams are the reason of their numerous applications and interests in respect of their joining (*Malekjafarian M. et al.*; 2012). The paper includes the characterization of the essence of microstructure, properties and application of aluminum and aluminum composite foams, the limitations, and possibilities of their joining. The aim of the research is the consideration of methods of welding, soldering and gluing AlSi foams and AlSi- SiC composite foams, and the joint structure. The possibility of joining AlSi9 foams and AlSi9-SiC composite foams using selected binding materials was confirmed, and higher tensile strength of the joint than the parent material was also ascertained. Preparing foam edges for joining requires that cutting products should be removed from its surfaces (Abolghasemi F. M. *et al.*; 2012). It is difficult on mickro and nano porous structures due to irregular shape of pores and limited access to them. Contrary to mechanical cleaning, chemical treatment yields satisfactory results. A varying size of soldering gap restricts uniform distribution of the solder and flux within the joint. The capillarity of the gap is much reduced or does not occur in the immediate vicinity of pores. In case of open pores, the flux penetrates into the foam, which means only a non-corrosive flux can be used. Foam porosity causes a substantial use of filler metal and flux as they escape deeper into the foam. Another essential restriction in Al foam soldering is lack of methodologies of testing the geometry of edges prepared for soldering, or that for testing mechanical properties. Besides, criteria for soldered joint acceptance are not available. Apart from problems resulting from foam structure, soldering aluminum is considered as a difficult process due to low melting point, high thermal conductivity and expansion, and a large shrinkage while aluminum cools down. A great affinity of aluminum for oxygen requires that aggressive fluxes be used to remove a layer of oxides Al_2O_3 from the specimen surface before soldering (Nowacki *et al.*; 2015). The process of Al foam flame brazing, due to non-uniform heating of macro-areas of a specimen, causes non-uniform distribution of brazing metal in the pores and foam structure strain due to partial melting of cell walls. This phenomenon does not occur in hot air soldering.

Keywords: Al foams joining, AlSi foams, microstructure and mechanical properties of AlSi foams joints, AlSi -SiC composite foams

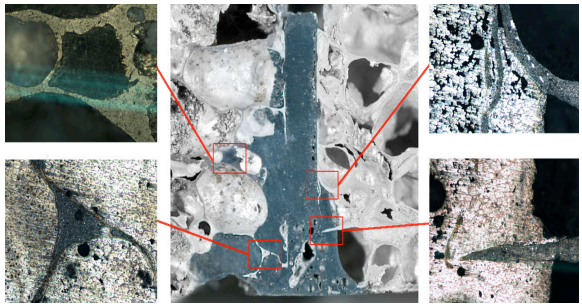

Figure 1: Al foam - Al foam brazed joint, Castolin FCW198 brazing metal, integrated macro- and micro-image

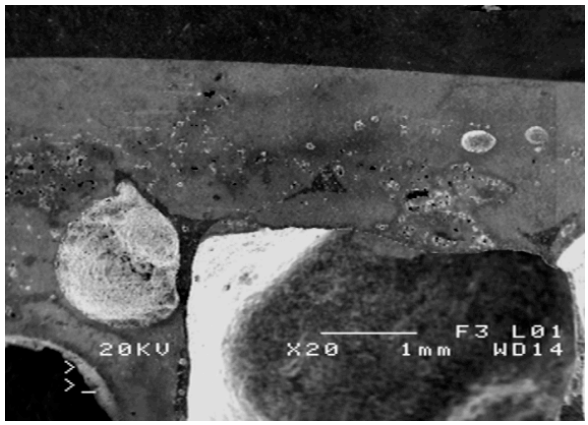

Figure 2: Al foam - Al sheet brazed joint, ZnAl22 brazing metal, macro- and micro- image. The microscopic image reveals melting and mixing of foam cell walls with filler metal and a visible pore not filled with liquid solder.

References:

Malekjafarian M., Sadrnezhaad S.K. (2012) Closed-cell Al alloy composite foams: Production and characterization, *Materials and Design* 42, 8–12

Abolghasemi F. M. Bordatchev E. V., Tutunea-Fatan O. R. (2012) An image-based methodology to establish correlations between porosity and cutting force in micromilling of porous titanium foams, *Int. J. Adv. Manuf. Technol*, 60, 841–851

Nowacki J. Moraniec K. (2015) Evaluation of Methods of Soldering AlSi and AlSi-SiC Particle Composite Al Foams, *J. of Materials Eng. and Perform*. 24, 426-433

Silicon Nanowire as an Effective Absorber for Solar Cell Application: Fabrication and Numerical Simulation

M. K. Hossain, [1,*] B. Salhi, [1,*] A. W. Mukhaimer, [1] and F. A. Al-Sulaiman[1, 2]
[1]Center of Research Excellence in Renewable Energy (CORERE), King Fahd University of Petroleum and Minerals (KFUPM), Dhahran 31261, Dhahran, Kingdom of Saudi Arabia
[2]Departmentof Mechanical Engineering, King Fahd University of Petroleum and Minerals (KFUPM), Dhahran 31261, Dhahran, Kingdom of Saudi Arabia

Abstract: Finite-difference time-domain simulations for single silicon nanowire (Si-NW) on crystalline silicon (c-Si) have been carried out to demonstrate enhanced light absorption and energy flow within the nanometric system. The observation was compared to those of flat c-Si slab only. Light absorption and energy flow distribution confirmed that Si-NW facilitates to confine photon absorption of several orders of enhancement whereas the energy flow is also distributed along the wire itself. To realize the potential of Si-NWs-based thin film solar cell, a simple process was adopted to acquire vertically aligned Si-NWs grown on c-Si wafer. Further topographic characterizations were conducted through scanning electron microscope.

Keywords: Simulation, Fabrication, photovoltaic solar cell, Silicon nanowires.

I. INTRODUCTION

OPTICAL properties of absorbing layer are critical to photovoltaic applications and therefore silicon nanowires (Si-NWs) have received immense attention as efficient light absorbers. Low cost, strong optical absorption, short collection length, efficient light trapping, etc. are the few unique properties amongst others that make Si-NWs extremely attractive and popular for various applications [1-3]. These advantages may substantially reduce the production cost of Si-NW-based solar cells while retaining efficiencies competitive with planar multicrystalline Si solar cells. Several methods have been reported so far to grow vertically aligned Si-NWs, *viz.* chemical vapor deposition (CVD), nanoparticles-assisted etching, reactive-ion etching, etc. [4-5]. It is noteworthy that integration of appropriate preparation process of Si-NWs into well-developed production lines is indispensable for industrial-scale low-cost solar cells production. Here in this investigation, we have reported characteristics of Si-NW on c-Si slab by numerical simulation and focused on key factors such as absorption profile, energy flow distribution, electromagnetic field and generation rate distribution. Due to space constrain, we have limited our discussion within two key observations, such as absorption profile and Poynting vector distribution. Si-NWs were grown vertically on c-Si wafer through a bottom-up technique, nanoparticles-assisted CVD and preliminary characterizations were carried out by scanning electron microscope (SEM).

II. MATERIALS AND METHODOLOGY

Finite different time domain (FDTD) analysis was carried out with a model of Si-NW on c-Si wafer. FDTD package of Lumerical Solution (ver 8.6) was employed to solve Maxwell's equations and further investigations were focused on absorption profile, energy transfer, EM field and exciton generation rate distribution at 740 nm wavelength of solar spectrum. The excitation wavelength was considered as such because of strong irradiation of AM 1.5G solar spectrum at this wavelength as well as being close to the band gap of c-Si and Si-NWs (i.e. 1.7 eV). To grow Si-NWs, silicon (1-1-1 oriented, n-type phosphorus-doped, resistivity < 1 ohm-cm) wafer was used as received. A well-cleansed wafer was immersed in 3:1 concentrated H_2SO_4/30% H_2O_2 for 15 min at 80°C followed by a deposition of thin gold (Au) layer. The specimen was annealed at 700 °C and subsequently exposed to silane at high temperatures in CVD. As-fabricated Si-NWs were characterized by SEM and high resolution SEM. The typical size of as-prepared Si-NWs was as long as few microns length. Depending on Au nanoparticles sizes, as-prepared Si-NWs were found to show a wide range of diameters.

III. RESULTS AND DISCUSSION

Three dimensional (3D) FDTD simulations were used to calculate the absorption profile and Poynting vector along single Si-NW (1.7 µm long, 150 nm diameter) on c-Si slab (1µm thickness with oxide layer of 200 nm) A plane wave with a specific wavelength (i.e. 740 nm) and polarization (transverse-magnetic (TM)) was modeled normally incident to c-Si slab and Si-NW on slab. In FDTD simulation, electromagnetic field ($\vec{E}$, $\vec{H}$) are calculated with Maxwell's equations solver in time domain at each point on the 3D simuation grid.

Due to exceptional light trapping capability, it has been demonstrated that 1% Si material in the form of Si-NWs is enough to provide similar amount of solar absorption absorbed by conventional c-Si-based p-n junction solar cell. Fabry-Perot like absorption mode with regular pattern was observed in simulated ab-

sorption profiles for c-Si slab without Si-NW as shown in Fig. 1 (a). On the contrary, this absorption profile was confined more like Bloch-mode in Si-NW on c-Si slab system as shown in Fig. 1 (c).

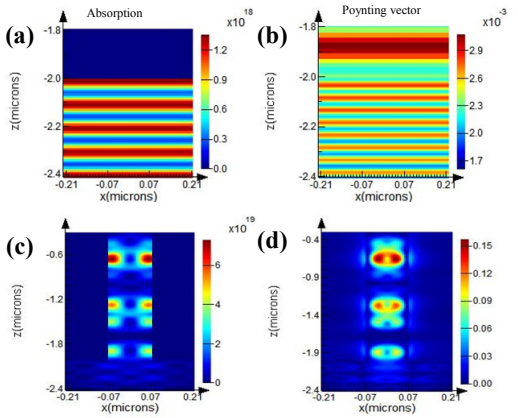

Fig. 1 Absorption and energy profile at 740 nm wavelength. (a) Fabry-Perot mode like distribution in c-Si slab without Si-NW, (b) Poynting energy flow distribution in c-Si slab without Si-NW, (c) confined and enhanced absorption distribution in Si-NW on c-Si slab and (d) confined energy flow all the way down to the bottom of Si-NW.

In absorbing layer, excitons (i.e. free electron-hole pairs) are generated in presence of energy that is usually transferred to by absorbing photons of solar radiation. Hence correlated absorption profile and Poynting power flow distribution at specific wavelength of solar spectrum for an individual Si-NW is very important to define such nanowires-based solar cell performances. Poynting vectors for c-Si slab without Si-NW and with Si-NW are shown in Fig. 1 (b) and Fig. 1 (d) respectively. It was observed that Poynting energy distribution followed the absorption pattern in c-Si slab only whereas energy distribution in Si-NW gets enhanced at the top and decays slowly all the way down to the bottom of the nanowire.

Vertically aligned Si-NWs were fabricated on c-Si wafer through a cost-effective bottom-up process. Details of mechanism and steps are mentioned in experimental section. In brief, the process was consisted of four simple steps, viz. i) ultrathin layer of Au coating on c-Si wafer, ii) sintering to turn the film into Au nanoparticles, ii) CVD to grow Au nanoparticles-assisted Si-NWs and iv) removal of Au nanoparticles. SEM measurements confirmed a variety of lengths (e.g. few microns) and diameters (e.g. 50 to 200 nm) of Si-NWs. Figure 2 shows typical SEM micrographs of as-fabricated Si-NWs in c-Si wafer. Figure 2 (b) represents a magnified view of a small cross-section marked by dotted white square in Fig. 2 (a). It is noteworthy that Si-NWs were grown nicely whereas some of the Au nanoparticles were remained unused as catalyst. In nanoparticles-assisted Si-NWs growth are highly dependent on the size and shape of the seeds (i.e. Au nanoparticles here in this study). It was revealed clearly that different sizes of Au nanoparticles were used as catalyst to grow Si-NWs of various diameter as shown in Fig. 2 (b).

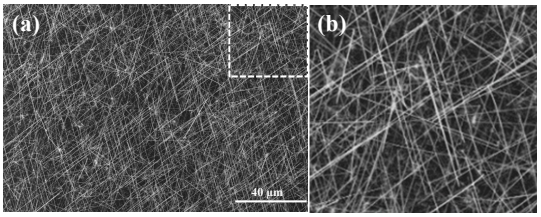

Fig. 2 SEM micrographs. (a) Wide view of as-fabricated Si-NWs on c-Si wafer and (b) Magnified images of the small area marked by white dotted square in Fig. 2a.

IV. CONCLUSION

We had shown through FDTD simulation that nanometric system, such as Si-NWs on c-Si, effectively enhanced absorption and energy distribution with reference to those observed in c-Si slab only. Vertically aligned Si-NWs on c-Si wafer was carried out in a cost-effective bottom-up process. SEM observation confirmed that Au nanoparticles as seeds to grow Si-NWs are indeed key element to optimize nanowires length and diameter. Following the simulated predictions on inherent optical and geometrical properties of such Si-NWs, an optimum design and development of nanowires-based solar cell will be more handy and available. It is evident that such solar cell needs to be efficient enough to compete with traditional c-Si solar cell.

ACKNOWLEDGMENT

Authors are thankful to Center of Research Excellence in Renewable Energy (CoRERE), King Fahd University of Petroleum and Minerals (KFUPM) for the support in this work.

REFERENCES

[1] A. Polman, and H. A. Atwater, “Photonic design principles for ultrahigh-efficiency photovoltaics”, *Nat. Mater.,* vol. 11, pp. 174–177. 2012.

[2] X. Zhao, C. M. Wei, L. Yang, and M. Y. Chou, “Quantum confinement and electronic properties of silicon nanowires”, *Phys. Rev. Lett.*, vol. 92, pp. 236805-1–236805-4, 2004.

[3] P. Krogstrup, H. I. Jorgensen, M. Heiss, O. Demichel, J. V. Holm, M. Aagesen, J. Nygard, and A. F. Morral, “Single-nanowire solar cells beyond the Shockley-Queisser limit”, *Nat. Photonics*, vol. 7, pp. 306–310, 2013.

[4] N. Shin, and M. A. Filler, “Controlling silicon nanowire growth direction via surface chemistry”, *Nano Lett.*, vol. 12, pp. 2865–2870, 2012.

[5] E. Garnett, P. Yang, “Light trapping in silicon nanowire solar cells”, *Nano Letters*, vol. 10, pp. 1082–1087, 2010.

Acid hydrolysis to improve the production of Bacterial Cellulose Nanocrystals

P. Paximada[1], E.A. Dimitrakopoulou[1], C. Fasseas[2], I. Mandala[1]

[1]Agricultural University of Athens, Department of Food Science and Human Nutrition, 75 Iera Odos, 11855, Votanikos, Athens, Greece

[2]Laboratory of Electron Microscopy, Dept. Crop Science, Agricultural University of Athens, Greece

1.Introduction

Cellulose is the most abundant biopolymer on earth, being the major structural component of plants. Although plants are the major sources of cellulose, it is known that certain bacteria also produce cellulose as an extracellular polysaccharite (Chawla et al,2009). BC exhibits many other important properties, such as high water holding capacity, high degree of polymerization and crystallinity and high mechanical strength (Martinez-Sanz et al, 2011 ; Ougiya et al., 1997). For many applications, cellulose fibers must be subjected to acid hydrolysis with strong acids (Martinez Sanz et al, 2011; Bondeson, 2006; Habibi et al, 2010). Hydrolysis of cellulose with strong acids removes disordered or paracrystalline areas of cellulose fibers, leading to the extraction of rod-shaped cellulose nanocrystals (BCNCs) with smaller length and width than the initial fibers (Tingaut et al, 2012). The morphology and properties of the produced BCNCs depends on the initial cellulose morphology and the acid hydrolysis conditions. This work aims at examining various factors that affect cellulose nanocrystals (BCNCs) extraction from bacterial cellulose (BC).

2. Materials and methods

Bacterial cellulose was extracted from *Komagataeibacter sucrofermentans* (DSM 15973) cultivations, using a synthetic medium (Hestrin & Schramm,1954). Cellulose was mixed with deionized water and acid (1M sulphuric or hydrochloric) and incubated in water bath at 40^{o}C for 24h. Pictures of the microstructure of BCNCs were taken using a TEM JEOL 100s. The gravitational stability of suspensions upon storage was measured using a Turbiscan MA 2000 apparatus (FormulAction, Toulouse, France). Rheological measurements of the suspensions were performed on a stress-controlled rheometer (Discovery HR-3, TA Instruments, New Castle, DE, USA) equipped with a concentric cylinders geometry (30mm cup diameter, 28mm bob diameter). Oscillatory measurements were also performed on the BC emulsions.

3. Results and discussion

The morphology of cellulose fibers can be altered when a treatment (i.e. acid hydrolysis) is applied. TEM micrographs showed that hydrolysis leads to decrease in the fibril's length and width. Specifically, BCNCs treated with sulphuric acid exhibit more alterations in their structure (smaller length and width) and they are less bundled than the untreated BC (Fig. 1).

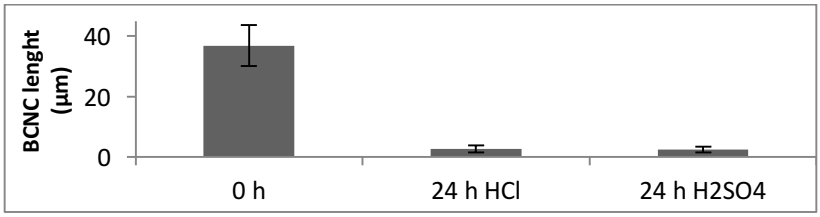

Figure 1: Length of the produced bacterial cellulose nanocrystals.

Phase separation of BCNC suspensions was recorded for 18 days. Results show that the longer the acid treatment, the lower the phase separation is. Furthermore, the lowest phase separation was recorded at 24h hours of treatment with sulphuric acid at 40^{o}C. Viscosity of the BCNC samples is dependent on the type of acid that is used and the lowest viscosity at 24h of treatment was recorded for hydrolysis with HCl at 40^{o}C (Fig 2).

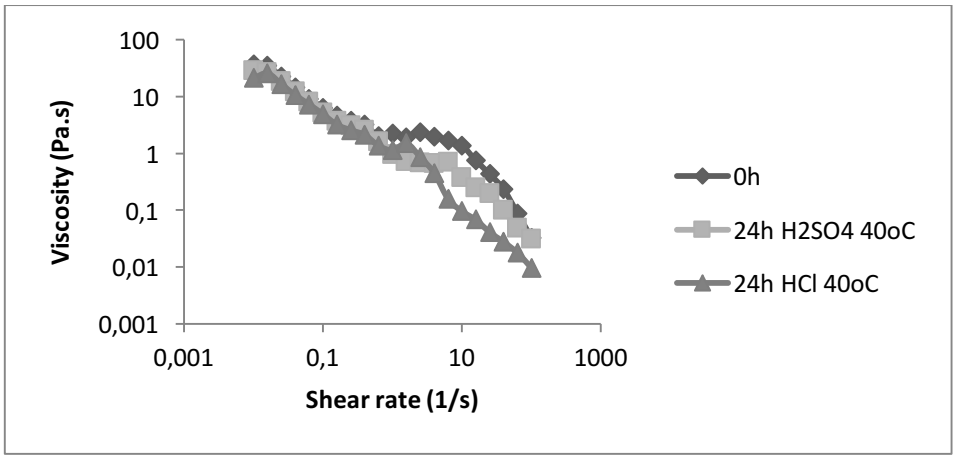

Figure 2: Viscosity of bacterial cellulose treated with different acids

4.Conclusions

Acid hydrolysis leads to bacterial cellulose nanocrystalls with decreased length and width, especially when H_2SO_4 is used. After 24h of treatment, samples exhibit lower phase separation and the lowest was recorded for the samples treated with H_2SO_4. The viscosity profile of all samples showed shear thinning behavior. In conclusion, acid hydrolysis alters the morphology and properties of BC. Especially, treatment with H_2SO_4 for 24h enhances the properties of BC fibrils.

References

1. Bondeson D., Mathew A., Oksman K (2006) Optimization of the isolation of nanocrystals from microcrystalline cellulose by acid hydrolysis, *Cellulose*, 13, p. 171 –180
2. Chawla P.R., Bajaj I. B., Survase S. A., Singhal R.S.: (2009) Fermentative Production of Microbial Cellulose, *Food Technology and Biotechnology*, 47 (2) 107–124
3. Habibi Y., Lucia A.L., Rojas J.O., (2010) Cellulose Nanocrystals: Chemistry, Self-Assembly, and Applications *Chem. Rev. 110, p.* 3479–3500
4. Hestrin, S., & Schramm, M. (1954). Synthesis of cellulose by Acetobacter xylinum. II. Preparation of freeze-dried cells capable of polymerizing glucose to cellulose. *Biochem J, 58*(2), 345-352.
5. Martinez-Sanz M., Lopez-Rubio A., & Lagaron J. M. (2011). Optimization of the nanofabrication by acid hydrolysis of bacterial cellulose nanowhiskers. *Carbohydrate Polymers, 85,* 228-236.
6. Ougiya H., Watanabe K., Morinaga Y., & Yoshinaga F. (1997). Emulsion- stabilizing effect of bacterial cellulose. *Bioscience, Biotechnology and Biochemistry, 61* (9),1541-1545.
7. Tingaut P, Zimmermann T, Sebe G. (2012) Cellulose nanocrystals and microfibrillated cellulose as building blocks for the design of hierarchical functional materials<,Materials Chemistry 22

Modal parameter identification of perforated microplates from output data only

J. Lardiès
Institut FEMTO-ST, DMA, Rue de l'Epitaphe, 2500 Besançon, France

ABSTRACT

In several applications the design of MEMS includes perforated microplates supported by an elastic suspension which can oscillate. To control such oscillations it is necessary to know the modal parameters of the microplate such as eigenfrequencies, damping and stiffness. The purpose of this communication is to identify the vibratory parameters of a perforated microplate from the measure of the microplate displacement only. Dynamic measurements of a perforated microplate are conducted in time domain and a comparison between experimental and analytical results is presented.

Key-Words
MEMS, microplate, oscillating system, time domain, modal parameters, identification, subspace method

1. INTRODUCTION

The design of MEMS includes oscillating elements and components which are often perforated microplates supported by an elastic suspension. The main purpose of perforations is to reduce the damping and spring forces acting in the MEMS due to the fluid flow inside and around the micro structure. The study of the damping caused by surrounding fluid and by the dissipations in the material is very important to predict the dynamic response of the microsystem and to estimate some important parameters such as the quality factor. G. De Pasquale and T. Veijola [1] used numerical strategies for the estimation of the damping force acting on a perforate movable MEMS, using FEM methods with ANSYS. It was shown that ANSYS results contained a systematic error at small perforations and were not usable for large perforations. Our purpose is to identify the modal parameters of a perforated microplate : the eigenfrequency, the damping ratio and the stiffness from the displacement response only of the microstructure.

2. THE SUBSPACE IDENTIFICATION METHOD

The subspace identification method assumes that the dynamic behaviour of a vibrating system can be described by a discrete time state space model [2,3]

$$\boldsymbol{z_{k+1} = A\, z_k + w_k} \qquad \text{state equation} \qquad (1)$$

$$\boldsymbol{y_k = C\, z_k + v_k} \qquad \text{observation equation} \qquad (2)$$

where $\boldsymbol{z_k}$ is the unobserved state vector of dimension n; $\boldsymbol{y_k}$ is the (mx1) vector of observations or measured output vector at discrete time instant k; $\boldsymbol{w_k}$ contains the external non measured force or the excitation which can be a random force, an impulse force, a step force...and $\boldsymbol{v_k}$ is a measurement noise. $\boldsymbol{A}$ is the (nxn) transition matrix describing the dynamics of the system and $\boldsymbol{C}$ is the (mxn) output or observation matrix. The subspace identification problem deals with the determination of the two state space matrices $\boldsymbol{A}$ and $\boldsymbol{C}$ using output-only data $\boldsymbol{y_k}$. The modal parameters of a vibrating system are obtained by applying the eigenvalue decomposition of the transition matrix $\boldsymbol{A}$ [2,3]

$$\boldsymbol{A = \Psi\, \Lambda\, \Psi^{-1}} \qquad (3)$$

where $\boldsymbol{\Lambda} = diag(\lambda_i)$, i=1,2,…,n, is the diagonal matrix containing the complex eigenvalues and $\boldsymbol{\Psi}$ contains the eigenvectors of $\boldsymbol{A}$ as columns. The eigenfrequencies F_i and damping factors ξ_i are obtained from the eigenvalues which are complex conjugate pair

$$F_i = \frac{1}{2\pi\, \Delta t}\sqrt{\frac{[\,ln(\lambda_i\, \lambda_i^{*})\,]^2}{4} + [\,cos^{-1}(\frac{\lambda_i + \lambda_i^{*}}{2\sqrt{\lambda_i\, \lambda_i^{*}}})\,]^2} \qquad (4)$$

$$\xi_i = \sqrt{\frac{[\,ln(\lambda_i\, \lambda_i^{*})\,]^2}{[ln(\lambda_i\, \lambda_i^{*})]^2 + 4[\,cos^{-1}(\frac{\lambda_i + \lambda_i^{*}}{2\sqrt{\lambda_i\, \lambda_i^{*}}})\,]^2}} \qquad (5)$$

with Δt the sampling period of analyzed signals.
Define the ($mpx1$) future data vector as $\boldsymbol{y^{+}_k = [y^T_k, y^T_{k+1}, . . ., y^T_{k+p-1}]^T}$ and the ($mpx1$) past data vector as $\boldsymbol{y^{-}_{k-1} = [y^T_{k-1}, . . ., y^T_{k-p}]^T}$, where the superscript T denotes the transpose operation. The ($mpxmp$) covariance matrix between the future and the past is

$$\boldsymbol{H = E[y^{+}_k\, y^{-T}_k] = \begin{bmatrix} R_1 & R_2 & . & R_p \\ R_2 & R_3 & . & R_{p+1} \\ . & . & . & . \\ R_p & R_{p+1} & . & R_{2p-1} \end{bmatrix}} \qquad (6)$$

where E denotes the expectation operator. $\boldsymbol{H}$ is the block Hankel matrix formed with the (mxm) individual theoretical auto-covariance matrices $\boldsymbol{R_i = E[y_{k+i}\, y^T_k] = CA^{i-1}G}$, with $\boldsymbol{G=E[x_{k+1}\, y^T_k]}$. In practice, the auto-covariance matrices are estimated from N data points [2]. The block Hankel matrix $\boldsymbol{H}$ can be written as

$$\boldsymbol{H = \begin{bmatrix} C \\ CA \\ . \\ CA^{p-1} \end{bmatrix} [G\ AG . . . A^{p-1}G] = O\, K} \qquad (7)$$

By identification we obtain the block observability matrix $\boldsymbol{O}$ and the block controllability matrix $\boldsymbol{K}$

$$O = \begin{bmatrix} C \\ CA \\ . \\ CA^{p-1} \end{bmatrix} \quad \text{and} \quad K = [G \;\; AG \ldots A^{p-1}G \;\;] \quad (8)$$

This last matrix can be written as $K = [K_1 \;\; A^{p-1}G] = [G \;\; K_2]$ where the block matrices K_1 and K_2 are

$$K_1 = [G \;\; AG \ldots A^{p-2}G] \text{ and } K_2 = [AG \ldots A^{p-1}G] \quad (9)$$

K_1 and K_2 are $nxm(p-1)$ matrices obtained by deleting respectively the last and the first block column of the block controllability matrix K. It is easy to show that $K_2 = A\,K_1$ and the transition matrix obtained by the deleted block column of the controllability matrix method can then be calculated via pseudo-inverse $A_K = K_2 K_1^{+}$ .The eigenvalues of the transition matrix A_K can be used to identify the modal parameters and one gets $\lambda(A_K) = \lambda(K_2 K_1^{+})$.

3. MODAL PARAMETER IDENTIFICATION OF A PERFORATED MICROPLATE

The perforated microplate supported by an elastic suspension as shown in Figure 1, and the model used to study the microplate behavior is constituted by the following parameters : the plate mass m concentrated in the center of the plate, the damping coefficient c and the stiffness coefficient k.

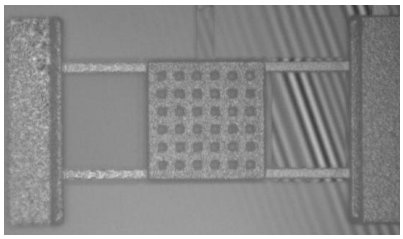

Figure 1. Optical image of the perforated microplate

The dynamic measurements are conducted in time domain by means of a laser vibrometer and Figure 2 shows the time response of the center of the microplate. Only this time response is used in our subspace identification procedure where the sampling frequency is 2 MHz and 3000 time samples are used.

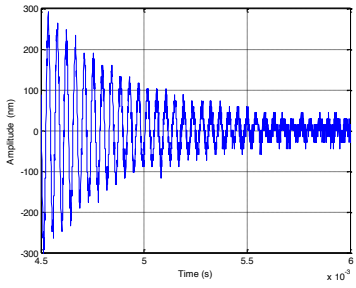

Figure 2. Displacement response of the microplate

The perforated microplate area is $A = 3.127\text{x}10^{-8}$ m^2 and its mass is $m = 3.814\text{x}10^{-9}$ kg. The microplate stiffness is given by $k = m\,(2\,\pi F)^2$ and the damping coefficient is $c = 4\,\pi\, m\, F\, \xi$ where F is the resonance frequency of the perforated microplate and ξ the damping factor. These modal parameters are obtained by an average over the orders of the stabilization diagram [2] on frequency and damping ratio obtained by the subspace approach and presented in Figure 3.

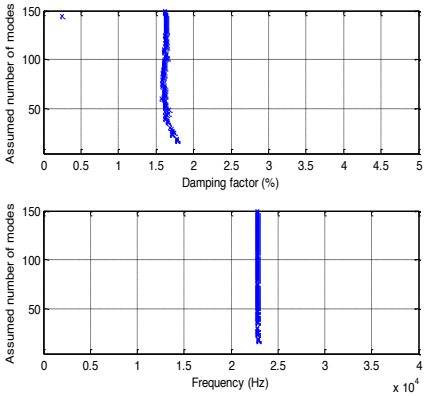

Figure 3.Stabilization diagram on frequency and damping ratio

Table 1 shows the identified microplate parameters and Figure 4 shows a comparison between the measured time response of the perforated microplate and the reconstructed response obtained from the identified modal parameters.

Resonance frequency F	Damping factor ξ	Stiffness coefficient k	Damping coefficient c
22810 Hz	1.62 %	78.33 N.m^{-1}	17.71x10^{-6} N.s.m^{-1}

Table 1. Parameters identification of the perforated microplate

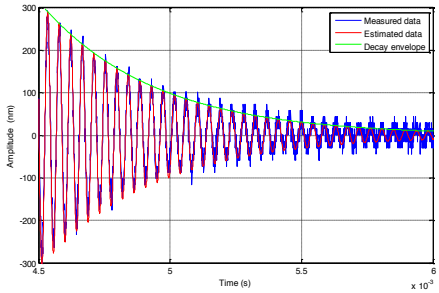

Figure 4. Comparison between the measured (in blue) and the reconstituted (in red) displacement response

4. CONCLUSION

The effectiveness of the subspace identification procedure developed in the paper has been applied to modal parameter identification of a perforated microplate. Analytical and experimental results are presented showing the accuracy of the method.

References:

[1] De Pasquale G. and Veijola T. (2008) Comparative numerical study of FEM methods solving gas damping in perforated MEMS devices, *Microfluid Nanofluid* 5, 517-528

[2] Lardiès J and Ta Minh-Ngi (2011) Modal parameter identification of stay cables from output-only measurements, *Mechanical Systems and Signal Processing*, *25*, 133-150.

[3] Juang J.N. (1994) *Applied System Identification*, Prentice Hall, New-Jersey, U.S.A

Kinetic Study of Functionalization of Carbon Nanomaterials

T.P. Dyachkova, E.N. Tugolukov, I.V. Anosova, A.G. Tkachev
Tambov State Technical University, Department "Technology and Methods of Nanoproducts Manufacturing", Tambov, Russian Federation
nanotam@yandex.ru

Abstract
This report presents the results of a study on kinetic regularities of multiwalled carbon nanotubes (MWCNTs) functionalization by liquid and gaseous oxidizing agents. It was shown that the gas-phase oxidation under optimum conditions yields highly functionalized materials with minimum consumption of those agents. Besides, it was proposed to use the hydrogen peroxide vapor as oxidant, since this leads to the predominant formation of hydroxyl groups on the MWCNTs surface, thereby providing interactions with polar polymer matrices. The optimum conditions for this vapor functionalization of the MWCNTs were determined. The advantage of the proposed method is the ease of its industrial implementation and the lack of environmentally hazardous waste.
High-quality polyaniline composites were synthesized from carbon nanomaterials functionalized with oxygen groups. Kinetic regularities of carbon nanotubes (MWCNTs) and graphene nanoplatelets (GNPs) modification by polyaniline were studied. The important electrophysical properties of the obtained composites were determined, and their promising applications were reviewed.

Keywords: multiwalled carbon nanotubes, graphene nanoplatelets, functionalization, oxidation, oxidative polymerization, nanocomposites.

Introduction

Carbon nanomaterials are highly variable and possess unique physical properties. Presently, multiwalled carbon nanotubes (MWCNTs) and graphene nanoplatelets (GNPs) appear to be one of the most common and available materials. Nevertheless, their use in composite materials is often limited owing to their tendency to agglomerate. To improve the dispersibility of these materials in polymers and solvents, their surface may be functionalized by covalent attachment of various functional groups (hydroxyl, carboxyl, fluoride, amine, etc.) [1]. The functionalization is particularly valuable with respect to graphene-based multilayered carbon nanostructures, since their agglomeration ability is especially strong due to large contacting surfaces.
The functional groups provide different kinds of interactions between the carbon nanostructures and polymer molecules: 1) electrostatic interaction, 2) hydrogen bond formation, and 3) covalent bond formation. Sometimes, these interactions may lead to the formation of composite polymer layers on the surface of carbon nanomaterials. For instance, this can happen when modifying functionalized MWCNTs and GNPs with conducting polymers (polyaniline and polypyrrole).
Due to the above-mentioned factors, functionalized MWCNTs- and GNPs-based composites are becoming more widely used in the manufacture of structural, building and electrode materials [2]. This, in turn, raises the problem of obtaining functionalized and modified forms of carbon nanostructures in the industry. However, scaling the MWCNTs and GNPs functionalization requires a detailed study on its kinetic regularities, apart from determining the optimum technological regimes, in order to synthesize materials with controlled characteristics [3].

Materials and methods

"Taunit-M" (d = 8 ÷ 15 nm, $l \geq 2$ μm) and "Taunit-MD" (d = 30 ÷ 80 nm, l = 20 μm) MWCNTs and GNPs (h = 3 ÷ 5 nm) produced at "NanoTechCenter" Ltd. (Tambov, Russia) were used (Fig. 1).

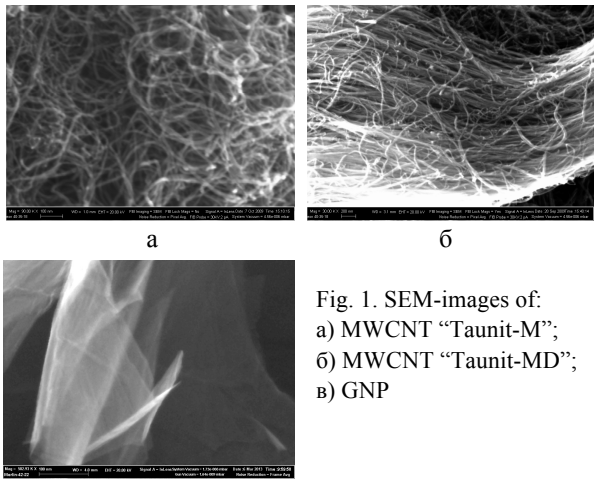

а б в

Fig. 1. SEM-images of:
а) MWCNT "Taunit-M";
б) MWCNT "Taunit-MD";
в) GNP

The MWCNTs surface was functionalized with oxygen groups. The procedure comprised boiling in concentrated HNO_3, oxidation in the presence of HNO_3 vapor, and treatment in the presence of H_2O_2 vapor.
Defects in the initial (pristine) and functionalized MWCNTs were examined by Raman spectroscopy (laser excitation wavelength 473 nm).
The surface functional groups were identified by XPS and FTIR spectroscopy. The number of COOH groups (mmol) per unit mass of the MWCNTs was assessed by trimetric [4] and thermogravimetric analyses.
The MWCNT and GNPs were modified with polyaniline via oxidative polymerization of aniline [5]. The specific surface area, electrical resistivity and capacitance were evaluated for the obtained samples

Results and discussion

The oxidation of the MWCNTs contributes to the appearance of defects on their surface. Moreover, when treating in the presence of HNO_3 vapor, the surface structure of the nanotube is broken down to a lesser extent compared to the boiling in liquid HNO_3 (Fig. 2).

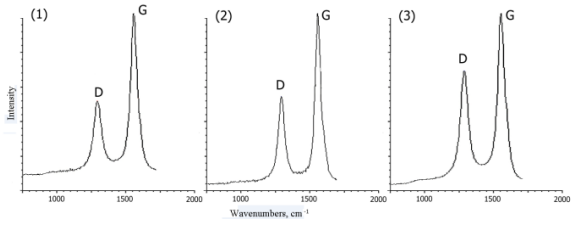

Fig. 2. Raman spectra of the "Taunit-MD" MWCNTs: (1) - untreated, (2) - oxidized in the presence of HNO_3 vapor (t = 140°C; τ = 5 hrs), and (3) - oxidized in boiling HNO_3 (τ = 5 hrs)

FTIR spectra of the initial and oxidized MWCNTs (Fig. 3) are characterized by the absorption bands at 2920, 2850, and 1460 cm^{-1} (all - due to the presence of C-H bonds, as well as at 1630cm^{-1} (due to >C=C<) and 3450 cm^{-1} (due to O-H). A weak band corresponding to the vibrations of the C=O bonds in carboxyl groups (1740 cm^{-1}) can be observed in the FTIR spectrum of the MWCNTs oxidized in boiling HNO_3. As for the material oxidized in the presence of HNO_3 vapor, this peak is relatively pronounced.

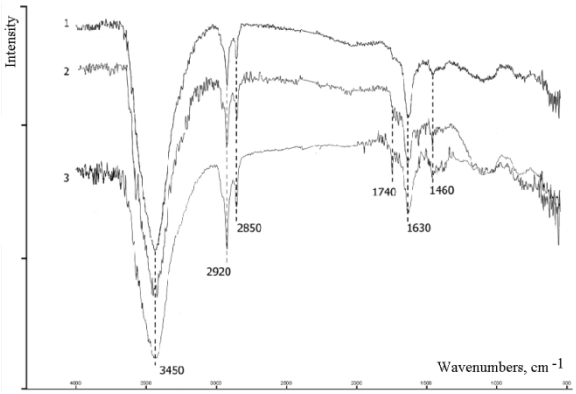

Fig. 3. FTIR spectra of initial MWCNTs "Taunit-MD" (1), MWCNTs oxidized in boiling concentrated nitric acid (2) and its vapor (3)

Therefore, the treatment of the MWCNTs in the presence of HNO_3 vapor promotes deeper oxidation and the availability of more carboxyl groups in comparison with boiling HNO_3. This fact is confirmed by the titration data (Fig. 4).

The rate for the gas-phase oxidation of the MWCNTs with HNO_3 is significantly higher than for the liquid-phase oxidation. The achieved functionalization degree is also correlated with the specific surface area of the carbon material.

Thus, if higher functionalization degrees (D_f) are required, it is suitable to treat MWCNTs in the presence of oxidizing agent vapor.

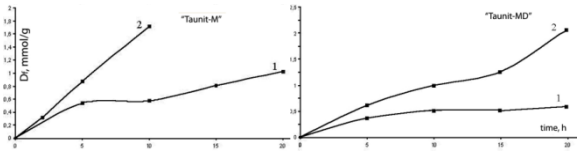

Fig. 4. The time dependences of the degree (D_f) of the "Taunit-MD" and "Taunit-M" MWCNTs functionalization by carboxyl groups. Conditions: liquid-phase (1) and gas-phase (2) oxidation with HNO_3

In this regard, the oxidizing agent consumption per unit weight of the product is reduced by one order, thereby making the problem of acids and gaseous reaction products recycling less acute.

The use of H_2O_2 vapor as a reagent for MWNTS oxidation appears to be even more attractive. In this case, according to the XPS data, the OH-groups are primarily formed on the MWCNTs surface, but the functionalization degree is negligible. However, after treatment in the presence of H_2O_2 vapor, the MWCNTs have proven themselves to be agents for composites modification that provide conductive and radio-frequency shielding properties.

The method and degree of pre-functionalization also affect the kinetics of the polyaniline modification of the MWCNTs (Fig. 5).

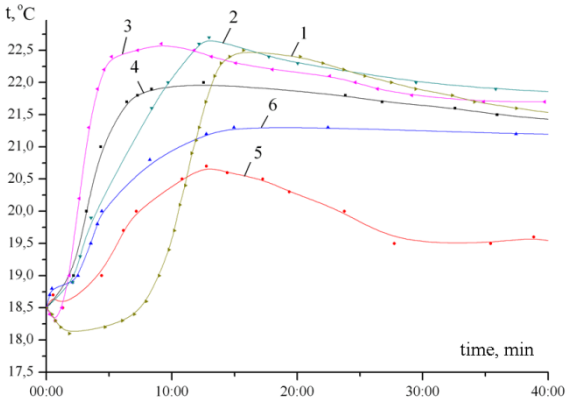

Fig. 5. Changes in the temperature during the aniline polymerization: without MWCNTs (1), with the "Taunit-M" MWCNTs - initial (pristine) (2), with metal-oxide catalyst impurities removed (3), oxidized in HNO_3 (4)-(6) – D_f = 0.2 (4), 0.4 (5), and 0.7 (6) mmol/g

The most qualitative polyaniline coating is formed at D_f = 0,4 mmol/g. The resulting composite is characterized by the highest electrical conductivity and capacitance values (> 3 $Ω^{-1}cm^{-1}$ and 350 F/g, respectively).

The oxygen groups located on the GNPs surface also contribute to the compatibility with the polyaniline macromolecules which form a relatively uniform granular layer.

The regularities elucidated in the present research will be considered when functionalizing and modifying carbon nanomaterials at pilot and industrial scales. Besides, they will make it possible to correctly select appropriate engineering materials for equipment manufacturing, perform more precise technological calculations, and obtain composite

materials and modifiers with required specified properties.

Conclusions

The method and oxidizing conditions for MWCNTs must be chosen depending on further applications of the functionalized material. The oxidation in the presence of H_2O_2 vapor enables obtaining hydroxylated MWCNTs with small defects and a low functionalization degree, which can be successfully used as a component of conducting materials and composites possessing radi-frequency shielding properties. The MWCNTs oxidized with HNO_3 present a higher functionalization degree. They can be utilized in polymer composites with improved mechanical properties.

The presence of oxygen functional groups enhances the interaction between polyaniline and carbon nanomaterials. Nevertheless, when modifying MWCNTs, it is necessary to find an optimum prefunctionalization degree in order to observe the best composites properties. GNPs do not require additional oxidation, since they initially contain functional groups on their surface.

Aknowlegments

The work was carried out within the framework of supporting the cooperation between Russian higher education institutions, state scientific institutions and organizations implementing complex projects on creation of high-tech production (RF Government Decree of April 9, 2010 No. 218; Contract of August 14, 2014 No. 02.G25.31.0123).

References:

[1] Kharitonov, A.P., Tkachev A.G., Blohin, A.N., Dyachkova, T.P., Maksimkin, A.A. Chukov, D.I. (2015) Reinforcement of epoxy resin composites with fluorinated carbon nanotubes, *Compos. Sci. Technol.*, 107, 162-168.

[2] Kondrashov, S.V., Dyachkova, T.P., Bogatov, V.A., Mansurova, I.A., Marakhovskii ,P.S., Fokin, A.S. (2013) Utilization of carbon nanotubes for enhancing the heat resistance of epoxy binders, *Inorg. Mater. Appl. Res.*, 5, 394-399.

[3] Dyachkova, T.P., Melezhyk, A.V., Gorsky, S.Yu., Anosova, I.V., Tkachev, A.G. (2013) Some aspects of functionalization and modification of carbon nanomaterials, *Nanosystems: Physics, Chemistry, mathematics*, 5, 605-621.

[4] Boehm, H.P. (2002) Surface oxides on carbon and their analysis: a critical assessment, *Carbon*, 40, 145–149.

[5] Konyushenko, E.N., Stejskal, J., Trchova, M., Hradil, J., *et al*. (2006) Multi-wall carbon nanotubes croated with polyaniline, *Polymer*, 2006, 47, 5715-5723.

Nanotechnology: Promises and challenges for future

Dr. Akbar S. Khan1, Senior Scientist and Program Director, CB Directorate, Defense Threat Reduction Agency, Fort Belvoir, Virginia, USA, Akbar.s.khan.CIV@mail.mil

Keywords: Nanoparticles, Safety, risks, chemical reactivity, filtration system, applied design, nano-particle drug delivery.

Abstract: Nanotechnology is science, engineering, and technology conducted at the nanoscale, which is about 1 to 100 nanometers. All things, both living and non-living, are constructed of atoms. The nano-scale sparks so much interest because when a substance is artificially created, structured atom by atom, it can have different or enhanced properties compared with the same substance as it occurs naturally, which includes increased chemical reactivity, optical, magnetic, or electrical properties. Nanotechnologies aim to exploit these properties to create devices, systems, and structures with new characteristics and functions. For example, researchers hope to construct from the very 'bottom' (that is to say, atom by atom) a substance as strong as diamond, but more flexible and far less expensive. It would also be possible to manufacture a substance in the shape and size needed such as a thin string as strong as steel.
So far Nanotechnology is applied in various areas (1) applied design a water filtration system on the nano-scale that is so efficient, it only lets water molecules through it. (2) Is used to create filters and sensors to screen out toxins or adjust flavors, and packaging to sense when the food inside is spoiling and alert the customer. (3) The ability to assemble Nano-scale particles that could be targeted at certain parts of the body or certain viruses in the blood. (4) Economical solar cells to make solar power economical and diminish our dependency on coal, oil, nuclear fuel and fuel wood. (5) To clean up the environment. To clean up oil spills, imagine a scrubber built from tiny nanotubes that could manipulate the atoms in an oil spill to render it harmless.
Just like any new technology, there are varieties of health, environmental and safety risks to this technology from free rather fixed manufactured nanoparticles. In initial studies, manufactured nanoparticles have shown toxic properties. They can enter the human body in various ways, reach vital organs via the blood stream, and possibly damage tissue. Due to their small size, the properties of nanoparticles not only differ from bulk material of the same composition but also show different interaction patterns with the human body. These promises and challenges of Nanotechnology will be presented here.

1. Introduction

Nanotechnology based research is turning out to be the major force behind a new industrial revolution. Both private and public-sector spending constantly increased in last 10 years. Nanoscale materials have been used for decades in applications ranging from window glass and sunglasses to car bumpers and paints as shown in Fig 1. Now, however, the convergence of scientific disciplines (chemistry, biology, electronics, physics, engineering etc.) is leading to a multiplication of applications in materials manufacturing, computer chips, medical diagnosis and health care, energy, biotechnology, space exploration, security and so on. Hence, nanotechnology is expected to have a significant impact on our economy and society within the next 10 to 15 years, growing in importance over the longer term as further scientific and technology breakthroughs are achieved. At the same time, scientists have raised concerns that the basic building blocks of nanotechnologies—particles smaller than one billionth of a meter—pose a potential new class of risk to health and the environment. The recommendation on the health concern calls for a precautionary approach based on risk research and good risk management to minimize the likelihood of nanoparticles bringing a new dimension to personal injury and property damage losses or posing third party liability and product-recall risks.

1.1. Nanomaterials: basic building blocks

This section outlines the properties of two of the most talked-about nanotechnologies: carbon nanotubes, nanoparticles. Some examples of Nanoparticles and their commercial use shown in table 1.

Carbon Nanotubes

Carbon nanotubes, long thin cylinders of atomic layers of graphite, may be the most significant new material since plastics and are the most significant of today's nanomaterials. They come in a range of different 8 structures, allowing a wide variety of properties. They are generally classified as single-walled (SWNT), consisting of a single cylindrical wall, or multiwalled nanotubes (MWNT), which have cylinders within the cylinders. When the press mentions the amazing properties of nanotubes, it is generally SWNT they are referring to. The following table summarizes the main properties of SWNT: However, SWNT are more difficult to make than MWNT, and confusion arises about the quantities of nanotubes actually being manufactured. Carbon Nanotechnologies of Houston, one of the world's leading producers, only makes up to 500g per day. One problem is that economies of scale are practically impossible with today's production technologies – the machines used to manufacture the tubes cannot be scaled up, so producing bigger quantities means using more machines. Another drawback is that it is difficult to make nanotubes interact with other materials. For example, to fully exploit their strength in composite materials, nanotubes need to be "attached" to a polymer. They
are chemically modified to facilitate this (a process known as "functionalization"), but this process reduces the very properties the nanotubes are being used for. In the long-term, the ideal solution would be to use pure nanomaterials, e.g. nanotubes spun into fibers of any desired length, but such a development is unlikely in the next couple of decades unless a radically more efficient production process is developed.

The most promising applications of nanotubes may be in electronics and optoelectronics8. Today, the electronics industry is producing the vital components known as MOSFETs (metal oxide semiconductor field effect transistors) with critical dimensions of just under 100 nm, with half that size projected by 2009 and 22 nm by 2016. However, the industry will then encounter technological barriers and fundamental physical limitations to size reduction. At the same time, there
are strong financial incentives to continue the process of scaling, which has been central in the effort to increase the performance of computing systems in the past. A new microchip manufacturing plant costs around $1.5 billion, so extending the technology's life beyond 2010 is important. One approach to overcoming the impending barriers while preserving most of the existing technology, is to use new materials.

With carbon nanotubes, it is possible to get higher performance without having to use ultra thin silicon dioxide gate insulating films. In addition, semiconducting SWNTs, unlike silicon, directly absorb and emit light, thus possibly enabling a future optoelectronics technology. The SWNT devices would still pose manufacturing problems due to quantum effects at the nanoscale, so the most likely advantage in the foreseeable future is that carbon nanotubes will allow a simpler fabrication of devices with superior performance at about the same length as their scaled silicon counterparts.

Other proposed uses for nanotubes:

Chemical and Genetic Probes. A nanotube-tipped atomic force microscope can trace a strand of DNA and identifychemical markers that reveal which of several possible variants of a gene is present in the strand. This is the only method yet invented for imaging the chemistry of a surface, but it is not yet used widely. So far it has been used only on relatively short pieces of DNA.

Mechanical memory **(nonvolatile RAM).** A screen of nanotubes laid on support blocks has been tested as a binary memory device, with voltages forcing some tubes to contact (the "on" state) and others to separate ("off"). The switching speed of the device was not measured, but the speed limit for a mechanical memory is probably around one megahertz, which is much slower than conventional memory chips.

Field Emission Based Devices. Carbon Nanotubes have been demonstrated to be efficient field emitters and are currently being incorporated in several applications including flat-panel display for television sets

or computers or any devices requiring an electron producing cathode such as X-ray sources (e.g. for medical applications).
Supersensitive Sensors. Semiconducting nanotubes change their electrical resistance dramatically when exposed to alkalis, halogens and other gases at room temperature, raising hopes for better chemical sensors.The sensitivity of these devices is 1,000 times that of standard solid state devices.

Hydrogen and Ion Storage. Nanotubes might store hydrogen in their hollow centers and release it gradually in efficient and inexpensive fuel cells. They can also hold lithium ions, which could lead to longer-lived batteries. So far the best reports indicate 6.5 percent hydrogen uptake, which is not quite dense enough to make fuel cells economical. The work with lithium ions is still preliminary.
Sharper Scanning Microscope. Attached to the tip of a scanning probe microscope, nanotubes can boost the instruments' lateral resolution by a factor of 10 or more, allowing clearer views of proteins and other large molecules. Although commercially available, each tip is still made individually. The nanotube tips don't improve vertical resolution, but they do allow imaging deep pits in nanostructures that were previously hidden.
Superstrong Materials. Embedded into a composite, nanotubes have enormous resilience and tensile strength and could be used to make materials with better safety features, such as cars with panels that absorb significantly more of the force of a collision than traditional materials, or girders that bend rather than rupture in an earthquake. Nanotubes still cost 10 to 1,000 times more than the carbon fibers currently used in composites. And nanotubes are so smooth that they
slip out of the matrix, allowing it to fracture easily.

1.2. The environmental, health and safety discussion related to nanoparticles
Along with the discussion of their enormous technological and economic potential, a debate about new and specific risks related to nanotechnologies has started. The catch-all term "nanotechnology" is so broad as to be ineffective as a guide to tackling issues of risk management, risk governance and insurance. A more differentiated approach is needed regarding all the relevant risk management aspects.
With respect to health, environmental and safety risks, almost all concerns that have been raised are related to free, rather than fixed manufactured nanoparticles. The risk and safety discussion related to free nanoparticles will be relevant only for a certain portion of the widespread applications of nanotechnologies.
Epidemiological studies on ambient fine and ultrafine particles incidentally produced in industrial processes and from traffic show a correlation between ambient air concentration and mortality rates. The health effects of ultrafine particles on respiratory and cardiovascular endpoints highlight the need for research also on manufactured nanoparticles that are intentionally produced.
In initial studies, manufactured nanoparticles have shown toxic properties. They can enter the human body in various ways, reach vital organs via the blood stream, and possibly damage tissue. Due to their small size, the properties of nanoparticles not only differ from bulk material of the same composition but also show different interaction patterns with the human body. A risk assessment for bulk materials is therefore not sufficient to characterize the same material in nano-particulate form. The implications of the special properties of nanoparticles with respect to health and safety have not yet been taken into account by regulators.

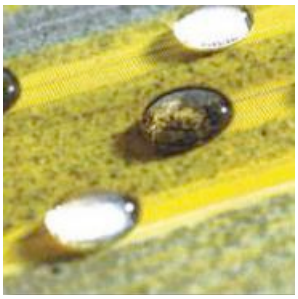

Figure 1: An illustration of water shield self-cleaning paint using Nano-particles

Table 1: Listing of different types of Nanoparticles and their commercial uses

Type	Examples for use
Metal oxides	
• silica (SiO_2) • titania (TiO_2) • aluminia (AL_2O_3) • iron oxide (Fe_3O_4, Fe_3O_3) • zirconia (ZrO_2) • zinc dioxide (ZNO_2)	• Additives for polymer composites • UV-A protection • Solar cells • Pharmacy /medicine • Additives for scratch resistance coatings
Fullerenes • C_{60}	• mechanical and trbological applications / additives to grease
Carbon Nanotubes • Single-wall carbon nanotubes	• Additives for polymer composites (mechanical performance, conductivity)
• Multiwall carbon nanotubes	• Electronic field emitters • Batteries • Fuel cells
Compound Semiconductors • CdTe • GaAs	• Electronic an optical devices
Organic Nanoparticles	• Micronised drugs and chemicals (vitamins, pigments, pharmaceuticals) • Polymer dispersions
Metals • Au • Ag • Ni	• Catalytic applications • Optoelectronics • Wound dressings

Nanoparticles raise a number of safety and regulatory issues that governments are now starting to tackle. At present, the exposure of the general population to nanoparticles originating from dedicated industrial processes is marginal in relation to those produced and released unintentionally e.g. via combustion processes. The exposure to manufactured nanoparticles is mainly concentrated on workers in nanotechnology research and nanotechnology companies. Over the next few years, more and more consumers will be exposed to manufactured nanoparticles. Labelling requirements for nanoparticles do not exist. It is inevitable that in future manufactured nanoparticles will be released gradually and accidentally into the environment. Studies on bio-persistence, bioaccumulation and eco-toxicity have only just started few years ago. More long term exposure studies need to be completed to have a clear picture on the toxicity of the nanoparticles.

References:

1. Satterfield, T., Kandlikar, M., Beaudrie, C. E. H., Conti, J., Herr Harthorn, B. (2009), 'Anticipating the perceived risk of nanotechnologies', *Nature Nanotechnology*, 4, 752-758.

2. Aitken, R., Borm, P., Donaldson, K., Ichihara, G., Loft, S., Marano, F., Maynard, A., Oberdörster, G., Stamm, H., Stonem V., Tran, L., Wallin, H. (2009), 'Nanoparticles – one word: A multiplicity of different hazards,' *Nanotoxicology*, 3, 263-264.

The influence of redistribution ions in subphase at the properties Langmuir monolayer

Chumakov A.S., Gorbachev I.A., Kossovich E. L., Ermakov A.V., Kim, V.P., Glukhovskoy E.G.
Saratov State University named after N.G. Chernyshevsky, Russia
email: lehahares@rambler.ru

Introduction

The process of formation and structure of the monolayer of course will depend on many factors like composition and concentration of surfactant, temperature etc. For example, in some of previously studies already have investigated the influence on the structure and composition of monolayers addition of various inorganic salt in subphase [1, 2] or the effects arised with change subphase pH [3, 4, 5].

Idea

In addition, one of the influencing parameters is the electric field, actually may be used as a technology control factor which enables to control and modify the structure of a monolayer. This assumption was made on the grounds that monolayer is a structure sensitive to small changes in acidity in subphase. And his subphase is a substance composed of molecules with large dipole moment, and the substance having some number of ions.

Experiment and discussion

In the case of application of the electric field in the normal direction, we have a significant change in the process of formation the individual phases of the arahidic acid (Arh) monolayer. Increase area in liquid phase was approximately 25% when applying a voltage to the electrodes (fig. 1). We explain the extension the liquid phase by the fact of change pH under ML surface. In this case, the changes in the monolayer formation process due not with sensitivity surfactant molecules to the electric field. This can be explained by the fact that water molecules have large dipole moment [6, 7]. After that, in deionized water with pH = 7 at 25°C hydrogen ion concentration ([H+]) and hydroxide ions ([OH-]) are identical and amount to 10^{-7} mol/l. These ions are separated and redistributed in electric field. That process will creating a gradient of acidity in the space between the electrodes.

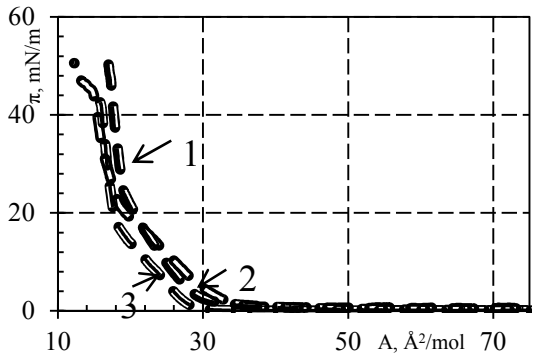

Figure 1 - compression isotherms of Arh monolayers on the surface of deionized water, 1 - intensity vector is directed upwards; 2 - intensity vector is directed downward; 3 - the electric field absence

To confirm the described mechanism (through redistribution of ions in the subphase and a change of local acidity), influence of the electric field in the subphase also was made computer modeling of area a monolayer of Arh under various external factors, in particular, under the action of electric field.

The first phase we were studied normal conditions and after 1 ps the simulation process by the method of molecular dynamics, structure becomes stable. If we continue to molecular-dynamic simulation we haven't big changes in monolayer structure. Self-assembling of monolayer on the water surface takes a short period of time - about 1 ns. The resulting structure is stable on the water surface, not destroyed it was confirmed by the simulation in long time (1 second) in the LAMMPS software package (fig. 2).

However, the most important issue of our work was to study the dependence of the structure of monolayers, depending on

presence of electric field and ions in the subphase (1 ion in 10,000 molecules of water). Without external electric field the subphase remained relatively neutral - ions arranged randomly into the water layer (t will be expected on the basis of physical concepts).

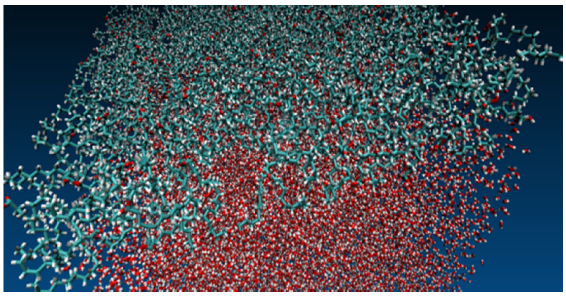

Figure 2 - configuration of monolayer

However, under the condition, to the availability of external electric field (with intensity about 100 V/cm) under the influence of ions presence and polarization of Arh molecules in the structure of the monolayer arise some gaps (which would display on the compression isotherm like to increase of the mean molecule area, i.e. the extension of the monolayer), caused by the increase in the concentration of molecules near to the ions. It should be noted that in this case the topology of gaps virtually unchanged over time. Example of gaps shown in Figure 3.

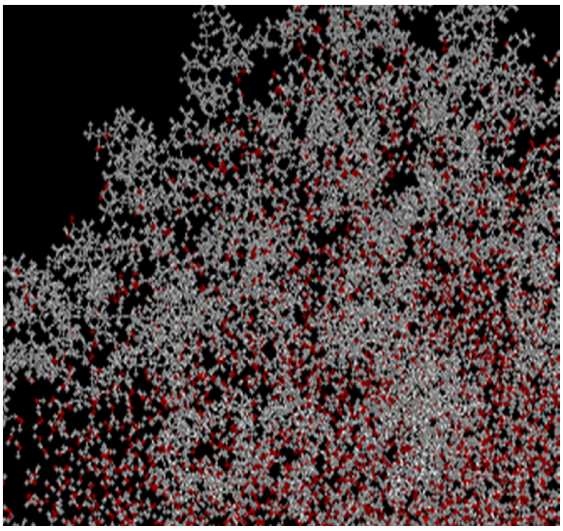

Figure 3 - gaps in the monolayer

Conclusion

Our experiments show what we can use the electrical field for control of monolayers properties. But the main part in this process - is the redistribution of ions in subphase and change pH in the area under monolayer.

In the model we can see gaps in monolayer – it would be interpreted like extension on ML compression isotherm.

Reference

1. *S. Cantin, Marie-Claude Fauré, F. Perrot et.al.* Structure and Kinetics of Fatty Acid Langmuir Monolayers on Zinc Salt Solutions. The Journal of Physical Chemistry. 2013.
2. *W. Bu, M. Mihaylov, D. Amoanu et.al.* X-ray Studies of Interfacial Strontium–Extractant Complexes in a Model Solvent Extrac-tion System. The Journal of Physical Chemistry. 2014.
3. *A. Datta, J. Kmetko, C.-J. Yu et.al.* pH-Dependent Appearance of Chiral Structure in a Langmuir Monolayer. The Journal of Physical Chemistry. 2000.
4. *G. Thakur, Roger M. Leblanc*. Conformation of Lysozyme Langmuir Monolayer Studied by Infrared Reflection Absorption Spectroscopy. Langmuir. 2009.
5. *H. Yu, W. F. van Gunsteren*. Charge-on-spring polarizable water models revisited: from water clusters to liquid water to ice. J. Chem. Phys. 2004.
6. *E. V. Tsiper*. Polarization forces in water deduced from single molecule data, Phys. Rev. Lett. 2005.

The work is supported by grant № 14-12-00275 of Russian Science Foundation and Saratov State University.

New Methods for Creating Nanocomposites based on Carbon Nanotubes and Graphene Nanoplatelets

E.A. Burakova, A.V. Gerasimova, A.V. Melezhyk, A.G. Tkachev
Tambov State Technical University, Department "Technology and Methods of Nanoproducts Manufacturing", Tambov, Russian Federation

Keywords: carbon nanotubes, graphene nanoplatelets, phenol-formaldehyde resin, nanocomposites.

Abstract

The use of phenol-formaldehyde resins (PFRs) in synthesizing dispersions of carbon nanomaterials makes it possible to increase the concentration of nanoparticles in solution by 2-3 orders of magnitude. In this regard, due to the presence of the PFR, the concentration of nanotubes in the solution after ultrasonic treatment reaches 11.4 g L^{-1} and the mutual orientation of the PFR-modified nanotubes takes place, so that their chaotic tangles become unraveled. The obtained results are also typical of graphene nanoplatelets (GNPs) and have an important impact on the synthesis of nanocomposite materials (NCMs).

1. Introduction

Carbon nanomaterials such as fullerenes, nanotubes (CNTs), nanodiamonds and graphene are widely used to make various advanced NCMs. Nanocomposite structures based on CNTs, GNPs and their modified forms are usually employed as radar absorbing materials, electrodes for chemical power sources and sensors [1- 11].

Chemical reduction and thermal decomposition of graphite oxide (GO) are one of the most common methods for obtaining graphene-based nanocomposite structures. However, the disadvantages of these methods are the high cost for graphene synthesis (since the technological process of oxidizing graphite to GO is rather complex) and the presence of defects.

The solution to the problem of synthesizing highly concentrated dispersions of few-layer GNPs and CNTs and removing the surfactant from the final product appears to be topical for the industrial production of CNTs- and graphene-based NCMs.

The aim of the present work is to study the possibility of employing a PFR as a reactive surfactant for obtaining stable aqueous dispersions of CNTs and graphene. It is known that low molecular weight phenol-formaldehyde oligomers synthesized via condensation of phenol with an excess of formaldehyde in an alkaline medium (resol-type PFRs) are soluble in water. In such resins, methylol groups possess high reactivity, due to which the resol-type PFR is able to modify the surface of the CNTs or graphene and thereby impart water solubility to these nanomaterials.

2. Materials and Methods

"Taunit-M" CNTs (diameter 8-20 nm) produced by "NanoTechCenter" Ltd. (Tambov, Russia) were used as starting materials. Their surface was oxidized by treating with an aqueous ammoniacal solution of ammonium persulfate. An expanded graphite compound (EGC),prepared according to the method described in [12] was used as a precursor for obtaining GNPs. It was subjected to hydrolysis and then rinsed with water. Stable aqueous dispersions were oprepared by sonication. The concentration of carbon nanoparticles in the obtained dispersions was determined by a photometric method.

3. Results and Discussion

To study the dispersion process for the CNTs and graphene, the starting material ("Taunit-M" CNTs or EGC) was added to a solution containing the resol-type PFR and sonicated (frequency 22 kHz). The samples of the the obtained dispersions were diluted with water , and the concentration of carbon nanoparticles was measured.

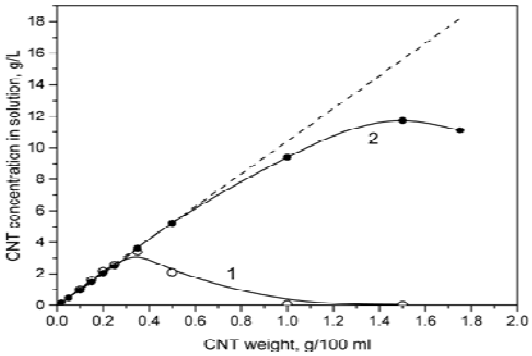

Fig. 1 The dependence of the CNT concentration in solution on the initial CNT weight in 100 mL of the mixture: 1 – starting CNTs; 2 – oxidized CNTs.

As seen in Fig. 1, for both starting and oxidized CNTs, the CNT concentration in the solution initially increases proportionally to the CNT weight, reaches the maximum value, and then decreases. In the initial section, almost 100 % of the CNTs passes into the solution (the observed concentration coincides with the calculated concentration). The decrease in the solubility at high CNT weight values may be related to the PFR adsorption on the CNTs. Thus, when performing the ultrasonic treatment in the PFR solution, the CNT concentration reaches 11.4 g L^{-1}, which exceeds the CNT concentration reported in the litera-

ture for common surfactants [13] by 2-3 orders of magnitude. Apart form the adsorption of the PFR molecules on the CNTs, the chemical interaction of the PFR with the surface groups of the oxidized PFR also takes place, which can be confirmed by increased solubility when increasing the temperature during the ultrasonic treatment (Fig. 2).

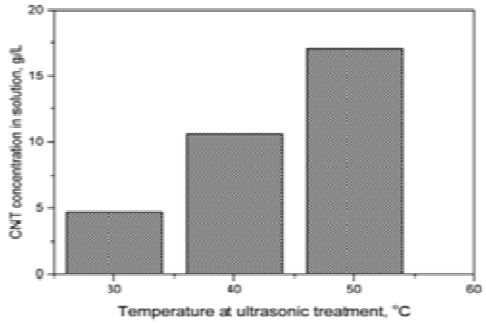

Fig. 2. The dependence of the CNT concentration in solution on the temperature.

The similar results were obtained for the GNPs. The combination of different PFR-modified carbon nanoparticles makes it possible to prepare various nanocomposites, and besides, the PFR is chemically bonded to the surface and does not require removing. If desired, further carbonization of the PFR may be performed in order to obtain pure carbon nanostructures. Changing the pH, which results in the self-assembly of nanoscale elements, appears to be one the the methods for creating NCMs based on PFR-modified nanoparticles.

As an example, in Fig. 3, the CNT and CNT+GNP films obtained after employing the PFR are demonstrated.

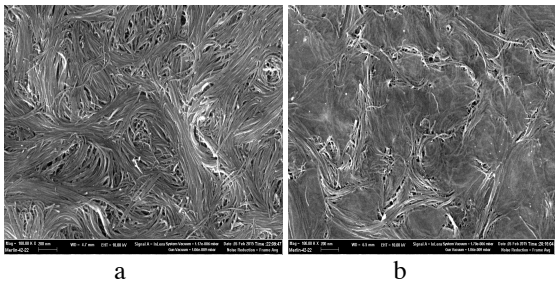

a b

Fig. 3. NCMs obtained in the presence of the PFR: a – CNT film; b – CNT+GNP film.

References:

1. 1D/2D carbon nanotube/graphene nanosheet composite anodes fabricated using electrophoretic assembly / S.-D.Seo, I.-S.Hwang, S.-H. Lee [et al.] // Ceramics International Volume 38, Issue 4, May 2012, Pages 3017–3021.

2. A facile approach to fabricate flexible all-solid-state supercapacitors based on $MnFe_2O_4$/graphene hybrids / W. Cai, T. Lai, W. Dai, J. Ye // Journal of Power Sources Volume 255, 1 June 2014, Pages 170–178.

3. A sulfur–polyacrylonitrile/graphene composite cathode for lithium batteries with excellent cyclability / J. Li, K. Li, M. Li [et al.] // Journal of Power Sources. – 2014. – Vol. 252. – P. 107–112.

4. An investigation on the photoelectrochemical properties of dye-sensitized solar cells based on graphene–TiO_2 composite photoanodes / M. Zhua, X. Li, W. Liu [et al.] // Journal of Power Sources. – 2014. – Vol. 262. – P. 349–355.

5. Binder free synthesis of MnO_2 nanoplates/graphene composites with enhanced supercapacitive properties / Z. Li, Y. Su, G. Yun [et al.] // Solid State Communications Volume 192, August 2014, Pages 82–88.

6. Carbon nanotube–polyaniline composites /C. Oueiny, S. Berlioz, F. Perrin // Progress in Polymer Science. – 2014. – Vol. 39. – P. 707–748.

7. Graphene nanosheets-poly(o-aminophenol) nanocomposite for supercapacitor applications / H. Heli, H. Yadegari, A. Jabbari // Materials Chemistry and Physics. – 2012. – Vol. 134. – P. 21 –25.

8. C. J. Hung. High energy density asymmetric pseudocapacitors fabricated by graphene/carbon nanotube/MnO_2 plus carbon nanotubes nanocomposites electrode / C.J. Hung, P. Lin, T. Y. Tseng // Journal of Power Sources. – 2014. – Vol. 259. – P. 145 –153.

9. Poly(ortho-aminophenol)/graphene nanocomposite as an efficient supercapacitor electrode / H. Heli, H. Yadegari // Journal of Electroanalytical Chemistry. – 2014. – Vol. 713. – P. 103 –111.

10. Electromagnetic interference shielding efficiency of polyaniline composites filled with graphene decorated with metallic nanoparticles / Y. Chen, Y. Li, M. Yip [et al.] // Composites Science and Technology Volume 80, 17 May 2013, Pages 80–86.

11. A simple synthesis of Fe_3O_4 nanoclusters and their electromagnetic nanocomposites with polyaniline / W. Shen, M. Shi, M. Wang [et al.] // Materials Chemistry and Physics Volume 122, Issues 2–3, 1 August 2010, Pages 588–594.

12. Synthesis of graphene nanoplatelets from peroxosulfate graphite intercalation compounds / A. V. Melezhyk, A. G. Tkachev // Nanosystems: Physics, Chemistry, Mathematics, 2014, 5 (2), P. 294–306.

13. The role of surfactants in dispersion of carbon nanotubes / L. Vaisman, H. D. Wagner, G. Marom // Advances in Colloid and Interface Science. – 2006. – Vol. 128–130 – P. 37–46.

Acknowledgement: The work was performed within the framework of the Federal Target Program "Research and Development in Priority Areas of the Scientific and Technological Complex of Russia for 2014-2020" (State Contract of July 22, 2014 No. 14.577.21.0091; Unique Identifier for Applied Scientific Researches: RFMEFI57714X0091).

SEEC Microscopy : An innovative optical technique for the live and label-free study of a enzymatic reaction in liquid

A.Egea,[1] N.Médard,[2,*] M.Métivier,[2] C.Vieu,[1]
[1]*LAAS-CNRS, 7 Avenue du Colonel Roche, 31400 Toulouse, France*
[2]*Nanolane, Technopole Université, 10 rue Xavier Bichat, 72000 Le Mans, France*

Introduction

Nowadays, label-free In-Vitro Diagnostic (IVD) is in higher demand due to the steric, electronic influence of labeled molecules on biological samples. However, in the absence of chemical amplification, it is a challenge for label-free biosensing to achieve the same degree of sensitivity as those exhibited by standard enzyme-linked immunosorbent assay (ELISA). In this sense, significant optical label-free biosensors are reported performing well: SPR, SPRi, QCM-D, OWLS… But even if these techniques show quite good sensitivity, none of them offer high-lateral resolution imaging and direct thickness measurements capacities.

We show here that the non-destructive and non-invasive SEEC Microscopy technique can be used to characterize a dynamic enzymatic reaction in real time with nanoscale lateral and thickness sensitivity (down to 1nm). This study was performed on 5µmx5µm patterns to illustrate the ability of the SEEC technique to perform ultra-high density multiplexing analyses.

Results and discussion

SEEC Microscopy is a new generation surface interaction technique offering new analysis capabilities such as the live nanoscale imaging, the live topographic study, the ability to perform label-free analyses in dry and in liquid, in static and in dynamic mode. The technique is also compatible with the use of microfluidic devices and can be combined with exiting analyses such as RAMAN, AFM, fluorescence, confoncale techniques. SEEC Microscopy implements new generation of sensitive sensors, the SEEC sensors displaying high contrast-enhanced performances. Successful analyses were recently performed on biologicial samples such as lipid layers, biofilms, biochips, DNA molecules. The technique can also be applied to the analysis of organic/inorganic samples such as polymer / polyelectrolytes / Langmuir-Blodgett films, nanopatterns, nanotubes, nanoparticles…

In this study, the enzymatic elongation of dextran catalyzed by DSR-S from glucose substrate was analyze in real-time. SEEC images recorded 15 and 120 minutes, respectively after the beginning of the enzymatic reaction, are displayed in Figure 1.

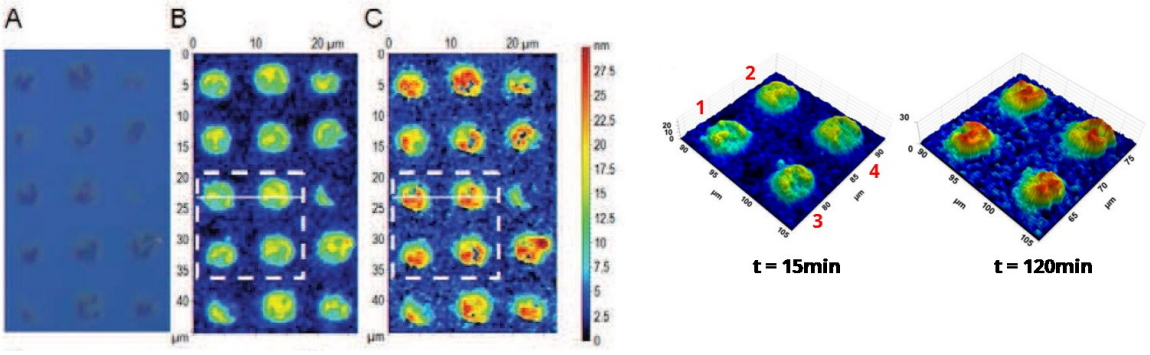

Figure 1: SEEC images and topographic images of enzymatic patterns observed at t=15min (A; B) and t=120min (C).

A rise of pattern step heights is clearly observed that confirms the ability of SEEC microscopy to monitor a molecular reaction on a nanostructure in a liquid environment in real time. Thanks to the imaging capability, multiplex SEEC analyses were performed. The average thickness measured on each spot varies from around 6 to 10nm.

Thickness evolution of the nanometric patterns as a function of the enzymatic reaction time is displayed in figure 2. Patterns show no clear thickness evolution during the first hour of enzymatic reaction. Then a net rise is observed from 60 minutes where pattern thickness increases by 4nm in less than an hour. The stability of the pattern thickness observed during the first hour of polymerization reaction is probably due first, to the time needed for the reaction to start, and second, to the z-sensitivity of the SEEC analysis in a liquid environment (approx. 1nm) that limits the detection of the increase in thickness during the first minutes.

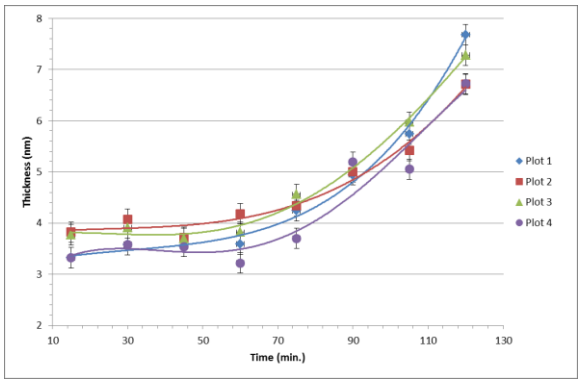

Figure 2: Evolution of pattern thicknesses as a function of the enzymatic reaction time.

Conclusion

This study shows that SEEC Microscopy permits multiplex in situ and real-time monitoring of biochemical reactions taking place on surface molecular patterns. Thanks to its label-free capacity, SEEC microscopy offers a fast and direct analysis of biomolecular reactions in a liquid environment. Nanoscale lateral sensitivity allows the study of patterns/chips with micrometric dimensions (down to 5µm). These capacities open a new way for label-free In Vitro-Diagnostic ultra-high density multiplexing assays.

Experimental part

Dextransucrase-based enzymatic reaction

In this study, patterns of dextransucrase (DSR-S) were printed onto a SiO_2 SEEC Sensor coated with a thin layer of PLL-g-dextran (figure 3). The sample was immersed in a liquid environment enriched with sucrose. Dextransucrase (DSR-S) catalyses the transfer of glucosyl from sucrose to generate a soluble polymer of D-glucosyl units.

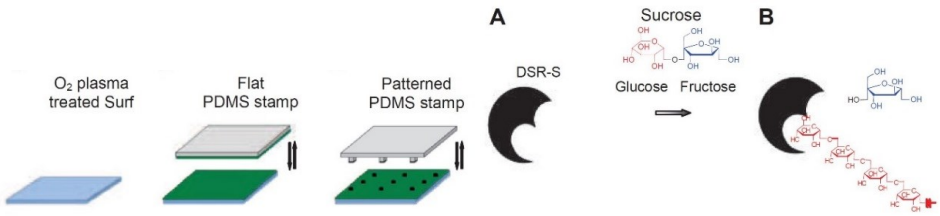

Figure 3: A. Steps for dextransucrase patterns elaboration B. Reaction of the dextran chains elongation

SEEC Microscopy technique

SEEC analyses were performed from a Sarfus Mapping HR station (Nanolane) and consumables SEEC Sensors bearing a SiO_2 toplayer (SiO_2 SEEC Sensor-Nanolane). Sarfusoft software enables the live recording of SEEC images as well as the thickness measurement of the nanometric patterns (accuracy: +/-0.4nm). The dextransucrase polymerization was observed for 120 minutes (figure 4).

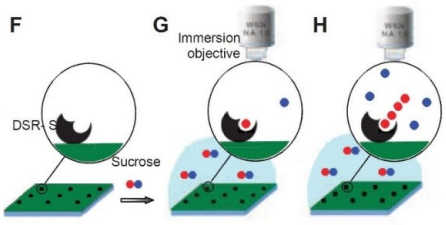

Figure 4: Dextransucrase polymerization reaction observed by SEEC Microscopy

References

A.M.C.Egea, M.Metivier, P.Croguennoc, M.Remaud-Simeon, C.Vieu, BioNanoScience, 2014, Vol.4, Issue 1, pp 37-45.

DNA detection using Si-nanosandwich

A. Chernev[1], N. Bagraev[2], L. Klyachkin[2], A. Emelyanov[1], M. Dubina[1]
[1] St. Petersburg Academic University – Nanotechnology Research and Education Centre RAS, 8/3 Khlopin str., St. Petersburg 194021, Russia
[2] Ioffe Physical-Technical Institute of the Russian Academy of Sciences, 26 Polytechnicheskaya str., St. Petersburg 194021, Russia

Abstract: DNA semiconductor detection and sequencing is considered to be the most promising approach for future discoveries in genome and proteome research which is dramatically dependent on the challenges faced by semiconductor nanotechnologies. DNA pH-sensing with ion-sensitive field effect transistor (ISFET) is well-known to be a successfully applied electronic platform for genetic research. However this method lacks fundamentally in chemical specificity. Here we develop the first ever silicon nanosandwich pump device, which provides both the excitation of DNA fragments' self-resonant modes and the feedback for current-voltage measurements at room temperature. This device allows direct detection of single-stranded label-free oligonucleotides by measuring their THz frequency response in aqueous solution. These results provide a new insight into the nanobioelectronics for the future real-time technologies of direct gene observations.

Keywords: DNA detection with semiconductor device, THz pumping, silicon nanosandwich, short oligonucleotides detection.

Real-time amplification and detection of nucleic acid has given rise to the development of life science research and molecular diag¬nostics. These methods became a basis of the techniques that are applied for express detection and quantification of small amounts of nucleic acid and have a wide array of applications. However these techniques for real-time detection of nucleic acid require precision optics as well as fluorescently labelled sequence-specific probes or fluo¬rescent dyes for DNA labelling. Therefore this is a huge disadvantage of such techniques due to the indirect oligonucleotides signal collection. Several attempts have been made to resolve this problem.
Recently, a semiconductor-based nucleic acid sequencer that uses the pH-sensing capabil¬ity of ion sensitive field effect transistors (ISFET) has been demonstrated1. Another device that is able to amplify and simultaneously detect DNA using embedded heaters, temperature sensors and ISFET sensor arrays appears to be also very effective2. The most important result of the works mentioned was to provide the amplification and the detection simultaneously. Nevertheless, despite the development of an ISFET technology3, there are still challenges that cannot be met with it. Since the principle of an ISFET-based sensor is the pH sensing mechanism that is not target-specific, this leads to the most crucial disadvantage of it.
Here we present a new method of oligonucleotides detection by the excitation of their self-resonant modes that correspond to the unique combination of the nucleotide sequence and the whole molecular shape.
Therefore the method suggested to detect the oligonucleotides is based on the interaction of Silicon nanosandwich with nucleic acids deposited on its surface. This Silicon nanosandwich represents the ultra-narrow p-type Silicon quantum well, confined by the delta barriers heavily doped with Boron on the n-Si (100) wafer. The edge channels of this QW have been shown to be effective source of THz emission4, 5. In order to enhance the selective THz line emission, the corresponding system micro cavities is inserted in the plane of QW. Such devices allow the creation of the THz spectra that are close to oligonucleotides self-resonant modes. Thus, the self-resonant modes excitation of oligonucleotides deposited in the QW plane becomes possible, with provided by feedback giving rise to the changes in the conductance of edge channels.

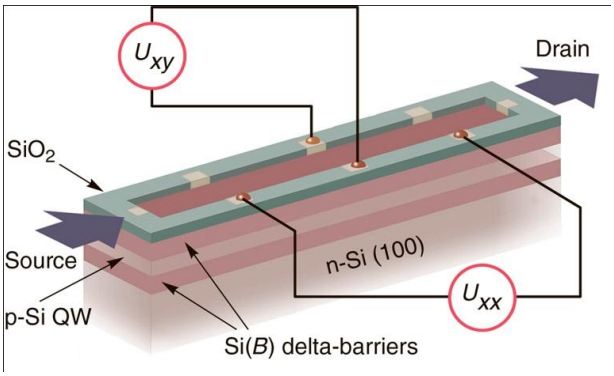

Figure 1: Silicon nanosandwich that represents the ultra-narrow silicon quantum well of the p-type Si confined by the delta-barriers heavily doped with boron on the n-type Si (100) wafer.

Single stranded oligonucleotides were synthesized with the Applied Biosystems's synthesizing equipment, purified with polyacrylamide gel electrophoresis and extracted in 0.3M Sodium acetate solution.

The investigated sequences were: 100-mer 5'-gcgctggctgcgggcggtgagctgagctcgcccccggg-gagctgtggccggcgcccctgccggttccctgagcagcggac-gttcatgctgggagggcggcg-3' and 50-mer 5'-gcgctggctgcgggcggtgagctgagctcgcccccggg-gagctgtggccg-3'. The concentrations were 0.22 and 0.98 mkg/mkl respectively.

Another important fine point is the microfluidic system. Due to a complicated structure design and the need of operating with electrolytes, a PDMS container-type microfluidic system was constructed on the surface of the device. It also prevents the evaporation of the 0.5 mkl solution drop from the device surface.

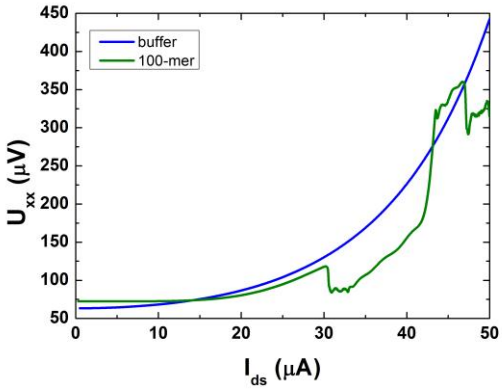

Figure 2: Uxx curves. Signal from Uxx electrode versus Isd DC, comparison of the oligonucleotide and non-oligonucleotide cases. Measurement was done at room temperature under the stabilization of the Drain-Source current.

The U-I characteristics were measured under the stabilization of the Drain-Source current within frameworks of the Hall geometry of Silicon nanosandwich. The changes of longitudinal Uxx and lateral Uxy (Hall) voltage appeared to demonstrate the resonant behavior (Fig.2, Fig.3) as a function of the Ids value. Besides the Ids steps are revealed that allows the definition of the frequency generation (f) using the relation f = I/en, where n is the number of holes in edge channels.

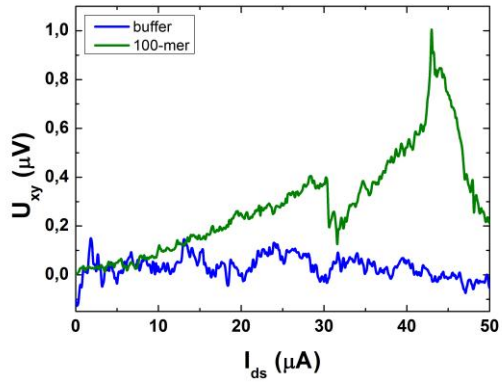

Figure 3: Uxy curves. Signal from Uxy electrode versus Isd DC, comparison of the oligonucleotide and non-oligonucleotide cases. Measurement was done at room temperature under the stabilization of the Drain-Source current.

Finally, the Raby splitting in the U-I characteristics was found under the deposition of the oligonucleotides, with the identification of their self-resonant modes.

The reported study was partially supported by RFBR, research project No. 13-00-12055 ofi_m.

References:

Jonathan M. Rothberg et al., (2011) An integrated semiconductor device enabling non-optical genome sequencing, Nature, Vol. 475.

Toumazou C. *et al*. (2013) Simultaneous DNA amplification and detection using a pH-sensing semiconductor system, *Nat*. *Methods* 10, 641–646.

I Lundstrom, M S Shlvaraman, C S Svenson and L Lundkvlst, (1975) Hydrogen-sensltlve MOS field effect transistor, Appl Phys Lett 26, 55 – 57

N.T. Bagraev, L.E. Klyachkin, A.A. Kudryavtsev, A.M. Malyarenko, V.V. Romanov, (2010) Superconductor Properties for Silicon Nanostructures. In "Superconductor", edited by A. Luiz, SCIYO, chap.4, p.p. 69-92.

N.T. Bagraev, L.E. Klyachkin, A.M. Malyarenko, B.A. Novikov (2007) Infrared and theraherz nanoelectronic devices for biology and medicine // Innovations Vol. 12 (110), C. 99-104.

Novel Fractal Metamaterial subwavelength structure for sensors application

Y Trabelsi[1], H Alkorre[2], J Stiens[3], M Kanzari[4] and R Vouncks[5]

[1,4] *Univesity of Tunis ELManar, National Engineering School of Tunisia (ENIT), Tunisia*
[2,3,5] *Vrije Universiteit Brussel, Belgium, Pleinlaan 2 ,1050 Brussel.*

Abstract:

The fractal metamaterial configurations , operating at the millimeter-wave scale are studied , in terms of design, fabrication and characterization.
Microwave sensors based on modified split-ring resonator (FSRR) structure operating at 140 GHz achieve a novel metamaterial where the resonance frequency is sensititive to specific geometric structure. Furthermore, we attainted a high transmittance left-handed band, achieved by the fractal process derived from conventionnel split ring resonators.
The resonance is more sensitive to the variation of the of the thin film thickness , width of metal SRR ,particular geometrical parameters and fractal order.
Both the double SRR structures and the influence of different geometrical parameters are investigated.The changes in the resonances frequency are examined upon variation of fractal geometrie inside the basic SRR cell.

Keywords :
Metamaterial ; sensing ; Thin-film sensor; Split Ring resonators, Fractal SRR ..

Introduction

Metamaterials are a new class of ordered composites that reveal particular properties not readily observed in nature. This type of materials contain a wide set of artifcially structured composites with tunable ε_{eff} and μ_{eff} that are inaccessible or difficult to obtain with naturally occurring materials. Moreover, metamaterials can manipulate electromagnetic wave beams in surprising ways and exhibit some interesting electromagnetic properties which are not readily offered in nature, such as the propagation of a backward wave component in a certain frequency range due to the so-called Faraday Effect, negative refraction [1] ,sensing [2-4]. The considered material has shown tremendous potential in many disciplines of science and technology.

Among the most sought after properties of metamaterials is the negative index of refraction. These properties arise from qualitatively new response functions that are not observed in the constituent materials and result from the inclusion of artificially fabricated, extrinsic, low dimensional inhomogeneities. Such material exhibits permittivity and permeability both negative and hence they are known as the Double Negative materials [5-7].
Double split ring resonators (SRR) are key components in these materials, also referred to as SRR particle, that provide a negative magnetic response to light.
The fractal acpect impose a similarity and a novel topology of SRR metamaterials and offers an intensely properties such as narrowband resonators [8], high losse and polarisation sensitivity [9].
Due to the interesting performances, the fractal process array have spurred a wide interest in metamaterials research operating in different frequency range and can intensely add a degree of freedom to control of electromagnetic waves on subwavelength length scales [10-16].
In the present work, we propose a microwave sensor design based on the modified split ring resonator (SRRs) array at the millimeter-wave regime.
In this design, a modified geometrical is introduced inside of a conventional square ring, resulting in a special SRR structure. The SRRs' resonance position is highly sensitive to the geometry of all modified metamaterial structure.
The basic specifically types of planar metamaterial slab can exhibit a strong localization and enhancement of fields, which may provide novel tools to significantly enhance the sensitivity and resolution of sensors, and open new degrees of freedom in sensing design aspect.
We can obtain a medium with a controllable fractal order response operating at 140GHz by introducing an artificial periodic array where in repeated elements of the metamaterial slab. The SRR metamaterial cells are composed of metallic-dielectric structures of square shapes. Moreover, the magnetic resonance of considered structures can be used to

obtain negative permeability (μ<0) and negative permittivity (ε<0).

Design , simulation and fabricated fractal thin film SRR

Design and simulation

The fundamental parameters of the medium : electric permittivity (ε) and magnetic permeability (μ) can be achieved from S parameters and using the interest ENZ approach is noted in the so-called epsilon-near-zero (ENZ) metamaterials, which possess a number of interesting properties associated with the near-zero permittivity [17,18].

In the basic SRR metamaterial the reflection/transmission coefficient measured in free space for the normally incident plane wave can be related to the parameters Γ and T by the following equations[8]:

$$S_{11} = \frac{\gamma(1-T^2)}{1-\gamma^2 T^2} \; ; \; S_{21} = \frac{T(1-\gamma^2)}{1-\gamma^2 T^2}$$

Where Γ and T are respectively the reflexion coefficient of the air sample interface and transmission coefficient. Also a typical investigation of the properties of ENZ materials and their interesting wave interaction properties have been studied in [17,18]. Metamaterial LHM Design using artificial substrate is patterned on Quartz Glass.

With relative permittivity ε_r=3.78 and dielectric loss tangent tan(δ)=0.027 .

We investigated two split-ring resonator structures consisting of two concentric square-shaped rings with two gaps at opposite sides. The rings are designed to show LHM behaviour at D-band frequency range, the geometric parameters (shown in Figure 1) witch represent the basic double split ring resonator (DSRR).

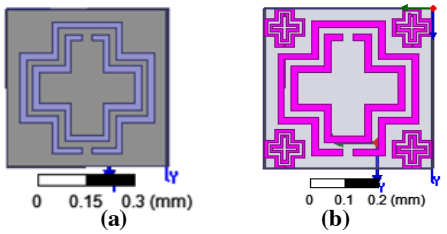

Figure 1: Top view of Geometrical Configuration metamaterials resonators of (a) : First fractal metamaterial (FFM) cell and (b): Second Fracal metamaterial (SFM) cell derived from SRR metamaterials.

For the design procedure, one unit cell of the metamaterial was positioned inside a waveguide with the setting of PEC and PMC boundary conditions at its side-walls to support a constant profile transverse electromagnetic wave. Waveguide ports were placed at the entrance and exit of the waveguide, serving as source and detector, respectively, for the GHz radiation perpendicularly incident on the sample.

The incident electromagnetic wave propagates along x direction, while the electric field (E) is kept along y direction and the magnetic field (H) is kept along the z direction (shown in Figure 2).

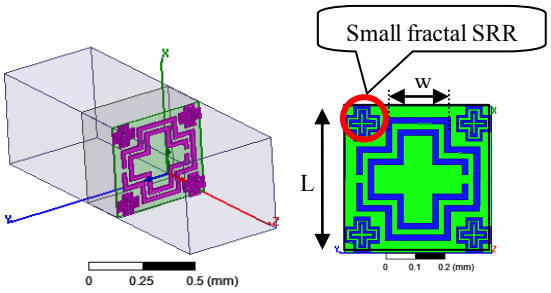

Figure 2: Design of two dimensional unit cell corresponding Second Fractal metamaterial (SFM) with thin film inserted beneath of the modified split ring resonator metal.

Transmission spectrum of the fully periodic symmetrical fractal SRR unit cell shown in figure 3 is simulated by HFSS over the frequency range from 110 GHz to 170 GHz by using PEC and PMC boundary conditions.

Excitation to LHM is given by wave port. The perfect electric conductor (PEC) type boundary conditions are applied at those surfaces of the computational volume which are perpendicular to the incident electric field vector. Similarly, perfect magnetic conductor (PMC) type boundary conditions are applied at those surfaces of the computational volume which are perpendicular to the incident magnetic field vector. The structure is placed inside an D-band waveguide with dimensions of 400 μm × 400 μm × 350 μm to investigate resonance frequency shift in different cases by simulation technique.

The novel SRR shaped thin film sensor design exhibits a dip on resonance in their transmission spectra. Furthermore, the proposed sensor can provide high sensitivity level and make it abundant technique for favorable sensors application.

It can be observed from different configurations a distinct magnetic resonant for zero reflexion coefficient where the resonant frequency shift with fractal order and further a geometries configuration. We noted that a high resonance level order -30 dB find around the operating frequency , precisely at 144GHz.

A thin film are putted under the substrate able to produces large and easily detectable change in the resonant frequency. It's clear that , the resonant frequency is tunable by the design and its quality depends on the geometric parameters.

The magnetic field distributions of the resonance modes are shown as insets in figure 3. To study the effects of the width of the thin film put in the underside split ring resonators on the response of the filter, three cases are considered. The spectrum clearly depends on the thicknesses of the thin film of silicon with relative permittivity ε_r=11.9.

By increasing the thicknesses the resonance shifts downwards as shown in figure 3. When the thicknesses is 8 μm the SRR resonate around 140 GHz. Moreover, the resonance frequency shift of this material is particularly sensitive to the changes in the SRR capacitance, which creates identical SRR using at microwave thin film sensing applications.

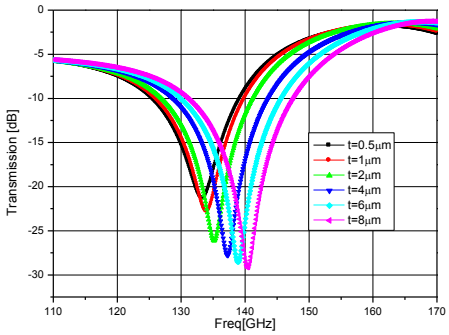

Figure 3: Transmission spectra of the 2nd order Fractal SRR unit cells for different thin film deposited a top of Quartz substrate thicknesses

The second Fractal metamaterial SRR capable to provide good adjustment between the operating frequency and increasing in magnetic resonance. The value of resonance frequency can be adjusted by changing design parameters such as metal width for each small cells added (Figure 2).
When we increase the metal width of modified split ring resonator the transmission dips T_R[dB] for corresponding resonnant frequency decresase with *increase* in a metal width.

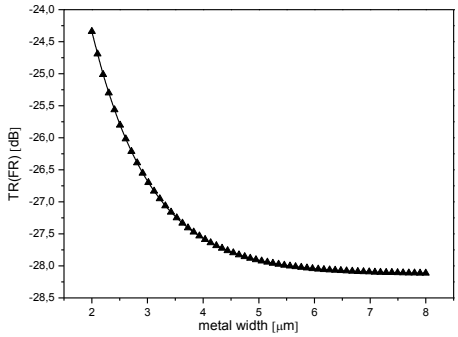

Figure 4 : Variation of resonant frequency further the metal width of separate small forms added by applying the fractal process at second order.

The resonance is interpreted in terms of the effect of electric excitation of magnetic resonance when the incident light is polarized perpendicularly to the plane of split ring resonators SRR and penetrate at the array at normal incidence . Consequently the splits play a key role in attaining magnetic resonance. The induced circulating currents inside the SRRs are still acceptable to flow but cannot oscillate independently of the external electromagnetic field any more.
In fact , a magnetic flux probing the metal rings will induce rotating currents in the rings, which create their peculiar flux to improve or oppose the incident field.
Owing to splits in the SRR, the resonator can support various resonant wavelengths much higher than the diameter of the rings. This does not happen in closed rings. The space between the rings produces huge capacitance values which lower the resonating frequency. The dimensions of the structure are small matched to the resonant wavelength.

Measurement and Fabrication :

The material consists of a two-dimensional array of repeated unit cells of aluminium strips and split ring resonators on interconnecting and disconnecting strips of standard circuit material. By measuring the transmission spectrum of the reflexion through a SRRs aluminum stroked at atop of Quartz substrate , we determine the effective n, appropriate to relation : $Z = \mu\,\varepsilon$.
The considered fractal SRR metamaterialwere fabricated by Liftoff micro-fabrication techniques. 500nm metal thick SRRs structures made of aluminium were patterned on-Quartz glass with thickness of 350 μm.
Figure 5 shows the photograph of a portion of the structure we have fabricated and tested.

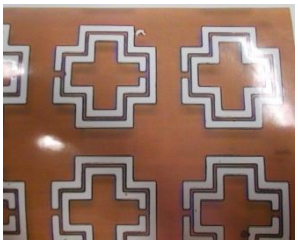

Figure 5: Portions of optical microscope images of metamaterial Fractal SRRs arrays.

The resonance by Fractal SRRs arrays was verified simply by measuring the transmission spectrum. Transmission measurements were performed by using two waveguides as a transmitter and a receiver, which were connected to the vector network analyser AB millimeter 8-350-2 (VNA) in the frequency range of 110 to 170 GHz.
In this method a specially fabricated sample holder is positioned by Mobil support that focuses the center of slab in the center of input beam antenna. After that we performed a through-reflect-line (TRL) calibration. The measurement in free space is done using the S-parameters through the Vector network analyzer (VNA) and starting the characterization measurements, where the two horn antennas were connected to a two port HP8510C vector network analyzer. For a whole characterization of a planar sample, the measure of S-parameters are used to find the permittivity and permeability of the materials with the help of equations.

Conclusion :

The fractal split ring resonator microwave metamaterials are designed, fabricated, and studied experimentally and theoretically. The amplitude of the transmission dips at the resonance frequencies increases gradually as the fractal order and thickness thin film increases, which indicate different types and emplacement of resonance frequencies.The measurements are carried out using quasi-optical technique in mm-wave frequency range.
The influence of the resonance strength tenability of SRRs-square fractal on left handed material is investigated though using the ENZ approach. The results show that the increas-

ing fractal level of the square SRRs results in the sharp resonant frequency in D band structure. The new type of artificial structures using fractal SRR components that exhibit both negative effective permittivity, and effective permeability.

References :

[1] M. Kang, J. Chen, H.-X. Cui, Y. Li, and H-T. Wang , "Asymmetric transmission for linearly polarized electromagnetic radiation," Opt. Express, Vol. 19, pp.8347-8356, 2011.

[2]Tao Chen , Suyan Li and Hui Sun , "Metamaterials Application in Sensing, Sensors 2012.

[3]Y. Ma, Huaiwu Zhang, Y. Li, Y. Wang and W. Lai , "Terahertz sensing application by using Fractal geometries of split ring resonators ", Progress In Electromagnetics Research, Vol. 138, 407-419, 2013.

[4] N. Naeem, N. Ismail, A. Alhawari, A. Reda Hassan Mahdi and M. Adzir , "Subwavelength negative index planar terahertz metamaterial arrays using spiral split ring resonators for near field sensing",International Journal of Applied Electromagnetics and Mechanics, Vol. 47, No. 3, 2015.

[5] D. R. Smith, W. J. Padilla, D. C. Wier, S. C. N. Nasser and S. Schultz, "A composite medium with simultaneously negative permeability and permittivity ", Physical Review Letters, Vol.84, No. 18, pp. 4184-4187, 2000.

[6] [Soukoulis, C. M. Soukoulis, S. Linden, and M. Wegener, "Physics: negative refractive index at optical wavelengths, Science", Vol. 315, 47-49, 2007.

[7] Zhe Wu, Jinfeng Zhu,Mingquan Jia, Haiping Lu and Baoqing Zeng , "A double-layer metamaterial with negative refractive index originating from chiral configuration " , 2010.

[8] F. Miyamaru, , Y. Saito, M. Takeda, B. Hou, L. Liu, W. Wen and P. Sheng , " Terahertz electric response of fractal metamaterial structures", Phys.Rev.B.,Vol.77, No. 4, 2008.

[9] Y. Ma, H.-W. Zhang, Y. Li, Y. Wang, and W. Lai, ,"Terahertz sensing application by using fractal geometries of split ring resonators",Vol. 138, Progress In Electromagnetics Research, Vol. 138, 407-419, 2013.

[10] De la Mata Luque, T. M., N. R. K. Devarapalli, and C. G. Christodoulou,"Investigation of bandwidth enhancement in volumetric left-handed metamaterials using fractals," Progress In Electromagnetics Research, Vol. 131, 185-194, 2012.

[11] He-Xiu Xu, Guang-Ming Wang, and Chen-Xin Zhang, "Fractal-Shaped Metamaterials and Applications to Enhanced-Performance Devices Exhibiting High Selectivity", International Journal of Antennas and Propagation, 2012.

[12] H.X. Xu, G.M. Wang, and C. X. Zhang,"Fractal-shaped UWB bandpass filter based on composite right/left handed transmission line", Electronics Letters, 2010.

[13] Yanbing Ma, Huaiwu Zhang, Yuanxun Li, Yicheng Wang and Weien Lai,"Terahertz sensing application by using Fractal geometries of split ring resonators", Progress In Electromagnetics Research, 2013.

[14] G. Volpe,G. Volpe and R. Quidant, "Fractal plasmonics: subdiffraction focusing and broadband spectral response by a Sierpinski nanocarpe", Optics Express, 2011.

[15] F. Miyamaru,Y. Saito, M. W. Takeda, B. Hou, L. Liu,W. Wen and P. Sheng, "Terahertz electric response of Fractal metamaterial structures," Phys. Rev. B., Vol. 77, No. 4, 045124, 2008.

[16]. De la Mata Luque, T. M., N. R. K. Devarapalli, and C. G. Christodoulou, "Investigation of bandwidth enhancement in volumetric left-handed metamaterials using fractals," Progress in Electromagnetics Research, Vol. 131, pp.185-194, 2012.

[17] M. Massaouti, A. Basharin, M. Kafesaki, M. F. Acosta, R. I. Merino, V. M. Orera, E. N. Economou, C. M. Soukoulis, and S. Tzortzakis , "Eutectic epsilon-near-zero metamaterial terahertz wave guide, " Optics Letters , Vol. 38, Issue 7, pp. 1140-1142, 2013.

[18] Andrea Alù, Mário G. Silveirinha, Alessandro Salandrino, and Nader Engheta, "Epsilon-near-zero metamaterials and electromagnetic sources : Tailoring the radiation phase pattern" , Physical Rewiew B 75, 2007.

Acknowledgments

The authors gratefully acknowledge the financial support provided by European Science Foundation (ESF). Also, the first author grateful all member of LAMI ETRO VUB, in particular Prof. Dr. Ir. Johan Stiens for this positive and cooperative attitude. Many thanks go also to Prof. Mounir Kanzari from LPMS laboratory, National engineering school, Tunisia.

BioConjugated Gold Nanoparticles for Enhaced Delivery and Cellular Uptakes

K. Rahme,[1,2,3*] J. Guo,[4] C. M. O'Driscoll,[4] J. D. Holmes[2,3]
[1] Department of Sciences, Faculty of Natural and Applied Science, Notre Dame University (Louaize), Zouk Mosbeh, Lebanon kamil.rahme@ndu.edu.lb
[2] Materials Chemistry and Analysis Group, Department of Chemistry and the Tyndall National Institute, University College Cork, Cork, Ireland
[3]Centre for Research on Adaptive Nanostructures and Nanodevices (CRANN), Trinity College Dublin, Dublin 2, Ireland
[4] Pharmacodelivery group, School of Pharmacy, University College Cork, Cork, Ireland

Abstract: Gold nanoparticles (AuNPs) hold the potential of being potential candidates for biomedical application especially as the contrast agent in bioimaging and drug delivery vehicles. Successful delivery of therapeutic cargos require the high cellular uptake of nanoparticles (NPs). In this study AuNPs with diameters 15, 30 and 80 nm were synthesised in water through chemical reduction of HAuCl4. The resultant AuNPs were characterised using UV-visible Spectroscopy, dynamic light scattering (DLS) and electron microscopy (EM). Protein (Transferrin) was successfully grafted onto AuNPs through an ethylene glycol linker as confirmed using DLS and EM. Moreover, study on cellular uptakes on ~ 30 nm AuNPs has shown that Transferrin (Tf) enhanced cellular uptake of AuNPs relative to untargeted AuNPs. The enhanced cellular uptake suggests that AuNPs-Transferrin may facilitate drug delivery via the ligand-receptor mediated pathway.

Keywords: gold nanoparticles, polyethylene glycol, protein, drug delivery, cellular uptake, biomedical applications.

Introduction

Gold nanoparticles (AuNPs) have demonstrated promising properties for biomedical applications. These properties includes size and shape dependent optical properties originated from the surface plasmon resonance band, chemical stability, a low cytotoxicity and an ease of bioconjuguation (Cobley et al, 2011). Moreover, the nanoscale nature of AuNPs provides opportunities to interact with biomolecules (i.e. antibodies, nucleotides, peptides, proteins) and living cells. Therefore, AuNPs have received considerable attention for a wide range of applications in optoelectronics, diagnostics, thermal therapy, drug and gene delivery and have contributed to the advancement of bionanotechnology (Tiwari et al; 2011; Alkilany et al; 2011). Attachment of neutral polymers such as polyethylene glycol (PEG) has been shown to increase the biological stability of NPs. However, attachment of PEG can dramatically decease the cellular uptake of NPs (Pozzi et al; 2014). To overcome this issue, PEGylated Au NPs can be conjugated with bioactive targeting ligands to facilitate site-specific delivery via ligand-receptor mediated endocytosis. In this study we extend our previous work on conjugation of AuNPs with proteins, where ApoE, BSA and Transferrin were grafted onto AuNPs through an ethylene glycol linker (Rahme et al.; 2014). Our results demonstrated that Transferrin (Tf) can enhance cellular uptake of Au NPs compared to untargeted Au NPs.

Materials and methods

Sodium citrate, sodium hydroxide ascorbic acid Tetrachloroauric acid trihydrate ($HAuCl_4.3H_2O$), 4,7,10,13,16,19,22,25,32,35,38,41,44,47,50,53Hexa decaoxa-28,29-dithiahexapenta-contanedioic acid di-*N*-succi-nimidyl ester, NHS-PEG-S-S-PEG-NHS with n=7 were purchased from Sigma Aldrich, and used as received.

Preparation of Gold Nanoparticles: 15 nm Au NPs were obtained by the Turkevich and Frens method using sodium citrate as both reducing and stabilising agent at high temperature (Au NPs-citrate), while AuNPs with diameter around 30 nm were formed using ascorbic acid as reducing agent in presence sodium citrate as stabilizer (Rahme et al.; 2013), and 80 nm AuNPs were formed using hydroxylamine-O-sulfonic acid at room temperature and in the presence of sodium citrate as stabilising agent (Rahme et al.; 2014).

PEGylation of Gold Nanoparticles: PEGylation was performed by adding PEG_{280}-S-S-PEG_{280}-NHS to the AuNP solution, stirring was maintained for 2 hours.

Protein bioconjugation: The pH of the Au NPs-PEG-NHS solution was adjusted to pH 7.5~9 with NaOH (0.1 M) solution, followed by the addition of the protein solution (~50 protein/particle) in citric buffer to the Au NP colloidal solution. The solution was left to react under stirring overnight at 4 °C prior to DLS measurement.

Fluorescin conjugation on AuNPs-Transferrin
To 4 mL of the solution AuNPs-Transferrin, was added (400 micrL of a freshly made solution (~ 1.5 mg for Fluorescin isothiocyante in 15 mL PBS buffer at pH 9), and left to stirr at 4 °C in the dark over night.

Cellular uptakes: : Prostate cancer PC3 cells (50,000 per well) were seeded in 12-well culture plates with glass bottoms (MatTek™) for 24 hr. 10 µg AuNPs were then applied to cells within 2 mL growth medium containing 10% FBS (fetal bovin serum, Sigma) and incubated under the normal growth conditions for 24 h. Following incubation, the media was replaced with fresh growth medium and live cells were observed using an Olympus FV 1000 microscope. Fluorescein was detected using excitation at 488 nm and emission of 505–530 nm (green).

Results and discussion

AuNPs with mean diameters of 15 nm were synthesised in water using a controlled chemical reduction of a $HAuCl_4$ solution with sodium citrate at high temperature. While AuNps of diameter ~ 30 and 80 nm were obtained at room temperature in the presence of sodium citrate as stabilising agent, using ascorbic acid and hydroxylamine-O-sulfonic acid as reducing agents respectively. In fact it is well known that citrate can not reduce Au^{3+} at room temperature (Rahme et al.; 2014). The obtained AuNPs have shown size dependent optical properties as verified from UV-visible spectroscopy, while TEM and DLS verified that the nanoparticles were with low polydispersity. Results in Figure 1 showed the size distribution in number from DLS on ~ 30 nm AuNPs before and after grafting Transferrin, the slight increase in size is a proof of successful bioconjugation of protein onto AuNPs.

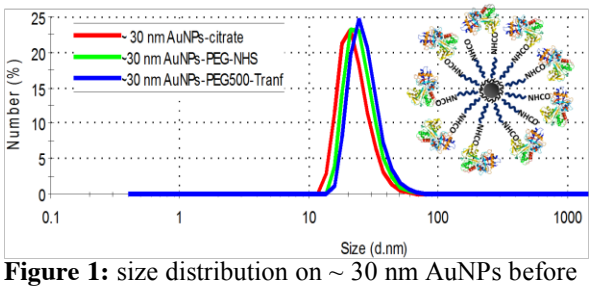

Figure 1: size distribution on ~ 30 nm AuNPs before and after bioconjugation with transferrin, the inset is a schematic illustrating the final nanparticle structure with an ethylene glycol and protein coating.

Transferrin is well known to bind Transferrin receptor (TfR) that is normally overexpressed on certain cancer cells (i.e. breast, colon and prostate cancer). The Tf-targeted delivery systems may facilitate cellular uptake via ligand-receptor mediated endocytosis (Daniel et al., 2012). In Figure. 2A, AuNPs-Tf achieved significant higher cellular uptake in PC3 cells (TfR-positive cells) in comparison with non-targeted counterpart, suggesting that the internalisation of AuNPs- Tf was due to ligand-receptor mediated pathway. In addition, when PC3 cells were treated with AuNPs-Tf Fluorescein the green fluorescence was observed inside cytoplasma, further comfirming internalisation of AuNPs (Figure. 2B).

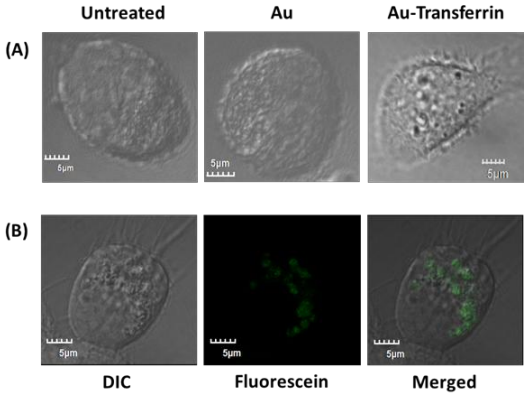

Figure 2: (A) Internalisation of AuNPs and AuNPs-Tf in PC3 cells following 24h post-transfection. The dark areas (gold) were observed in PC3 treated with AuNPs-Tf but not with non-targeted AuNPs. (B) Internalisation of AuNPs-Tf Fluorescein in PC3 cells following 24h post-transfection. These TEM images, left to right represented Differential interference contrast (DIC), Fluorescein, and merged images of DIC and Fluorescein. The data showed that Fluorescein were observed inside cells colocalising with dark areas (gold), suggesting cellular uptake of AuNPs-Tf Fluorescein in PC3 cells.

References:

Alkilany, A. M, Murphy, C. J. **(2011)** Toxicity and cellular uptake of gold nanoparticles: what we have learned so far? *J. Nanopart. Res.*, 12, 2313–2333.

Cobley, C. M., et al., **(2011)** Gold nanostructures: a class of multifunctional materials for biomedical applications. *Chem. Soc. Rev.* 40(1): p. 44-56.

Daniels T. R, et al., **(2012)** The transferrin receptor and the targeted delivery of therapeutic agents against cancer. *Biochim . Biophys. Acta* 1820, 291-317.

Tiwari, P. M., et al, **(2011)** Functionalized Gold Nanoparticles and Their Biomedical Applications *Nanomaterials, 1*, 31-63.

Pozzi. D., Lagana. A., et al. **(2014)** Effect of polyethyleneglycol (PEG) chain length on the bio–nano-interactions between PEGylated lipid nanoparticles and biological fluids: from nanostructure to uptake in cancer cells, *Nanoscale*, 6, 2782-2792.

Rahme, K. and Holmes, J. D. **(2014)** Hydroxylamine-O-sulfonic acid as a New Reducing Agent for the Formation of Nearly Monodisperse Gold Nanoparticles in water: Synthesis Characterisation and Bioconjugation. *NSTI Nanotech 2014 www.nsti.org, ISBN* 978-1-4822-5826-4 Vol. 1, 2014, pp. 147-150.

Influence of gate dielectric materials on electrical characteristics of 3D DG n-FinFETs with different channel materials

N Boukortt[1,2,*], B Hadri[1], L Torrisi[2], S Patanè[2], A Caddemi[3], and G Crupi[3]

[1] Department of Electrical Engineering, University of Mostaganem, 27000, Algeria
[2] Dipartimento di Fisica e Scienze della Terra, University of Messina, 98166, Italy
[3] DICIEAMA Department, University of Messina, 98166, Italy

E-mail: Nour.Boukortt@yahoo.fr

Abstract. This paper investigates the electrical characteristics of the nanoscale n-channel double gate fin field-effect transistor (FinFET) structures and their sensitivity to gate dielectric materials with different channel materials using SiGe and 3C-SiC in the channel region. In this work, the numerical tool Atlas Silvaco was used to simulate the device in three dimensions and evaluate the electrical characteristics of the device at 300K. The influence of the gate dielectrics on threshold voltage roll-off, subthreshold slope, transconductance, DIBL, leakage current, on-current, and On/Off current ratio has been investigated. Our simulation results show that high drain current and transconductance were obtained with SiGe channel material. The results also show that a higher value of gate dielectric constant can increase the drain current and improve the leakage current. DIBL is reduced with the increase in gate dielectric constant. We have obtained different and useful results which led us to the further manufacturing process in order to get the complete device.

1. Introduction

The new technology is oriented towards the miniaturization of electronic components and transistors in integrated circuits. The goal is to integrate more components per unit area and thus improve circuit performance while lowering their manufacturing cost as predicted by the "Moore's Law" [1].

The multi-gate transistors like FinFETs (Fin-Shaped Field Effect Transistor) are considered to be the best candidates to extend the use of CMOS technology beyond the barrier of 14 nm. Double-gate FinFET is considered one of the most promising device structures for future CMOS technology, which provides a better electrical control over the channel and thus allows increasing the device performances [2, 3].

For the FinFET, the body thickness T_{Fin} should be approximately half of the gate length L_G to provide better control of short channel effect (SCE). The drain induced barrier lowering (DIBL), subthreshold slope, and leakage current increase sensibly when L_G/T_{Fin} ratio is smaller than 1.5 [2, 3].

SiGe is an attractive material for advanced CMOS technology due to its enhanced carrier mobility in which the threshold voltage of the SiGe-channel device appears to be smaller with higher drain conductance and higher transconductance compared with Si-channel device [4].

Silicon carbide (SiC) also is a very promising semiconductor due to its physical and electrical properties, it has excellent material properties which make it superior to Si in a wide range of applications. SiC is an ideal choice for manufacturing devices designed to work at high temperature, high power, and high voltage. These properties have garnered increased interest in the use of SiC in many high-performances in micro/nano-technology devices and they are better for 3C-SiC (heteroepitaxial) than for the hexagonal SiC (4H- and 6H-) [5].

The new research introduces the use of high-κ gate materials to manufacture an electrical device in order to improve the current drive and to minimize the gate leakage current which decreases the power consumption. The reason behind using high-κ dielectrics is to improve the electrical characteristics of the device [6].

In this work, we investigate the device structure of a double gate n-FinFET with the channel made either of SiGe or 3C-SiC. In the simulation, the Shockley–Read–Hall (SRH) and Auger (AUGER) models were considered. The influence of the gate dielectric materials on threshold voltage, subthreshold slope, transconductance, DIBL, leakage current, on-current, and On/Off current ratio has been investigated. This study has been performed for four different gate dielectrics which are SiO_2, Si_3N_4, Al_2O_3, and ZrO_2. We observed that the best results are obtained when ZrO_2 is used as a gate oxide material by keeping in mind either speed and power consumption as major targets.

2. Device structure

The schematic structure used for our simulations is represented in figure 1. The different parameters of our structure are assumed as follows in table 1.

Table 1. Parameters of symmetrical DG n-FinFET.

Symbol	Designation	Value
L_D, L_S	Drain length and Source length (Silicon material)	11 [nm]
L_G	Gate length	8 [nm]
L_{ch}	Channel length (SiGe / 3C-SiC material)	10 [nm]
T_{OX} (ZrO_2)	Lateral oxide thickness (gate dielectric material)	1.5 [nm]
T_{FIN}	Fin thickness	4 [nm]
H_{FIN}	Fin Height	10 [nm]
N_A	Channel concentration	10^{16} [cm^{-3}]
N_D	Drain and Source concentration	10^{21} [cm^{-3}]

The DG-FinFET technology is based on vertical silicon fin characterized by the fin length (L_G), fin height (H_{FIN}), and the fin-thickness (T_{FIN}) as shown in figure 1 [7]. The channel region is formed by a little doped with doping concentration 10^{16} cm^{-3} (P-type). The doping concentrations of source/drain regions are assumed to be uniform and equal to 10^{21} cm^{-3} (n-type). The value of the gate work function is 4.6 eV. Figure 1 describes the structure of a DG n-FinFET.

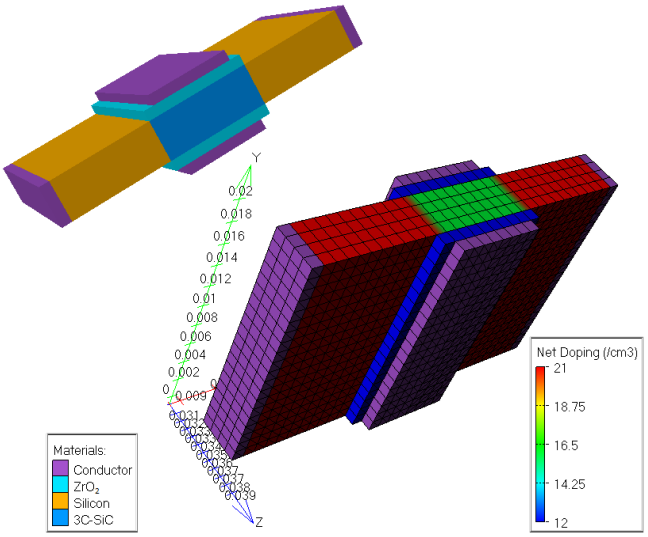

Figure 1. Illustrates the device structure of a DG n-FinFET in 3-D.

3. Device simulation using Silvaco-Atlas

The software package Silvaco-Atlas was used to design, examine, and simulate the structure and characteristics of the DG-FinFET device in three dimensions. The standard recombination models like Shockley–Read–Hall (SRH) and Auger (AUGER) models were considered in the ATLAS simulation. In figures 2 and 3, I_{DS}-V_{GS} transfer characteristics are shown on a linear scale and log scale for a double gate n-FinFET device structure. In figure 2, it is observed that the threshold voltage of a DG n-FinFET is 0.4 V with 3C-SiC channel material and 0.38 V with SiGe channel material at V_{DS} = 0.1 V. The simulation shows that the drain current of SiGe channel is larger than the current of 3C-SiC channel by about 0.54 mA respect to a n-FinFET device at V_{GS} = 1 V. The threshold voltage expression in case of a MuGFET (MultiGate Field-Effect Transistor) device structure can be expressed as [1]:

$$V_{Th} = \Phi_{ms} + 2\Phi_f + \frac{Q_D}{C_{ox}} + \frac{Q_{SS}}{C_{ox}} + V_{in} \tag{1}$$

Where Q_{ss} represents charge in the gate dielectric, C_{ox} is the gate capacitance, Q_D is the depletion charge in the channel, Φ_{ms} represents metal-semiconductor work function difference between the gate electrode and the semiconductor and Φ_f is the Fermi potential which for P-type silicon given by:

$$\Phi_f = \frac{KT}{q} ln \frac{N_A}{n_i} \tag{2}$$

Where k is the Boltzmann constant, T is the temperature, q is the electron charge, N_A is the acceptor concentration in the p-substrate, and n_i is the intrinsic carrier concentration.

When we insert a dielectric material, the capacitance increases by the relative dielectric constant κ. In this case, the capacitance is described by [6]:

$$C_{ox} = \frac{\kappa \varepsilon_0 A}{t_{ox}} \tag{3}$$

Where κ is the dielectric constant of the material ($\kappa = \varepsilon/\varepsilon_0$), ε_0 is the permittivity of free space, t_{ox} is the thickness of dielectric layer.

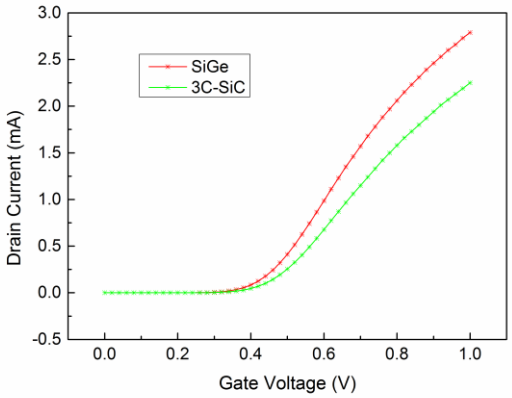

Figure 2. I_{DS}-V_{GS} characteristics on a linear scale for a DG n-FinFET at V_{DS} = 0.1 V.

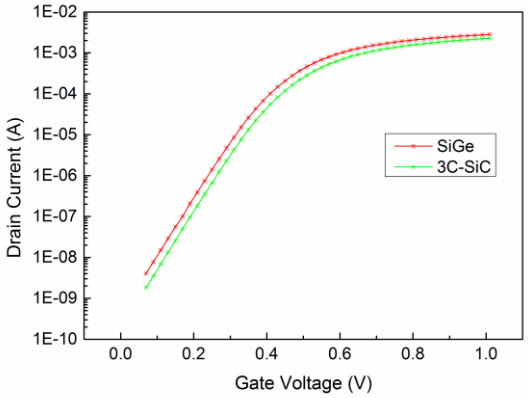

Figure 3. I_{DS}-V_{GS} characteristics on a log scale for a DG n-FinFET at V_{DS} = 0.1 V.

The transconductance g_m quantifies the drain current variation with a gate-source voltage variation while keeping the drain-source voltage constant [8, 9]

$$g_m = \frac{d\,I_D}{dV_{GS}} \tag{4}$$

Therefore, the value of g_m is extracted by taking the derivative of the I_{DS}-V_{GS} curve, the obtained value is 4.82 mA/V of a DG n-FinFET with 3C-SiC channel material and 6.12 mA/V of a DG n-FinFET with SiGe channel material at V_{DS} = 0.1 V and V_{GS} = 0.6 V.

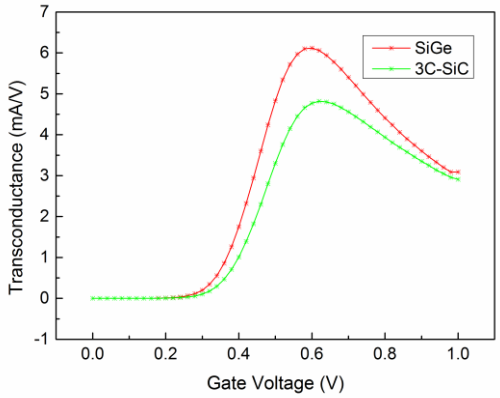

Figure 4. Transconductance versus V_{GS} for a DG n-FinFET at V_{DS} = 0.1 V.

Figure 4 shows the transconductance characteristics of a DG n-FinFET with two different channel materials at V_{DS} = 0.1 V. As can be seen in the figure, also the maximum transconductance of SiGe channel is higher than that of 3C-SiC channel by approximately 1.3 mA/V. These results reflect the faster carrier transport due to SiGe channel material with shorter gate length device (8 nm gate length). On the other hand, the transconductance decreases rapidly with increasing positive V_{GS} for both SiGe and 3C-SiC channel materials.

The subthreshold slope (SS) is the major parameter for calculating the leakage current. Furthermore, SS is calculated as in [8, 9]:

$$SS\ (mV/dec) = \frac{d\,V_{GS}}{d(\log_{10} I_{DS})} \tag{5}$$

A typical value for the SS parameter of a MuGFET is 60 mV /decade, (i.e., a 60 mV change in gate voltage brings about a tenfold change in drain current) [8, 10]. The subthreshold slope of our device is 69.50 mV/decade with SiGe channel material and 69.05 mV/decade with 3C-SiC channel material at V_{DS} = 0.1 V, as it is shown in figure 3.

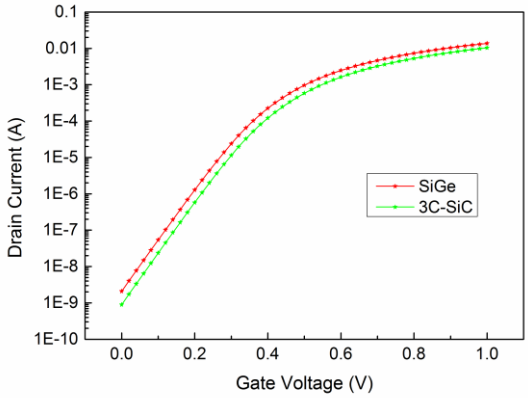

Figure 5. I_{DS}-V_{GS} characteristics on a log scale for a DG n-FinFET at $V_{GS} = V_{DS} = V_{DD}$ and $V_{DS} = 1$ V.

The threshold voltage (V_{th}) is a very important parameter for obtaining a higher on-current, which improves the circuit speed. In figure 5, it is observed that the on-current output is 10.35 mA with 3C-SiC channel material and 13.64 mA with SiGe channel material at $V_{GS} = V_{DS} = V_{DD}$ and $V_{DS} = 1$ V. Furthermore, I_{DS} is calculated as reported in [8]:

$$I_{DS}\,(nA) = 100\,\frac{W}{L}\,e^{\frac{q(V_{GS}-V_{Th})}{\eta KT}} \tag{6}$$

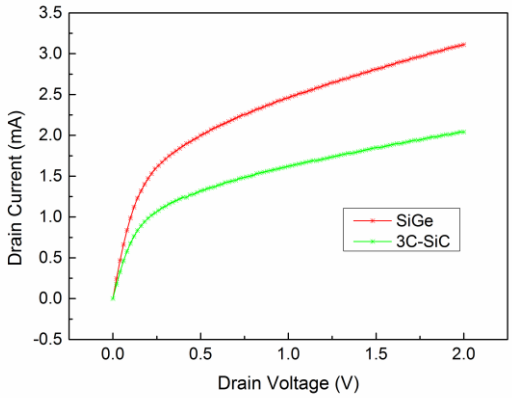

Figure 6. I_{DS}-V_{DS} characteristics for a DG n-FinFET at different channel material.

In figure 6 the measured output characteristics of DG n-FinFET is shown. The highest drain current is obtained by using SiGe material as the channel material.

The leakage current is directly related to the SS. Figure 5 shows that the drain leakage current is 0.89 nA with 3C-SiC channel material and 2.08 nA with SiGe channel material at $V_{GS} = 0$ V and $V_{DD} = V_{DS} = 1$ V. I_{off} calculated by the formula in [8]:

$$I_{off}\,(nA) = 100\,\frac{W}{L}\,10^{\frac{-V_{Th}}{SS}} \tag{7}$$

It is important to keep I_{off} very small, in order to minimize the static power dissipation even when the device is in the standby mode. The ratio I_{on}/I_{off} exceeds 10^6 for our device with two different channel materials, which indicates the excellent on-state and off-state characteristics.

The value of the drain induced barrier lowering (DIBL) is calculated by using the relation reported in [8, 9]:

$$DIBL\,(mV/V) = \frac{\Delta V_{TH}}{\Delta V_{DS}} \tag{8}$$

The DIBL is defined as the difference in threshold voltage when the drain voltage is increased from 0.05 V to 0.1 V. In our case, DIBL is 71.1 mV/V with 3C-SiC channel material and 81.46 mV/V with SiGe channel material for the DG n-FinFET at 8 nm gate length.

4. Effects of gate dielectric materials

The gate dielectric materials play a key role in the design of novel and high performances at nanoscale of electrical devices. It is well-known that high-κ materials are more suitable than the well-known SiO_2 due to the smaller thickness required which decreases the threshold voltage and improves the leakage characteristics of the device. Figure 7 illustrates the subthreshold slope variation for four different gate dielectrics which are silicon oxide (SiO_2, κ = 3.9), silicon nitride (Si_3N_4, κ = 7.55), aluminum oxide (Al_2O_3, κ = 9), and zirconium dioxide (ZrO_2, κ = 25) [6]. Both subthreshold slope and DIBL decrease as gate dielectric constant decreases for two channel materials (SiGe, 3C-SiC) as shown in the figures 7 and 8, respectively.

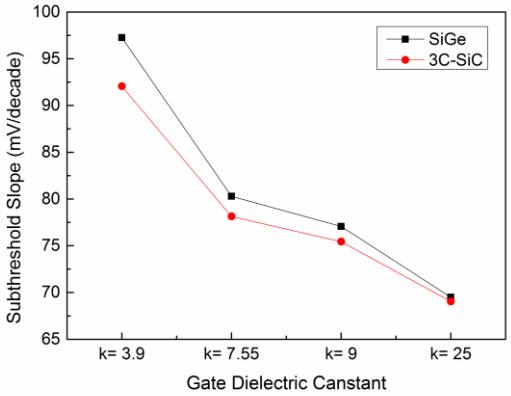

Figure 7. Subthreshold slope variation for different gate dielectrics at V_{DS} = 0.1 V.

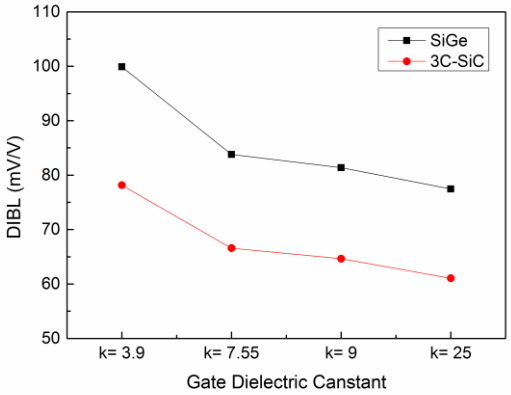

Figure 8. DIBL variation for different gate dielectrics at V_{DS} = 0.1 V.

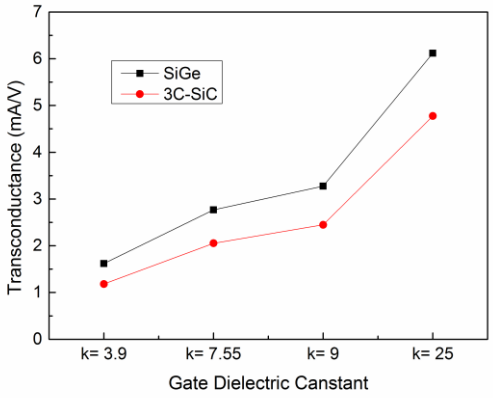

Figure 9. Transconductance variation for different gate dielectrics at $V_{DS} = 0.1$ V.

Figure 9 shows the variation of transconductance with different gate dielectrics at the gate-source voltage V_{GS} for which $g_{m\ max}$ is simulated. It can be seen that transconductance increases with the increase of dielectric constant. We can conclude, as already started, that the channel mobility is higher with a SiGe material, which reduces the parasitic and access resistance. Figures 10-12 illustrate the On-current, Off-current, and I_{On}/I_{Off} ratio characteristics with different gate dielectric constants for a DG n-FinFET, respectively. All these characteristics improve with an increase of dielectric constant κ; we can observe that the best results are obtained when ZrO_2 is used as a gate dielectric. I_{On} is also significant for device performance, I_{On} of SiGe channel material is higher as much as this of 3C-SiC channel material. Therefore, we can conclude that the SiGe channel material can be used to achieve higher on-current than that of 3C-SiC channel material.

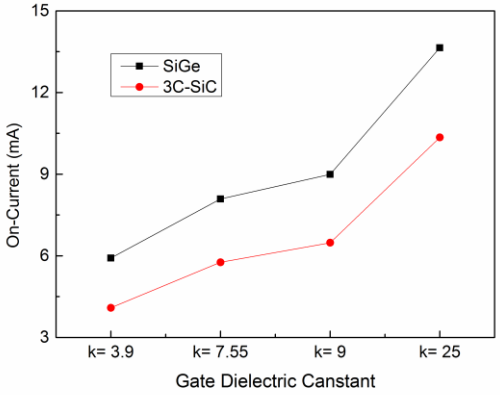

Figure 10. On-current variation for different gate dielectrics at $V_{GS} = V_{DS} = V_{DD}$ and $V_{DS} = 1$ V.

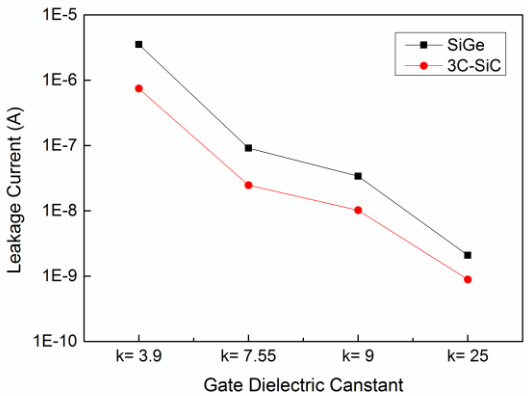

Figure 11. Leakage current variation for different gate dielectrics at $V_{GS} = 0$ V and $V_{DD} = V_{DS} = 1$ V.

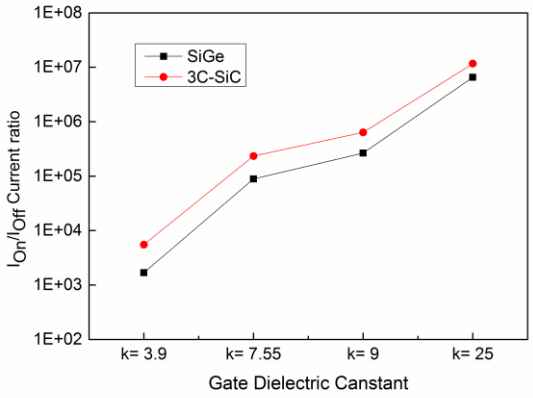

Figure 12. On/Off current ratio for different gate dielectrics.

5. Conclusions

In this work we have used the numerical simulation tool Atlas Silvaco to design, examine, and simulate the two different channel materials of DG n-FinFETs with different gate dielectric materials. As indicated by the three-dimensional simulation results, the carrier mobility of SiGe channel device is higher which the threshold voltage appears to be smaller with higher drain conductance and higher transconductance compared with 3C-SiC channel device. An increased value of κ improves electrical device characteristics.

This nanometer gate device has thus shown to provide improved control of the channel, allowing more efficient reduction of the leakage current at 8 nm gate length.

References

[1] Colinge J P 2008 FinFETs and Other Multi-Gate Transistors (New York: Springer US) p 355

[2] Huang X, Lee W C, Kuo C, Hisamoto D, Chang L, Kedzierski J, Anderson E, Takeuchi H, Choi Y K, Asano K, Subramanian V, King T J, Bokor J, and Hu C 2001 Sub-50 nm P-Channel FinFET *IEEE Trans. Electron Devices* **48** 880

[3] Hisamoto D, Lee W C, Kedzierski J, Takeuchi H, Asano K, Kuo C, Anderson E, King T J, Bokor J, and Hu C 2000 FinFET—A Self-Aligned Double-Gate MOSFET Scalable to 20 nm *IEEE Trans. Electron Devices* **47** 2320

[4] Selvakumar C R and Hecht B 1991 SiGe-Channel n-MOSFET by Germanium Implantation *IEEE Electron Device Lett.* **12** 444

[5] Chung G S, Kim K S, and Yakuphanoglu F 2010 Electrical characterization of Au/3C-SiC/n-Si/Al Schottky junction *J. Alloys Compd.* **507** 508

[6] Ortiz R P, Facchetti A, and Marks T J 2010 High-*k* Organic, Inorganic, and Hybrid Dielectrics for Low-Voltage Organic Field-Effect Transistors *Chem. Rev.* **110** 205

[7] Meinhard C, Zimpeck A L, and Reis R A L 2014 Predictive evaluation of electrical characteristics of sub-22 nm FinFET technologies under device geometry variations *Microelectron. Reliab.* **54** 2319

[8] Mohapatra S K, Pradhan K P, and Sahu P K 2013 Some Device Design Considerations to Enhance the Performance of DG-MOSFETs *Trans. Electr. Electron. Mater.* **14** 291

[9] Mohapatra S K, Pradhan K P, and Sahu P K 2014 Influence of High-k Gate Dielectric on Nanoscale DG-MOSFET *Int. J. Adv. Sci. Technol.* **65** 19

Efficient Design of Flexible and Low-cost Dual Band RFID inkjet printed antenna using silver nanoparticles ink

Ahmed M. Mansour[1,2], Bassant M. Hamza[1,2], Nader Shehata[1,3,4], Mohammed R. M. Rizk[1,2]
[1]Center of Smart Nanotechnology and Photonics (CSNP), SmartCI research center, Alexandria University, Alexandria, Egypt.
[2]Department of Electrical Engineering, Faculty of Engineering, Alexandria University, Alexandria, Egypt.
[3]Department of Engineering Mathematics and Physics, Faculty of Engineering, Alexandria University, Alexandria, Egypt.
[4]Bardley Department of Electrical and Computer Engineering, Virginia Tech, Blacksburg, Virginia, United States.

Abstract: This work aims to fabricate light and flexible antennas, printing techniques are used such as screen and inkjet procedures [1, 2]. In this paper, a dual band RFID is fabricated using new, efficient and low cost printing technique based on commercial inkjet printer. A simple CPW Z-shaped antenna is fabricated on a low cost paper substrate with conductive silver nanoparticles ink which has been selected to implement the antenna shape and to improve the characteristics of the antenna depending on their higher surface to volume ratio [3]. The fabricated antenna has been analyzed using a network analyzer with having dual bands frequency for this shape;one at 780 MHz and the other at 1.4 GHz. The surface morphology of the antenna has been analyzed using SEM with mean diameter of the nanoparticles around 100 nm, uniform surface distribution, and mean thickness of the printed layer around 230 microns. The resistance of the antenna has been improved through annealing up to less than 1 ohm/cm^2. This antenna design can be used for RFID tags and wireless sensor applications [4].

Keywords: printed antenna, inkjet-printing, , silver nanoparticles ink.

I- Introduction

Radio Frequency Identification (RFID) is an important wireless technology that has wide variety of applications, such as mobile radio communication devices. However the currently used fabrication techniques and materials are relatively costive and badly affect on the environment This clarifies how important is the use of renewable, enviromental friendly material in RFID tags and antennas with simple fabrication technique. In this paper, we use feasible and commercial method for printing on extremely low cost substrates for fabricating electronic circuits and RF structures using a normal inkjet printer with avoiding custom and expensive equipment. The used ink is silver Nano-particles inks ensure higher performance of inkjet-printing process. So, we would discuss the printing technique and the analysis of a simple printed antenna via silver nanoparticles ink.

II- Expermintal Work

A simple Z-shaped printed antennas is selected to be the printed antenna design due to its conformability and its higher gain [5-7]. The geometry of the antenna is shown in Fig.1. The paper substrate has relative permittivity of 4.01 and loss tangent of 0.07. The ink is filled via silver nanoparticles ink into a special cartridge to be fitted with the printer. The morphology of the surface is imaged using JEOL SEM. The printed antenna has been analyzed using a network analyzer. The antenna is connected with a SMA connector using conductive tape with resistance equls to 2 Ω / cm.

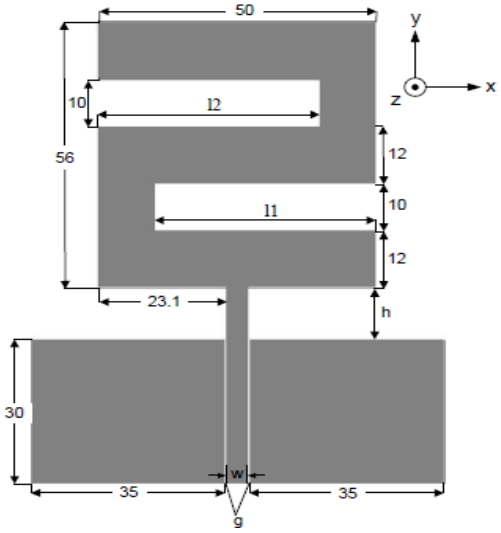

Figure 1: Figure illustrating Z-shaped CPW-fed printed antenna configuration (dimensions in mm)

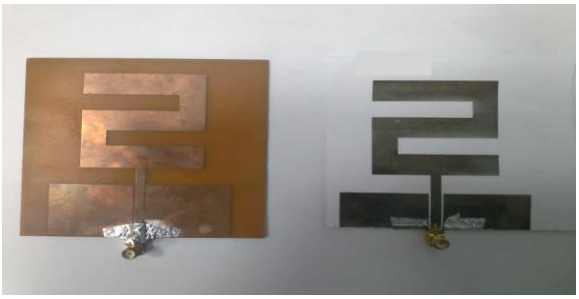

Figure 2: Figure illustrating Z-shaped antenna on glossy paper and PCB.

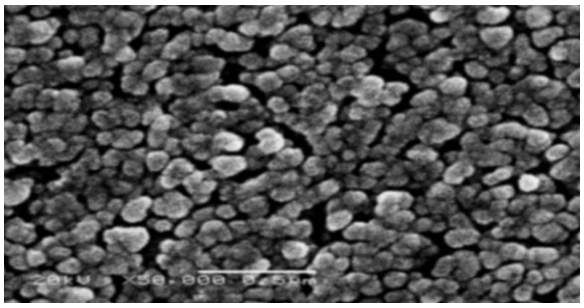

Figure 3: SEM image of the morphology of the antenna's surface

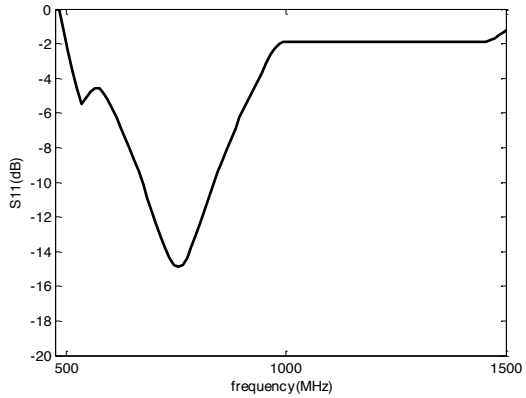

Figure 4: Network analyzer analysis of the printed antenna.

III- Results & Discussions

Both printed antennas on a board and on a glossy paper are shown in Fig. 2. Fig.3 shows the SEM image the morphology of the antenna's surface which is printed on a glossy paper at room temperature. The SEM image shows smooth and uniform morphology. The mean diameter of the nanoparticles is found to be around 100 nm, and the mean thickness of the printed layer around 230 microns. Fig. 4 shows the network analyzer characterization of the printed antenna with a notch band close to 900 MHz.

IV- Conclusion

This paper present an efficient design for RFID inkjet printed antenna on a flexible, low-cost and enviromental friendly material a using silver nanoparticles ink producing a dual band frequencies that can be used in different RFID applications. Our future work is try to testing the effect of expose samples to temperature, printing multilayer and both at different temperature value and how could this affect the return loss, radiation pattern, antenna gain ... etc.

References

[1] Zissis Konstas1, Amin Rida, Rushi Vyas, Konstantinos Katsibas, Nikolaos Uzunoglu1 and Manos M. Tentzeris, " A Novel "Green" Inkjet-Printed Z-Shaped Monopole Antenna for RFID Applications"

[2] Instant Inkjet Circuits: Lab-based Inkjet Printing to Support Rapid Prototyping of UbiComp Devices.UbiComp'13, September 8–12, 2013, Zurich, Switzerland. ACM 978-1-4503-1770-2/13/09.

[3] L.Yang, A.Rida, R.Vyas and M.M. Tentzeris, "RFID Tag and RF Structures on Paper Substrates using Inkjet-Printing Technology," IEEE Transactions on Microwave Theory and Techniques, vol. 55, no.12, part 2, pp. 2894-2901, Dec. 2007.

[4] K.P. Ray and Y. Ranga, "CPW-fed modified rectangular printed monopole antenna with slot," Microwave and Optoelectronics Conference, 2007 IMOC 2007 SBMO/IEEE MTT-S International, pp.79-81, Oct. 29 2007-Nov. 1 2007.

[5] Rod Waterhouse," Printed Antennas for Wireless Communications," ISBN: 978-0-470-51069-8, Oct. 2007.

[6] Johan Sidén and Hans-Erik Nilsson ," RFID Antennas – Possibilities and Limitations ", Radio Frequency Identification Fundamentals and Applications, Design Methods and Solutions, Book edited by: Cristina Turcu, ISBN 978-953-7619-72-5, pp. 324, February 2010, INTECH, Croatia.

[7] NAWALE SAGAR.S. 1M.Tech. Student, E&TC Department, Rajarambapu Institute of Technology, Islampur, Maharashtra, India,"WIDEBAND MICROSTRIP PATCH ANTENNA USING CPW FEEDLINE", Proceedings of International Academic Conference on Electrical, Electronics and Computer Engineering, 8th Sept. 2013, Chennai, India ISBN: 978-93-82702-28-3

Identification of Ductility Function in Titanium Nitride Nanocoating Deposited on Polycarbonate-urethane of Ventricular Assist Device

A. Milenin,[1] M. Kopernik,[1] S. Kąc,[1]
[1]AGH University of Science and Technology, Al. Mickiewicza 30, 30-059, Kraków, Poland

Introduction: The Polish left ventricular assist device (LVAD - RELIGA_EXT) will be made of thermoplastic polycarbonate-urethane (Bionate II) with deposited athrombogenic nano-coatings: gold (Au) and titanium nitride (TiN) (M.Kopernik *et al*.; 2014). The two scale solid numerical model developed in the Polish Artificial Heart Programme in Authors' FEM code was composed of a macro model of blood chamber and a micro model of TiN/Bionate II system (A.Milenin *et al*.; 2009). The input and validation data for the multiscale model was reached in tension test for Bionate II, nanoindentation test and inverse analysis for TiN. Due to the macro model validation, the results of a digital image correlation were compared with the FEM results computed on external surfaces of the blood chamber of LVAD (A.Milenin *et al*.; 2012). However, a fracture occurrence has been observed on the boundary between the coating and the substrate in the LVAD. The FEA of stress and strain states in a micro and a macro scale models has confirmed the possibility of fracture (Figure 1). Consequently, the fracture criterion must be identified. The goal of present work is development of the experimental *in situ* SEM's tensile and micro-shear tests, the numerical model of the tests, and then, its interpretation. The critical strains taken from experiment and considered as the effective strains in the model of test are the values which are the function of triaxiality factors for the tested samples.

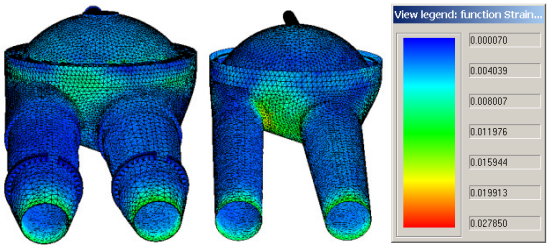

Figure 1: The distribution of strain intensity on external (left) and internal (right) surfaces of POLVAD-EXT chamber (temperature of chamber 25 C, P=37 kPa).

To determine the stress state of the material in the zones of possible fracture the distribution of triaxility factor (k) was modeled. Results (Figure 2) showed that in a location where fracture is possible the amount of triaxility factor is 0.15. For this reason, two types of experiments was developed. Tensile tests were used to evaluate the effect of coating parameters on critical strain. Shear tests were used to determine the critical strain under loading of blood chamber.

The shape of the sample for the shear test (Figure 3) was designed based on the observed condition of the stress state in the blood chamber (triaxiality factor 0.15).

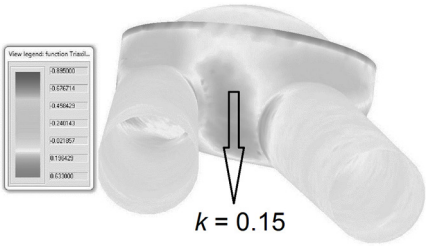

Figure 2: The distributions of triaxiality factor in the FE model on internal surface of blood chamber.

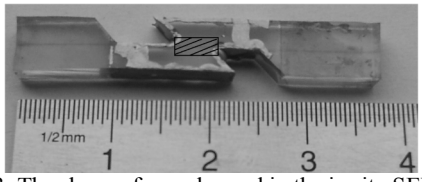

Figure 3: The shape of sample used in the in situ SEM's micro-shear test with marked area by hatched rectangle in the center of the sample.

Experimental part: The tensile and shear tests in a micro chamber for the SEM has been performed in order to calibrate the fracture model of the TiN/Bionate II system for different thicknesses of deposited coating (Figure 4).

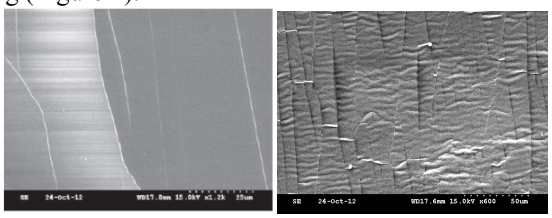

Figure 4: The SEM's image of 50 nm of TiN coating stretched 40 N (left) and 100 nm of TiN coating stretched 60 N (right) with fracture in TiN during tensile test.

The micro-shear and tensile tests was performed directly during the Scanning Electron Microscope (SEM) observation. The center part of each specimen was analysed under SEM. During shear tests the samples were elongated by steps, and tensile force in the range from 0 to 18 N and elongation from 0 to 1356 µm were applied. After each step of elongation the surface of deformed thin film was observed using SEM (magnification from 35 to 12 000 x) in order to detect cracks appearance.

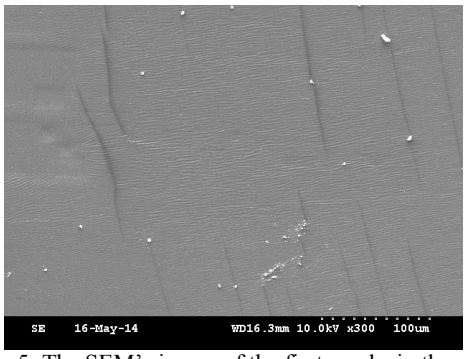

Figure 5: The SEM's image of the first cracks in the micro-shear test (force 8 N).

Multi scale FEM model: Basing on experimental boundary conditions, the micro model of tension test has been developed in the Authors' FE code with implemented fracture criterion. The defined fracture criterion depend on effective strain ε_i and critical deformation function $\varepsilon(k)$:

$$\frac{\varepsilon_i}{\varepsilon(k)} < 1.$$

The interpretation of micro test results: The interpretation of micro tension and shear test results has been done using the inverse algorithm. The FE models of tests were created for determination the conditions of fracture. The variation of values of critical deformation function in the test has been calculated in the stage of the test, in which the initiation of fracture has been occurred. The fracture parameter in each test has been computed. The difference between experimental and computed value of the fracture parameter at the moment of the fracture has been adopted as the objective function. The minimum of the objective function has been reached by a variation of the parameters of critical deformation function.

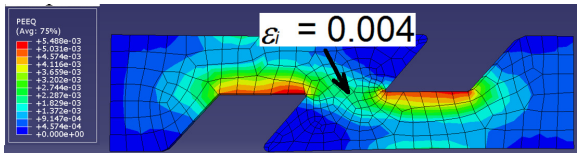

Figure 6: The distributions of effective strain in the FE model of micro-shear test.

Practical implementation: The micro scale model enriched with the fracture model enables the prediction of fracture and the comparison of different variants of macro and micro parameters of the LVADs. For example, numerical model shown, that in one of the designs of blood chamber with an internal pressure 35 kPa having deformation exceeding permissible (Figure 7).

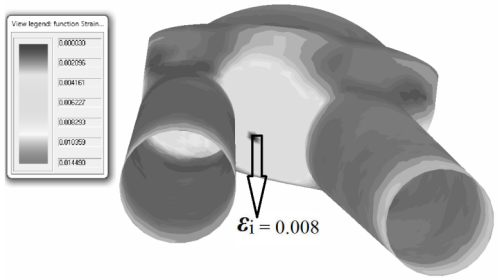

Figure 7: The distributions of effective strain in the FE model of blood chamber (internal surface).

Conclusions:

The multi-scale FE model of left ventricular assist device was proposed for determination of the failure areas of TiN coating.

It was observed that under pressure loading of blood chamber set on its inner surface, the stress state in failure areas is different from linear. For this reason, use of only the tensile test is not enough to fracture model calibration. Therefore, the model of fracture of the TiN coating have to be designed around this stress state.

The physical simulation of the failure area of blood chamber was proposed for a micro-shear test of samples composed of TiN and Au nano-coatings deposited on polymer. The results of FE calculations showed that the value of triaxiality factor in samples used in the micro-shear test is similar to the value reached in the failure areas of blood chamber.

In the experiment and numerical model of micro-shear test the critical strain (effective strain) was determined in the TiN nano-coating and it is 0.004 for triaxiality factor $k = 0.15$.

Keywords: nanocoating, micro tension test, finite element method (FEM), fracture, ventricular assist device (VAD), titanium nitride (TiN).

References:

A. Milenin and M. Kopernik, Multiscale FEM model of artificial heart chamber composed of nanocoatings, *Acta of Bioengineering and Biomechanics*, vol. 11, no. 2, pp. 13–20, 2009.

A.Milenin, M.Kopernik, D.Jurkojć, M. Gawlikowski, T. Rusin, M. Darłak, R. Kustosz, Numerical modelling and verification of polish ventricular assist device, *Acta of Bioengineering and Biomechanics*, 14/3 (2012) 49-57.

M. Kopernik, A. Milenin, S. Kąc, M. Wróbel, Stress-Strain analysis in TiN nanocoating deposited on polymer with respect to Au nanointerlayer // *Journal of Nanomaterials*, 2014, ID 813587, 1-12

Acknowledgements: Financial assistance from the Ministry of Science and High Education of Poland, project AGH no. 11.11.110.291 is acknowledged.

Parametric study on Fiber Bragg Grating for sensitivity improvement

Ishac Kandas[1,2], Nader Shehata[1,2,3], Effat Samir[2], Mohamed Hagras[4], Hatem A. Khater[4]

[1]Department of Engineering Mathematics and Physics, Faculty of Engineering, Alexandria University, Egypt.
[2]Center of Smart Nanotechnology and Photonics (CSNP), Smart Critical Infrastructure (SmartCI) research center, Alexandria University, Egypt.
[3]Bradley Department of Electrical and Computer Engineering, Virginia Tech, United States.
[4]Naval Research & Development Department, Egypt.

Abstract: Recently, Fiber Bragg Gratings (FBGs) are attracting great attention in many applications such as underwater acoustic sensing. In this novel work, it is aimed to improve the sensitivity of FBG through analyzing the relationship between the detected light power and the wavelength shift due to the applied pressure of the acoustic signal. The performance of various apodization profiles has been investigated. Among some selected apodization profiles, Cauchy profile has been proved to give the best performance. Then, by applying to different photodetectors, the results show that InGaAs detector type is more suitable than Ge one. At certain index modulation depth, a maximum wavelength shift is calculated for different lengths of FBG, after which wavelength shift would saturate. These results could be applied in developing the sensitivity of acoustic sensors.

Keywords: Fiber Bragg Grating, apodization profile, photodetector, Acoustic sensor.

Introduction :

Fiber Bragg grating (FBGs) are becoming increasingly important in optical communication systems and sensing applications[1]. Many applications were recorded for FBGs. One of the most vital applications is sensing [2]. Either reflection spectrum or transmission one can be used as a sensing tool. For acoustic emission (AE) detection , Pizo-type sensor (PZT) can be used . Due to its many drawbacks [3], FBG becomes a promising sensor for AE. Simplicity, small size, multiplexing probability , high sensitivity [1, 3] make FBGs being better than PZT in sensing AE. The change on the pressure due to the AE would change the transmission or reflection spectrum. The shift in the FBG wavelength, λ_B is considered an indicator for the pressure change. The operational range and pressure sensitivity are the main targets to enhance the performance of FBG sensor.

Theory :

In the same way of X-ray reflection due to periodic arrangement of atoms , a periodic refractive index variation in the core of an optical fiber will exhibit specific reflections with an angle π (i.e. back-reflection) at the Bragg condition :

$$\lambda_B = 2n_{eff}\Lambda \quad (1)$$

where λ_B is the peak reflection amplitude wavelength, n_{eff} is the effective refractive index of the guided mode and Λ is the grating period. The refractive index of the core of the Bragg grating is given by:

$$n = n_o + \Delta n(z)\cos(\frac{2\pi}{\Lambda}z + \theta(z)) \quad (2)$$

where n_o is the background refractive index of fiber, θ (z) is slowly varying function of z represents the chirp parameter, and Δn (z) is the amplitude of the index modulation along the grating which can be written as :

$$\Delta n(z) = \Delta n h(z) \quad (3)$$

where Δn is the maximum amplitude of the index modulation (index modulation depth), and h (z) is the apodization profile. The used apodization profiles can be found in [4,5]. For sensing AE , two FBGs are used [2]. The transmission of FBG_1 is the input of FBG_2. then, the reflectivity of FBG_2 is detected by the photodetector. The total intensity received by the photodetector is :

$$W = \int \rho(\lambda)\alpha(\lambda)I_s(\lambda)[1-R_1(\lambda)]R_2(\lambda)d\lambda \quad (4)$$

where $\rho(\lambda)$ is the wavelength sensitivity function of the photodetector, $\alpha(\lambda)$ is the light power attenuation factor of the light route , $I_s(\lambda)$ is the intensity of the incident light, $R_1(\lambda)$, $R_2(\lambda)$ are the reflectivity of FBG_1 and FBG_2, respectively. When AE is applied, the pressure will make a shift on FBG1 spectrum and FBG_2 is not affected (is used as a reference). Then, the total received intensity can be written as:

$$W = \int \rho(\lambda)\alpha(\lambda)I_s(\lambda)[1-R_1(\lambda-\Delta\lambda(p))]R_2(\lambda)d\lambda \quad (5)$$

where $\Delta\lambda(p)$ is the wavelength shift due to the pressure p of AE. Another way to increase the sensitivity is to make the FBG_2 affected in opposite way of FBG_1[2]. so,

$$W = \int \rho(\lambda)\alpha(\lambda)I_s(\lambda)[1-R_1(\lambda-\Delta\lambda(p))]R_2(\lambda+\Delta\lambda(p))d\lambda \quad (6)$$

Results and Discussion :

First of all, the apodization profiles were tested to see which one will produce maximum sensitivity . The simulation uses uniform FBG of length 0.75 cm , and index modulation depth of value 2×10^{-4}. Constant response of the photodector was assumed. Also, constant intensity of the incident light (Fig. 1) .

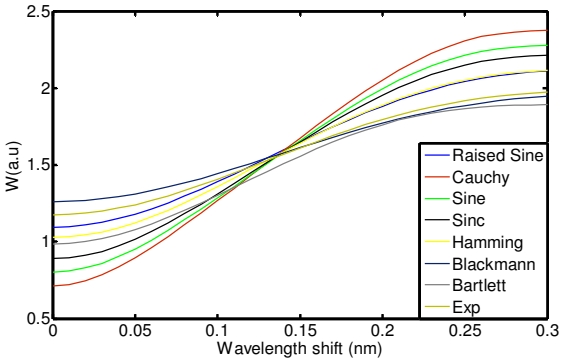

Fig. 1 The received intensity , W for different apodization profiles.

As shown , Cauchy profile is the best one as it provides the maximum slope. Another analysis were done for different types of photodetectors at 1550 nm range . The used photdetectors are Ge, InGaAs. For all cases, the Cauchy profile was applied. we compared the performance of the two photodetectors and the case of constant response (Fig.2). We could find that InGaAs is much better than Ge one.

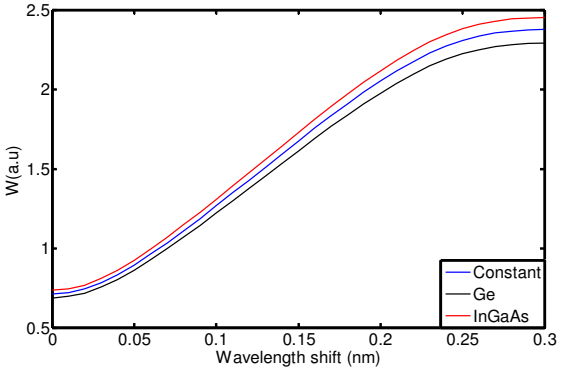

Fig.2 Response of different types of photodetectors

It is important to calculate the maximum wavelength shift before saturation. Figure 3 shows the maximum wavelength shift for different FBG lengths. The two FBGs are used as sensing element.

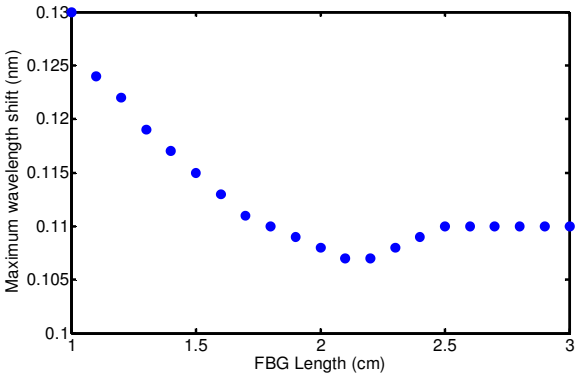

Fig.3 Maximum wavelength shift versus different lengths of FBG.

As seen, increasing the length decrease the maximum shift. . For example, at Δn equals 2×10^{-4}, There is a value (~ 2 cm) after which the maxmium wavelength shift is almost the same.

Conclusion :

The performance of FBG as an acoustic sensor is evaluated. To increase its sensitivity, Cauchy profile is selected among some apodization profiles to modulate the refractive index. Also, InGaAs detector type showed better performance than Ge one. At certain index modulation depth, a maximum wavelength shift is calculated for different lengths of FBG. The calculation of maximum wavelength shift is important for not reaching the saturation region.

References:

[1] Graham Wild and Steven Hinckely, "Optical Fibre Gratings for Acoustic Sensors" Proceeding of 20th International Congress on Acoustic Sensors, ICA (2010).

[2] Xingjie Ni,Yong Zhao, JianYang, "Research of anovel fiber Bragg grating under water acoustic sensor" Sensors and Actuators A **138**, 76-80 (2007).

[3] Dae-Cheol Seo, Dong-Jin Yoon, IL-Bum Kwon and Seung-Suk Lee, "Sensitivity enhancement of fiber optic FBG sensor for acoustic" Proc. of SPIE Vol. 7294 729415:1-10 (2009).

[4] Sher Shermin A. Khan and Md. S. Islam, "Determination of the Best Apodization Function and Grating Length of Linearly Chirped Fiber Bragg Grating for Dispersion Compensation" JOURNAL OF COMMUNICATIONS **7**, 840-846 (2012).

[5] Ishak l. Naguib, Moustafa H. Aly and Ali M. Okaz,"Tunble Third Order Dispersion Compensator Using Nonlinearly Chirped Polymer Fiber Bragg Grating, "ICCTA 2008, Egypt.

Novel Nano Rods of

N-nicotinyl,N ,N -bis(hexamethylenyl)Phosphorictriamide

Nasrin Oroujzadeh[1,*], Elham Delpazir[1]

[1]Institute of Chemical Technology, Iranian Research Organization for Science and Technology (IROST), Tehran, Iran

Abstract

Nano rods of N-Nicotinyl N',N"-bis (hexamethylenyl) phosphoric triamide with formula $C_5H_5NC(O)NHP(O)(NC_6H_{12})_2$ and the diameter of 89.3-123 nm was synthesized and characterized by FT-IR, SEM and EDX methods. The desired nano compound obtained from the reaction of N-Nicotinyl phosphoramidic dichloride with hexamethyleneimine using ultrasonic waves.
Keywords: Nanoparticles, Ultrasonic, Phosphoramide, Nicotinamide, hexamethyleneimine.

1. Introduction

Phosphoramides including -C(O)N(H)P(O)- moiety have received considerable attention due to their unique properties like anti-HIV, anti-HCV, antibacterial and anticancer drugs [1]. Nicotinamide (known also as vitamin PP, pellagra protective, Vitamin B3, etc.) is pyridine type ligand with wide range of chemical and biological applications [2-4] Nicotinamide is a part of the pyridine nucleotides as NADC and NADPC that plays a crucial role in biological oxidative chemistry and is essential for the human body plays a crucial role in biological oxidative chemistry [2,3]. Herein we chose a phosphoric triamide containing N-Nicotinyl group, with formula $C_5H_5NC(O)NHP(O)(NC_6H_{12})_2$. We could successfully synthesized nano rods of this compound using ultrasonic situation, then it was characterized by FT-IR, SEM and EDAX methods. Since nano scale materials have stronger and better properties due to their smaller size, we expect our new synthesized nanoparticles to show better biological and pharmacological activities in comparison to their macro size analogues.

2. Experimental

Synthesis:

Intermediate **A** was prepared by the reaction of phosphorus pentachloride with nicotinamide and one step oxidizing with formic acid. Then a mixture of hexamethyleneimine and acetonitrile, was added drop-wise to a solution of precipitate **A** in acetonitrile at 0 $^{\circ}$C and the mixture was placed in an ultrasonic bath for 3 hs. After

that, the solution was evaporated and the precipitate was filtered and washed with distilled water.

3. Results and discussion

In this work, using ultrasonic method, nanoparticles of a new N-nicotinyl phosphoramide compound with the formula $C_5H_5NC(O)NHP(O)(NC_6H_{12})_2$ was synthesized and characterized by FT-IR, SEM and EDX methods. Results confirmed the desired nano compound. The size and morphology of this compound, obtained from its FE-SEM micrograph (Fig.1), indicates that the diameters of nano rods are in the range of 89.3-123 nm**.**

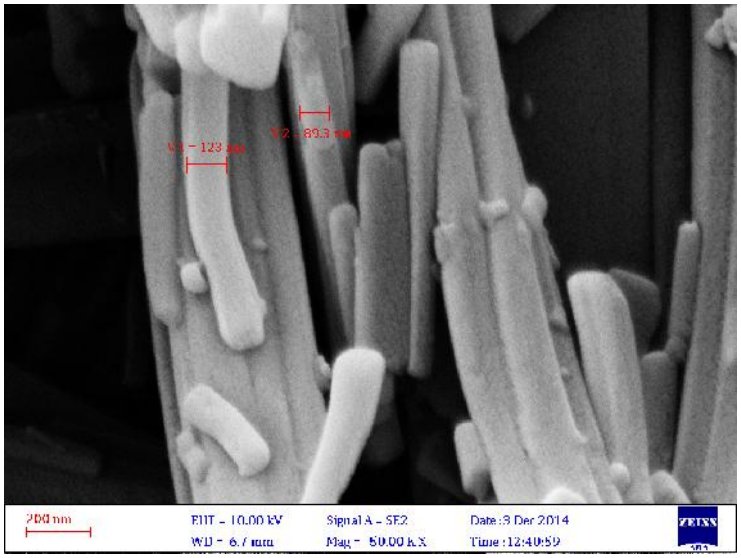

Fig. 1. The SEM image of the synthesized compound

4. Conclusions

Novel nano rods of a phosphoric triamide compound with formula $C_5H_5NC(O)NHP(O)(NC_6H_{12})_2$ and the diameter of 89.3-123 nm synthesized using ultrasonic method and characterized by FT-IR, SEM and EDX methods.

References

[1] Mehellou Y,.McGuigan C,Brancale A, Balzarini J, *Bioorg. Med. Chem. Lett.* 17, 3666 (2007).

[2] Mazzini S, Monderelli R, Ragg E, Scaglioni L, *Chem J. Soc. Perkins Trans* 2, 285(1995).

[3] Magel E.A, Hillinger C, Wagner T, Holl W. *Phytochem.* 57, 1061 (2001).

[4] I.S. Ahuja, I. Prasad, Inorg. Nucl. Chem. Lett. 12, 777–784 (1976).

Study of chairlity by High Resolution Optical Microscope of Si-CNT Prepared by Plasma Sputtering without catalyst

Bassam M. Mustafa, Anwar M. Ezzat and Mohammad M. Uonis

Department of Physics, College of Science, Mosul University, Mosul, Iraq

Abstract: Fabrication of Si-CNT (silicon- carbon nano tube) junction is done by plasma sputtering of Carbon from graphite rods in Argon gas atmosphere, without catalysts for thicknesses 10 – 82 nanometer . Study of images of the specimen by SEM , Raman , x-ray and the energy dispersive x-ray (EDXR) spectra shows peaks characteristics of the carbon nanotubes .Study of chairlity is first done by study of transmission and reflection images of the carbon layer using high resolution optical microscope , then images are amplified more by computer software .Transmission images shows two dimensional nanotubes structures . Images taken by reflection of white light from the carbon layer on Si-C junction, shows clearly zigzag nanotubes chairlity , The second step is making I-V measurements using gold electrodes , Which clearly shows semiconducting behavior ensuring the zigzag chairlity .

Keywords: Carbon nanotubes, Plasma sputtering, Si -C junction, chairlity.

Introduction

Carbon nanotubes (CNTs) have attracted much attention due to their unique properties [1]. Several methods such as arc discharge , laser ablation , and different forms of chemical vapor deposition (CVD) have been used to synthesize CNT [2] . Si wafers are used as substrates for MWNTs or SWNTs carbon nanotubes . Catalysts are used widely , but the fact that no catalyst was largely ignored or forgotten . More recently , a broad array of growth routes using pure carbon systems without any catalyst particle addition have emerged[3].

. In this research we use a somewhat new way to prepare Carbon nanotubes CNTS on Silicon wafer by means of plasma sputtering of the carbon from graphite rods in the presence of a Argon gas without any catalysts[4,5] ,and to study the chairlity of CNT in carbon using high resolution optical microscope and amplification software .The I-V characteristics of the junction have to be studied also.

Experimental method and discussion

Figure (1a) shows cross sectional views of the Si-CNT sample with upper and lower gold electrodes. The samples are studied by SEM and Raman which proves the existence of CNT as in Figures1 a,b and c.

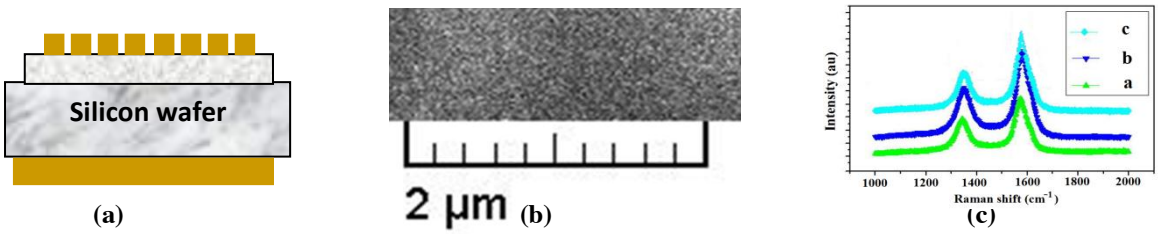

Figure 1: a) cross section of Si-CNT ; b) SEM of CNT layer ;c) Raman spectrum for thickness (10-82 nm)

Study of chairlity is first done by study of transmission and reflection images of the carbon layer using high resolution optical microscope , then images are amplified more by computer software . Figures 2 a and b shows two dimensional Transmission reflection images carbon layer without computer amplification .

.

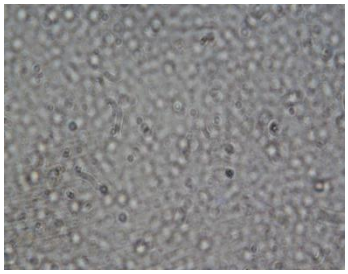

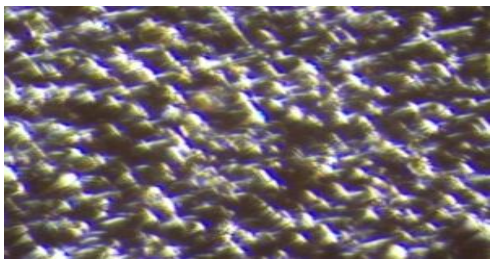

Figure 2: a) shows transmission two dimensional images nanotubes structures; b) shows reflection two dimensional images nanotubes structures

Reflection Images are taken by reflecting white light from high intensity source very near to the objective lens of the optical microscope at acute angle with respect to the carbon layer on Si-C junction, shows clearly zigzag nanotubes chairlity as in figure 3a .

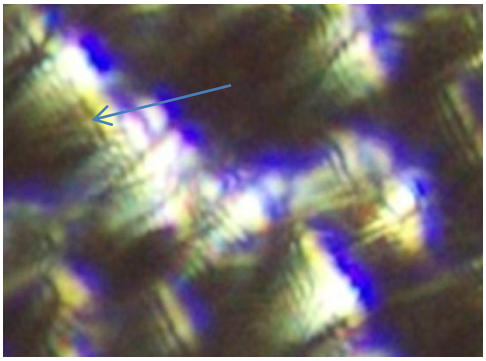

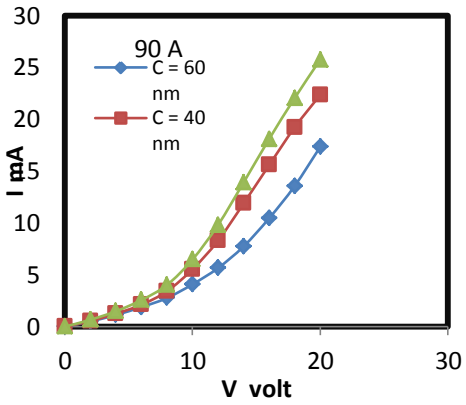

Figure 3 : a) reflection image after 850%amplification showing the zigzag chairlity ; **b)** I-V characteristics of Si-CNT junction using gold electrodes .

To ensure our conclusion about the zigzag chairlity of our CNT , second step was making I-V measurements using gold electrodes , Which clearly shows semiconducting behavior ensuring the zigzag chairlity as shown in Figure 3b .

References

[1] Guifu Zou*, Hao Yang, Menka Jain et al (2009)" C A R B O N , Vol. 4 7 , pp. 9 3 3. –9 3 7 .
[2] Andrea Szabó , Caterina Perri , Anita Csató et al (2010) Materials,V.3,pp 3092-3140. www.mdpi.com/journal/materials .
[3] Mark Hermann Rümmeli1,2*, Alicja Bachmatiuk1et al (2011),. Nanoscale Research Letters Vol. 6: p.303.
[4]Uonis, M. , Mustafa, B. and Ezzat, A. (2014) World Journal of Nano Science and Engineering, ,Vol. 4, pp.90-96
[5]Uonis, M. , Mustafa, B. and Ezzat, A. (2014). World Journal of Nano Science and Engineering, vol. 4,pp.105-11.

Synthesis, Characterization and Catalytic Performance of Supported Nickel Nanoparticles in Methane Steam Reforming

S. Ali, M.J. Al-Marri, M. M. Khader*
Gas Processing Center, College of Engineering, Qatar University, Doha, P. O. Box 2713, Qatar

Abstract: Two nickel based catalysts namely nickel supported on 10wt%silica/alumina (Ni/SA) and nickel nanoparticles dispersed over 10wt%silica/alumina (Ni.NPs/SA) were synthesized and their catalytic activities for the steam reforming of methane were investigated. Ni/SA was prepared using deposition precipitation method while for the synthesis of Ni.NPs/SA nanoparticles were synthesized as a first step and dispersed over the surface of the substrate. Catalysts were characterized using various analytic techniques such as transmission electron microscopy (TEM), nano-scanning electron microscopy (NSEM), X-ray photoelectron spectroscopy (XPS), nitrogen physisorption, temperature programmed reduction (TPR) and temperature programmed oxidation (TPO). Methane steam reforming was carried out in quartz fixed bed reactor (in temperature range between 600-900^{0}C and at atmospheric pressure) connected online to a mass spectrum. Among the catalyst tested, Ni nanoparticles supported on 10wt%SiO_2.Al_2O_3 exhibited better catalytic performances in methane steam reforming than that of Ni/SA. In all temperature studied Ni.NPs/SA catalyst exhibited high methane conversions (100% methane consumption was achieved at operating temperature of 750^{0}C), high selectivities to H_2 and excellent thermal stability. Even under the sever conditions of S/C = 1, at an operating reaction temperature of 750^{0}C (for a period of 60 hours), it showed stability, higher methane conversions, better selectivities to H_2 and excellent resistance to coke deposition as compared to that of Ni/SA catalyst.
Keywords: steam reforming, Ni nanoparticles, coke deposition.
Corresponding: ali.sardar@qu.edu.qa

1. Introduction

Steam **r**eforming of methane is a well established industrial catalytic process which deals with the conversion of natural into synthesis gas or hydrogen which are subsequently transformed chemicals of higher values [1]. Due its activity, ready availability and low cost, Ni-based catalysts are generally are the preferred choices for industrial applications [2]. One of the major issues in design of methane steam reforming is the carbon formation which leads to carbon deposition in different forms such as carbonaceous and filamentous carbon etc [3]. Due to structure sensitive nature of carbon deposition and methane steam reforming, the particle Ni size has been reported to be an important factor for the steam reforming of methane. It has been reported that smaller crystals of nickel possess more open surfaces [4]. Since carbon formation is a structure sensitive reaction and will not proceed when the particle size of nickel is below the critical size and hence smaller Ni particles have been reported [5] to more resistant to coking. In the present work a comparison of coke resistance and stability of conventional Ni based catalyst supported on alumina modified with 10wt% silica with nickel nanoparticles supported on 10% silica-alumina.

2. Experimental

Ni/SA catalysts decorated with three layers of Ni were prepared using precipitation deposition method. Prepared samples were dried overnight at 100^{0}C and calcined at 900^{0}C for 3 hours with slow heating and cooling rates. Similarly Ni.NPs/SA catalyst was synthesized according to the reported literature.

The catalysts were characterized by TEM (Zeiss LIBRA 200 TEM operated at 200kV), X-ray diffraction (XRD), H_2-TPR (Micromeritics).Catalytic performances of the catalysts for methane steam reforming were investigated in a plug-flow fixed-bed quartz reactor connected with online Quadrapole mass spectrum.

3 Results and discussions

For both catalysts metal particles were well distributed over the substrate; however average metal particle size for Ni/SA was found to be bigger compared to that of Ni.NPs/SA. The average metal particle sizes for Ni/SA and Ni.NPs/SA was found to be 18-20 nm and 8-10 nm respectively (Figure 1).

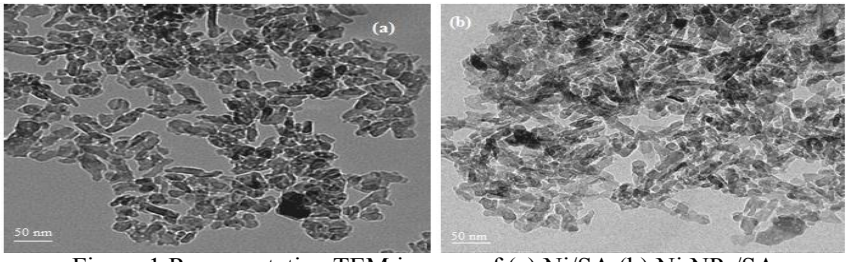

Figure 1.Representative TEM images of (a) Ni/SA (b) Ni.NPs/SA

3.2 Catalytic performances

As demonstrated in Figures 2, both of the catalysts exhibited different catalytic performances. In all temperature ranges Ni.NPs/SA was found to be better in performance in methane steam reforming than Ni/SA. The difference in the catalytic activities could be attributed to the difference in the physicochemical properties of the catalysts. For Ni.NPs/SA there was a linear increase in CH_4 conversion with increase in reaction temperature 650^0C to 900^0C. This trend was in accordance with the literature [6]. For Ni/SA with increase in reaction temperature there was a slight increase in CH_4 conversion in temperature range between 700-750^0C and remained almost constant in rest of the rest temperature ranges. As demonstrated in Figure 2c, for both catalysts the ratios of H_2/CO decreased with increase in operating temperature. Contrary to Ni/SA the effects of temperature on the ratios of H_2/CO were more pronounced for Ni.NPs/SA. Various other researchers have also documented a similar trend of H_2/CO ratios with an increase in reaction temperature [7,8].

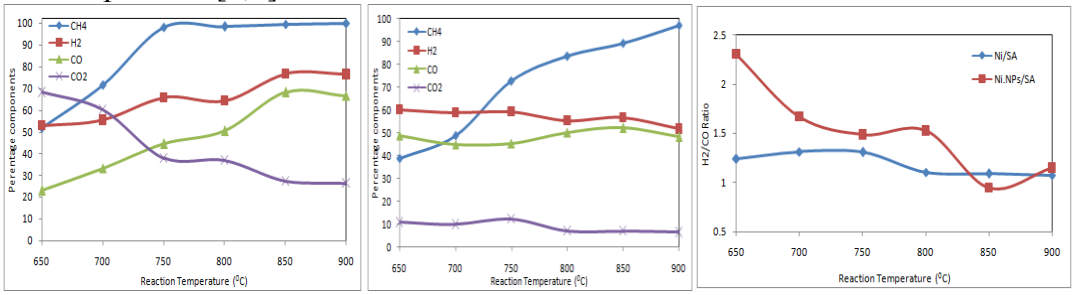

(a) Ni.NPs/SA (b) Ni/SA (c) Effects of temperature on H_2/CO ratios

Figure 2: Catalytic behavior of the catalysts

As can be seen in Figure 3, respective deactivation degrees under identical set of conditions for Ni/SA and Ni.NPs/SA were 35% and 10% respectively. For Ni.NPs/SA the difference in initial and terminal activities was small and its stability was maintained for all period on time of stream of the stability. On the other hand Ni/SA had a higher degree of deactivation it increased with time while Ni.NPs/SA showed resistance to deactivation. These results were confronted by the results of TPO and BET measurements of the spent catalysts.

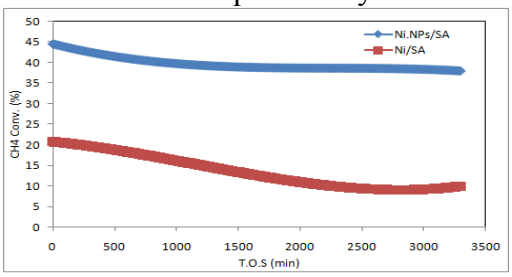

Figure 3: Catalytic stability in time on steam at C/S ratio of 1 at 750^0C.

4. Conclusions

In all temperature ranges (650-800^{0}C) Ni.NPs/SA catalyst was found to be better in performance in methane steam reforming than Ni/SA which was attributed to the difference in the physicochemical properties of both catalysts. Catalytic performance of Ni.NPs/SA was clearly affected by the reaction temperature. In the catalytic stability experiment in the time on stream of sixty hours, under critical C/S ratio of one, Ni.NPs/SA catalyst exhibited stable catalytic performances and neither deactivation nor sintering was observed.

5. Acknowledgments

This paper was made possible by a NPRP Grant # 6 - 290 - 1 - 059 From the Qatar National Research Fund (a member of Qatar Foundation). The statements made herein are solely the responsibility of the authors

6. References

[1] Alvarez-Galvan MC, Mota N, Ojeda M, Rojas S, Navarro RM, Fierro JLG. Direct methane conversion routes to chemicals and fuels. Catal Today 2011;171:15-23.

[2] Ayabe S, Omoto H, Utaka T, Kikuchi R, Sasaki K, Teraoka Y, et al. Catalytic autothermal reforming of methane and propane over supported metal catalysts. Appl Catal A 2003;241:261.

[3] Dias JAC, Assaf JM. Autothermal reforming of methane over Ni/g-Al2O3 catalysts: the enhancement effect of small quantities of noble metals. J Power Sourc 2004;130:106.

[4] H. S. Bengaard, J. K. Nørskov, J. Sehested, B. S. Clausen, L. P. Nielsen, A. M. Molenbroek and J. R. Rostrup-Nielsen, *Journal of Catalysis* 209 (2002) 365

[5] Sprung C, Arstad B, Olsbye U. Methane steam reforming over Ni/NiAl2O4 catalyst: the effect of steam-to-methane ratio. Top Catal 2004;54:10-19.

[6] Carvalho LS, Martins AR, Reyes P, Oportus M, Albonoz A, Vicentini V, et al. Preparation and characterization of Ru/MgOeAl2O3 catalysts for methane steam reforming. Catal Today 2009;142:52-60.

[7] Jones G, Jakobsen JG, Shim SS, Kleis J, Andersson MP, Rossmeisl J, et al. First principle calculations and experimental insight into methane steam reforming over transition metal catalysts. J Catal 2008;259:47-60..

[8] Lucredio AF, Assaf EM. Cobalt catalysts prepared from hydrotalcite precursors and tested in methane steam\ reforming. J Power Sources 2006;159:67-72.

Silica-based nanocoating and LDHs sensors for enhancement of paperboard barrier properties

V M Dias[1,3], A Kuznetsova[2], J Tedim[2], A A Yaremchenko[2], I Portugal[1] and D V Evtuguin[1]

[1] CICECO - Aveiro Institute of Materials, Department of Chemistry, University of Aveiro, 3810-193 Aveiro, Portugal
[2] CICECO - Aveiro Institute of Materials, Department of Materials and Ceramic Engineering, University of Aveiro, 3810-193 Aveiro, Portugal

Abstract. Conventional solutions to enhance paperboard barrier properties for packaging are limited essentially to film coating by synthetic polymers that hinder end-of-life disposal or recycling. This work presents an alternative procedure, paperboard nanocoating using formulations prepared by sol-gel method with silica precursors such as tetraethyl orthosilicate (TEOS), 3-aminopropyltriethoxysilane (APTES) and others, and Zn(2)-Al-NO_3 type layered double hydroxides (LDHs) that can act as anion/water sensors. After deposition on the paperboard surface the silica-based formulations were infrared cured thus ensuing *in situ* formation of a cellulose-silica barrier. The coated paperboards were characterized by scanning electron microscopy (SEM), contact angle measurements, water vapour transmission rate (WVTR) and oxygen permeation (J_{O_2}). Best results were obtained for TEOS-APTES nanocoating, with WVTR and J_{O_2} being reduced by ca. 60-70 % in comparison to uncoated paperboard. The incorporation of LDHs presented a positive effect mainly for WVTR.

1. Introduction

Paperboard surface coating by synthetic or biodegradable polymers can be utilized to ensure water vapour barrier properties in paperboard-based food containers [1,2]. Sol-gel methods are proven and convenient for organic-silica nanocoating since silica particles are generated in situ, through hydrolysis and condensation reactions of silicon alkoxides, and randomly dispersed on the paper surface thus forming an impermeable interface between three-dimensional silica network and cellulose fibres [3,4].

In this work silica-based formulations were prepared by sol-gel synthesis using TEOS and other precursors with or without the addition of Zn(2)-Al-NO_3 layered double hydroxides (LDHs). Structurally, LDHs consist of layers of positively-charged, mixed-metal hydroxide between which anions and water molecules are intercalated. Their most relevant property is anion-exchange, which can be used to reduce the permeability of protective coatings to relevant anions via entrapment [5]. Also, LDHs can be used as anion/water sensors since the structural changes occurring in the presence of these species can be followed by X-ray diffraction [5,6]. After deposition of the formulation on the paperboard surface *in situ* formation of cellulose-silica hybrids occurs where silica domains are dispersed in a nanometric scale [3].

[3]To whom any correspondence should be addressed. E-mail: vania.dias@ua.pt

2. Experimental

2.1. Synthesis of silica-based nanocoating

Industrially produced paperboards (210 g/m^2 and 0.29-0.30 mm thickness) with a surface treatment on one side (30-35 g/m^2 of a slurry of $CaCO_3$ and Al_2O_3 particles mixed with a synthetic resin emulsion) were supplied by Prado Karton SA (Tomar - Portugal). Hereafter these paperboards will be designated as 'uncoated'.

Silica-based formulations were prepared by sol-gel synthesis, figure 1, using tetraethyl orthosilicate (TEOS) or a mixture of TEOS (95%) and a secondary precursor (e.g. dimethyldiethoxysilane (DEDMS), 3-aminopropyltriethoxysilane (APTES), and octyltriethoxysilane (OTES)). The formulations were deposited on the treated side of the paperboard surface ((ca. 2-3 g/m^2), using a conventional roll-to-roll technique and afterwards were cured by heating with an infrared lamp. Some formulations were prepared with the addition of Zn(2)-Al-NO_3 type layered double hydroxides (LDHs).

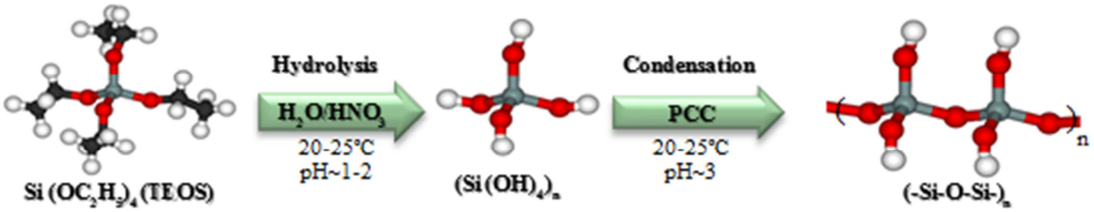

Figure 1. A simplified view of sol-gel processing of silica formulation.

2.2. Characterization methods

Water vapour barrier properties of uncoated and silica-nanocoated paperboard were measured by the "desiccant method" at 26 ± 1ºC and 52% relative humidity using a saturated aqueous magnesium nitrate solution (ASTM E96-95) [7]. Air was continuously circulated throughout the chamber using an air-fan. The samples, in triplicate, were periodically removed and weighed, during three days. Water vapour transmission rate (WVTR, g m^{-2} day^{-1}) were obtained from the linear representation of the experimental data, namely sample weight gain $\Delta w = (w - w_0)$ versus time (t), as expressed by equation (1).

$$\Delta w = A \times \mathrm{WVTR} \times t \quad (1)$$

where A is the exposed area of the paperboard sample (19.6 cm^2).

Oxygen permeation (J_{O_2}) measurements were performed using air in one side of paperboard and nitrogen flow on the other side. Oxygen partial pressure ($p(O_2)$) was measured under steady-state conditions at the inlet ($p(O_2)_{in}$) and outlet ($p(O_2)_{out}$) of the sample holder, at room temperature and zero total pressure gradient across the paperboard sample. Specific oxygen permeation fluxes (J_{O_2}, m^3 m^{-2} day^{-1}) across the sample were calculated with the experimental data using equation (2).

$$J_{O_2} = \left(F_{N_2}/A\right) \times \left((p(O_2)_{out} - p(O_2)_{in})/P\right) \quad (2)$$

where F_{N_2} is the inlet nitrogen flow rate, P is the total pressure and A is the paperboard sample surface area (0.785 cm^2) [8].

Contact angles were measured in a DataPhysics Instrument OCA 20 using the sessile drop method and water, formamide and diiodomethane as probe liquids. Owens-Wendt-Rable-Kaeble (OWRK) model was used to predict polar and dispersive components [9][10]. Paperboard surfaces were characterized

in terms of morphology by scanning electron microscopy (SEM), using a FEG-SEM Hitachi SU-70 microscope operating at 15 kV.
Physical and mechanical properties were evaluated by different tests; the tensile strength was determined according NP EN ISO 1924-2, burst strength was determined by NP EN ISO 2758 and Bendtsen roughness and porosity were determined following NP EN ISO 8791. The determination of air permeation was measured by the Gurley method (NP 795 ISO 5636-5).

3. Results and Discussion

Silica-coated paperboard surfaces were characterized in terms of morphology by SEM. SEM images (figure 2) of paperboard transversal cuts (delimited by dashed lines) reveal the position of silicon (red areas) on the side where the formulation was applied (right side). The industrial surface treatment of paperboard prevents the penetration of the silica formulation and therefore reduces the amounts required to achieve good barrier results.

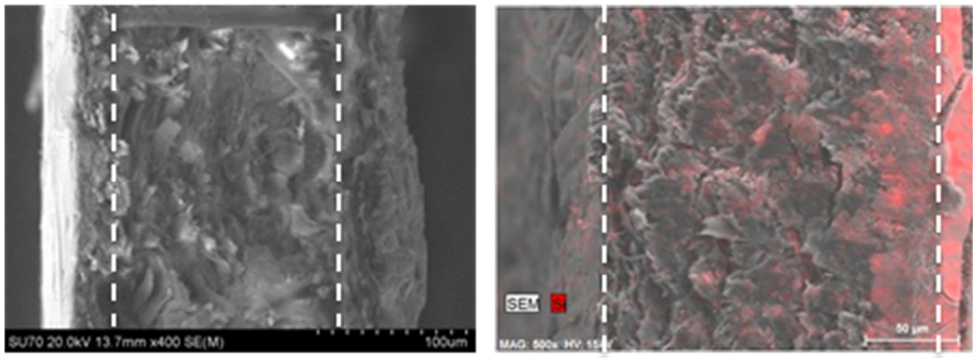

Figure 2. SEM-EDS images of paperboard surfaces without (cross section – left) and with silica formulation (TEOS_DEDMS: cross section – right).

Surface energy results for uncoated and silica-coated paperboard are present in figure 3 and revealed an increase in the total surface energy, especially for the polar component, when comparing the results for paperboard uncoated and coated with TEOS and TEOS_LDHs formulations. In general, the presence of secondary silica precursor (DEDMS, APTES or OTES) in TEOS formulation decreased the paperboard total surface energy and especially its polar component (figure 3). However, the polar component presents the highest value when APTES is used possibly due to the presence of amine groups, which can form hydrogen bonds with water molecules conferring a hydrophilic character to the coated surface. In general, the incorporation of LDHs in the silica formulations increases the polar component of the surface energy (figure 3).

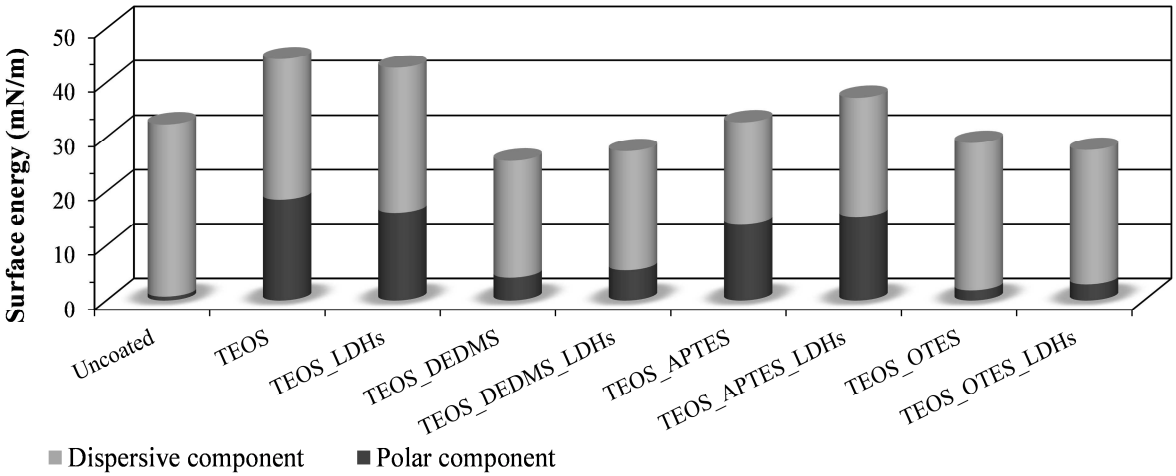

Figure 3. Contribution of the polar and dispersive components to the total surface energy of industrial paperboard before (uncoated) and after coating with several silica based formulations with and without LDHs (Zn(2)Al-NO_3).

The paperboards were characterized in terms of physical and mechanical properties. The results, presented in table 1 for industrial paperboard before (uncoated) and after coating with various silica based formulations reveal that silica formulations doesn't change the basic physical characteristics of the paperboard used as based material. In fact in some cases it even improves their properties, such as burst strength and tensile index (table 1). Silica formulations increase the roughness of the paperboard surface being this increase more significant for the formulation containing octyl groups (TEOS_OTES and TEOS_OTES_LDHs). The results also show that the incorporations of LDHs improve the properties of the silica coating, such as burst strength, tensile index and roughness.

Table 1. Physical and mechanical properties of industrial paperboard before (uncoated) and after coating with various silica based formulations with and without LDHs.

	Tensile Index (Nm/g)	Bendtsen Roughness (ml/min)	Bendtsen Porosity (ml/min)	Burst strength (kPa)
Uncoated	65	88	12	535
TEOS	66	129	10	590
TEOS_LDHs	67	118	10	593
TEOS_DEDMS	67	145	10	572
TEOS_DEDMS_LDHs	67	138	10	606
TEOS_APTES	66	147	10	582
TEOS_APTES_LDHs	68	138	10	593
TEOS_OTES	66	204	10	569
TEOS_OTES_LDHs	68	216	10	613

3.1. Barrier Properties

The WVTR values for industrial paperboard (uncoated) decrease considerably with silica nanocoating, with and without the incorporation of a Zn(2)Al-NO_3 (LDHs) (figure 4). The use of TEOS or a mixture of TEOS and other secondary silica precursors (DEDMS, APTES and OTES) has a significant effect on WVTR increases hydrophobicity of the nanocoated surface and improves water barrier properties (WVTR decreased about 13% for TEOS and ca. 60% for TEOS with a secondary silica precursor). These results arise from better adhesion of the silica nanocoating on the paperboard surface due to strong hydrogen bonding of paperboard hydroxyl groups and silica [11–13].

LDHs were introduced in the silica formulations to act as nanosensors due to their anion-exchange properties. Their presence increase total surface energy and its polar component (figure 3), as compared to other silica nanocoatings, however WVTR decreased about 76% (TEOS_APTES_LDHs and TEOS_OTES_LDHs) as compared to uncoated paperboard, which means that LDHs can also act as water scavengers, figure 4 [14].

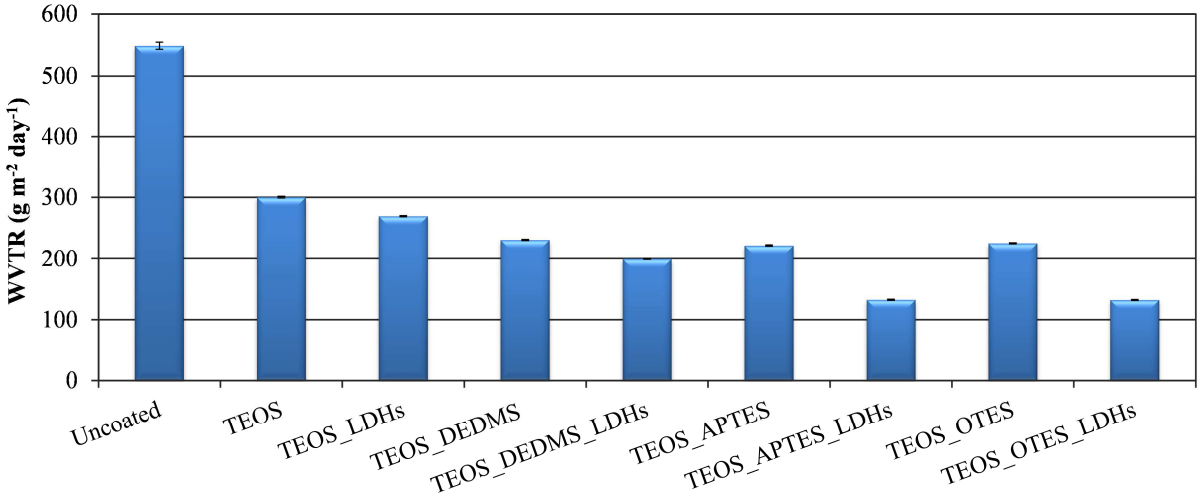

Figure 4. WVTR of industrial paperboard before (uncoated) and after coating with various silica based formulations with and without LDHs.

Practically all examined silica-based nanocoatings conferred oxygen barrier properties to paperboard, figure 5. Oxygen permeability (J_{O_2}) for the uncoated paperboard was reduced by 55 % after coating with TEOS and by 63 % or 68% after coating with the formulation TEOS_DEDMS or TEOS_APTES respectively. This can be explained by the formation of a silica network on the paperboard surface that prevents water penetration into the paperboard fibers and also reduces oxygen permeability, figure 5.

The particularly high oxygen permeability observed for paperboard coated with TEOS_OTES formulation might be due the presence of bulky organic radicals in the silica precursor (OTES) that affects negatively the density of the inorganic silica networks, creating paths for the oxygen permeation and consequently increasing the oxygen permeation rate.

The presence of LDHs in silica formulation increase oxygen permeability about 20-25% when compared with the base formulation. The LDHs can cause changes in the dense silica network formation, which is responsible for prevention of permeation of gas molecules.

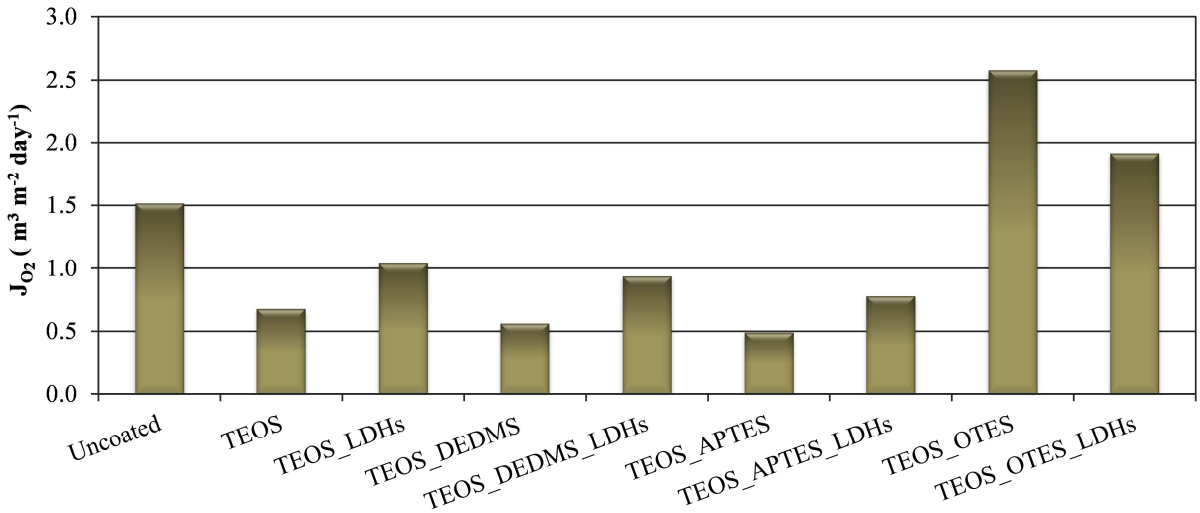

Figure 5. O_2 flux of industrial paperboard before (uncoated) and after coating with various silica based formulations with and without LDHs.

4. Conclusions

The results of this work reveal that water vapor transmission rate and oxygen permeability of industrial paperboard decreased in the presence of silica nanocoating with and without Zn(2)-Al-NO_3 (LDHs). The TEOS_APTES formulation is the most promising to impart water and oxygen barrier properties suitable for packaging applications, reduced WVTR in 60% and oxygen permeability in 68%.

5. References

[1] Hirvikorpi T, Vähä-Nissi M, Harlin A and Karppinen M 2010 *Thin Solid Films* **518** 5463–6

[2] Han J, Salmieri S, Le Tien C and Lacroix M 2010 *J. Agric. Food Chem.* **58** 3125–31

[3] Sequeira S, Evtuguin D V., Portugal I and Esculcas A P 2007 *Mater. Sci. Eng. C* **27** 172–9

[4] Portugal I, Dias V M, Duarte R F and Evtuguin D V 2010 *J. Phys. Chem. B* **114** 4047–55

[5] Tedim J, Kuznetsova A, Salak A N, Montemor F, Snihirova D, Pilz M, Zheludkevich M L and Ferreira M G S 2012 *Corros. Sci.* **55** 1–4

[6] Buchheit R G, Guan H, Mahajanam S and Wong F 2003 *Prog. Org. Coatings* **47** 174–82

[7] ASTM E 96-95 1995 *In Annual Books of ASTM Standards* vol 552 pages 785–92

[8] Yaremchenko A A, Kharton V V, Avdeev M, Shaula A L and Marques F M B 2007 *Solid State Ionics* **178** 1205–17

[9] Owens D K and Wendt R C 1969 *J. Appl. Polym. Sci.* **13** 1741–7

[10] Figueiredo A B, Evtuguin D V, Monteiro J, Cardoso E F, Mena P C and Cruz P 2011 *Ind. Eng. Chem. Res.* **50** 2883–90

[11] Purcar V, Stamatin I, Cinteza O, Petcu C, Raditoiu V, Ghiurea M, Miclaus T and Andronie A 2012 *Surf. Coatings Technol.* **206** 4449–54

[12] Parale V G, Mahadik D B, Mahadik S A, Kavale M S, Wagh P B, Gupta S C and Rao A V 2013 *Ceram. Int.* **39** 835–40

[13] Mah S K and Chung I J 1995 *J. Non. Cryst. Solids* **183** 252–9

[14] Chen H, Zhang F, Fu S and Duan X 2006 *Adv. Mater.* **18** 3089–93

Acknowledgments
This work was developed in the scope of the project CICECO-Aveiro Institute of Materials (Ref. FCT UID /CTM /50011/2013), financed by EU funds of FP7 program (FP7-NMP-2011-LARGE-5 – NANOBARRIER project). Authors also thank the technical assistance of Prado Karton SA.

Combined Mechanical Disordering – Reactive Synthesis, possible method of Bulk Nanocrystalline Intermetallics obtaining from stoichiometric powder mixture of components

Radu L. Orban[1], Alan Lawley[2], Magdalena Orban[3]
[1] Professor, [3]Associate Professor, Technical University of Cluj-Napoca, Romania, [2] Emeritus Professor, Drexel University, Philadelphia, PA, USA, E-mail: Radu.Orban@stm.utcluj.ro

Abstract: A promising way to overcome the known high brightness at ambient temperature of intermetallics with the purpose to improve their cold workability/machinability is their obtaining in a bulk nanocrystalline state. The presented research results prove that, for the known, widely applied, route of their obtaining by Self-propagating High-temperature Synthesis (SHS) from the stoichiometric mixture of powdered components, this is possible by a controlled Mechanical Structural Disordering (MD) of stoichiometric mixture of components, without to allow ignition of the compound synthesis reaction, followed by the as obtained nanocrystalline powder Reactive Sintering (RS) under an appropriate pressure, to obtain the desired compact. The nanocrystalline powder resulted by MD has a high energetic state, allowing development of synthesis reaction by diffusion at a low enough temperature to preserve, in the processed compact, the powder nanocrystalline structure, but, combined with the applied pressure, to be able to assure its good consolidation.

1. Introduction

Increasing exigencies concerning performances of materials for high temperature applications in severe oxidation and corrosion conditions, promoted especially - but not limited – by the developments in aerospace and energy production technology, have determined a special attention to intermetllics, being known their outstanding properties in these respects [1]. So, beside Nickel and Titanium aluminides (NiAl and γTiAl) – of high melting points and high oxidation resistance up to ~ 1000 °C NiAl, respectively to ~ 800 °C TiAl) - both already in course of application [1], new materials, resistant at extremely high temperatures – more than 1500 °C, are required in aircraft gas turbines and spacecraft airframes, as well as in other emerging applications [2]-[4]. However, upon C. Leyens et al. [5], further material and technological developments are necessary for their practical implementation to assure the full security and avoid the associated risks. Consequently, important research efforts are being carried out for NiAl and TiAl performances improvement and technolological developments [6]. Among them, a big attention is paid to the amelioration of their poor ductility and low fracture toughness at ambient temperature determined by their inter-atomic strong bonds and low symmetry of the formed super-lattices, which prohibits the operation of five independent slip systems required for plastic flow [3]. Consequently, they exhibit a high brightness at ambient temperature that leads to poor workability/machinability – limiting their applications [4], [6]. Fortunately, it was established that a notable ambient ductility improvement is possible by their obtaining in nanocrystalline state [7].

Intermetallic compounds have negative Standard Gibbs Free Energy of Formation [8]. As a result, they are produced by methods based on the Self-propagating High-temperature Synthesis (SHS), starting either from bulk components – e.g. in ExoMelt Process [9] or from powdered components – in Reactive Sintering [10]. Because at methods involving melting, the obtained product is subjected to a certain contamination and also is difficult to control its microstructure - formed at cooling after casting [9], for the most applications is preferred their elaboration by Reactive Sintering [4],[6].

Irrespective of the elaboration method, in the normal cooling conditions one result compounds with polycrystalline microstructure, consisting of super lattices of specific types [3], which determine their above-mentioned high brightness at ambient temperature. Obtaining in nanocrystalline state of intermetallics elaborated through melting route could be, in principle, possible by melt spinning, the resulted products being nanocrystalline ribbons or flakes [11]. To

obtain bulk nanocrystalline intermetalics they have to be consolidated by sintering in appropriate conditions to avoid grain growth, e.g. by Spark Plasma Sintering (SPS) [12] – both steps being very expensive. If the Reactive Sintering is applied, the obtained quite coarse polycrystalline structure of sintered compacts can not be refined e.g. by Severe Plastic Deformation [13] due to their high brightness.

Apparently, the only possibility is to synthesize the desired intermetallic from its reactive powdered components – (b), figure 1 [14], by Reactive Mechanical Alloying (RMA), carried out e.g. by ball milling to reach the ignition temperature (a) of the compound synthesis, T_{ig}, followed by the formed compound further Mechanical Structural Disordering (MD) by the milling time

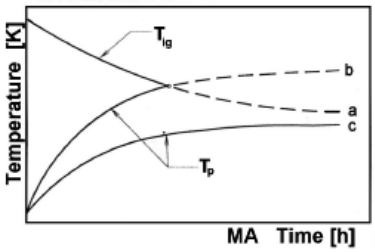

Figure 1. Temperature variation with MA time of: (a) ignition of the possible synthesis reaction; (b)/(c) powder mixture which undergoes / doesn't undergo a synthesis reaction.

extending to the right of the crossing point – accompanied by the milling bowl cooling. But, the as obtained nanocrystalline compound is also in the powdered state and, to obtain a nanocrystalline compact again must be consolidated by SPS.

To avoid this last expensive step, the present paper, representing a development of a previously idea of the authors [15], investigates the possibility to obtain bulk nanocrystalline intermetallic compounds from stoichiometric powder mixture of components, in two steps: i) controlled MD, applied to the stoichiometric elemental powdered component mixture – determining their strong cold working and energetic state increasing - conducted only up to the particle obtaining in nanocrystalline state, without to be reached the ignition temperature, T_{ig}, of the synthesis reaction (before a-b crossing point, Fig. 1); ii) Compound reactive synthesis from the as obtained nanocrystalline powder mixture, combined with its consolidation.

It is expected that, due to the high energetic state of nanocrystalline powder and intimate mixture of components, both synthesis and consolidation (e.g. under an appropriate pressure – i.e. by SHS in thermoexplosion mode under pressure) are possible in solid state, by diffusion [16], at a low enough temperature to preserve the nanocrystalline structure in the obtained bulk material, as well as the integrity of the formed compact. NiAl intermetallic compound has been selected as representative for the method viability proving.

2. Experimental procedure

To establish the thermodynamic possibility of NiAl synthesis from the stoichiometric mixture of powdered components without of the other Ni-Al possible compounds, the ΔG^0_f values of their formation have been calculated up to their melting points, with a step of 100 [K], with the formula:

$$fG^0_{f/r,T} = \Delta H^0_{298} + \int_{298}^{T} \Delta C_p * dT - T * (\Delta S^0_{298} + \int_{298}^{T} \Delta C_p / T * dT) \quad [8]$$

where $\Delta H^0_{298}/\Delta S^0_{298}$ are the enthalpy / entropy of compound formation and ΔC_p – heat capacity change of reactants to products, all taken over from literature [17]. As the results comparison – in a graphically plotted form, presented in §. 3.1, confirmed this, its elaboration has been considered. Goodfellow atomized AL006031 Aluminum Powder, of the max. particle size 60 μm, purity 99.9 %, respective carbonyl NI006021 Nickel of particle size 3 ÷ 7 μm, purity 99.8%, in the stoichiometric proportion, have been homogenized for 3 h in a Turbulla blender. The MD process was performed in a Pulverisette 6 (Fritsch) planetary ball mill, using hardened tool steel bowl and balls, with the absolute rotation speed of 90 rot/min and of bowl rotation speed of 150 rot/min. The balls had diameters between (19.05 ÷ 6.35) mm, their total weight/powder ratio 10:1 and that of bowl volume occupancy of ~2/3. The MD process was carried out under Argon of high purity (class 5.0). For its monitoring, at each 3 hours a sample of powder was taken off from the bowl

and analyzed by SEM and XRD. Just before the compound synthesis reaction starting, the MD process was stopped; a new powder sample was taken off for SEM and XRD analysis – performed using Co kα_1 radiation. Then, cylindrical compacts of 15 mm diameter and 10 mm height were realized by cold pressing with 400 MPa in a steel die, with die wall lubrication. Subsequently, they were placed in a graphite die with cavity and active parts of punches painted with zirconia suspension and subjected to Reactive Sintering (RS) by Self-propagating High-temperature Synthesis (SHS) in thermoexplosion mode under a pressure of 50 MPa, in a vacuum furnace, following an adequate Temperature – Vacuum degree - time cycle. This was previously established on the basis of a performed DSC analysis, so that be able to assure synthesis reaction occurring predominant by diffusion, and simultaneous powder consolidation. The samples of powder mixture for each 3 h MD time, previously taken off from the mill bowl, as well as the final compact were characterized by XRD, using the Mach!)[18] and WinPLOTR (Version: Feb. 2015, [19] computer programs for XRD patterns indexation respectively for the FWMH of the main peaks determination, necessary for crystal grain size calculation by the Sherrer's relation [20]. To prove the nanocrystalline structure of the obtained NiAl compact, its crystal grain size was determined by the same Sherrer's relation and its structure analyzed by HRTM.

3. Results and discussion

3.1. Thermodynamic possibility of NiAl synthesis

Variation with temperature of the calculated values of ΔG^0_f of the possible reactions between Ni-Al components is presented in figure 2. As can be seen, the Ni_3Al formation has the lowest value of ΔG^0_f. However, it can further react with the excess of Al from the adopted stoichiometric mixture for NiAl formation, to form NiAl as the Standard Gibbs Free Energy of this reaction has also negative value. Finally, as the ΔG^0_f values for NiAl have negative values up to its melting point, it is thermodynamically stable and, therefore, the obtained bulk material is expected to keep both its initial nanocrystyalline structure, integrity and shape of the formed compact.

3.2. Compositional and Morphological evolution of Ni-Al powder mixture during MD

In figure 3 is presented XRD pattern of the initial, homogenized, Ni-Al powder mixture (0h MD time). As can be seen, it contains only Ni and Al peaks proving that during the homogenization process the purity of powder mixture has been preserved, without a notable contamination. Taking into consideration the adopted MD conditions (see §. 2), the same situation is expected after MD.

To illustrate the morphological evolution of Ni-Al powder mixture during MD, for the economy of space, only SEM images for the initial state, for 3 h MD time and for powder in the final structural disordered state obtained by MD, i.e. for 9 h MD time, is presented in figure 4.

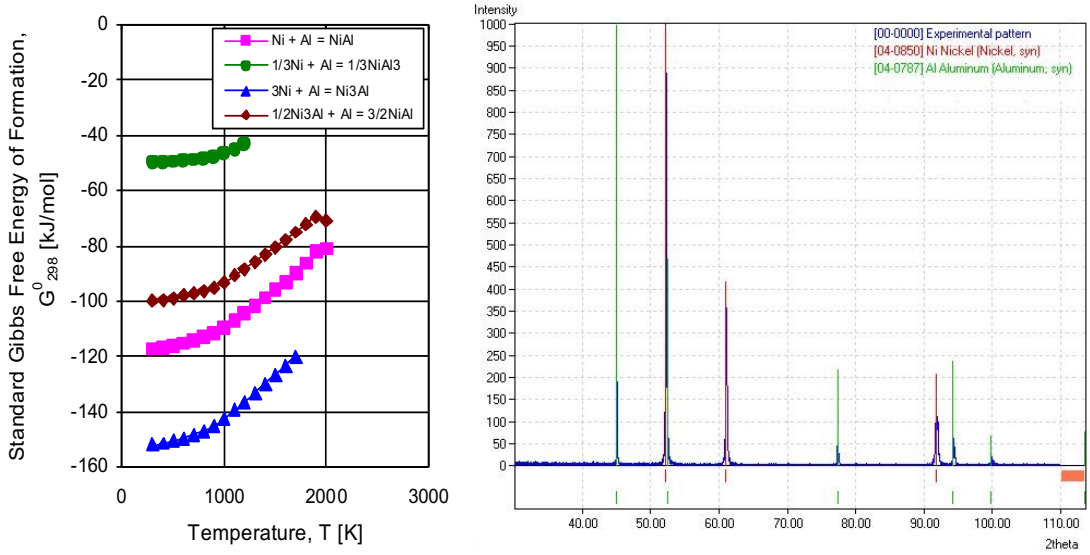

Figure 2. Standard Gibbs Free Energy of Ni-Al compounds formation plotted vs. temperature.

Figure 3. Indexed diffraction pattern of the initial Ni-Al powder mixture (0 h MD). Only Ni and Al peaks have been detected by the Match program.

As can be seen, the first image (0 h MD) reveals the big difference in the particle size between the Al and Ni, but also a good homogeneity of their mixture. For 3h MD time, instead, these components have loosed their identity particle being much flattened, while for 9 h MD - conglomerates of very fine particles (most of them below ~ 1 μm), were formed. The MD process continuation, in the same conditions, till 12 h, led to the Ni-Al compounds synthesis and, consequently, the MD process of Ni-Al powder mixture was limited to 9h.

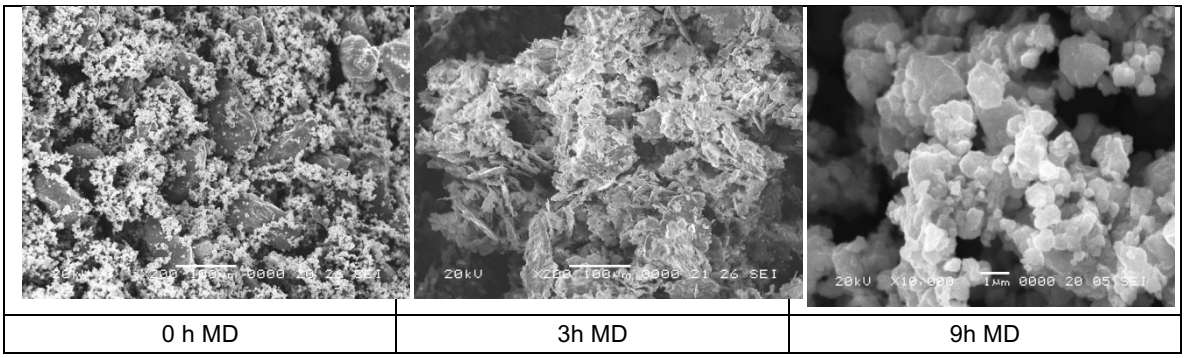

Figure 4. SEM images of Ni-Al powder mixture in the main steps of MD.

3.3. XRD pattern evolution of Ni-Al powder mixture during MD process

Evolution of XRD pattern of Ni-Al powder mixture during MD, graphically represented in 3D with the WinPLOTR program (figure 5), clearly reveals the expected broadening of diffraction peaks as MD time increases, but also their height decreasing and even their flattening for high diffraction angles. However, for the main peaks, Ni (111) and Al (111) – of nominal (PDF) diffraction angles, 2θ, of 52.18, respectively 44.99 degrees (see figure. 3), it is possible determination of FWMH necessary for the grain size calculation. It is also to be observed that no additional peaks appeared, proving, as expected, that no notable contamination occurred.

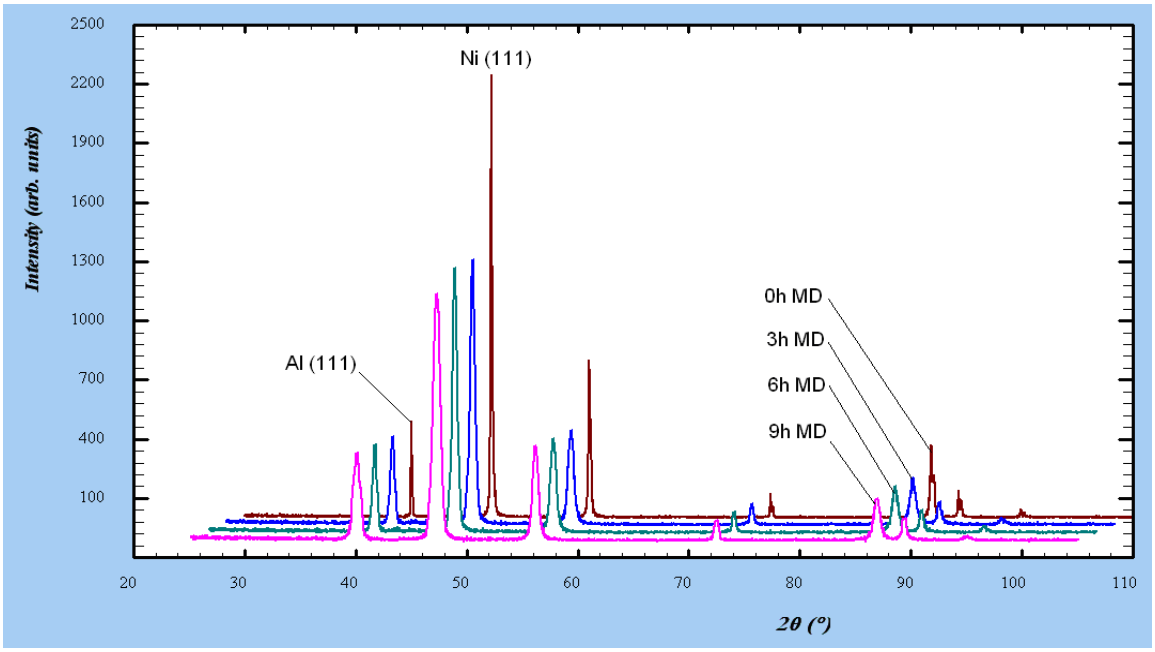

Figure 5. 3D representation of determined XRD patterns for the adopted MD times.

3.4. Determination of FWHM values

Determination of FWHM values for all XRD patters, performed with the same WinPLOTR program, was limited to the main, above-mentioned, most representative peaks. For economy of space, in Figure 6 are presented, for exemplification, only the main data from Reports given by the

Nickel Peak (111)

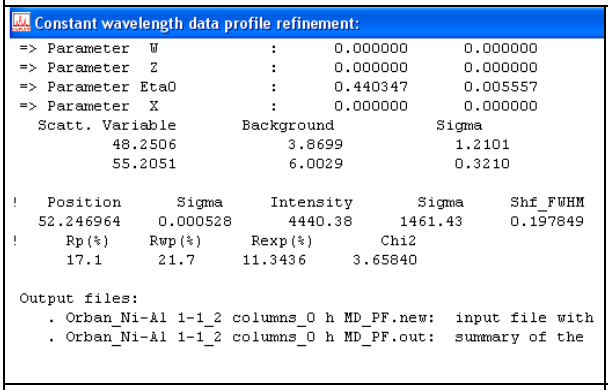

0 h MD

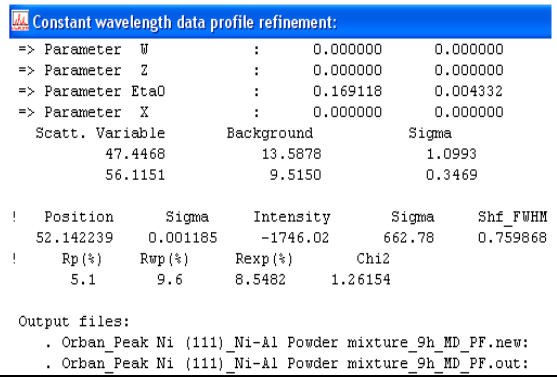

9 h MD

Figure 6. Reports on FWHM values calculation for Ni (111) peaks, 0 and 9 h MD.

WinPLOTR program, corresponding to Ni (111) peak, for 0h and 9h.MD times. Similar reports have been obtained for Al (111) peak, as well as for both (not included hire for economy of space), in XRD patterns corresponding to each adopted MD time. It is to be observed that they contain, among others, the determined Position of the analysed peak and value of its FWHM, both with high accuracy.

3.5. Crystal grain size calculation for the adopted MD times and results evaluation

Crystal grain size was calculated by Sherrer's relation in Excel program, using determined FWHM values and measured positions, 2θ, of the respective peaks. As etalon, for each component has been adopted the respective FWHM value determined on XRD pattern for 0h MD time. All these data, as well as the calculated medium values of crystal grain sizes, are given in table 1. As expected, a pronounced decreasing of their values for both components occurred as MD time increased, being surprising that, even for 3 h MD, they reached a nanocrystalline state..

Table 1. Determined X-Ray Diffraction Data for MD Ni-Al powder mixture and for the obtained compact, and calculated crystal grain size values corresponding to them.

MD Time	*Reflection*	*Measured FWHM*	*Etalon FWHM*	*Diffraction Line Broadening*	*Measured Reflection Angle,2θ*	*Calculated Crystal Grain Size*
[h]	Element (Diffr. Plane)	[deg]	[deg]	[rad]	[deg]	[nm]
0	Ni (111)	0.197849	0.197849	0.0000000	52.246964	-
3		0.231009		0.0000043	52.229412	**81.039**
6		0.635954		0.0000772	52.181969	**19.4065**
9		0.759868		0.0001656	52.142239	**13.177**
0	Al (111)	0.155349	0.155349	0.0000000	45.050568	-
3		0.222542		0.0000079	45.00288	**59.407**
6		0.478931		0.0000627	44.963909	**21.951**
9		0.733578		0.0001567	44.946358	**13.872**

	NiAl (110)	0.723899	0.3349	0.0001259	52.157642	**15.063**

3.6. Establishment of behaviour of powder mixture subjected to 9h MD at the synthesis reaction
Behaviour at synthesis reaction of Ni-Al powder mixture subjected to 9h MD is shown by DSC pattern (figure 7). As can be seen, it doesn't contain the endothermic peak corresponding to Al

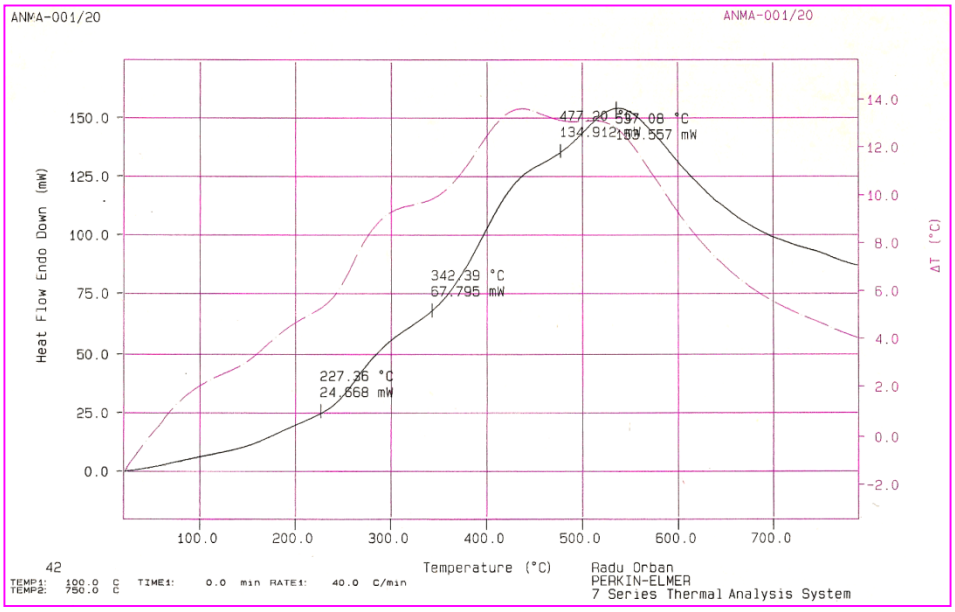

Figure 7. DSC pattern, at heating, for **Ni**-Al powder mixture subjected to 9h MD. Heating rate, atmosphere: 10°C/min, Ar 5.0.

melting, as at the non-activated Ni-Al powder mixture [9]. This proves that, really, the synthesis reaction occurs, as expected, in solid state and, as can be seen, gradually, with a maximum temperature of 537.08 10°C. Consequently, only a small grain growth is possible, being expected that in the obtained product will be kept the above-determined nanocrystalline state of powder.

3.7. Characterization of the elaborated compacts
For capitalization of the high reactivity of MD-ed powder mixtures subjected to 9 h MD time, the elaboration, by reactive sintering, of the envisaged compact was started immediately after MD process stopping. It was carried out following, as has been mentioned (§. 2), an appropriate cycle established on the basis of the DSC analysis [15]), in a vacuum of 10^{-7} Pa, at nominal temperature of 800 °C. As has been provided by the thermodynamic analysis (§. 3.1.), its XRD pattern (Fig. 8), revealed the direct synthesis of NiAl compound (red lines), even if very small proportions of Ni_3Al (green lines) and of un-reacted Ni (brown lines) have been identified.

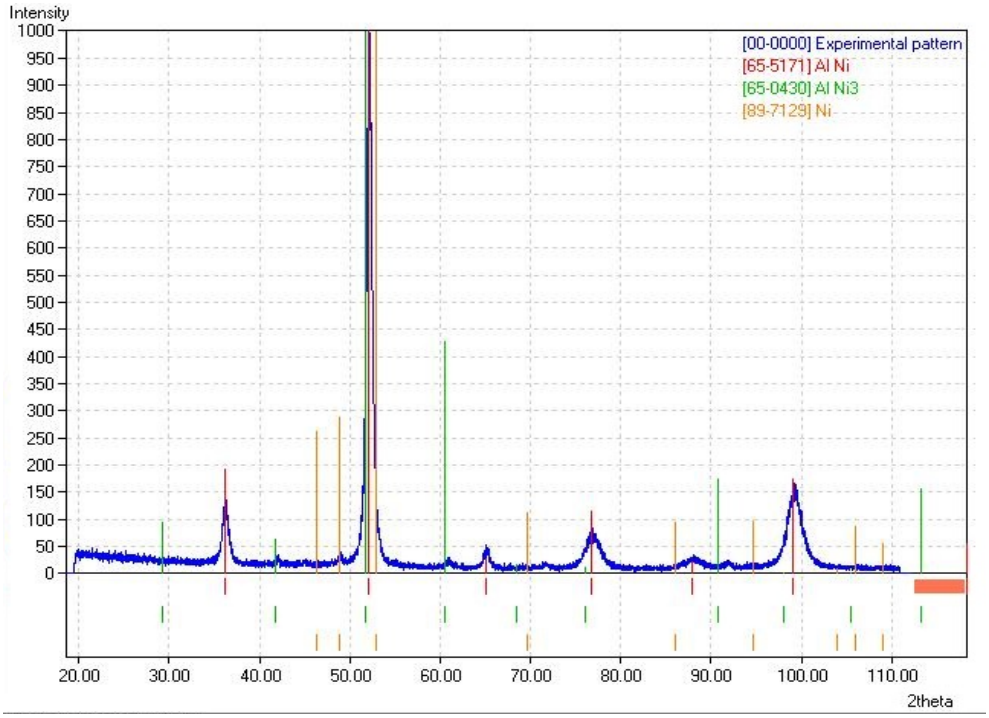

Figure 8. Diffraction pattern of the processed NiAl compact.

In order to establish if the desired purpose of performed research has been reached - the compacted compound obtaining in a nanocrystalline state – the value of FWHM for the main peak of the obtained NIAl compact, namely the (110) peak, of the nominal diffraction angle, $2\theta = 52.2$ degree, has been also determined by WinPLOTR program, its Report being given in figure 9-a, while the calculated medium crystal grain size value of the processed NiAl compact is inserted in Table 1. As can be seen, this value, ~15 nm, confirms the expected result, namely a nanocrystalline NiAl compact has been obtained. Its crystal grain size is a little higher then of components, showing that, as expected, a certain grain growth occurred. For a supplementary proof, its microstructure was investigated by HRTM (figure 9-b), being clearly observed the atomic planes of a random orientation.

4. Conclusions

The presented results prove the possibility of compacts of intermetallic compounds obtaining in the nanocrystalline state with the purpose to improve their ambient temperature ductility and,

implicitly workability/machinability. The controlled Mechanical structural Disordering (MD) of

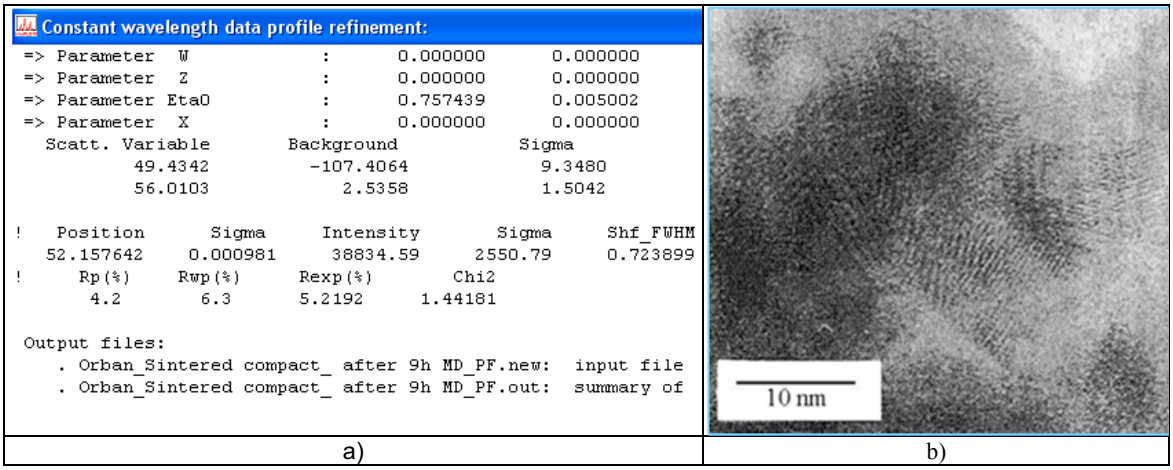

Figure 9. (a) Report on FWHM determination for NiAl (110) peak; (b) HRTM image of the obtained NiAl compact.

stoichiometric mixture of powdered components up to their obtaining in nanocrystalline state, without synthesis reaction ignition, proved to determine, beside crystal grain drastic refining, their intimate mixture – probably forming a solid solution of extended solubility in which the components could not be identified by SEM analysis, and subsequently its sever cold hardening. Consequently, a significant increasing in their energetic state occurred, becoming possible the compound synthesis in solid state, by diffusion. The process required a low enough temperature allowing preservation, in the compact, of the nanocrystalline structure of components, while simultaneous pressure application made possible its good consolidation.

5. References

[1] Sauthoff G 2008 *Intermetallics* (New York: J. Wiley & Sons) pp 1-13
[2] Fleischer R L 2000 *Intermetallic Compounds* vol 2 pp 241-263
[3] Umakoshi Y 2005 *Materials Science and Technology* VCH & Co.KGaA vol 6/7 pp 251-310
[4] Stoloff N S et al 2000 *Intermetallics* **8** 1313–20
[5] Leyens C et al 2006 *JOM* **58** 17-21
[6] Cinca N et al 2013 *J.Mat. Res.Techn.* **2** 75–86
[7] Suryanarayana C and Koch C C 2000 Hyperfine *Interactions* 5–44
[8] Ragone D V 1995 *Thermodynamics of Materials* vol 1 (New York: J. Wiley & Sons) p 336
[9] Deevi S C and Sikka V K 1997 *Intermetallics* **5** No 17-27
[10] Liu G et al 2013 *Internat. J. Refract. Metals and Hard Mat.* **39** 90-102
[11] http://amt-advanced-materials-technology.com/processing/melt-spinning/
[12] Munir ZA et al 2006 *J. Mat. Sc.* **41** 763-777
[13] Estrin Y and Vinogradov A 2013 *Acta Ma.***61** 782-817
[14] Orban R L 2004 *Rom.Rep.in Phys.***56** 557-570
[15] Lawley A, Koczak M J and Orban R L 1995 *Proc. EuroPM'95* Birmingham UK (EPMA)
[16] Ferro R and Saccone A 2008 *Intermetallic Chemistry* (Amsterdam:Elsevier) pp 566-572
[17] Kubaschewski O 1993 *Materials Thermochemistry* (Oxford: Pergamon Press NY p. 323
[18] * * * 2007 *Match Phase Identification from Powder Diffraction* (Paris: ESRF)
[19] Rodriguez C J 1993 *Physica B* **192** 55-69
[20] Cullity B D 1995 *Elements of X-ray Diffraction* Sec. ed. (New York: J. Wiley & Sons) p. 248